Efficient simulation of non-linear kerb impact events in ground vehicle suspensions

Hubertus v. Chappuis
Dipl. Ing. MSc

A Thesis submitted in partial fulfilment of the Degree of Doctor of Philosophy of Loughborough University.

Wolfson School of Mechanical and Manufacturing Engineering
Loughborough University
Loughborough, Leicestershire LE11 3TU
UK

April 2012

Loughborough University

Abstract:

In the increasing competition which pervades the automobile sector, it is necessary to develop simple methods to enable prediction of suspension loading level envelope in an early development stage. For this purpose, the FORD specified standard driving manoeuvres, based on kerb strike and pothole braking, inducing worst case loading scenarios are employed. The damaging nature of these tests and the relatively expensive physical prototypes make simple simulation models essential. These models should cope with an initial rudimentary assessment, but must suffice to predict the maximum wheel centre loads with a reasonable degree of accuracy.

Enhanced model features are required to represent edge-type tyre deformation and impulsive bumper deflection. State of the art approaches are physical tyre models extended to rim clash modelling and rheological bumper models embedded in an multi-body system (MBS) environment. These enhancements lead to increased complexity.

The thesis proposes a minimal parameter vehicle model, tailored to predict vertical suspension loads caused by the FORD kerb strike manoeuvre. Since the focus is put on model simplicity, an in-plane bicycle model is extended to 7 degrees of freedom. Non-linear and hysteretic characteristics of the bump-stop elements are included through use of a spatial map concept, based on displacement and velocity dependent hysteresis. Furthermore, a static tyre model is described to predict the radial stiffness against penetration of an edge and flat-type rigid body geometry. The full mathematical model is derived on the basis of the shell theory and represented in terms of few geometrical input parameters. A distinct tyre model, representing the tyre belt as a multi-link chain is also derived to confirm the assumptions made in the simple mathematical model. Model validation is supported through experiments at both component and system levels. It is shown that the bumper map concept provides an accurate, yet simple alternative to a rheological model, if applied to polyurethane foam type bumpers. This approach is also confirmed for the tyre model, substituting a comprehensive physical model approach.

Keywords: Vehicle Suspension, tyre modelling, spatial map concept, multi-body system

This thesis is dedicated to
my parents and my family

Acknowledgements:

I thank my research supervisors Prof. Homer Rahnejat, Mr. Paul King and Dr. George Mavros for many fruitful debates, their friendly guidance, passion in the topic and their outstanding academic advice and support.

I also thank Ford Motor Company for continuously sponsoring this project despite the economic downturn 2008 – 2009, which has been the worst crisis seen in automotive industry since WW-II.

This thesis would not have been possible without the patience and support of my Ford supervisor Armin Lepold and his predecessor Gerhard Ammon, who always encouraged me to continue. Furthermore, I am grateful for the inspiration and motivation I received from my colleagues and friends, Dr. Burkhard Pfingsthorn and Dr. Andreas Müschen. I also thank Stanislaus Kazimierczyk for his FE calculations provided to confirm the tyre results. Last, but not least, I want to thank the FORD test engineers Dr. Peter Günther, Dirk Beismann and Jens Goldbeck for their support to set up the bumper and tyre test rigs. If you ever get the mission to fly to the moon in a 'Tin Lizzy', these gentlemen are the right ones to take with you.

Table of contents

Chapter 5: Jounce bumper simulation model

Chapter 6: Minimal parameter in plane static tyre model

Chapter 7: Model Validation

Chapter 8: Parameter study

Chapter 9: Source Code structure

Notation

a	Chapter 1: Tyre belt ring radius	[m]
	Front wheel center to vehicle CoG	[m]
ac	Max possible radial belt extension	[m]
b	Chapter 1: Tyre belt width	[m]
	Rear wheel center to vehicle CoG	[m]
bc	Sidewall radian length	[m]
bt	Width of tyre belt	[m]
c	Wheel center vertical distance to vehicle CoG	[m]
ci	Components of stiffness matrix	[N/m]
cl	Tyre belt bar element width	[m]
cx	Longitudinal vehicle suspension stiffness	[N/m]
cz	Vertical vehicle suspension stiffness	[N/m]
d	Distance between belt steel layers, equations (1.17), (1.18)	[m]
	Height of belt cross section, equation (1.19)	[m]
f	Radial tyre deflection	[m]
fc	Tyre sidewall warpage deformation	[m]
fe	External forces	[N]
fmax	Maximum radial tyre deflection to rim contact	[m]
fx	Chapter 2: Lateral external force applied to vehicle element	[N]
	Chapter 4: Belt deformation in radial direction	[m]
fz	Chapter 2: Belt deformation in circumferential direction	[m]
	Chapter 4: Vertical external force applied to vehicle element	[N]
g	Gravity constant	[m/s^2]
h	Chapter 4: Vehicle CoG height to ground	[m]
	Appendix A: Integration step size	[s]
h_L	Height of tyre belt cross section	[m]
hp	Tyre patch length in flat contact to ground	[m]
hrim	Half tyre planar patch length in rim contact	[m]
hs	Kerb height	[m]
k	Belt bedding factor	[/]
k_r	Tyre radial stiffness of sidewall foundation	[N/m]
k_θ	Tyre circumferential stiffness of sidewall foundation	[N/m]
ls	Tyre radial sidewall span length	[m]
my	Pitch moment applied to body	[Nm]
m1	Front wheel unsprung mass	[kg]
m2	Rear wheel unsprung mass	[kg]
m3	Body sprung mass	[kg]

n	Belt line moments directed radial	[Nm/m]
p	Chapter 1: Belt line load directed lateral	[N/m]
	Chapter 4: Tyre inflation pressure	[Pa]
q	Chapter 2: belt line load directed radial	[N/m]
q	Chapter 4: generalized system coordinate	[m, rad]
q	Chapter 6: rope line load	[N/m]
q_r	External radial line force	[N/m]
q_θ	External tangential line force	[N/m]
ri	Tyre bead radius	[m]
sh	Tyre sidewall lateral slack hang in deformed tyre condition	[m]
t	Chapter 2: belt line load directed circumferential	[N/m]
	Time	[s]
tc	Membrane thickness of shell element	[m]
u	Chapter 2: Belt deflection directed circumferential	[m]
	Chapter 6: Exponent to derive sidewall force	[/]
v	Belt deflection directed lateral	[m]
w	Belt deflection directed radial	[m]
x	Lateral degree of freedom for vehicle model	[m]
z	Vertical degree of freedom for vehicle model	[m]
A	Three dimensional array for spline coefficients	[/]
[C]	Vehicle stiffness matrix	[N/m, Nm/rad]
CJB1	Front jounce bumper stiffness	[N/m]
CJB2	Rear jounce bumper stiffness	[N/m]
CRB1	Front rebound stop stiffness	[N/m]
CRB2	Rear rebound stop stiffness	[N/m]
D	Tyre ring bending stiffness	[Nm/rad]
[D]	Vehicle damping matrix	[kg/s]
E	Elasticity modulus	[N/mm^2]
Ekin	Kinetic energy	[Nm]
Epot	Potential energy	[Nm]
F	Chapter 2: Belt cross section area of the steel layer	[mm^2]
F	Chapter 5:Bumper force map feedback force	[N]
F0 – F5	Front suspension geometry parameters	[m]
Fc	Radial tyre force	[m]

Fe	External force vector apllied to vehicle system	[N]
Fg	Tyre belt circumferential force	[N]
Fgcorr	Corrected tyre belt circumferential force	[N]
FJB1	Front jounce bumper contact force	[N]
FJB2	Rear jounce bumper contact force	[N]
FRS1	Front rebound stop contact force	[N]
FRS2	Rear rebound stop contact force	[N]
Fp	Pneumatic force acting on single belt chain element	[N]
Fr	Belt longitudinal force	[N]
Fri	Sidewall force on rim increment	[N]
Fs	Tyre belt radial sidewall force	[N]
Fsw	Sidewall force acting on single belt chain element	[N]
Fsw1	Sidewall force for max. radial belt extension (stretched span)	[N]
Fsw2	Sidewall force for max. radial belt deflection (rim contact)	[N]
Ftm	Total top mount force	[N]
Fw	Wheel force on spindle	[N]
G	Shear modulus	[N/mm^2]
H	Horizontal rope force (rope under constant line load)	[N]
Ip	Polar moment of area	[mm^4]
Ix	Lateral belt moment of area	[mm^4]
Iy	Lateral moment of area	[mm^4]
J	Moment of inertia	[kgm^2]
JB1z	Front jounce bumper deflection	[m]
JB2z	Rear jounce bumper deflection	[m]
K	Ring membrane stiffness	[N/m]
L	Wheel base	[m]
Le	Effective length affected by radial tyre deflection	[m]
[M]	Vehicle inertia tensor (mass matrix)	[kg, kgm^2]
N	Inflation tension force	[N]
Po	Chapter2: Inflation pressure	[N/m^2]
Px	Horizontal (x-) force component at free end of belt chain	[N]
Pz	Vertical (z-) force component at free end of belt chain	[N]
Q	Belt radial shear force	[N]
Qsg	Tyre sidewall line load attached to belt	[N/m]
Qsr	Tyre sidewall line load attached to rim	[N/m]
R	Chapter 2: Tyre ring radius	[m]
R	Chapter 6: Tyre sidewall radius variable in-between ri and Ra	[m]
R0 – R5	Chapter 4: Rear suspension geometry parameters	[m]
R1, R2	Chapter 6: Curvature radii of double curved shell elements	[m]

Ra	Outer wheel radius (belt)	[m]
RB1z	Front rebound stop deflection	[m]
RB2z	Rear rebound stop deflection	[m]
Rk	Minimal sidewall curvature radius	[m]
Rm	Mean sidewall radius in-between ri and Ra	[m]
S	Tyre deflection vector (chain model)	[m]
S0	Amplitude of harmonic actuation	[m]
S1x,z	Front wheel centre initial distance to kerb at t = 0	[m]
S2x,z	Rear wheel centre initial distance to kerb at t = 0	[m]
To	Belt circumferential force	[N]
U1x,z	Front wheel centre distance to kerb edge	[m]
U2x,z	Rear wheel centre distanzce to kerb edge	[m]
UJB1	Front free wheel travel to jounce bumper contact	[m]
UJB2	Rear free wheel travel to founce bumper contact	[m]
URB1	Front free wheel travel to rebound stop contact	[m]
URB2	Rear free wheel travel to rebound stop contact	[m]
V	Chapter 2: Belt lateral shear force	[N]
V	Velocity of element deflection	[m/s]
W	Work	[Nm]
α	Radial sidewall force angle relative to belt	[rad]
α_t	Belt element subdivision angle	[rad]
β	Chapter 2: Belt wire layer angle	[rad]
β	Tyre belt contour angle for radial edge deformation	[rad]
γ	Chain element angle without radial deformation	[rad]
γ_1	Direction angle kerb edge to wheel centre	[rad]
δr	Virtual deflection	[m]
δW	Virtual work	[Nm]
ε	Sidewall force direction relative to negative z- axis	[rad]
φ	Chapter 2, 6: Tyre circumferential angle	[rad]
φ	Chapter 4: Body pitch angle	[rad]
φ	Chapter 5: Phase angle	[rad]
ρ	Material density	[kg/m^3]
$\sigma 1$	Plane one membrane stress in double curved shell element	[Pa]

$\sigma 2$	Plane two membrane stress in double curved shell element	[Pa]
ψ	Belt torsion angle	[rad]
ω	Circular velocity of element actuation	[rad/s]
θ	Tyre circumferential angle	[rad]

Glossary of terms and abbreviations

ADAMS	Automatic dynamic analysis of mechanical Systems
BiP	Brake into pothole
CD	vehicle size scale in between medium (C) and large (D)
CoG	Centre of gravity
DoF	Degree of freedom
DoK	Drive over kerb
FEA	Finite-element analysis
FEM	Finite-element method
FoE	Ford of Europe
FORTRAN	Formula transition
JB	Jounce bumper
MBS	Multi-body system
OEM	Original Equipment Manufacturer
PU	Polyurethane
RBS	Rebound stop
RS	Road spring
SaK	Skid against kerb

Chapter 1: Introduction

As the computation performance increased over the past years, the trend goes towards enhanced simulation model complexity taking more and more physical effects and structure details into account. A high grade model complexity enables to optimize the design in a final stage. However, in an advanced stage of a chassis development, only the main dimensions and parameters are available whereas final details are not established. In this stage, concept studies and basic investigations are required and model simplicity is preferred to complexity for an easy model set up and variation.

In the advanced chassis development stage, the load assumption defines the basis for any following design activity. Therefore, a simple vehicle simulation model and simple driving events specified are beneficial for an initial load assumption, as suspension loads and deflections are related to both vehicle features *and* driving manoeuvres. Arbitrary manoeuvres in general lead to combined body rotation modes, a superposition of roll-, pitch- and yaw-motion. To analyse such events, three dimensional vehicle modelling is required, which does not ideally match with the desire of model simplicity. To address this aspect, FORD has specified worst case driving manoeuvres 'Skid against Kerb' (SaK), 'Drive over Kerb' (DoK) and 'Brake into Pothole' (BiP), intended to investigate the lateral-, vertical- and longitudinal suspension travel- and load range. As neither DoK nor BiP manoeuvre are expected to cause relevant roll- or yaw motion, the latter events are applicable to a simplified plane vehicle model approach.

1.1 FORD specified standard driving manoeuvres

The Skid against Kerb (SaK) manoeuvre describes a side impact of a sliding vehicle against a kerb with the intention to cause the maximum lateral loads. This driving event is not further considered in this thesis, dedicated to predict the vertical suspension loads.
The DoK manoeuvre, as shown in Figure 1.1, is intended to generate the maximum vertical suspension force and wheel centre deflection relative to the body and represents the central aspect of this research project. The manoeuvre is defined by a straight crossing of a bar with rectangular cross section in a free roll mode decoupled from power train. The intention is to simulate a kerb strike. Such events cause large scale vertical

deflections of the suspension, in general limited by a jounce bumper element, its initial contact position and deformation range. The bumper engagement during the DoK manoeuvre is of an impulse kind nature and in most cases causes a deformation using the full bumper deflection range.

The vehicle speed is specified for two velocity levels, 25 and 40 kph. Kerb height can be adjusted for different vehicle classes to cope with various tyre- and ground clearance dimensions.

Figure 1.1: Drive over Kerb (DoK) and Brake into Pothole (BiP) driving manoeuvre

The BiP manoeuvre (Figure 1.2) is intended to generate the maximum longitudinal suspension forces and wheel centre deflection. The manoeuvre is initiated with a 100% braking at approximately 1.5 meters in front of a rectangular pothole. The braking point is adjusted to remain a pothole entrance velocity of 35 km/h at the entry edge. As the brakes are blocked permanent, the wheel remains in full slide mode during the pothole pass. According to experience, the maximum lateral suspension load level occurs during the wheel clash against the rear pothole edge. To test abuse load cases, a belt to rim clash in contact with the kerb edge is intended for both BiP and DoK manoeuvre.

Figure 1.2: Brake into Pothole (BiP) driving manoeuvre

The simple rectangular obstacle cross section geometry used in both events allows an easy transition into a mathematical formulation. Furthermore, the boundary conditions (speed level, obstacle geometry) can easily be adjusted and reproduced to physical testing and simulation.

1.2 Instigation of research work

A common feature of both tests is an impulse like jounce bumper and tyre engagement which cause large scale deflections over the full deformation range and a belt to rim clash against the kerbstone. This aspect drives the challenge for the tyre and bumper simulation approach aligned with the requirement of simplicity.

In FoE, current simulation models are based on three dimensional, full vehicle MBS models in conjunction with a flexible tyre model, the so called F-tyre **[3]**. This physically based, comprehensive dynamic tyre model is represented by an MBS structure that takes structural- and pneumatic force response caused by belt and sidewall deformations into account. It is intended to simulate longitudinal-, lateral- and vertical force response. To set up and parameterise such models is a complex task and requires several standardized physical tests **[8]**. In FoE, the demand for a simplified tyre model was raised, condensed to cope with the limited boundary conditions in connection with the exclusive application to BiP and DoK application.

Another important aspect in abuse driving simulation is the bumper dynamic force transfer. The current bumper simulation approach in FoE is based on a simple static force response curve in combination with a viscous damping. It is FoE experience and addressed in literature **[56]** that the dynamic force response of foam type bumper elements made of polyurethane can significantly deviate from static behaviour. Whereas the static force response can easily be recorded from physical testing, a damping coefficient can not be measured directly. This shortfall can be avoided by the use of rheological models that will be discussed in the subsequent literature review. With these models, dynamic force response features can be simulated accurately, but in general they do not fulfil the demand of model simplicity. Kerb strike simulations performed with the current simple bumper model approach revealed peak load level within a wide band width of twenty to eighty kN, depending on the estimated damping value. Measured vertical bumper peak loads recorded on a front McPherson suspension of a FORD CD

car achieved a level of forty kN during kerb strike tests. This uncertainty reinforces the need for an improved bumper simulation method that addresses the bumper specific hysteresis features in case of impulsive load application.

1.3 Aim of the Project

The aim of this project is to set up a minimal parameter vehicle model tailored to simulate the FORD specified DoK event. It is intended to predict the worst case vertical loads envelope for wheel centre and jounce bumper in the advanced development stage. The model shall be applicable for upfront engineering, parameter studies and plausibility checks based on a minimal set of input parameters.

Special focus shall be set on a simple modelling approach for bumper and tyre subjected to impulsive kind loads caused by the nature of kerb strike events. Thus, the tyre model shall be condensed to the limited scope of a simplified kerb contact. It shall be applicable to simulate the static force response for full range tyre deflection against an edge type radial deflection. To cope with the demand of model simplicity, only the pneumatic induced force response shall be addressed, whereas the tyre structure compliance shall be neglected.

The bumper simulation concept shall take the hysteresis features into account. Bumper- and tyre model validity shall be demonstrated on the basis of kerb strike relevant component tests.

The vehicle model shall be set up for a FORD specified CD car and assessed to bumper measurements gained from physical kerb strike tests. Finally, a parameter study shall reveal the plausibility of the model results. The following literature study in particular addresses these items.

The objectives can be summarized as follows:

- Develop a minimal parameter vehicle model, tailored for the simulation of the vertical suspension load after kerb strike. It shall be adapted to the FORD specified boundary conditions for DoK and shall also protect upgrade compatibility to simulate the BiP event at a later stage.

- Generate a valid alternative to a rheological approach for a bumper model that takes the velocity induced hysteresis into account.

- Derive a tyre model to simulate the pneumatic induced static force response against flat and edge type radial deformation.

- Validate the bumper and tyre models by an assessment to appropriate physical testing on component level.

- Validate the vehicle model equipped with the bumper and tyre simulation approaches on system level by a full vehicle DoK testing.

- Carry out a parameter study to verify the plausibility of the vehicle model on basis of a specific FORD vehicle.

1.4 Novelty

The bicycle model as shown in Figure 1.59 at the end of the literature study, derived as an MBS simulation, is a known concept. The novelty aspects in this thesis are considered for the concepts used to simulate the jounce bumper element, presented in chapter 3, and the tyre simulation model, described in chapter 4.

The jounce bumper simulation is based on a spatial map concept and takes the velocity related hysteresis of polyurethane type bumper elements into account. The mathematical concept enables the direct transfer of measured force response data into a map of standardized format, embedded into a feedback loop to the solver. This approach represents an alternative to the rheological model published in **[56]**.

A mathematical model, aimed to analyse the internal tyre structural stress and the force response to radial deformation, is presented in this thesis. The mathematical model describes a simplified tyre structure and is based on classical structure approaches, in particularly shell theory **[58]**, **[59]**, **[60]**. It can effectively be used to analyse the internal tyre structural stress and the quasi static force response against a flat- and edge type radial deformation.

Beside the mathematical model, a plane, truss-type flexible ring model is discussed. This model is considered to be applicable for the contact deformation against arbitrary geometries. The virtual work principle is used in combination with a numerical iteration to provide solutions for a static force response curve. The flexible ring model was used to confirm the solutions gained from the mathematical model. Both models were assessed to physical test results. The virtual work principle is of advantage because it provides solutions without the burden involved with the solving of either an equation system but pays the price with a computer intensive iteration. The algorithm is casted in the format of 'stand alone' software, independent from the central solver used for the vehicle model. Both mathematical and flexible ring tyre models are based on four parameters derived from cross section geometry and pneumatic pressure.

Chapter 2: Literature study

2.0 Structure of study

The thesis intends to cover aspects of vehicle, tyre- and bumper dynamics subjected to harsh vertical driving manoeuvres. This chapter is devoted to review of literature addressing vehicle dynamics, with a focus on large scale vertical suspension travel or abusive driving manoeuvres that cause large tyre radial deformation. Subsequent, a brief introduction is made to general methods for modelling mechanical systems and their application to vehicle, tyre and polymeric element simulations. As a large number of vehicle, tyre and polymeric models exist, targeted for very different purposes of investigations, a selection of these is made with regard to harsh vertical and longitudinal driving events. The overview of vehicle modelling is extended to gain an insight into the physical aspects of the tyre contact patch and related simulation methods. With regard to abusive manoeuvres, a key role is envisaged for jounce bumper load transfer characteristics. Thus, the study is extended to a general summary of mechanical properties of elastomers and the commonly employed simulation approaches, where additionally sources dealing with bumper testing and simulation are discussed. The study culminates with description of underlying choices made in various modelling approaches in literature.

2.1 Vehicle testing and simulation under abusive manoeuvres

An abusive driving manoeuvre is intended to investigate a vehicle subjected to loads that are beyond the usual levels expected in the normal operational envelope of a vehicle usage. High/impulsive loads typically occur while traversing extreme obstacles such as potholes or kerb sides. Such manoeuvres reveal the system loading limits for plastic deformation and are also intended to confirm the so-called *chain of failure* event, which highlight failed components with defined load levels.

These investigations are in general performed through physical testing and thus are quite cost intensive, as prototype vehicles in most cases are partially destroyed through the testing procedure. Therefore, there is interest in an effective simulation approach.

An early abusive simulation study was performed by Rai and Solomon in 1982 **[1]**. The authors set up a 3D vehicle simulation model using ADAMS, a standardized commercial multi-body system (MBS) software. The vehicle model incorporated 26 DoF. A simple tyre model, based on a linear spring and viscous damper was used. Separate jounce and rebound bumper models were linked through external FORTRAN subroutines to the ADAMS environment. Bumpers were defined as non-linear force-deflection curves, based on fourth order polynomial fits of measured characteristics. The simulation was intended to analyze the lower ball joint forces of a McPherson strut front suspension. Thus, the kinematics and inertias of the control arm, steering knuckle, strut and the tie rod were included in the MBS model. The driving manoeuvres included kerb side impact, rail track and chuck hole crossing as shown in Figure 2.1. The intention was to define an envelope for the ball joint loads.

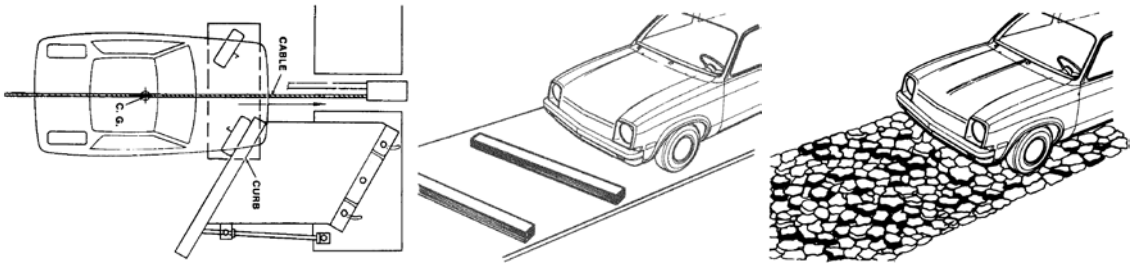

Figure 2.1: Kerb side impact, rail track and chuck-hole crossing abusive manoeuvres **[1]**

The authors published the various force traces obtained for the ball joint load time history (Figure 2.2) and concluded that a more comprehensive tyre and bumper simulation method would be required for the proper simulation of vertical suspension loads.

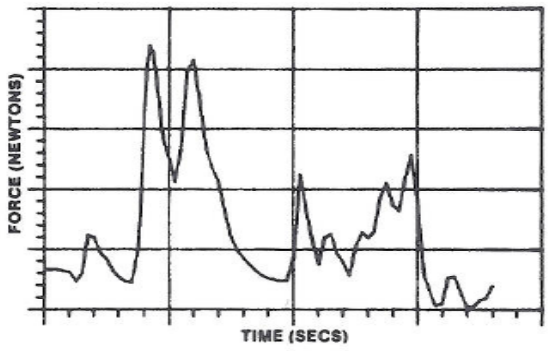

Figure 2.2: Ball joint load simulation results after railroad crossing **[1]**

Unfortunately, no scales were provided with their graph plots (Figure 2.2).

Appropriate tyre models which included features allowing a more detailed coverage of effects induced by kerb strike events were proposed by Bäcker and Gallrein **[2]** and Gipser **[3]**. These models enable deformation of a belt, extending to the wheel rim clash, which is typically encountered during kerb strike.

Haga et al. **[4]** assessed these models for durability studies in the first instance. They set up a full quarter car front suspension on a rotating drum, shown in Figure 2.3 in order to activate tyre excitation. The drum was equipped with elliptic cleats of different sizes up to a vertical height of 46 mm in order to cause longitudinal and radial tyre actuation.

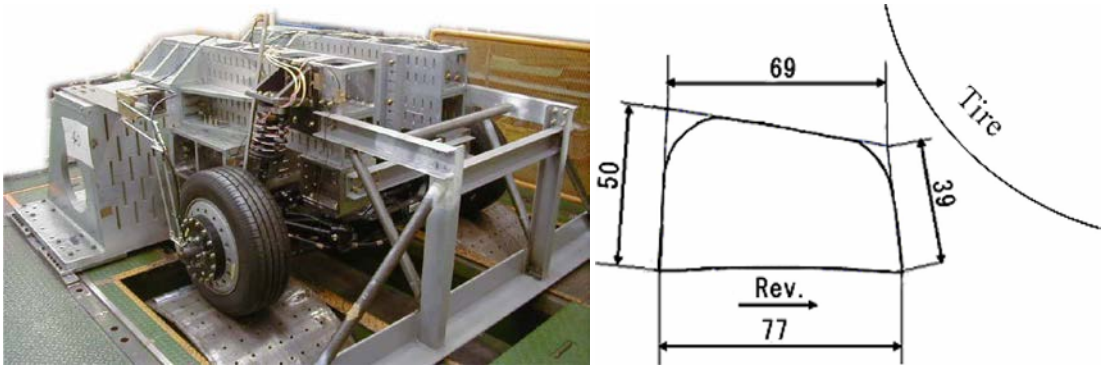

Figure 1.3: Drum rig set up and 46 mm height cleat geometry **[4]**

Data acquisition was performed for speed of 20 and 40 km/h. An assessment of flexible tyre belt models demonstrated close correlation with the measurements of the vertical force as shown in Figure 2.4.

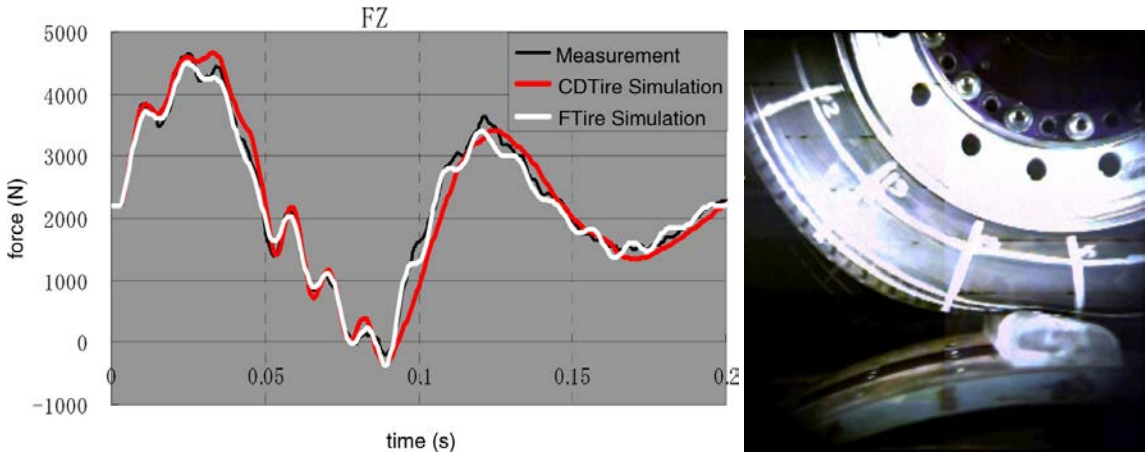

Figure 2.4: Vertical force assessment for a 48 mm cleat at 20 km/h **[4]**

The illustration on the right side of the Figure reveals that even at the maxium vertical force position, the cleat does not cause a belt-to-rim clash condition, which would be expected for an abusive kerb strike event. Thus, Haga et al. **[4]** extended the testing conditions to large tyre deformations and applied it to a single tyre test rig, tailored for severe events **[5]**. The drum rig was replaced by a horizontal test bench to establish roll-over kinematic conditions which matches closer to prevailing longitudinal loading conditions. These are expected for obstacle roll-over manoeuvres on flat ground. A cleat crossing event, as shown in Figure 2.5, addresses these issues. Consequently, the CDTire model 40 (addressed later in the thesis) was extended by Bäcker and Gallrein **[6]** to cope with very large tyre deformations that cause a belt to rim clash conditions.

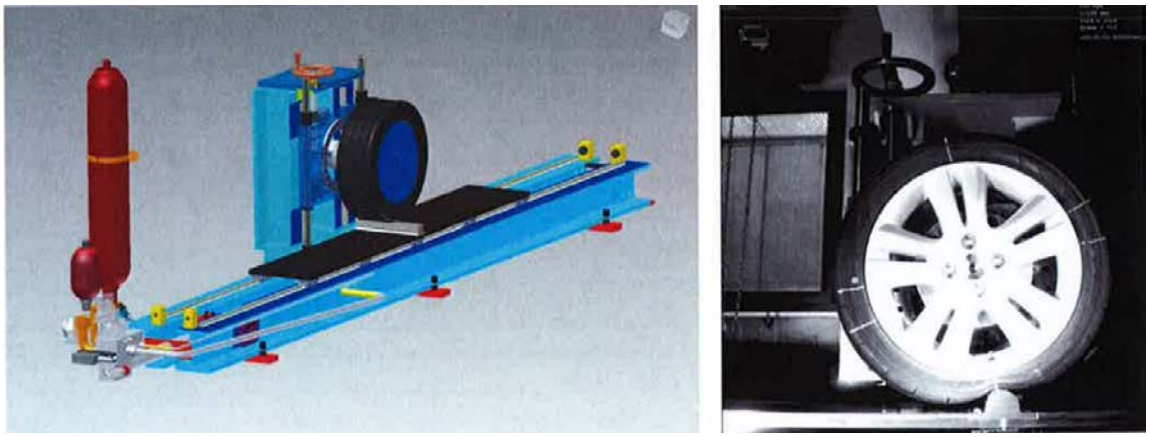

Figure 2.5: Principal set up and operation of the Fraunhofer LBF horizontal test rig for large deformations **[6]**

Vertical and horizontal forces were recorded for simulation studies involving use of a cleat of 40 mm height, using a 205/45 R 16 sized tyre at 5 km/h as shown in Figure 2.6.

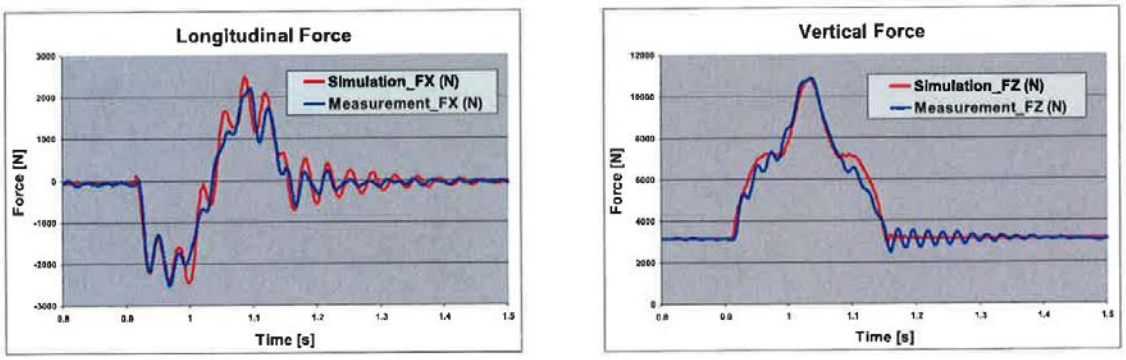

Figure 2.6: Longitudinal (FX) and vertical force (FZ) after cleat crossing at 5 km/h for tyre size 205/45 R16 **[6]**

These sources demonstrate the general force response characteristics of a full range radial tyre deformation, followed by a moderate belt to rim clash. This effect is seen as a relevant feature which needs to be appreciated in any simulation study of kerb strike events.

An alternative proposal for a full vehicle simulation on basis of an MBS model that includes FEM structures was performed by Yoon and Kye **[7]** in 2004. The vehicle model was set up as a hybrid approach on the basis of an MBS structure, embedding single FEM component structures. Figure 2.7 illustrates the model concept, exemplarily for the lower control arm of a McPherson front suspension.

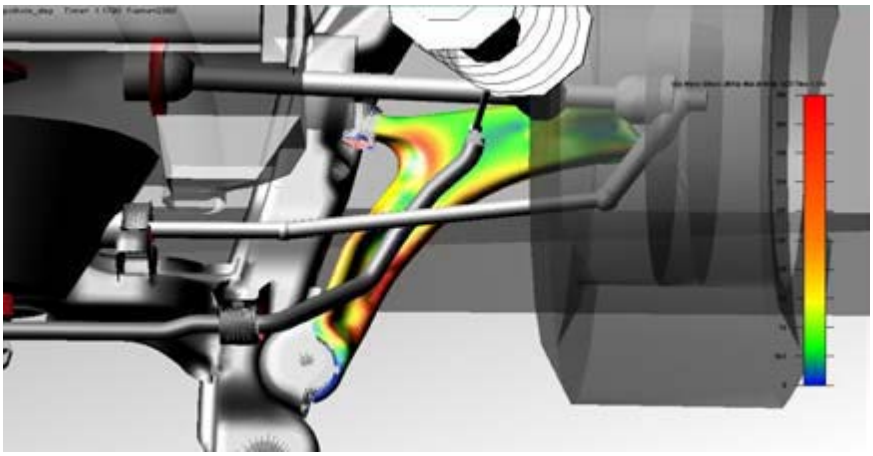

Figure 2.7: Lower control arm FEM structure embedded into MBS vehicle model **[7]**

The vehicle model was equipped with a flexible tyre model using FTire, provided by Gipser **[8]** to simulate a severe pothole crossing at 50 km/h and a five inch (12.7 cm) square kerb profile, crossing at a speed of 30 mph. The FTire is addressed in more detail in the following tyre paragraph. Results for the vertical wheel centre forces are shown in Figure 2.8.

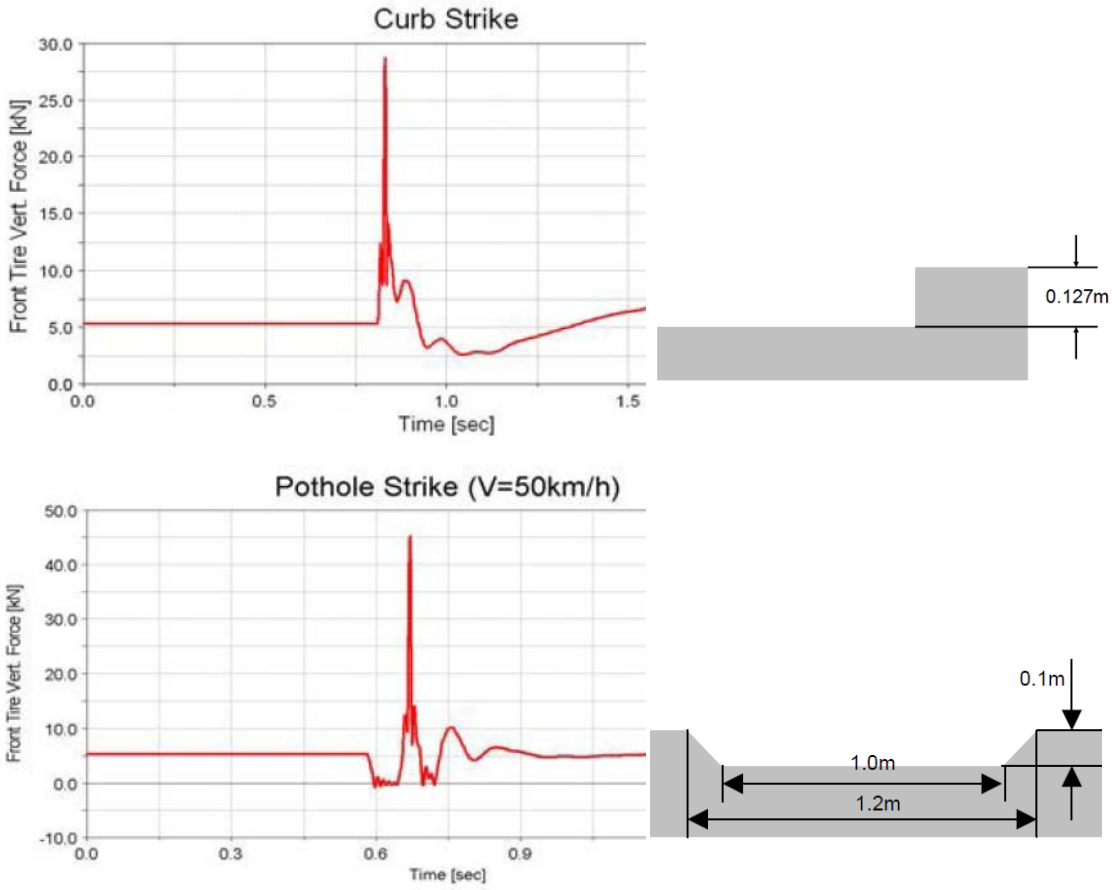

Figure 2.8: Pothole geometry and vertical wheel force simulation results for pothole- and kerb crossing **[7]**

It is noted that the peak load reported for the pothole braking manoeuvre exceeds the level observed for the kerb strike event. The following item addresses general methods used for structural analysis.

2.2 General simulation approaches used for structure analysis

Common to all physical-based simulation approaches, aiming to model machines and mechanisms is the problem of defining appropriate structural properties and represent these in a mathematical formalism. Broadly, three main methods for description of structures are used **[9]**:

- continuous structure
- Finite Element (FE) structure and
- Multi – Body system (MBS) structure

A vehicle, as any other physical solid structure, by its nature is a *continuous* system. Mass and stiffness are distributed continuously within the structural geometry. However, analytical formulations which describe a continuum are known for simple structure geometries only, such as rope, beam, plate, disc or shell elements. Unfortunately, the number of solutions found for such structures is even more limited, because certain simplifying assumptions have to be made, such as homogeneity, isotropy as well making restrictive conditions **[10]**, **[11]**. As the result of these shortcomings, the continuous structural approach is not suitable for detailed overall vehicle modelling, but remains useful to analyse discrete problems such as a modal structural analysis e.g. applied to an elastic ring representing a tyre belt **[12]**.

Finite Element structures consist of elastic, straight line edged elements endowed with inertial properties **[13]**. The elements are linked by nodes and therefore approximate the structural geometry by a polygon contour (grid). The element stiffness and inertial properties are usually idealized by shape functions derived from beam, plate or shell theories and are related to the grid nodes which transmit load. The sub-division of a structure into elements (discretization), in general, is performed using numerical algorithms. This process results in a set of linear equations according to the number of elements. In case of improper discretization, e.g. large element size not suitable to recognize localized conditions, the numerical results found for stress and strain can significantly deviate from the intended real physical structural behaviour. On the other hand, a fine level of discretization can easily raise the number of equations to an excessive level. Thus, a convergence study is needed to establish an appropriate size and

number of elements. FE structures are mainly used for static stress-strain and modal analyses, but in general exceed the computational available power to simulate comprehensive driving manoeuvres in the time domain.

Other than the FEM, the *Multi-Body system* approach, as applied in this thesis, is based on the concept of sub-dividing a continuum into a set of linked single elements. Structural elastic and inertial properties are addressed separately in the model by two sets of elements. Elasticity and damping are described by massless spring and damping elements which link the structural elements (these are the system compliances), whereas the inertia properties are represented by rigid bodies only. In contrast to the FEM approach, the MBS structural sub-division depends on the engineering judgement intended to align the properties of the structural model with the simulation task. This implies that different simulation purposes in general would lead to a unique model architecture.

1.2.1 Mathematical formulation of an MBS system

The rigid bodies of an MBS structure are defined by their inertia properties, their position and orientation in space and by the nature of their linkages to other bodies and any attachments to the ground **[16]**. The mathematical formulation is condensed to the dynamic force balance comprising:

- inertial forces of the rigid bodies
- structural internal forces
- external applied forces

This force balance leads to a set of second order ordinary differential equations; the equations of motion. In general, each rigid body has six DoF, three translational and three rotational. For each DoF, an equation of motion can be set up. Thus, the number of equations corresponds to the number of 6p, where 'p' stands for the number of bodies used in the model architecture. However, the total number of system DoF can be reduced by kinematic constraints such as joints, or restraints such as massless bars or straps. These constraints can be of holonomic or non-holonomic in nature, depending on whether their formulation depends on the element location only (holonomic) or their state of motion (rheonomics). Furthermore, constraints can be separated for being time-

dependent (rheonomic) or time-independent constraints (scleronomic) **[16]**. By taking this into account, the system number of DoF reduces to f = 6p – m, where 'm' represents the number of constraint functions.

1.2.1.1 System kinematics

All approaches applied to set up the equations of motion initially depend on the kinematic formulation of the velocity and acceleration state. This state needs to be derived upfront (initial conditions) for each rigid body of the system. The system state is defined by the components of the *position* vector $\boldsymbol{q} = (q_1, q_2, \ \ldots \ , q_f)^T$ which contains all the system DoFs. These coordinates are known as the generalized and represent the minimal set, mandatory to comprehensively describe the system motions. To analyse this minimal number of degrees of freedom, the Chebychev-Gruebler – Kutzbach equation can be used **[14]**, where f is the number of generalized coordinates, p = number of bodies, c = number of constraint elements in the system and Nj stands or the number of constraints of the j'th constraint element.

$$f = 6(p-1) + \sum_{J=1}^{c} iN_j \tag{2.1}$$

An instant derivation of the CoG (centre of gravity) velocities from generalized coordinates can be a difficult task, especially if complex kinematic constraints need to be recognized. Alternatively, the system state is also defined by the three components of a *position* vector $\boldsymbol{r}_S = (x_S, y_S, z_S)^T$ derived for an inertial coordinate system. The vector points on the CoG position of each rigid body and is extended by three orientation angles α, β, γ, which describe the body rotational orientation relative to the inertial system. Besides the DoF, the position vector includes also the kinematic constraint formulations. Despite the fact that the minimal parameter vehicle model proposed in chapter 4 does not contain kinematic constraints and thus, a derivation of constraint formulations was not applied in this thesis, the following shall present the general method of how constrained formulations can be derived.

Location and *position* vectors are related by the Jacobian matrices for translation $\boldsymbol{J}_T$ and rotation $\boldsymbol{J}_R$ **[14]**, **[15]**, **[16]**. Matrix $\boldsymbol{J}_T$ describes the relation between the Cartesian position vectors $\boldsymbol{r}_{Si}$ and the generalized coordinates $\boldsymbol{q}$ of the MBS system.

$$\boldsymbol{J}_{Ti} = \frac{\partial \boldsymbol{r}_{Si}}{\partial \boldsymbol{q}^T} = \begin{bmatrix} \frac{\partial x_{Si}}{\partial q_1} & \frac{\partial x_{Si}}{\partial q_2} & \cdots & \frac{\partial x_{Si}}{\partial q_f} \\ \frac{\partial y_{Si}}{\partial q_1} & \frac{\partial y_{Si}}{\partial q_2} & \cdots & \frac{\partial y_{Si}}{\partial q_f} \\ \frac{\partial z_{Si}}{\partial q_1} & \frac{\partial z_{Si}}{\partial q_2} & \cdots & \frac{\partial z_{Si}}{\partial q_f} \end{bmatrix} \tag{2.2}$$

This matrix allows the formulation of the translational velocities and accelerations of the CoG positions relative to the inertial system by means of the matrix operations:

$$\begin{aligned} \boldsymbol{v}_{Si} &= \boldsymbol{J}_{Ti} \cdot \dot{\boldsymbol{q}} + \bar{\boldsymbol{v}}_{Si} \\ \dot{\boldsymbol{v}}_{Si} &= \boldsymbol{J}_{Ti} \cdot \ddot{\boldsymbol{q}} + \dot{\boldsymbol{J}}_{Ti} \cdot \boldsymbol{q} + \dot{\bar{\boldsymbol{v}}}_{Si} \end{aligned} \tag{2.3}$$

where:

$$\bar{\boldsymbol{v}}_{Si} = \frac{\partial \boldsymbol{r}_{Si}}{\partial t} = \left(\frac{\partial x_{Si}}{\partial t}, \frac{\partial y_{Si}}{\partial t}, \frac{\partial z_{Si}}{\partial t} \right)^T, \qquad \dot{\bar{\boldsymbol{v}}}_{Si} = \frac{\partial^2 \boldsymbol{r}_{Si}}{\partial t^2} = \left(\frac{\partial^2 x_{Si}}{\partial t^2}, \frac{\partial^2 y_{Si}}{\partial t^2}, \frac{\partial^2 z_{Si}}{\partial t^2} \right)^T$$

and:

$$\dot{\boldsymbol{q}} = \frac{\partial \boldsymbol{q}}{\partial t} = \left(\frac{\partial q_1}{\partial t}, \frac{\partial q_2}{\partial t}, \quad \cdots \quad , \frac{\partial q_f}{\partial t} \right)^T, \qquad \ddot{\boldsymbol{q}} = \frac{\partial^2 \boldsymbol{q}}{\partial t^2} = \left(\frac{\partial^2 q_1}{\partial t^2}, \frac{\partial^2 q_2}{\partial t^2}, \quad \cdots \quad , \frac{\partial^2 q_f}{\partial t^2} \right)^T$$

The rotational Jacobian matrix $\boldsymbol{J}_{Ri}$ describes the relationships between the infinitesimal components of the rotation vectors $\boldsymbol{s}_i$ and the generalized coordinates $\boldsymbol{q}$. These differential components of the rotation vectors $\partial \boldsymbol{s}_i / \partial \boldsymbol{q}^T$ are derived from the total rotation matrix $\boldsymbol{S}_i$ (which may be either of roll-pitch and yaw or Euler transformations):

$$\boldsymbol{S}_i = \begin{pmatrix} \cos\beta_i \cdot \cos\gamma_i & -\cos\beta_i \cdot \sin\gamma_i & \sin\beta_i \\ \cos\alpha_i \cdot \sin\gamma_i + \sin\alpha_i \cdot \sin\beta_i \cdot \cos\gamma_i & \cos\alpha_i \cdot \cos\gamma_i - \sin\alpha_i \cdot \sin\beta_i \cdot \sin\gamma_i & -\sin\alpha_i \cdot \cos\beta_i \\ \sin\alpha_i \cdot \sin\beta_i + \cos\alpha_i \cdot \sin\beta_i \cdot \cos\gamma_i & \sin\alpha_i \cdot \cos\gamma_i - \cos\alpha_i \cdot \sin\beta_i \cdot \sin\gamma_i & \cos\alpha_i \cdot \cos\beta_i \end{pmatrix}$$

by the partial derivation:

$$\frac{\partial \boldsymbol{S}_i}{\partial q_j} \cdot \boldsymbol{S}_i^T = \frac{\partial \boldsymbol{s}}{\partial t} = \begin{pmatrix} 0 & \frac{\partial s_{iz}}{\partial q_j} & \frac{\partial s_{iy}}{\partial q_j} \\ \frac{\partial s_{iz}}{\partial q_j} & 0 & \frac{\partial s_{ix}}{\partial q_j} \\ \frac{\partial s_{iy}}{\partial q_j} & \frac{\partial s_{ix}}{\partial q_j} & 0 \end{pmatrix}$$

which then establishes the Jacobian matrix of rotations $\boldsymbol{J}_R$

$$\boldsymbol{J}_{Ri} = \frac{\partial \boldsymbol{s}_i}{\partial \boldsymbol{q}^T} = \begin{bmatrix} \frac{\partial s_{ix}}{\partial q_1} & \frac{\partial s_{ix}}{\partial q_2} & \cdots & \frac{\partial s_{ix}}{\partial q_f} \\ \frac{\partial s_{iy}}{\partial q_1} & \frac{\partial s_{iy}}{\partial q_2} & \cdots & \frac{\partial s_{iy}}{\partial q_f} \\ \frac{\partial s_{iz}}{\partial q_1} & \frac{\partial s_{iz}}{\partial q_2} & \cdots & \frac{\partial s_{iz}}{\partial q_f} \end{bmatrix} \tag{2.4}$$

and finally leads to the matrix equation for the angular velocities and accelerations:

$$\boldsymbol{\omega}_i = \boldsymbol{J}_{Ri} \cdot \dot{\boldsymbol{q}} + \overline{\boldsymbol{\omega}}_i$$
$$\dot{\boldsymbol{\omega}}_i = \boldsymbol{J}_{Ri} \cdot \ddot{\boldsymbol{q}} + \dot{\boldsymbol{J}}_{Ri} \cdot \dot{\boldsymbol{q}} + \dot{\overline{\boldsymbol{\omega}}}_i$$

with:

$$\overline{\boldsymbol{\omega}}_i = \frac{\partial \boldsymbol{s}_i}{\partial t} = \left(\frac{\partial s_{ix}}{\partial t}, \frac{\partial s_{iy}}{\partial t}, \frac{\partial s_{iz}}{\partial t} \right)^T, \qquad \dot{\overline{\boldsymbol{\omega}}}_i = \frac{\partial^2 \boldsymbol{s}_i}{\partial t^2} = \left(\frac{\partial^2 s_{ix}}{\partial t^2}, \frac{\partial^2 s_{iy}}{\partial t^2}, \frac{\partial^2 s_{iz}}{\partial t^2} \right)^T$$

As mentioned before, the effort required to derive the kinematics of the translational and rotational body motions by means of matrix operations pays back in case of complex systems, as the process can be performed in a fully schematic manner.

1.2.1.2 System dynamics formulation by equations of motion

A significant volume of literature exists in dealing with the derivation of the equations of motion e.g. **[17]**, **[18]**, three general concepts are commonly used:

- Newton – Euler method

- D' Alembert principle
- Constrained Lagrangian dynamics

(a)- The Newton – Euler formulation

Historically, the Newton – Euler approach marks the origin method. After kinematic formulations are established by the vectors and matrices $\boldsymbol{r}_{Si}, \boldsymbol{S}_i, \boldsymbol{v}_{Si}, \boldsymbol{\omega}_i, \dot{\boldsymbol{v}}_{Si}, \dot{\boldsymbol{\omega}}_{Si}$, the equations of motion are derived separately for each single body with regards to translation (Newton) and rotation (Euler). This leads to two matrix equations for the forces and moments $\boldsymbol{f}_i, \boldsymbol{m}_{ip}$ by making use of the principles of linear and angular momentum as:

$$\begin{aligned} \boldsymbol{f}_i &= m_i \cdot \dot{\boldsymbol{v}}_{Si} \\ \boldsymbol{m}_{iP} &= \boldsymbol{J}_{iP} \cdot \dot{\boldsymbol{\omega}}_i + \dot{\boldsymbol{J}}_{iP} \cdot \boldsymbol{\omega}_i \end{aligned} \qquad (2.5)$$

In the general case discussed here, the vectors $\boldsymbol{f}_i, \boldsymbol{m}_{iP}$ contain both, external applied forces $\boldsymbol{f}_{Ei}, \boldsymbol{m}_{EiP}$ and the internal reaction forces respectively, moments: $\boldsymbol{f}_{Zi}, \boldsymbol{m}_{ZiP}$.

The (3, 3) matrix $\boldsymbol{J}_{iP}$ represents the rotational inertial tensor for each of the 'i' rigid bodies, aligned parallel to the inertial system, thus:

$$\boldsymbol{J}_{iP} = \begin{pmatrix} J_{xxP} & -J_{xyP} & -J_{zxP} \\ -J_{xyP} & J_{yyP} & -J_{yzP} \\ -J_{zxP} & -J_{yzP} & J_{zzP} \end{pmatrix} \qquad J_{xxP} = \int \left(y_P^2 + z_P^2\right) dm \qquad J_{xyP} = \int \left(x_P^2 + y_P^2\right) dm \qquad \ldots$$

Similar to the schematic approach, applied for the kinematic formulations, the Newton – Euler equations of motion can now be set up in a format of standardized matrix vector operations by using:

$$\dot{\boldsymbol{J}}_{iP} = \dot{\boldsymbol{S}}_i \cdot \boldsymbol{S}_i^T \cdot \boldsymbol{J}_{iP}$$

in combination with the Jacobian matrices derived before to express $\boldsymbol{v}_{Si}, \boldsymbol{\omega}_i$. This leads to:

$$\overline{\boldsymbol{M}}_{(\boldsymbol{q},t)} \cdot \ddot{\boldsymbol{q}}_{(t)} + \overline{\boldsymbol{g}}_{(\boldsymbol{q},\dot{\boldsymbol{q}},t)} = \overline{\boldsymbol{d}}_{(\boldsymbol{q},\dot{\boldsymbol{q}},t)} \tag{2.6}$$

where $\overline{\boldsymbol{M}}$ describes a (6p,f) mass matrix, $\overline{\boldsymbol{g}}$ contains coriolis and centrifugal force vector and $\overline{\boldsymbol{d}}$ describes the vectors of the active external forces $\overline{\boldsymbol{d}}_{\boldsymbol{E}}$ and the internal reaction forces $\overline{\boldsymbol{d}}_{\boldsymbol{Z}}$. The latter forces, in general, are unknown but can be eliminated by a left side multiplication with the (f,6p) total Jacobian matrix $\boldsymbol{J}^{\boldsymbol{T}}{}_{ges}$.

$$\boldsymbol{J}^{\boldsymbol{T}}{}_{ges} = (\boldsymbol{J}_{T1}^{T} \quad \boldsymbol{J}_{T2}^{T} \quad \ldots \quad \boldsymbol{J}_{Tp}^{T} \quad \boldsymbol{J}_{R1}^{T} \quad \boldsymbol{J}_{R2}^{T} \quad \ldots \quad \boldsymbol{J}_{Rp}^{T})$$

which then appears in its final format as:

$$\begin{aligned} \boldsymbol{J}_{\boldsymbol{ges}}^{\boldsymbol{T}} \cdot (\overline{\boldsymbol{M}}_{(\boldsymbol{q},t)} \cdot \ddot{\boldsymbol{q}}_{(t)} + \overline{\boldsymbol{g}}_{(\boldsymbol{q},\dot{\boldsymbol{q}},t)}) &= \boldsymbol{J}_{\boldsymbol{ges}}^{\boldsymbol{T}} \cdot \overline{\boldsymbol{d}}_{(\boldsymbol{q},\dot{\boldsymbol{q}},t)} \\ \boldsymbol{M}_{(\boldsymbol{q},t)} \cdot \ddot{\boldsymbol{q}}_{(t)} + \boldsymbol{g}_{(\boldsymbol{q},\dot{\boldsymbol{q}},t)}) &= \boldsymbol{d}_{(\boldsymbol{q},\dot{\boldsymbol{q}},t)} \end{aligned} \tag{2.7}$$

where the first term summarizes the inertial forces and moments, followed by the gyroscopic and centrifugal components and the generalized forces on the right side of the equation.

(b)- D' Alembert principle: formulation using the virtual work principle

For the case that the internal reaction loads $\boldsymbol{f}_{Zi}, \boldsymbol{m}_{Zip}$, caused by system constraints are not of interest, the derivation of the equations of motion can be simplified by applying D' Alembert's principle of virtual work **[19]**. By the nature of holonomic constraints, its reaction forces $\boldsymbol{d}_{\boldsymbol{Z}}$ do not contribute to the virtual work, as these forces are orthogonally applied to the bodies DoF. Thus, their scalar product with the generalized coordinate vector is zero always:

$$\boldsymbol{d}_{Z}^{T} \cdot \delta\boldsymbol{q} = 0$$

Thus, the task reduces to the formulation of the virtual work equations for each system DoF to those of inertial and potential forces only.

(c)- Lagrangian dynamics

An even more sophisticated method was developed by Lagrange, who extended the D'Alembert's principle of virtual work to include the system kinetic energy E_k **[16]**:

$$E_k = \frac{1}{2} \cdot \sum_{i=1}^{p} \left(\boldsymbol{v}_{Si}^T m_i \boldsymbol{v}_{Si} + \boldsymbol{\omega}_i^T \boldsymbol{J}_{iP} \boldsymbol{\omega}_i \right) \tag{2.8}$$

As shown for Newton – Euler, the translational and rotational velocities $\boldsymbol{v}_{Si}, \boldsymbol{\omega}_i$ can be derived by using Jacobian matrices that in addition are used to derive a generalized force vector $\boldsymbol{d}$ as follows:

$$\boldsymbol{d} = \sum_{i=1}^{p} \left(\boldsymbol{J}_{Ti}^T \boldsymbol{f}_i + \boldsymbol{J}_{Ri}^T \boldsymbol{m}_{iP} \right)$$

The forces and moments $\boldsymbol{f}_i, \boldsymbol{m}_{iP}$ contain both, external and reaction loads applied to each as:

$$\boldsymbol{f}_i = \boldsymbol{f}_{Ei} + \boldsymbol{f}_{Zi} \qquad \boldsymbol{m}_{iP} = \boldsymbol{m}_{EiP} + \boldsymbol{m}_{ZiP}$$

The generalized forces $\boldsymbol{d}$ are related to the kinetic energy according to the Lagrange equation

$$\frac{d}{dt}\left(\frac{\partial E_k}{\partial \dot{\boldsymbol{q}}} \right) - \frac{\partial E_k}{\partial \boldsymbol{q}} = \boldsymbol{d} \tag{2.9}$$

After applying partial derivatives with respect to the generalized coordinates $\boldsymbol{q}$, $\dot{\boldsymbol{q}}$ and time, the equations of motion appear in its final matrix format as:

$$\boldsymbol{M}_{(\boldsymbol{q},t)} \cdot \ddot{\boldsymbol{q}}_{(t)} + \boldsymbol{g}_{(\boldsymbol{q},\dot{\boldsymbol{q}},t)} = \boldsymbol{d}_{(\boldsymbol{q},\dot{\boldsymbol{q}},t)}$$

For the special case, where the applied forces can be considered to be conservative (potential forces like gravity or spring forces that cause no deviation of the system's energy state), the generalized force vector $\boldsymbol{d}$ can be expressed by the potential energy

$$\boldsymbol{d} = -\frac{\partial E_p}{\partial \boldsymbol{q}} + \frac{\partial W_E}{\partial \boldsymbol{q}}$$

where W_E represents the work applied by external forces and the Lagrange formula exhibits in the format

$$\frac{d}{dt}\left(\frac{\partial E_k}{\partial \dot{\boldsymbol{q}}}\right) - \frac{\partial E_k}{\partial \boldsymbol{q}} + \frac{\partial E_p}{\partial \boldsymbol{q}} = \frac{\partial W_E}{\partial \boldsymbol{q}} \tag{2.10}$$

This expression was used for the derivation of the equations of motion for the vehicle model set up in this thesis.

1.2.1.3 Numerical treatment of equations of motion

To solve the equations of motion derived for a mechanical system, in general represented as a coupled set of ordinary second order differential equations, a mathematical integration is required. Analytical solutions in the frequency domain are applicable to systems of a few degrees of freedom only, e.g. quarter car suspension **[20]**, **[21]**. For more detailed models, a numerical solution in the time domain is appropriate. From the large number of numerical methods existing, the Runge-Kutta integration turns out to be universally used, because of its good balance between accuracy and numerical effort. This is described in the appendix A, *numerical methods used*, and in **[22]**, **[23]**.

2.3 Vehicle simulation models

In general, the purpose of a vehicle model is to analyse its dynamic response in:

- longitudinal
- lateral and
- vertical

directions for defined driving manoeuvres. The manoeuvres themselves can be categorized as addressing one of the following items:

- handling
- comfort
- NVH

The *handling* describes the vehicle behaviour subjected to lateral and longitudinal tyre patch forces developed in cornering, braking and accelerations. Such events are performed on relatively even roads of long wave low frequency, vertical contour profiles. Force transfer is mainly determined by the tyre to ground contact friction characteristics.

In case of rough, short wave road profiles like a cleat, the vertical excitation dominates the aspect of a vehicle *comfort* ride analysis.

An NVH analysis is intended to investigate the relevant modal behaviour with regards to the system eigen-frequencies. The emphasis is put on the system response for a variety of the excitation frequencies (frequency sweep). Whereas NVH investigations in general are restricted to small amplitudes, handling and comfort ride analysis can also include large displacement excitations. Thus, the first two categories; *handling* and *comfort*, can be separated in terms of the severity of their impact upon the vehicle system, namely:

- durability and
- abuse

Durability driving events are used to generate component load time histories for the purpose of strength and fatigue analysis and provide the database needed to confirm the

expected lifetime of the system. These tests should cover the operational loads considered for a normal customer usage profile, whereas abuse manoeuvres should confirm the envelope of the system load limits for component plastic deformations (failure criteria). They are also intended to reveal the chain of evnts leading to failure, as mentioned earlier. This concept is aimed to avoid the transfer of excessive loads to those suspension components that must not be isolated for safety reasons, such as lower ball joints in a McPherson strut. These so-called *victim* components, e.g. the lower control arm of a McPherson suspension, are designed to yield at a defined load level, tailored to relax the load path by plastic deformation in an abuse case.

It is a matter of fact that the ideal vehicle model to simulate arbitrary driving manoeuvres does not exist in comprehensive sense. Thus, the model concept in general needs to be adopted for simulation purposes. A model, that combines all the six degrees of freedom (three dimensional, full vehicle model e.g. **[24]**, **[25]**, will necessarily lead to a high degree of complexity. It remains an engineering task to condense a model to those degrees of freedom that are relevant for the analysis of the dynamic behaviour within the frequency range of interest. The decision as to which degrees of freedom are relevant for simulation purposes depends on the driving manoeuvre to be analysed. In the case of a straight kerb crossing/climbing event, no relevant roll motion is expected. Therefore, the model complexity can be condensed to cover an in-plane motion only. Models, condensed to contain the essential relevant degrees of freedom only, are called minimal model and can be found in e.g. **[21]**, **[26]**. These may be considered as dynamics within a reduced configuration space. Such models can effectively be used for optimization tasks as demonstrated in **[27]**. The following discussion about existing vehicle models is ordered by degree of complexity and focuses on vertical load simulation studies.

2.3.1 Quarter car suspension model

The most rudimentary model to study pure vertical body motions is the quarter car suspension model shown in Figure 2.9 **[21]**.

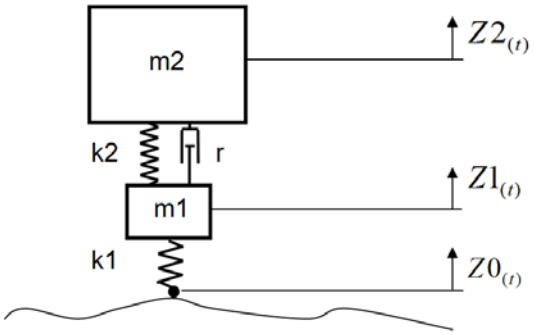

Figure 2.9: Quarter car suspension model **[21]**

The model comprises two lumped masses, the un-sprung wheel m1, including brakes and suspension and the sprung body mass m2, representing a quarter of the vehicle body. The tyre stiffness is given as k1, whilst k2 is an equivalent stiffness to represent the vertical vehicle suspension. Damping is assumed to be viscous and is neglected for the tyre. Longitudinal and lateral response, as well as rotational body motion (pitch, roll and yaw rigid body modes) are neglected. For the assumption of linear spring and damper elements, an analytical solution can be readily obtained in the frequency domain which allows the mathematical formulation of a transfer function H to describe the relationship between an input signal $\hat{z}_0$ (harmonic displacement excitation caused by the road profile) and the output signals $\hat{z}_1, \hat{z}_2$ (motions of masses m1, m2).

$$H_1(j\omega) = \frac{\hat{z}_1}{\hat{z}_0} = -\frac{k_1}{m_1}\left(\frac{\omega^2 - j\omega\frac{r}{m_2} - \frac{k_2}{m_2}}{\omega^4 - j\omega^3\frac{r(m_1+m_2)}{m_1m_2} - \omega^2\frac{m_1k_2 + m_2(k_1+k_2)}{m_1m_2} + j\omega\frac{rk_1}{m_1m_2} + \frac{k_1k_2}{m_1m_2}} \right)$$

$$H_2(j\omega) = \frac{\hat{z}_2}{\hat{z}_0} = \frac{k_1}{m_1}\left(\frac{j\omega\frac{r}{m_2} + \frac{k_2}{m_2}}{\omega^4 - j\omega^3\frac{r(m_1+m_2)}{m_1m_2} - \omega^2\frac{m_1k_2 + m_2(k_1+k_2)}{m_1m_2} + j\omega\frac{rk_1}{m_1m_2} + \frac{k_1k_2}{m_1m_2}} \right)$$

By means of Fourier series, the method can be extended to the application of an arbitrary periodic signal, which can be transformed into a set of single harmonic functions. A superposition of the single harmonics reconstructs the original signal. In case of a linear

system, also the transfer functions found for each single harmonic excitation of the set can be superimposed to analyse the system response **[21]**.

Models like this are mainly used to describe ride comfort effects and to detect the relevant frequency bands where amplified excitation of the masses m_1 and m_2 are observed.

2.3.2 Plane vertical vehicle models

The structure concept of a quarter car suspension model can be extended to include also the **pitch** motion by using a planar model, also known as a bicycle model. Models for different applications are shown in Figure 2.10.

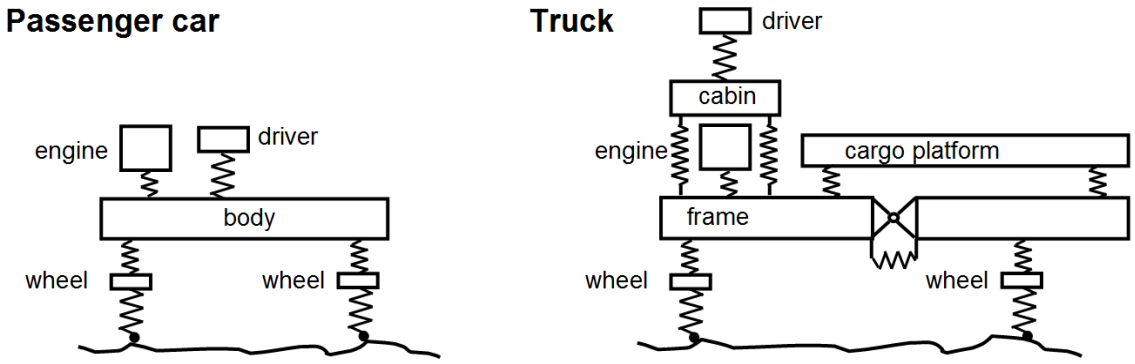

Figure 2.10: Samples for plane vehicle model architecture **[21]**

This concept decouples the front and rear axles, but integrates them into the vehicle body. The approach can easily be extended to allow the application of longitudinal loads by introducing an additional D0F as described in more detail in chapter 2.

2.3.3 Spatial vehicle models

To also include roll and yaw rotations, the model needs to be extended to a spatial model as shown in Figure 2.11.

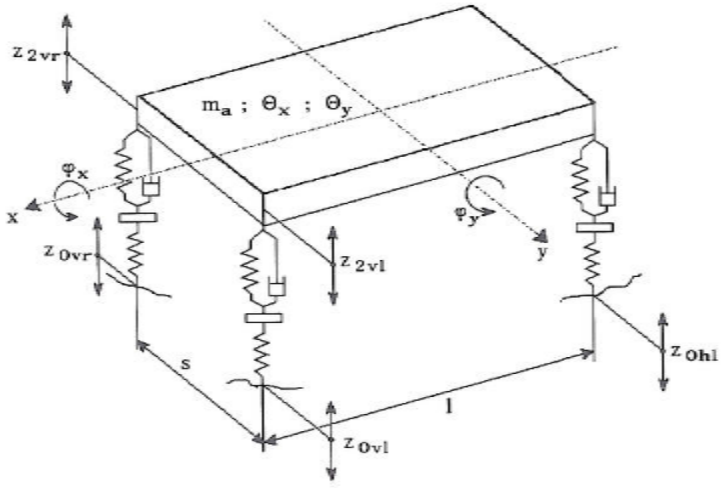

Figure 2.11: Three dimensional vertical model **[21]**

This concept can further be improved in order to enable an analysis of bending and torsion modes by discretisation of the body structure as shown in Figure 2.12.

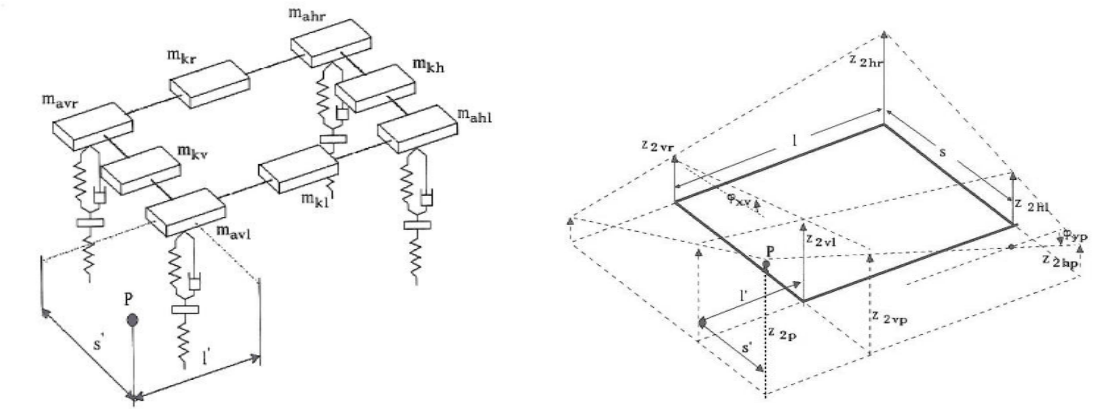

Figure 2.12: Three dimensional model and warp body mode for discretised body structure **[21]**

Although such models can still be analysed by linked transfer functions **[21]**, the modelling in the format of an MBS system, as already described, is seen as the more appropriate approach and, therefore, is preferred by most research workers.

2.3.4 Spatial models that include suspension kinematics

One thing that the vehicle models discussed so far have in common is that a detailed modelling of the suspension kinematics is generally neglected. Furthermore, the non-linear character of the suspension force response, typically seen at large wheel travels, in

the state of bumper engagement, are not considered. An example for a model approach that addresses these items was presented by Rahnejat **[14]** on the basis of a double wishbone front quarter suspension shown in Figure 2.13.

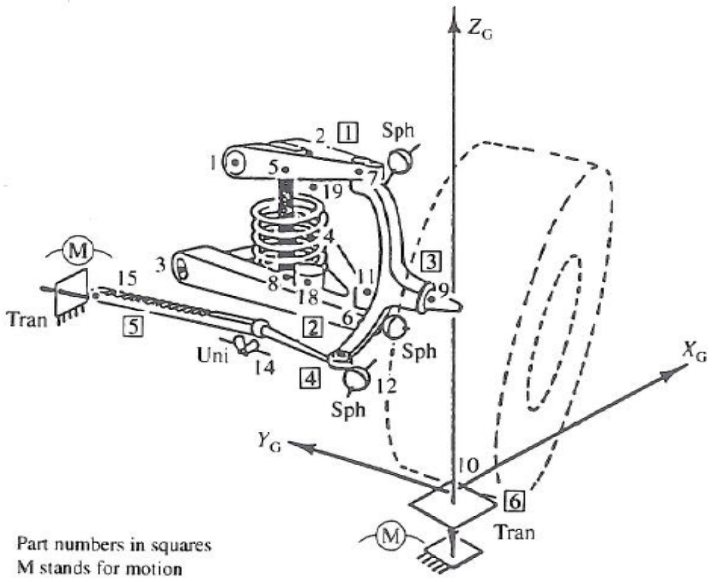

Figure 2.13: The quarter SLA suspension model **[14]**

The suspension consists of five parts, two control arms, steering knuckle, spindle and wheel, subjected to a vertical load defined by the quarter of the total vehicle mass of 1600 kg. All suspension parts are considered to possess translational and rotational inertia, linked by idealized spherical (ball joints) and revolute joints (bushings). The model is subjected to a single bump crossing, where the tyre patch motion, imposed by the bumper contour, was derived from a kinematic roll over trace. The event results in a heavy impact taken by a vertical jounce bumper. Bumper element and tyre force response W are modelled as follows:

$$W = K\delta^n + C\frac{dz}{dt} \tag{2.11}$$

In this formula, K is the tyre stiffness, C is a (viscous) damping coefficient, dz/dt describes the damper actuation speed, and bumper deformation velocity and δ stands for the contact deformation of tyre respectively bumper. By choosing the power *n* to be smaller, equal or greater than unity, a regressive, linear or progressive spring characteristics can be established individually for tyre or bumper. Figure 2.14 illustrates

the kinematic deflection and simulation results gained for the bumper force at time instant t = 0.4 sec.

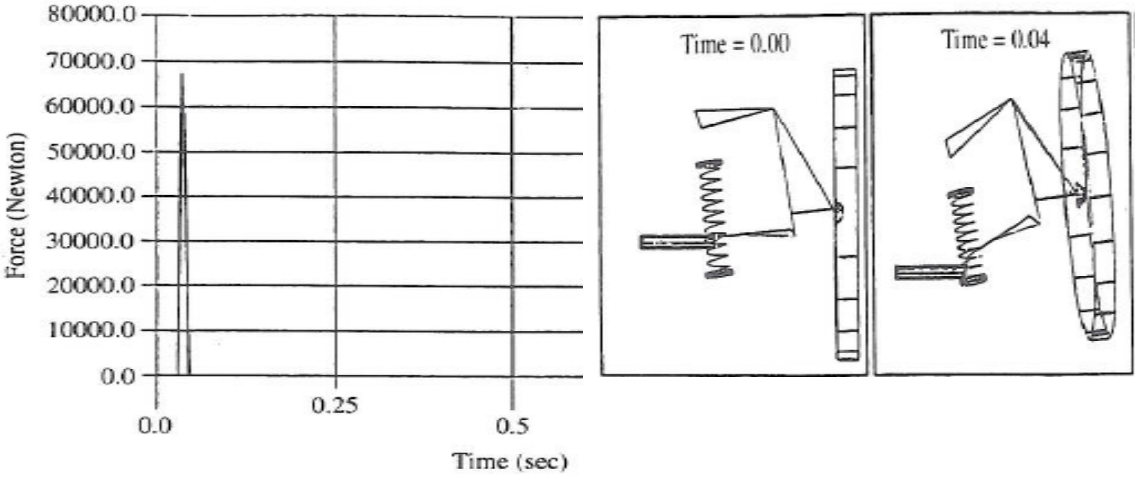

Figure 2.14: Jounce bumper reaction force and animated sequence of suspension articulation **[14]**

This result already demonstrates the necessity of a structural invariant simulation approach by recognizing a bumper model for the prediction of a vertical force level transferred to the body structure. To further improve simulation accuracy, a general trend is to increase the level of model detail. For the application to vertical load simulation, the main focus is set on the simulation of bushings, bumpers and tyre behaviour under dynamically applied loads.

A further example for a fully non-linear model approach that includes bushings and a rigid tyre model was presented by Ammon et al. **[28]**. The authors propose a modular model architecture where the substructures as the tyre, hydraulic steering, bumpers etc, are linked to a core vehicle model. This architecture combines modules of large difference in stiffness. To avoid a common small integration time step size for the entire model, adequate to cope with the 'stiffest' subsystem, a decentralized solving and independent time step size control was realized in the solver algorithm. Special emphasise was put upon the tyre model, a distinguished rigid ring approach called BRIT (Brush and Ring Tyre Model). A more detailed description of tyre and bumper simulation approaches is given below.

2.3.5 Vehicle model parameter set up

To set up a model, its parameters, such as inertial properties, stiffness and damping coefficients need to be established. Two approaches are common practise:

- Direct parameter measurement performed for single components
- System response parameter identification

The first item can be seen as a classical approach **[29]**. The parameters are established by individual component analysis / measurements. The latter method (system response) requires the existence of a parametric model in advance of the parameter identification process. A system response measurement is embedded into a feedback loop with the model for a recursive identification of the specific model parameters **[30]**.

It can be observed that the number of parameters required to set up the model in general increases with model complexity.

2.4 Tyre simulation models

The tyre is the direct and exclusive interface to the ground and therefore a key element for vehicle dynamics. As discussed for the vehicle model, the purpose of a tyre model is to simulate longitudinal, lateral and vertical dynamics. With the thesis intention to be focused on the simulation of DoK, the emphasis is put upon the vertical and longitudinal aspects of tyre mechanics and simulation approaches. In general, two modelling approaches are identified:

- mathematical model
- physical modelling

The intention addressed with a *mathematical* model is to establish appropriate shape functions that replicate common characteristics known from recorded force response traces. This approach avoids the need to consider the physical mechanism of action, which otherwise needs to be realised in a *physical* modelling concept. A mathematical formulation, which describes the common shape of the force response trace, can be derived for e.g. a polynomial. Equipped with a unique set of coefficients (parameters), the formulation can be adapted to best fit the recorded trace.

2.4.1 Mathematical tyre models

An example for a mathematical model, intended to calculate the tyre vertical force response caused by a radial penetration against a flat rigid ground, is given by Rahnejat **[14]**:

$$W_{vert} = W_{stiff} \pm W_{damp} \tag{2.12}$$

The two components mark the tyre stiffness and damping terms, where the damping W_{damp} is positive for jounce and negative for rebound. The stiffness term W_{stiff} is represented by the vertical tyre stiffness value *K*, the radial deflection δ and an exponent *n*. As the static force response against radial belt penetration can be of progressive, linear or regressive character, depending on the geometry of the penetrating body, an exponential function was chosen:

$$W_{stiff} = K \cdot \delta^{n}$$

The exponent *n* typically reveals values around 1.1 for flat tyre patch contact to rigid ground (progressive characteristics) and is found to be less then one (regressive) for edge type contacts. A quasi static force response shape against flat ground in the absence of damping is shown in Figure 2.15.

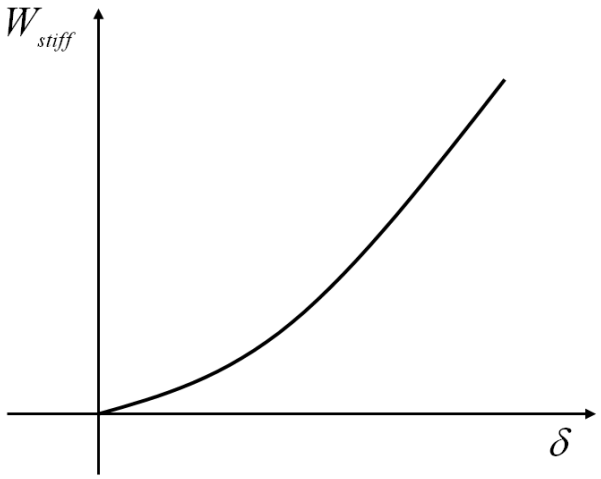

Figure 2.15: Vertical tyre force (stiffness contribution) **[14]**

The damping term depends on the radial tyre deformation rate over time.

$$W_{damp} = C \cdot d\delta / dt$$

Such mathematical model concepts can be categorized as a heuristic approach and can also be derived for the lateral and longitudinal force responses as shown in **[31]**, **[32]**, **[33]**, but in contrast to the vertical force response characteristics, the lateral forces acting in plane of tyre patch depend significantly on friction. Therefore, some general characteristics of rubber contact friction will be addressed before these models are presented.

2.4.1.1 Tyre patch contact friction properties

Rubber friction is velocity (rate) dependent and thus can be modelled using viscoelastic elements. A general variation of friction coefficient μ with sliding velocity *v* is shown in Figure 2.16, taken from **[21]**.

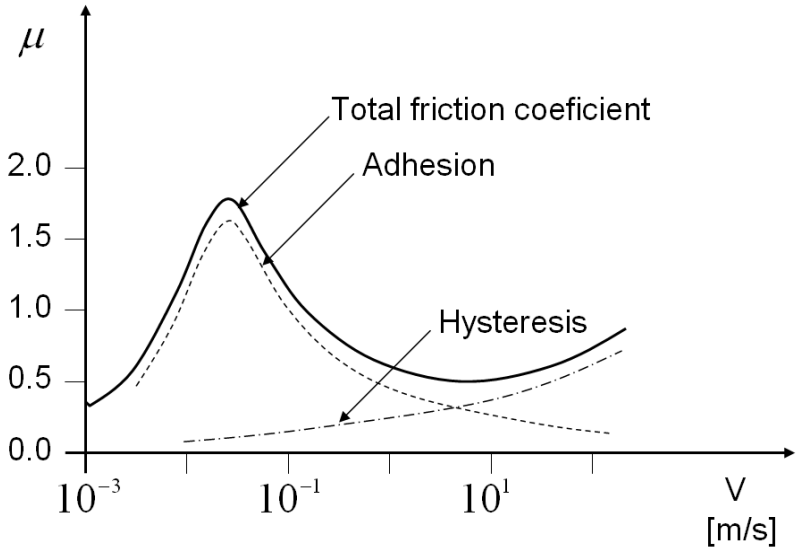

Figure 2.16: Total friction components from adhesion and hysteresis **[21]**

The graph shows the total friction coefficient μ with the sliding velocity V. The total friction characteristics can be explained as a superposition of two components, adhesion and hysteresis. The *adhesion* describes the bonding forces on basis of single molecule contact (poles). The integral value of the poles distributed over the tyre contact patch area determines the adhesive component of the friction coefficient. In the sliding mode, instant bonding forces of single molecule will cause a stretching of linked molecule chains directed *in plane* of the sliding contact area, until bond braking occurs at the limit

of adhesion. Based on this concept, the pole contact force frequency increases with the sliding velocity and, in an analogy with the case of resonance, the adhesion losses achieve a maximum at a specific excitation frequency. This frequency is a specific material property of both the rubber and ground surfaces.

The second component takes the roughness of the contact surface into account. An uneven surface contour enforces a molecule chain actuation *vertical* to the sliding contacting plane. Therefore, flat surfaces cause a smooth increase of the friction resistance with sliding speed, whereas rough surface reveal a higher gradient. Thus, the accumulated work caused by the vertical pole motion (*hysteresis*) continuously increases with the sliding speed.

2.4.1.2 Brush model

The descriptive brush model developed by Willumeit **[21]** allows a simple mathematical formulation of the tyre lateral and longitudinal force responses in conjunction with the above mentioned contact friction characteristics. Because the brush model in conjunction with the rubber contact friction behaviour is fundamental for the understanding of Pacejka's Magic Formula tyre model (discussed later), the brush model is briefly highlighted here. Willumeit **[21]** considers the belt as a flexible band, equipped with radial brush elements. After transition into the contact area, these brushes bend and cause discrete elemental reactions which represent the linear shear stress distribution τ. A brush bending condition for free roll motion in absence of driving or braking wheel moments is shown in Figure 2.17.

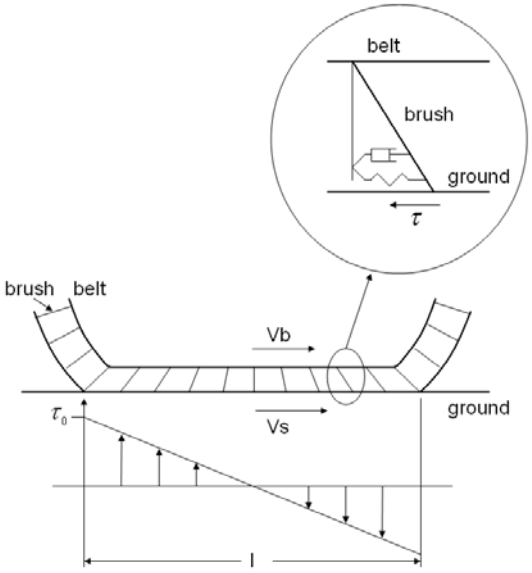

Figure 2.17: Brush model **[21]**

A kinematic relation for the belt and brush end velocities is determined by the difference of the radii of belt and ground. In case of a driving moment, the belt velocity Vb increases and decreases in braking. Thus, driving and braking slips can be defined as follows:

$$\delta_{dr} = \frac{Vb - Vs}{Vb} \qquad \delta_{br} = \frac{Vs - Vb}{Vs} \tag{2.13}$$

It is noted that the condition shown in Figure 2.17 confirm a negative driving slip although the accumulated shear stress is zero.

Figure 2.18 a, b demonstrate the shear stress distribution for no slip (Vb = Vs) and under slip conditions (Vb > Vs). The model is based on the assumption that the initial shear state τ_0 which describes the brush shear condition in transition to ground, shown at the left hand side of the tyre patch contact, remains constant. This is assumed to be independent of the actual drive or brake slip level. Furthermore, the shear stress is considered to change linearly along the contact length, depending on the slip. Although a physical slip relative to ground is considered for the belt, a bonding contact to ground is assumed for the brushes in bending mode for any slip level (a) and (b) in Figure 2.18.

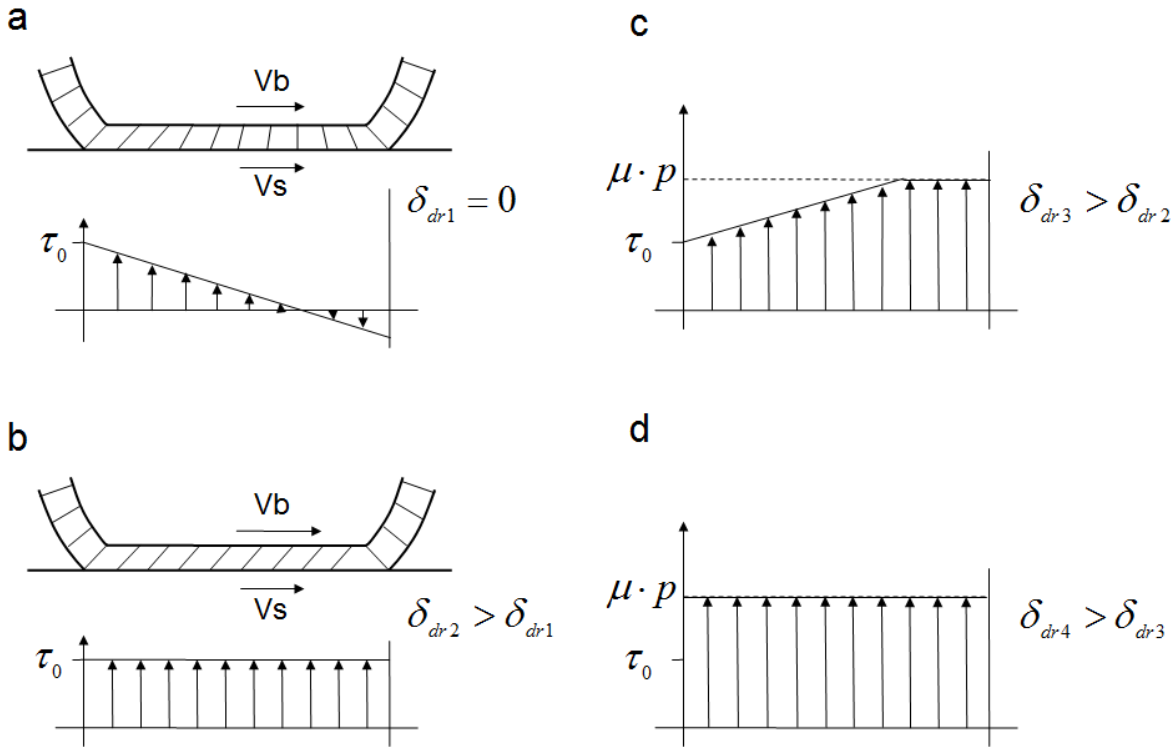

Figure 2.18: Brush model for zero- and positive increasing driving slip **[21]**

The maximum shear stress is reached for the brushes in transition to the sliding mode (c) when the bending forces exceed the friction limit as indicated by the dashed line. The limit is defined by the level $\mu \cdot p$, where μ is the tyre patch friction coefficient and *p* the contact pressure, assumed to be constant over the tyre patch length. A circumferential force Fu, directed longitudinal to the tyre contact patch, can be derived from the integral of the shear stress over the tyre patch area of width b. Thus, $\tau_{(x)}$ is a linear shape function depending on the prevailing drive slip condition δ_{dr}.

$$Fu = \int_0^l \tau_{(x)} \cdot b \cdot dx \tag{2.14}$$

The integral achieves its maximum value for the sliding condition along the full contact patch length (Figure 2.18 d).

Similar considerations can be made for a brake slip condition. Figure 2.19 shows the characteristic shape of a longitudinal force in the tyre patch as a function of drive and brake slip for the assumption of a constant friction coefficient.

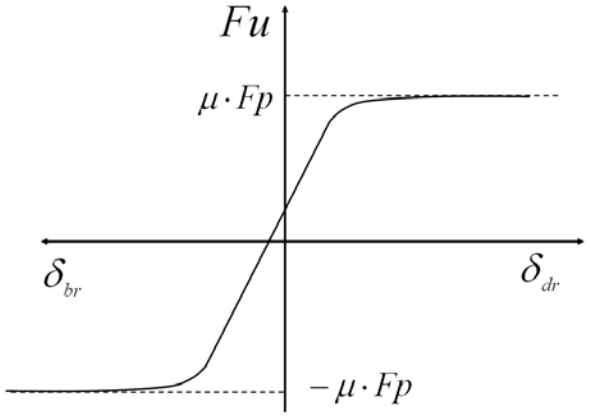

Figure 2.19: Longitudinal friction force Fu as function of driving slip for constant friction coefficient **[21]**

With this assumption, the aspects discussed for adhesion and hysteresis with regards to their affect on the friction coefficient, have been neglected thus far. The model was therefore extended to a case of variable friction for the sliding brush and by applying the friction coefficient as a function of slip. In Figure 2.16, it is visible that the adhesive friction initially rises with slip, but drops in the transition to hysteresis-induced friction. This leads to a drop in friction force at higher slip values as indicated in Figure 2.20:

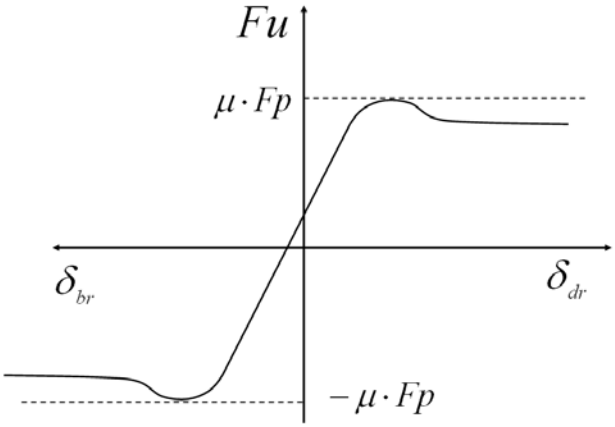

Figure 2.20: Longitudinal friction force Fu as function of driving slip for slip dependent friction **[21]**

These aspects are incorporated in the *'Magic Formula'* tyre model as described below.

2.4.1.3 Pacejka's 'Magic Formula'

Analogous considerations, as applied for the longitudinal force response, can be assigned also to steady state side force and reaction moment behaviour. This leads to similar characteristics for the self-aligning torque and slip angle as shown in Figure 2.21.

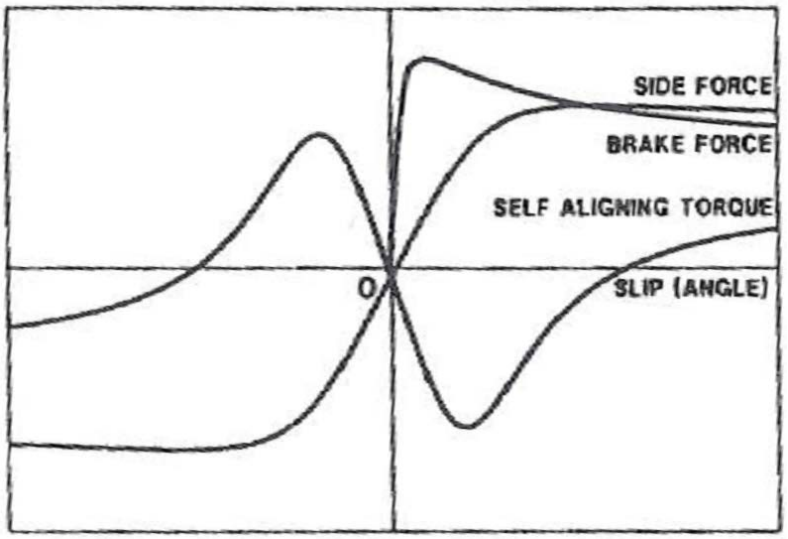

Figure 2.21: Steady state tyre characteristics **[32]**

Pacejka et al. **[32]** derived a common mathematical formulation, which commonly fits for all force components, known as 'magic formula'. The equation can be tuned to fit the curves by adjusting four coefficients B, C, D and E, where:

B = stiffness factor, C = shape factor, D = peak factor and E = curvature factor

where: Sh = horizontal shift, Sv = vertical shift

The 'Magic Formula' is:

$$y(x) = D \cdot \sin\{C \cdot \arctan(B \cdot x - E \cdot [B \cdot x - \arctan(B \cdot x)]\} \tag{2.15}$$

$$Y(X) = y(x) + Sv$$

$$x = X + Sh$$

Figure 2.22 illustrates the effect of coefficient variation, in this case the curvature factor E was varied.

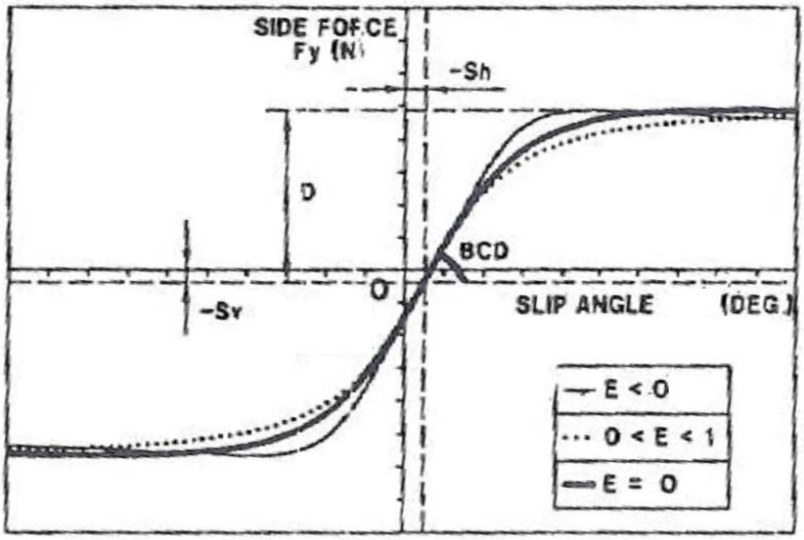

Figure 2.22: Coefficients appearing in tyre magic formula **[32]**

The mathematical models, in general, are very effective with regards to calculation time, as they are analytical as opposed to numerical. On the other hand, they allow neither an insight nor interpretation with regard to the structural system behaviour during load transfer. The examples addressed in this review are restricted to quasi-static applications or steady state conditions only. To obtain a better understanding about cause and effects and also to include dynamic features into the simulation, physical models may be preferred, although additional effort for the numerical treatment needs to be taken into account.

2.4.2 Physical tyre models

Other than mathematical models, the physical tyre modelling is aimed to describe the force transfer by addressing the inertial and elasticity properties of the tyre structure. This can either be achieved by a direct analytical formulation of the continuous structure (e.g. ring model) or based on a transfer of the continuous tyre structure in discrete elements as discussed for the vehicle structure concept previously.

2.4.2.1 Rigid ring model

From a descriptive viewpoint, the assumption of a single rigid ring element represents the most rudimentary approach for a continuous tyre structure (see Figure 2.23).

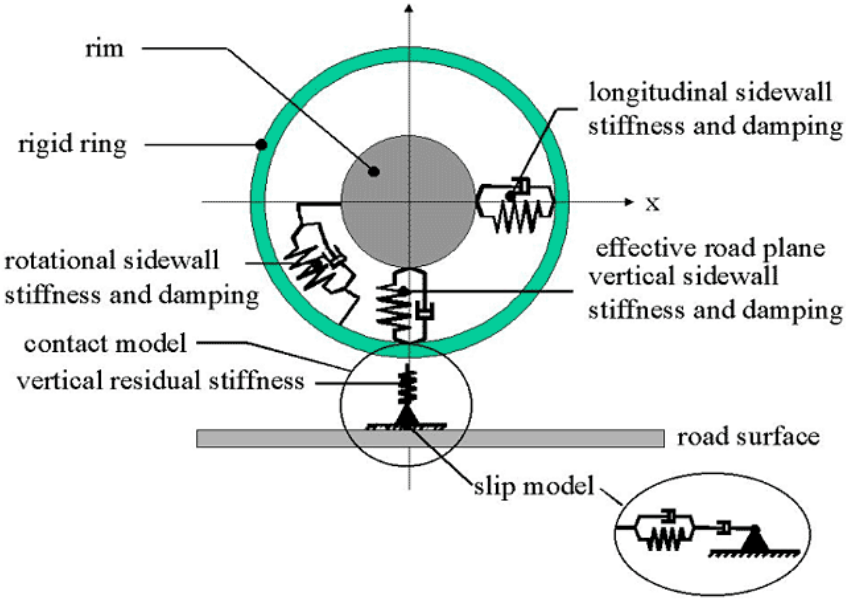

Figure 2.23: Schematic representation of the rigid ring model **[35]**

The ring has a mass and represents the rotational and lateral inertia of the tyre. In case of a rotation, it also can take gyroscopic reactions into account. As the elasticity properties are neglected in a rigid ring, the tyre structural stiffness and damping properties are addressed by visco-elastic elements to simulate longitudinal, lateral and radial load transfers from the tyre contact patch to the wheel rim. The ring contour describes the road profile depending on the contour curvature. To model the contact with the ground, a slip model, such as the brush model, can be appended. An example for a rigid ring model, available in a commercial software package, was developed by Oertel and Fandre, the so called '**R**eifen**mod**el für **K**omfortuntersuchung' or RmodK, also known as the Comfort Durability Tyre (CDTyre). Its simplest representation is the model 20, shown in Figure 2.24. It is designed as a planar structure, intended for ride and comfort analysis, applicable to long wavelength surfaces **[34]**.

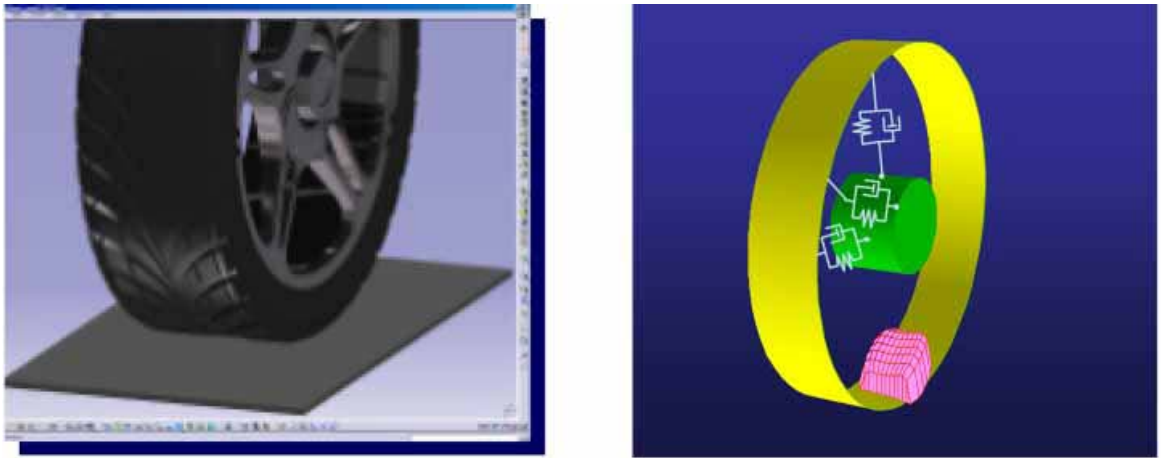

Figure 2.24: CD Tyre Model 20, resp. RmodK20 **[34]**

It is obvious that the *scan* properties of a rigid ring model are limited to smooth ground profiles and cannot easily cope with the demand for a realistic roll over simulation if applied to a short wavelength road contours or obstacles such as a cleat. To distinguish the model response capability to traverse short wave profiles or sharp road irregularities, the so-called enveloping properties, a tandem mechanics proposed by Schmeitz (2004) **[35]** was combined with a rigid ring approach to develop the SWIFT tyre model, based on a rigid ring approach. The virtual tandem mechanics transforms the real road profile (scanned signal) into a tyre effective excitation contour as a function of road height, forward slope and local curvature.

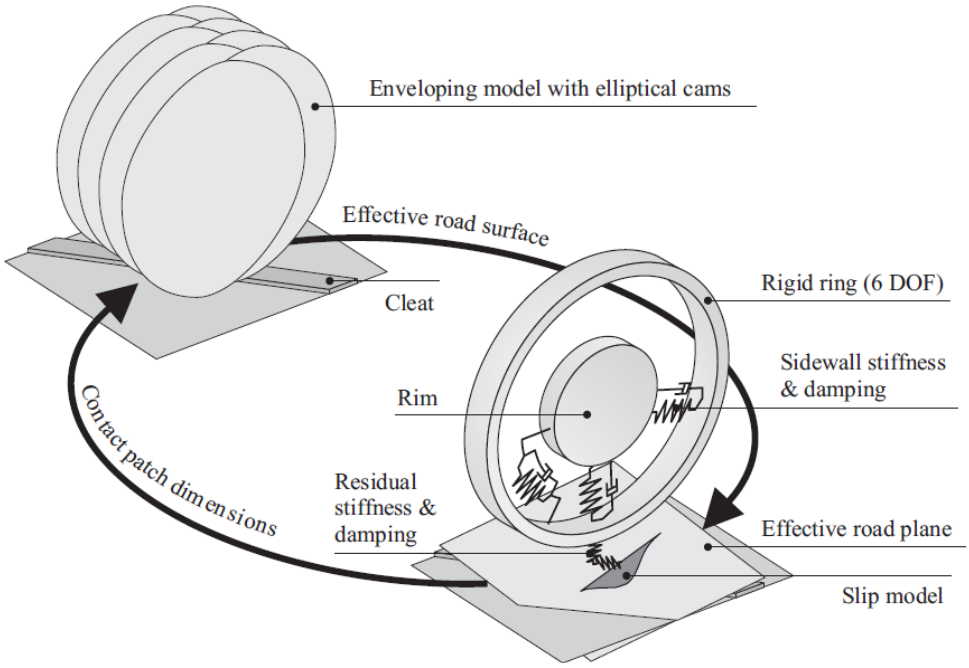

Figure 2.25: Schematic representation of the SWIFT model **[35]**

The model consists of two rigid elliptical discs that are assembled in a distance 'ls' related to the tyre patch length. Both discs do not rotate, but can move in vertical direction. Each disc has at least one contact point to the ground, thus can be considered as a slider which describes the road contour in a slow motion. The effective road profile is then related to the mid-point's vertical displacement w' and an inclination angle β_y of the slider shown in Figure 2.26.

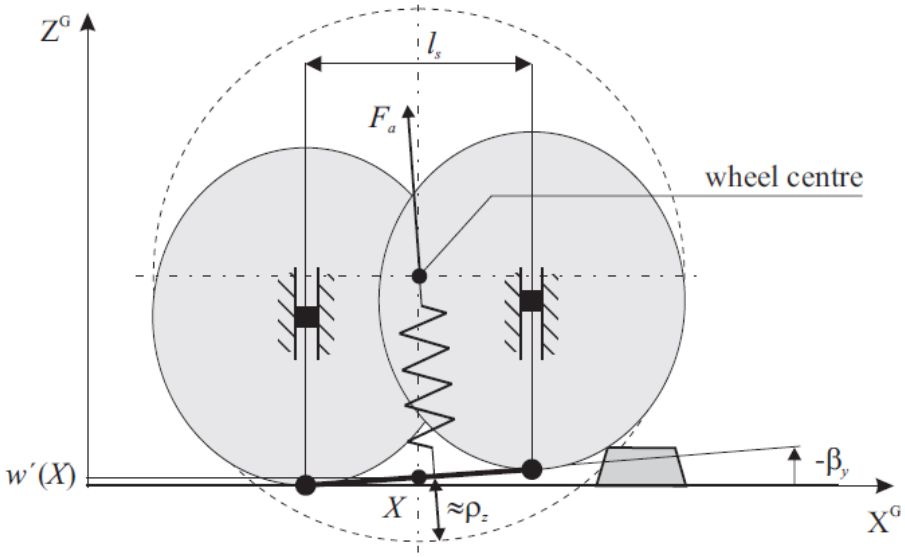

Figure 2.26: Tandem-cam enveloping model **[35]**

The cam dimensions are established from a best fit assessment of a real tyre roll-over signal versus a best fit cam profile signal gained from the slider mechanism. As the enveloping features of a tyre are related to its pneumatic pressure and the tyre patch length, the model can be extended to address the pressure influence on the enveloping properties, using a relationship that describes the patch length 'a' as function of the vertical tyre deflection ρ_z, where p_{a1}, p_{a2} are fitting parameters, r_0 is the unloaded tyre radius and ρ_z is the tyre vertical deflection.

$$a = p_{a1} \cdot r_0 \cdot \left(\frac{\rho_z}{r_0} + p_{a2} \cdot \sqrt{\frac{\rho_z}{r_0}} \right) \tag{2.16}$$

Despite these applications, the desire for an extension towards a flexible ring structure is obvious for the purpose of road profile excitation simulations, especially if applied to large radial tyre deflections and rim clash conditions.

1.4.2.2 Flexible ring modelled as a continuous system

Early physical modelling approaches make use of the classical beam theory, applied to the elastic ring. An early model for an in-plane thin ring structure of homogeneous isotropic material to analyse its modal behaviour was provided by Timoshenko in 1932 **[12]**. In 1965, Böhm **[36]** extended the planar flexible ring towards a 3D spatial model, where he represents the tyre belt by the mathematical formulation of a continuous structure. This was equipped with a radial and lateral bedding to take into account the sidewall effects of a tyre carcass. Böhm derived the equations of motion for the four DoF, namely the radial (w), circumferential (u) and lateral (v) belt deflection, radial and lateral belt bending and also recognized the belt torsion (ψ). The following lists the equations of motion:

$$
\begin{aligned}
&EF \cdot \frac{u'' + v'}{a^2} - \frac{1}{a} \cdot Q - k_\tau \cdot u + t_{(\varphi)} = \ddot{u} \cdot \rho \\
&T_0 \cdot \frac{w''}{a^2} + \frac{1}{a} \cdot V' - k_s \cdot w + p_{(\varphi)} + p \cdot b \cdot \psi = \ddot{w} \cdot \rho \\
&T_0 \cdot \frac{v'' + v}{a^2} - EF \cdot \frac{u'' + v'}{a^2} - \frac{1}{a} \cdot Q' - k_a \cdot v + q_{(\varphi)} + p \cdot b \cdot \frac{u' + v}{a} = \ddot{v} \cdot \rho \\
&\frac{d \cdot \tan\beta}{2a} \cdot \left(T_0 \cdot \frac{v' - u}{a} + EF \cdot \frac{u'' + v'}{a^2} \right) + \frac{GIp}{a} \cdot \left(\frac{w''}{a^2} - \frac{\psi''}{a} \right) + \frac{EIx}{a} \cdot \left(\frac{w''}{a^2} + \frac{\psi}{a} \right) + \\
&\qquad + k_T \cdot \psi - h_L \cdot p_{(\varphi)} = -\ddot{\psi} \cdot Ip \cdot \rho
\end{aligned}
\tag{2.17}
$$

The remaining unknowns, belt cross-section shear forces Q (radial) and V (lateral), are addressed by two further equations:

$$
\begin{aligned}
&\frac{d \cdot \tan\beta}{2a} \cdot T_0 \cdot \frac{w''}{a} - EI_y \cdot \frac{v''' + v'}{a^2} + Q + h_L \cdot t_{(\varphi)} = 0 \\
&\frac{d \cdot \tan\beta}{2a} \cdot \left[T_0 \cdot \left(\frac{v'' + v}{a} - 1 \right) - EF \cdot \frac{u' + v}{a} \right] - \frac{GIp}{a} \cdot \left(\frac{w'}{a^2} - \frac{\psi'}{a} \right) + \frac{EIx}{a} \cdot \left(\frac{w'''}{a^2} + \frac{\psi'}{a} \right) + \\
&\qquad + V - \frac{w'}{a} \cdot k_\tau \cdot \left(\frac{b}{2} \right)^2 + n_{(\varphi)} = \frac{\ddot{w}'}{a} Ix \cdot \rho
\end{aligned}
\tag{2.18}
$$

Torsional and bending stiffness, as well as the bedding compliances were analytically derived on the basis of geometrical data taken from the sidewall and the belt steel inlays. Böhm used the model in a numerical example to analyse the belt deflection and torsion for a rectangular shaped side load distribution, derived from Fourier series and also for modal analysis. The model is computational effective, but its application is restricted to small deflections only.

The mathematical formulation of equations of motion for an elastic ring structure is given by Soedel in 1981 **[37]** for a planar structure taking radial and circumferential deformation into account. The equations of motion derived for the radial and tangential deflection of a flexible ring were found as follows:

$$\begin{aligned} &\frac{D}{R^4}(u_r'''' - u_\theta''') + \frac{K}{R^2}(u_r + u_\theta') + \frac{N}{R}(2u_\theta' - u_r'') + k_r u_r + bd\rho\ddot{u}_r = q_r + \frac{N}{R} \\ &\frac{D}{R^4}(u_r''' - u_\theta'') - \frac{K}{R^2}(u_r' + u_\theta'') - \frac{N}{R}(2u_r' - u_\theta'') + k_\theta u_\theta + bd\rho\ddot{u}_\theta = q_\theta \end{aligned} \tag{2.19}$$

Continuous structure models are typically be used for modal analysis to investigate the system natural frequencies or the structural damping. Such an application is provided by Popov et al. **[38]** where the authors use a flexible continuous ring tyre model as a baseline to investigate the simplest single-valued proportional damping in assessment to more sophisticated approaches discussed in the paper. For a correlation to physical testing, the tyre structure was assembled to a rigid supported wheel in absence of ground contact. Single point radial penetration was performed in the format of a frequency sweep to gain structure excitation signals from sensors distributed uniformly along the tyre belt contour. The agreement between physical experiment and theoretical results is witnessed by an assessment of the frequency response functions.

2.4.2.3 Flexible ring modelled as a discretized truss or a beam model

An alternative to modelling the belt as a continuous structure is the discretization approach, where the belt structure is subdivided into single elements linked by revolute

joints. The elements can either be assumed rigid (truss type) or elastic in bending (beam type). Pacejka **[33]** distinguishes between these two concepts as:

1) Truss models neglect the belt bending stiffness
2) Beam models include the belt bending stiffness

Tsotras and Mavros **[39]** used the analytical equations (2.19) derived for the continuous ring structure as a baseline to benchmark both the truss and the beam concepts. The study confirmed that the beam model achieves almost perfect agreement with the predictions of the ring model throughout the frequency range. It also shows that differences are negligible for modal analysis within the low frequency range.

A commercial model for an in-plane flexible ring is the CDTire model 30 proposed by Gallrein et al, **[2]**. As shown in Figure 2.27, a discretized chain-like structure of single mass points, radially supported by Kelvin-Voigt elements attached to the rim was used to model the belt. Additional elements attached to the rim address the radial belt to rim contact stiffness and are intended to model a belt-to-rim clash condition. The single belt masses are equipped with sensor type visco-elastic elements in outboard direction to define the contact to the ground.

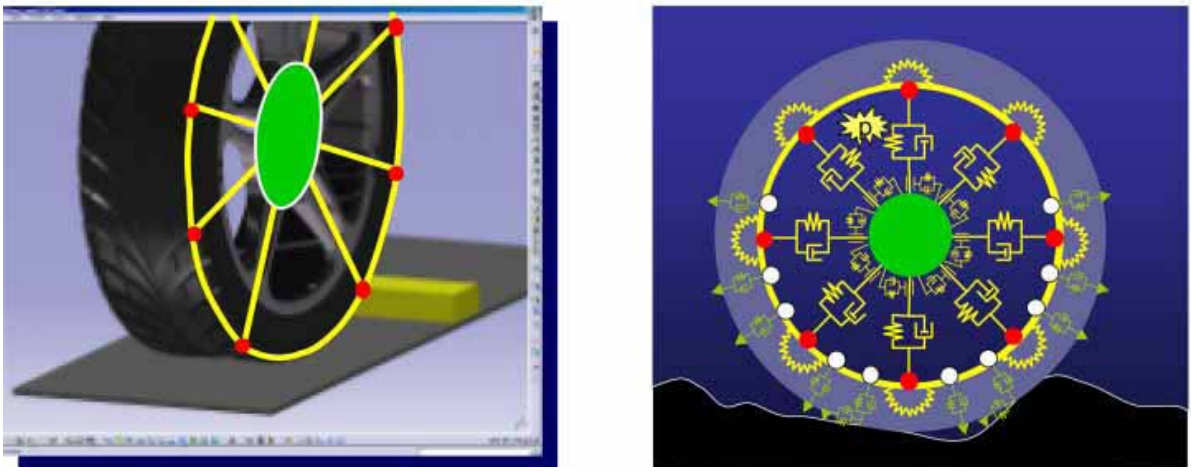

Figure 2.27: CDTire Model 30, resp. RmodK30, an in-plane flexible ring model **[34]**

This model can cope with large in-plane deformations as expected in a cleat type obstacle crossing and was used by Haga **[5]** to investigate the vertical and longitudinal tyre force responses in a traversing over an elliptic cleat. For the belt-to-rim clash

simulation, the model was equipped with additional contact elements at the rim contour as shown in Figure 2.27.

The effect of these elements on the rim clash force response simulation is demonstrated by Baecker and Gallrein **[6]** as shown in Figure 2.28. These features are considered to be essential for a realistic kerb strike simulation. The model addresses this aspect by the superposition of two radial force components, a linear component (index LIN), used to represent the stiffness of the belt-to-rim contact and a non-linear part (index NL), describing the radial deflection force required for the pneumatic tyre structural deformation. Thus:

$$f^R(r) = f^R_{LIN}(r) + f^R_{NL} \tag{2.20}$$

Both components are functions of the radial deflection 'r', Figure 1.28 illustrates the force response with (right) and without rim contact stiffness formulation.

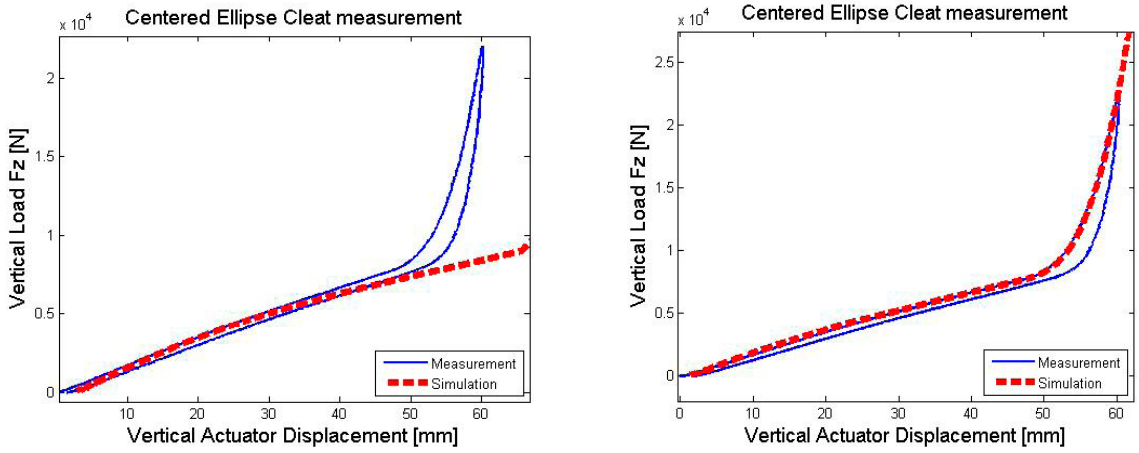

Figure 2.28: Force response in rim clash condition with and without rim contact formulation **[6]**

Although the flexible ring model exemplarily represented by the CDTire model 30 is suitable for radial, longitudinal and lateral loads, the concept of a single ring remains limited to 2D load profiles and obstacle contours that do not vary along the tyre width and are positioned perpendicular to the direction of travel. To cope with the demand of 3D obstacle geometries, such as cleats with variable height or arbitrarily positioned cobble stones, an obvious approach is to combine a set of coupled flexible rings as realized in the model 40 of the CDTire family.

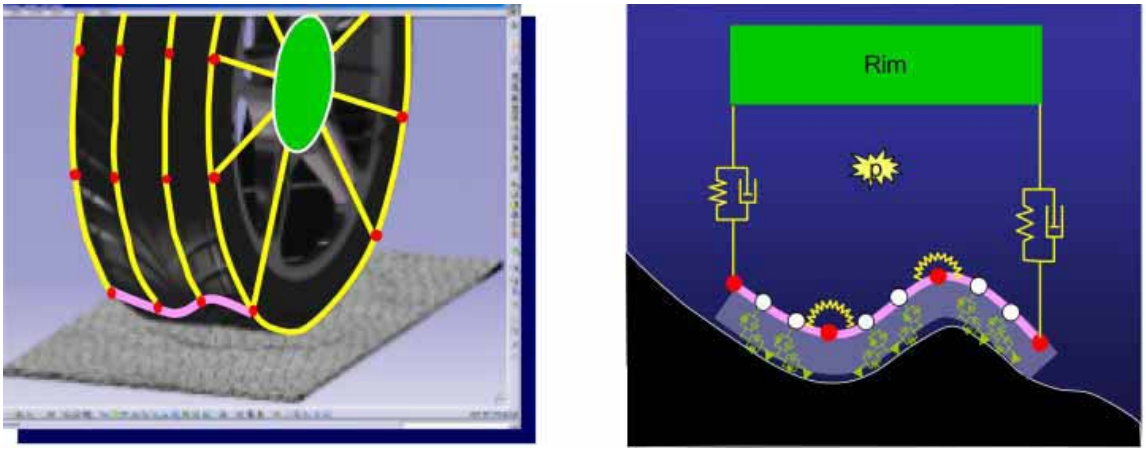

Figure 2.29: 3D tyre model combining a set of flexible ring structures **[34]**

In its latest version **[40]**, the belt to rim contact formulation used in model 40 was extended with a flexible rim model to further improve the contact simulation. A comparison for flexible- (red) and rigid rim found for harsh cleat crossing simulation at 11 km/h is shown in Figure 2.30:

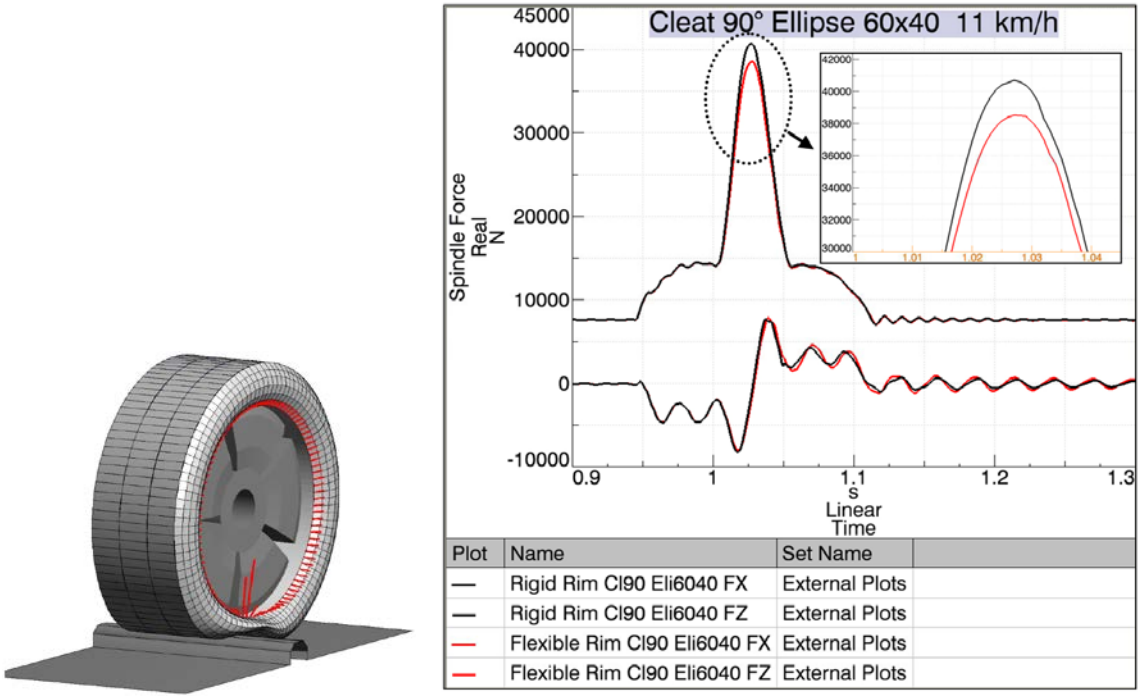

Figure 2.30: Rim flexibility impact on contact force during cleat crossing **[40]**

2.4.2.4 Flexible tyre modelled as MBS structure

The tyre models discussed up to now can be interpreted as extensions of the Magic Formula, a mathematical description of the tyre typical stationary force transfer characteristics, embedded in a ring type structure analysis. In its subsequent development status as discussed in the foregoing, these models achieve high accuracy assessed to measurements also for short wavelength and uneven rigid road profiles. For a ground surface considered to be not rigid, such as mud, the concept is assumed to be less compatible, if ever. To improve the model concept from these kinds of limitations, an alternative approach was proposed by Gipser **[3]**. This model disregards the ring structure and alternatively builds the tyre belt by discrete elements in the mathematical format of an MBS system. The steel belt is modelled by 50 up to 150 rigid block elements. Each rigid assumed block element can perform lateral and rotational in-plane and out-of-plane motion, suspended by elastic spring and damper elements that interlink the neighbouring elements and also provides attachments to the rim. The stiffness of the in-plane belt elements is quite high, corresponding to a steel belt structure and are related to the pneumatic tyre pressure in order to represent the additional stiffening effects caused by the sidewalls. Figure 2.31 shows the structural components of the so-called Flexible Tire, briefly FTire.

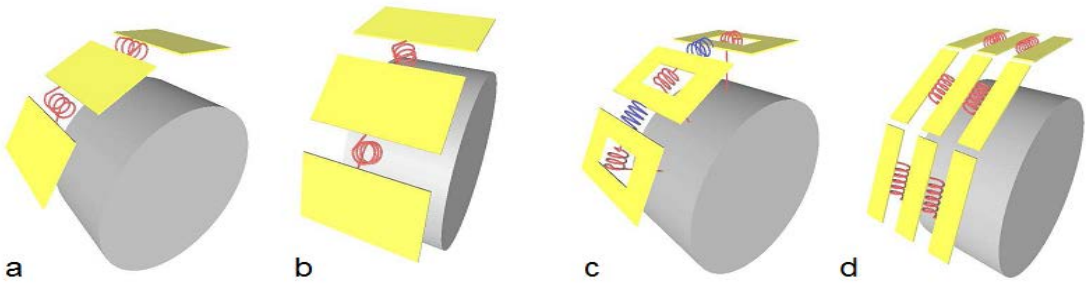

Figure 2.31: FTire belt stiffnes components, a) in-plane bending, b) out-of-plane bending, c) belt torsion against rim (red) and twist in between blocks (blue) and d) lateral bending **[3]**

Instead of a brush model, a number of 5 to 40 contact elements are used to simulate the frictional properties in the contact tyre patch. The elements are aligned parallel in the longitudinal direction attached to each block element as shown in Figure 2.32.

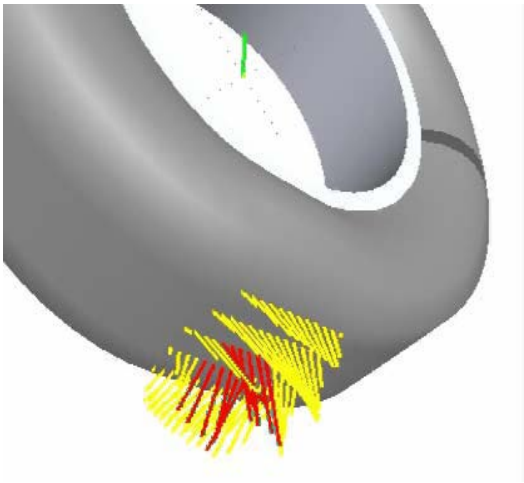

Figure 2.32: Contact elements attached to belt blocks **[3]**

The contact elements are free of inertia and linked by Maxwell elements to the belt blocks and its neighbouring elements. The deflection of the contact elements depends on the road profile as well as the position state of the block elements relative to each other. The belt blocks tangential and radial deflections results from the equilibrium condition of the block shear- and friction forces, where the friction forces are a function of the shear velocity of the block relative to the ground and its contact pressure.

Solutions are provided by a numerical integration of the equations of motion in the time domain. Conventional solvers, in general, tend to have problems in solving small inertias attached to stiff springs, as used in the belt representing linked block structure. Such problems can be caused by large accelerations gained for relatively small deflections due to the small inertias. This can lead to extremely small step sizes and the calculation is stopped in case the step size falls below the smallest digital unit defined by the machine precision. To cope with this aspect, a local subsystem integration solver is used that runs with a unique step size control algorithm, independent of the interaction with the calling MBS solver, e.g. ADAMS.

This tyre model concept allows the modelling of the force response and distribution of a tyre patch in contact to arbitrary 3D ground surface contours and even extreme, abusive type kerb strike manoeuvres as shown in Figure 2.33 (right).

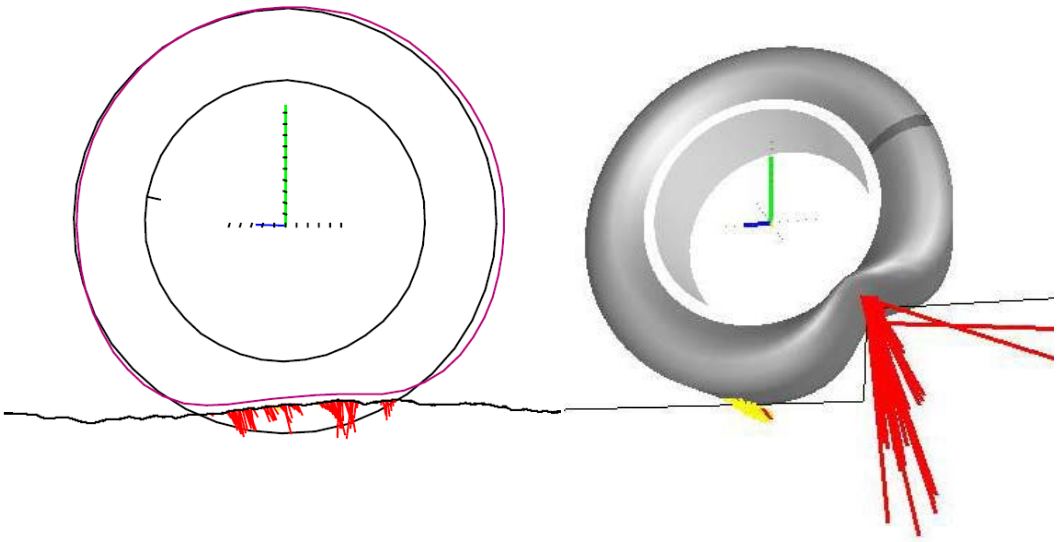

Figure 2.33: Tyre patch force distribution in contact to rough ground (left) and abuse type kerb strike simulation **[3]**

2.4.2.5 Flexible tyre modelled as FEM structure

The largest discretization level in general is achieved by the application of the finite element method FEM to model a tyre structure. A visual example is shown in Figure 2.34.

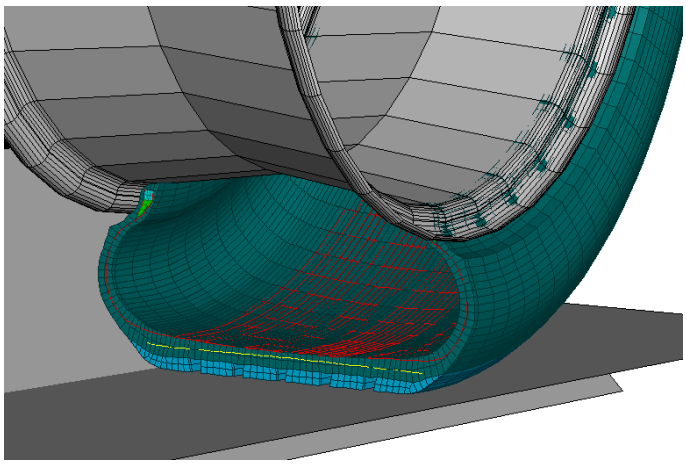

Figure 2.34: ABAQUS FE tyre model example taken from **[41]**

A principle advantage of the FEM structure is the fact that only the geometry and the orientation of individual tyre components like steel and textile cord belt plies in conjunction with its material properties are required to set up the entire tyre model. Thus, this alleviates the user from the task of defining the need for a structural concept and its

discretization. Furthermore, the FEM concept does not require a structural analysis to define system properties like stiffness and damping features as demanded for an MBS model. The FEM model is generated on a 2D tyre substructure that represents the cross sections as shown in Figure 2.35. The substructure is then extended along the rim radius to form the final 3D torus structure.

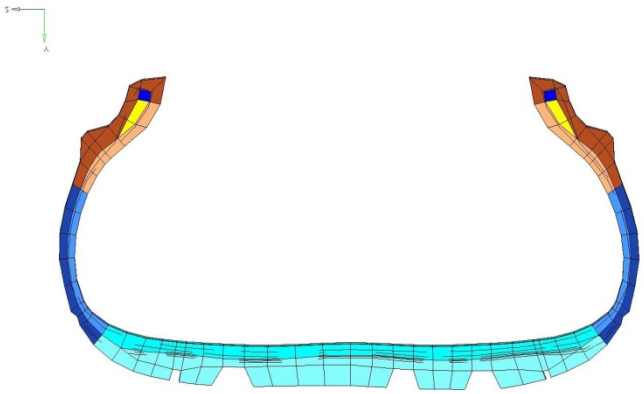

Figure 2.35: 2D substructure of a FEM tyre model **[42]**

FEM tyre models represent a very detailed level of the tyre structural components and, therefore, they can effectively be used for detailed static analysis as e.g. footprint pressure distributions **[42]** shown in Figure 2.36.

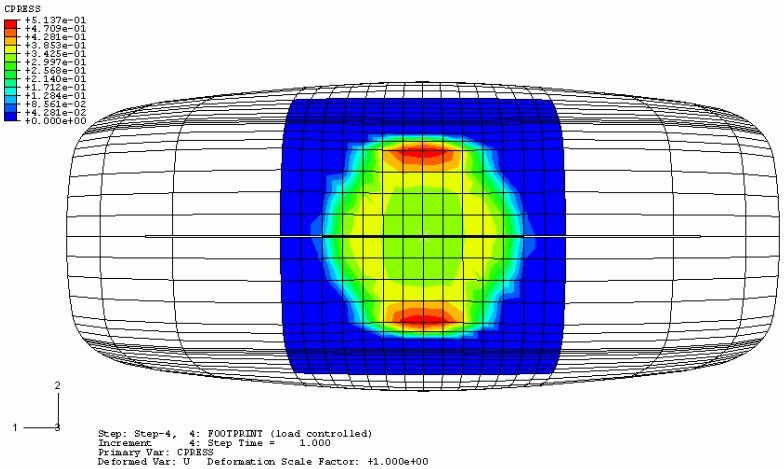

Figure 2.36: Footprint stress distribution analysis **[42]**

As the FEM method defines both stiffness and inertia for each element, modal effects such as the system relevant eigenmodes can easily be analysed as well as for a complex structure.

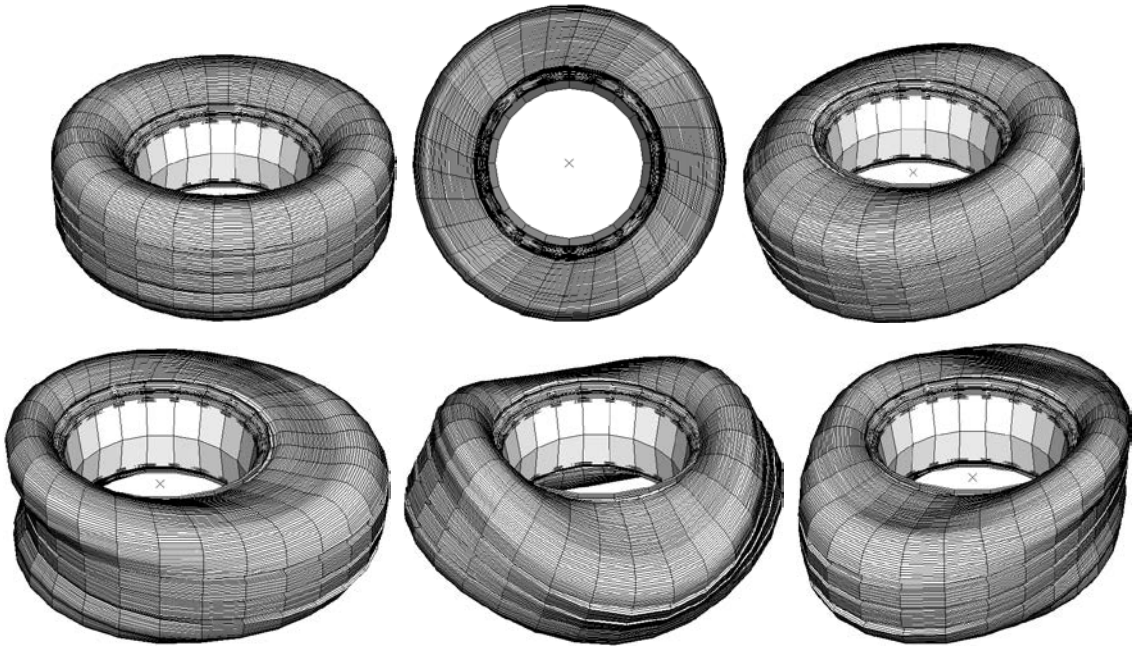

Figure 2.37: Six eigen-modes for a free finite element tyre **[41]**

The FEM tyre model concept has the drawback of a high level of detail with the demand for significant computational power, equivalent to the discretization level, when used to analyze driving events in the time domain. As such studies are performed mainly by using MBS structure models, a modal reduction process can be applied to the FE structure aimed to reduce the number of DoF [**41**]. Of course, by reducing the number of nodes, also the frequency range and number of eigenmodes, that can be analyzed, will reduce. This aspect sets a limit for the application of the modal reduction method. However, with this concept, an FEM based tyre model can be transferred into a format feasible to be used as a substructure, embedded in an MBS environment.

2.4.3 Tyre model parameter identification

What all models discussed so far have in common is that a proper parameter determination would be essential for the simulation quality. Other than FEM models, which depend on the comprehensive knowledge of material and geometry data only, the parameterisation task has two aspects. Firstly, the handling related parameters are needed to best fit the Magic Formula coefficients and secondly the structure related parameters such as belt bedding factors, compliance or bending stiffness are needed for ring

structure models. Both parameter sets are, in general, established on the basis of dynamic tyre physical testing on a drum rig as shown in Figure 2.38.

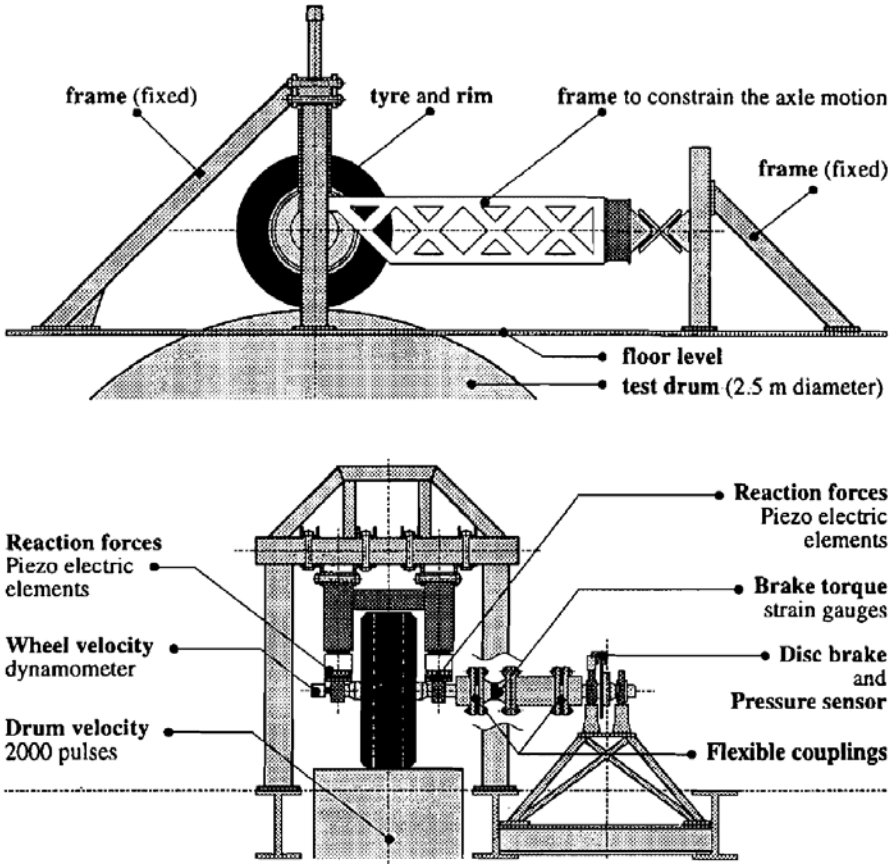

Figure 2.38: Tyre drum test rig **[43]**

For the RmodK, the CDTire model, its structure eigen-frequencies are also needed. In case of MBS models such as FTire, the element inertias and the properties of the linking elements need to be determined. As an example, a CDTire model 40 data set can contain up to 190 parameters. It is noted that each parameter data set needs to be established unique for every pneumatic pressure level. Although the parameterization in many cases is embedded into an automated feedback control loop strategy which transfers measured data directly into a parameter data set as shown in Figure 2.39 **[2]**, a physical testing on a drum, for each pneumatic pressure level in general is usually required.

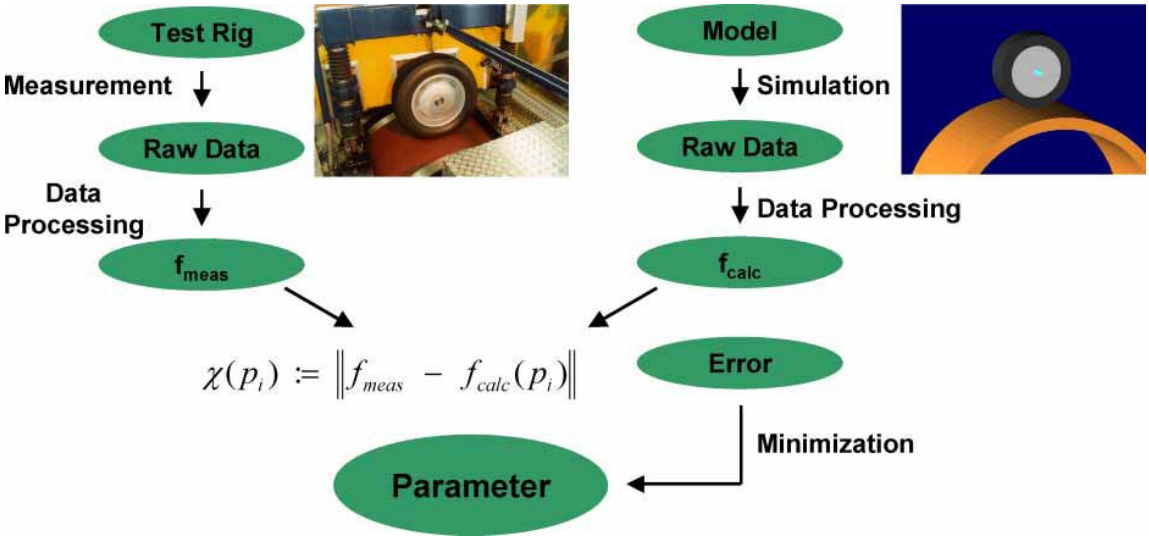

Figure 2.39: Automated parameter identification in a feedback loop testing on drum **[2]**

To avoid the effort of setting up unique data sets for each single pneumatic pressure level, the SWIFT model was applied to a concept that allows an extrapolation of the parameter data set gained for a single pneumatic pressure. In this manner, a range of inflation pressures, which envelopes the initial data set **[35]** can be covered. However, despite these efforts to gain properly calibrated parameter sets by means of widely automated processes, its identification requires intensive testing and therefore is regarded as a costly operation.

2.4.4 Summary and conclusions from tyre literature review

The tyre models discussed in this review represent pure mathematical and also physical approaches summarized in Table 2.1.

TYRE MODEL OVERVIEW

Model Concept	Structure	Main Application	Road profile	Model Representatives
Mathematical / emperical	none	handling	flat ground	Pacejka Magic Formula
	none	ride	flat ground	vertical force response formula
Physical	rigid ring	handling / ride	2D long wave	RmodK 20 / CDTire 20 / Swift
	flexible ring	ride / comfort / NVH / durab.	2D short wave	RmodK 30 / CDTire 30
	3D flexible ring	ride / comfort / NVH / abuse	3D road scan	RmodK 40 / CDTire 40 / F-Tire
	FE models	ride / comfort / NVH / abuse	3D road scan	ABAQUS FE Tire

Table 2.1: Tyre models overview

The models cover a wide range of complexity commencing from empirical models, such as the Magic Formula, which can be expressed by a few coefficients only, up to a detailed FEM modelling approach. The model choice depends on the application task and also on the computational performance available. An overview about the complexity, in relation with the various simulation tasks intended, is shown exemplarily for the discussed CDTire in Figure 2.40.

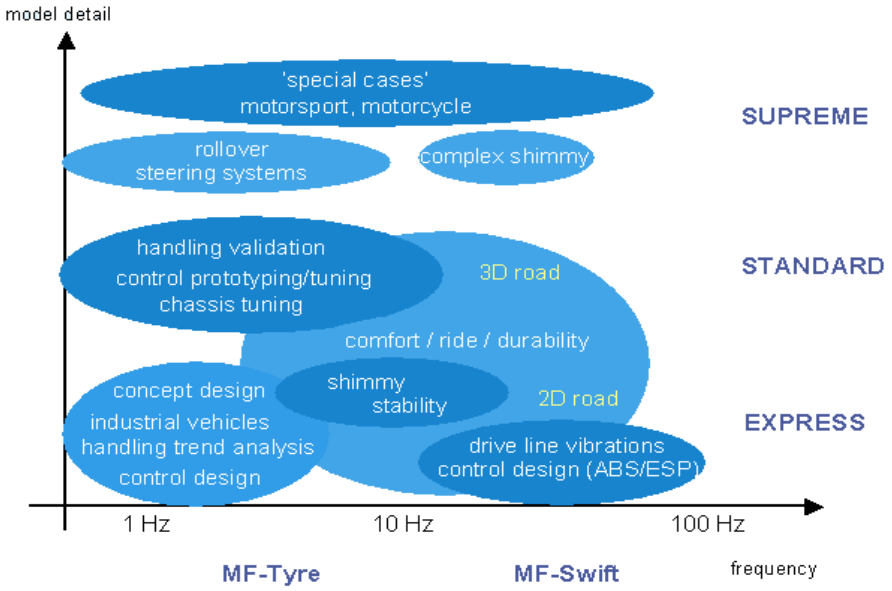

Figure 2.40: Model complexity over frequency range and simulation purpose based on the CDTire model family **[34]**

For the simulation of for example a kerb strike manoeuvre, as intended in this thesis, the diagram reveals a high end demand for the model detail level, even within a low frequency range in between 1 to 10 Hz. The model detail level must be defined by a number of parameters required for the model set up as shown in Figure 2.41.

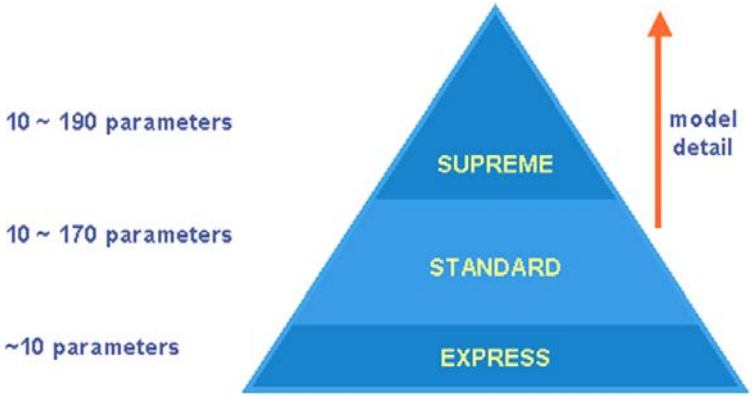

Figure 2.41: Model detail level and number of parameters for the CDTire family **[34]**

To analyze the peak wheel spindle force for an abusive kind single kerb strike event, the inertia of the tyre structure is considered to have a negligible impact on the peak load level, because the tyre structure mass is hardly affected by the kerb deformation. The tyre structure modal behaviour relevant for NVH performance in the higher frequency range is also not seen to be relevant for a single event kerb strike simulation. It is considered that the model level of detail can significantly be reduced for the assumption that the description of the structural compliance can be neglected. Aligned with this assumption, the necessity for a detailed description of the structure compliance is no longer required. To confirm the validity of this assumption, an overview about the main effects contributing to quasi-static vertical force is given in Figure 2.42.

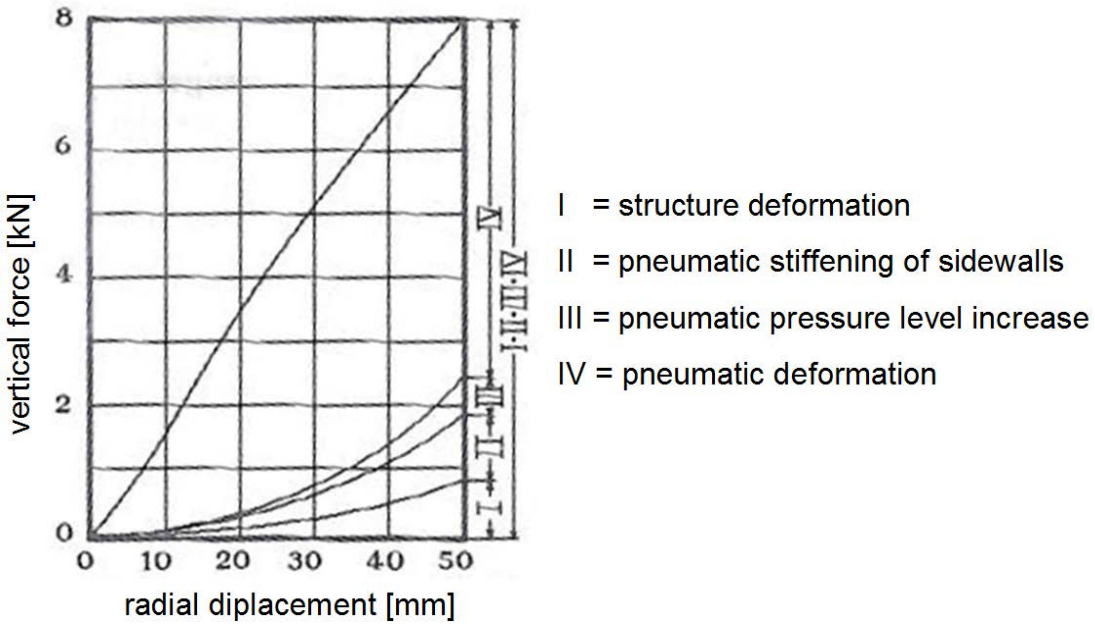

Figure 2.42: Components of vertical tyre force for deflection against flat rigid ground **[21]**

It can be seen that the main contributor to the vertical load magnitude is the pneumatic pressure resistance against flat deformation of the tyre patch, component (IV), followed by the force increase caused by the pneumatic stiffening effect on the sidewalls, component (II). The vertical force contribution caused by the structural deformation (I) is about ten percent for the case shown and depends on the tyre architecture, whereas the increase in pneumatic pressure effect on vertical force (III) is negligible.

In this thesis, a quasi-static tyre model is proposed to simulate the in-plane radial force transfer for a flat and an edge-type deformation is proposed. The model is defined by only a few geometrical parameters taken from the tyre cross-section in conjunction with the pneumatic pressure. Neither a parameter determination process, based on physical tests on a drum, nor an investigation of specific material data properties, such as those needed for FEM tyres, are required to set up the model. Model concept simplicity is achieved by focussing on the pneumatic components II and IV only, namely the sidewall stiffening and resistance against tyre patch deformation for a radial, edge-type deformation.

2.5 Bushings and Bumpers in chassis applications

A vehicle these days is unthinkable without bushing and bumper elements. Polymers are used as base material in such components, intended to reduce noise and vibrations, tune the ride and handling dynamics, attenuate harsh impacts and to limit wheel travel. Focus is set on the latter aspect in this thesis.

The literature survey related to this subject commences with general physical properties of rubber-like materials concerning their static and dynamical behaviour. It continues with known concepts for modelling this behaviour and then proceeds with current design concepts used for jounce bumper elements in chassis applications for conventional passenger cars.

2.5.1 Physical properties of polymers at static deformation

The operational deformation range of steel components in general is limited to a narrow linear elastic range and rarely exceeds a strain level of 1%, whereas polymer elements allow strains up to several hundred percent **[44]**, **[45]** without residual strain deformation after relaxation. Their elastic force response is of linear characteristic only for a small deformation range and changes to a viscous – elastic behaviour with rising actuation frequency (dynamic hardening).

The reason for these differences compared with metals can be explained by physical effects aligned with the polymer material structure. Metals, as most other solid materials, are of crystalline structure. Each element (molecule) is located at a certain grid place, linked to other elements by intermolecular grid forces. The location of the molecules in the grid is defined by the state of minimum potential energy. A deformation caused by an external force is equivalent to a raise in potential energy, thus the elasticity of such materials is called *elastic energy*. A simple imagination for elastic energy is given in Figure 2.43:

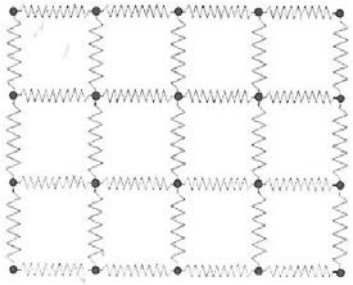

Figure 2.43: Energy elasticity of crystalline material **[44]**

In contrast to the solids, polymers consist of long chain molecules that are distributed with irregular orientation. The chains are not fixed in position, but free to move relative to each other. After the polymerization process, the individual chains are cross-linked within the body volume as shown in Figure 2.44.

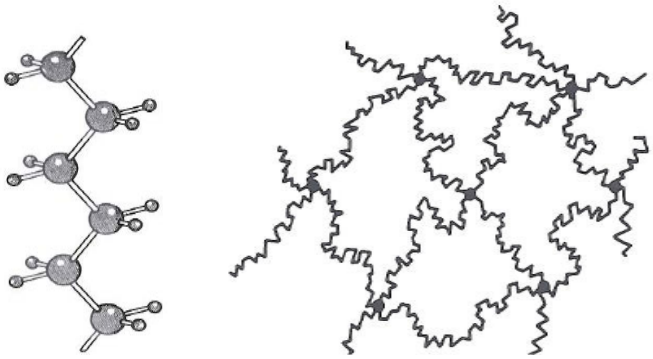

Figure 2.44: Polyethylene chain molecule in schematic form (left) and irregular polymer material structure (right) **[45]**

The chain orientation can be characterized as fully irregular in case all chain directions are represented equally, thus there is no overall direction. This state of minimal order or, in other words, maximum disorder is defined by the maximum level of entropy. For an axial load, the chains become aligned to the direction of deformation, thus its system entropy drops with rising orientation level shown in Figure 2.45. A material elasticity that depends on the system entropy level is called *elastic entropy.*

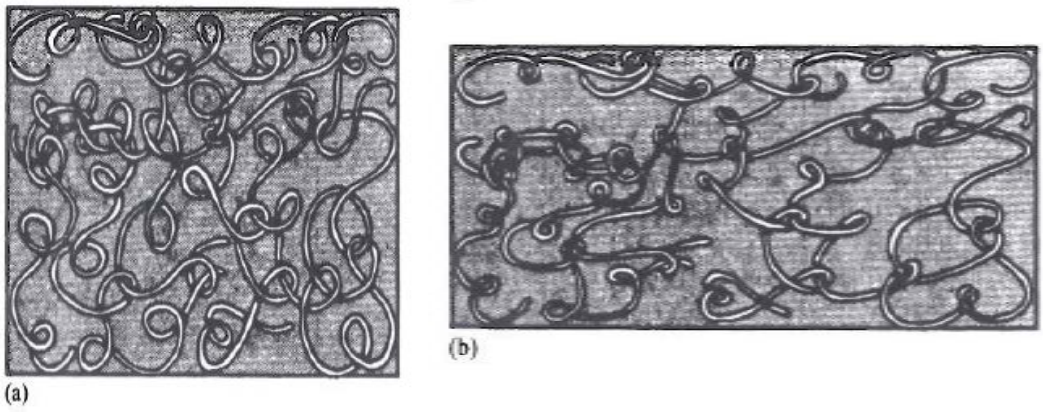

Figure 2.45: Maximum entropy level for relaxed polymer material (a) and reduced entropy in stretched condition (b) **[45]**

A typical trace for a force- elongation diagram is shown in Figure 2.46 (left). It was taken from a polymer material under uniaxial loading and reveals an elastic, but highly non-linear response characteristics. Furthermore, two other typical features, namely the hysteresis and the so-called Mullins effect can be observed on the right hand side of Figure 2.46, where the vertical axis is aligned with the material stress and the horizontal axis scales the material strain. The graphs show several compression and expansion loops performed towards three discrete strain levels, 0.3, 0.6 and 1.0, where the compression strokes trace the upper stress level, followed by the expansion at relaxed stress. This effect is known as hysteresis.

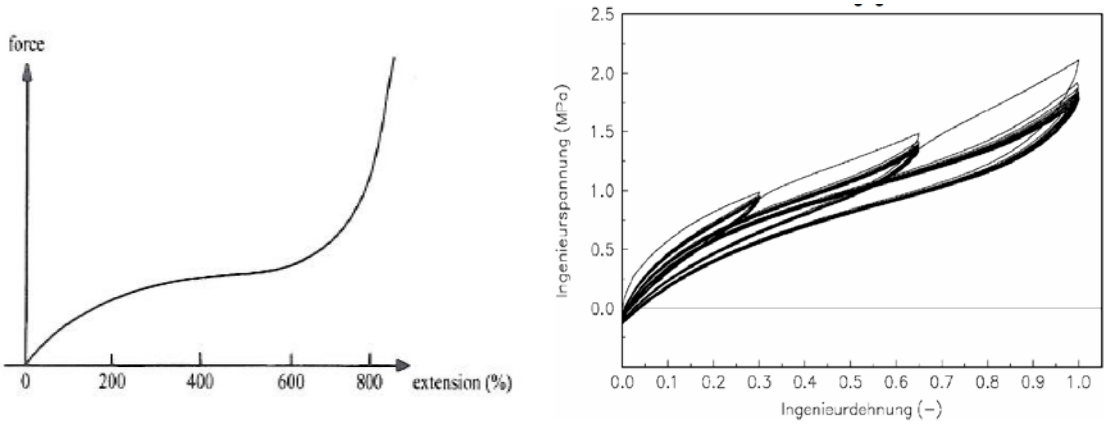

Figure 2.46: Non linear force response (left) **[45]** and Mullins effect (right) **[46]**

It further can be seen that the initial compression trace, indicated by the fine line, deviates from the compression traces gained from repetition loops towards the same deformation level. The repetition cycles show reduced hysteresis compared with the initial cycle, which can be interpreted as a superposition of both effects.

Both effects, hysteresis and Mullins, occur already at quasi-static deformation levels and can be explained by the polymer material structure. Hysteresis can be understood as internal friction between the chain molecules during deformation, whereas the Mullins effect is caused by local cracks of internal bonds in between the interlinked chains during initial deformation. The cracked bonds do longer contribute to the load transfer in subsequent cycles. Thus, Mullins can be seen as a non-recurring event, as long as the strain is not exceeded to the level achieved during initial deformation, whereas the hysteresis remains as a permanent material feature.

A further parameter that has an impact on the elasticity is the temperature. In case of elastic energy, rising temperature leads to reduced elasticity, as the molecules oscillate

relative to the grid position of maximum potential energy. The energy level drops with a rising amplitude. An elastic entropy material reveal a diminished elasticity module with rising temperature, because heat drives the molecular oscillation, thus it supports the state of maximum disorder. Ingredients, in most cases soot, behave like rigid particles of material embedded in the chain structure and are used to improve the durability. These particles do also have a rising effect on the material stiffness and significantly increase the coulomb type friction forces **[44]**. This holds not only for the static, but also under dynamic actuation, which will be addressed below.

1.5.2 Physical properties of polymers under dynamic deformation

As discussed for the static case, sliding motion of chain molecules relative to each other can be considered also for dynamic deformation of polymer materials. In contrary to the static case, where the resistance against deformation can be characterized by a drop in entropy that goes along with a coulomb type friction, the dynamic actuation reveals an additional, velocity related (viscous) frictional behaviour. However, at a certain frequency range, the chains can not follow the actuation any longer and, analogously, can be considered to behave like a hydraulically blocked viscous damper. The consequence is an increased resistance against deformation. In other words, the material stiffens up as shown graphically for a section contour along the rising frequency in Figure 2.47 (left cube section). This behaviour is in full analogy, but conversely to the effect of temperature as shown in the right cube section. If the temperature drops to a certain value, the material strength ramps up non-linearly from a *rubber-like* into the *glassy* state **[44]**, **[45]**.

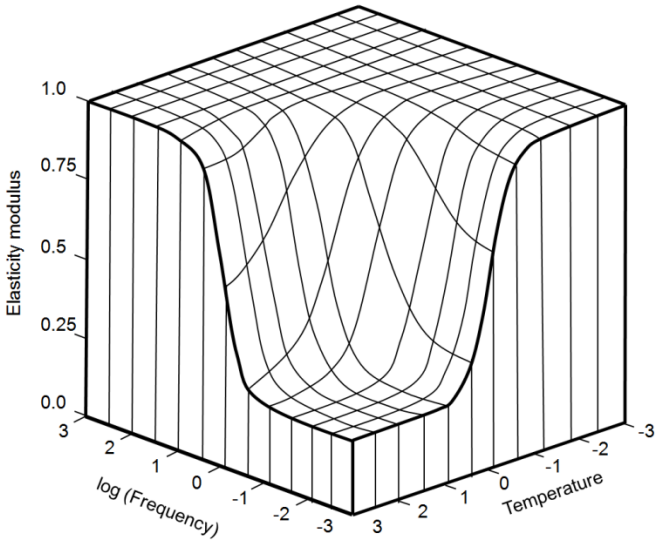

Figure 2.47: Material elasticity module over frequency and temperature developed from the original **[44]**

The glassy state can be imagined as a kind of frozen- (temperature related) or blocked (frequency) condition which then matches with the properties of elastic energy These effects are also known as *temperature*, *frequency*-hardening.

Frequency and temperature levels required to cause final transition into a glassy state, are in general not met by the upper operational range limits achieved in chassis applications. However, because of the wide transition range from rubber- to glassy frequency state (note the logarithmic scale of the frequency axis), already the start of transition to frequency hardening is a relevant feature, which needs to be taken into account in simulation approaches **[44]**.

2.5.3 Simulation of polymer material

Simulation approaches which address the dynamic response characteristics of polymers, can be categorized into three main concepts **[47]**, mathematical **[46]**, **[48]**, phenomenological **[49]**, **[50]**, **[51]** and physical models, that rebuild the structure geometry through FE elements.

1.5.3.1 Mathematical models

Mostly the first two approaches are of common practise. A simple mathematical model to simulate the force response of a jounce bumper is already discussed in section 2.4.4 and can be found in **[14]**.

$$W = K\delta^n + C\frac{dz}{dt}$$

This approach depends on the measured force response data to derive coefficients for stiffness K and damping constant C. Other authors use polynomials to derive element-typical force response shape functions **[48]**, **[49]**.

As mentioned before, mathematical models are favoured for their superior numerical efficiency, but often do not embody the exact hysteresis features.

1.5.3.2 Rheological models

A more pertinent method (phenomenological) can be achieved through use of a rheological model. The concept is based on a combination of spring- and damper elements that are assembled to a system. The rheology specifies two fundamental element types, Kelvin – Voigt and Maxwell **[19]**. A Kelvin – Voigt element consists of a spring and a viscous damper element aligned parallel, whereas the Maxwell element describes an in line configuration of both elements. Furthermore, an in line assembly of Kelvin-Voigt elements is called a Kelvin-Voigt group, a parallel assembly of Maxwell elements is named Maxwell group, shown in Figure 2.48, (a) and (b).

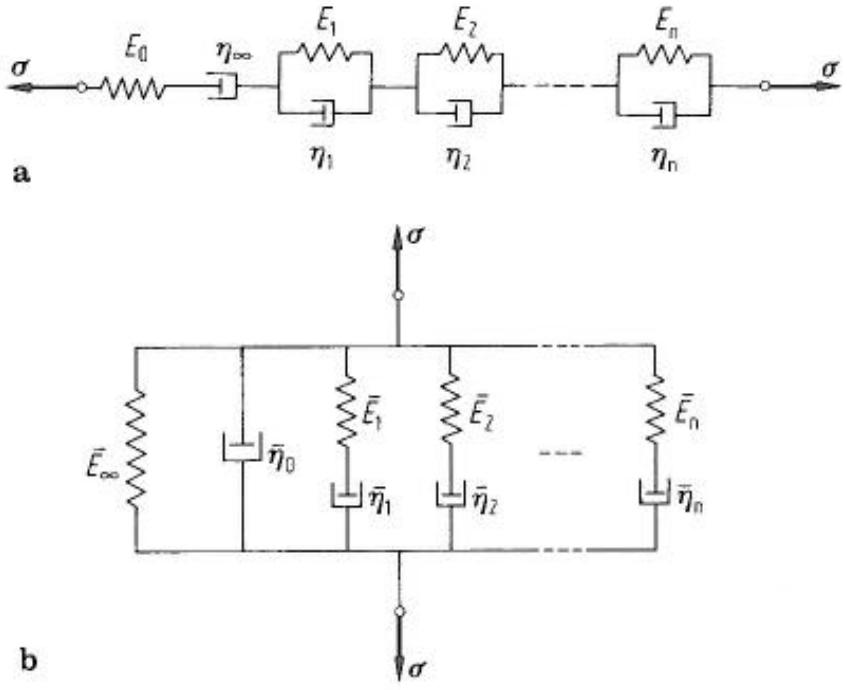

Figure 2.48: Kelvin-Voigt group (a) and Maxwell group (b) **[19]**

Both groups are effectively equivalent and can either simulate a solid material or a viscous fluid, depending on the parameter set up. For the parameters $\eta_\infty = \infty$, both configurations represent a solid material, whereas a viscous fluid is defined as $E_\infty = 0$. Equipped with this variability, the rheological concept covers a wide variety of material characteristics **[19]**.

It can be shown that the force response of the Maxwell group shown in Figure 2.49 can be adjusted to replicate the features of an entropy elasticity element. The model can be used to properly simulate the transition from rubber behaviour to the glassy state as shown in the cross-section along the logarithmic scaled frequency axis (left cube side). It also predicts the softening with rising amplitudes, as the coulomb friction impact fades out at a certain deformation range.

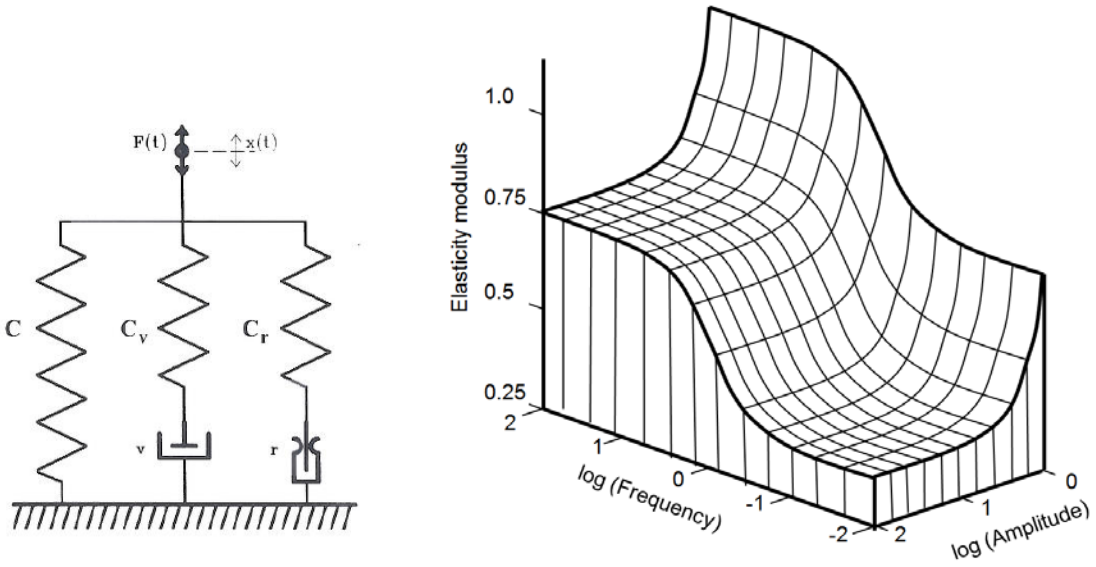

Figure 2.49: System model for viscous elastic material properties (left) and elasticity over excitation frequency and amplitude (right) **[44]**

An example of a more complex model, tailored to address the force response simulation derived for a hydro-bushing, is presented by Svensson and Hakansson **[52]** in Figure 2.50.

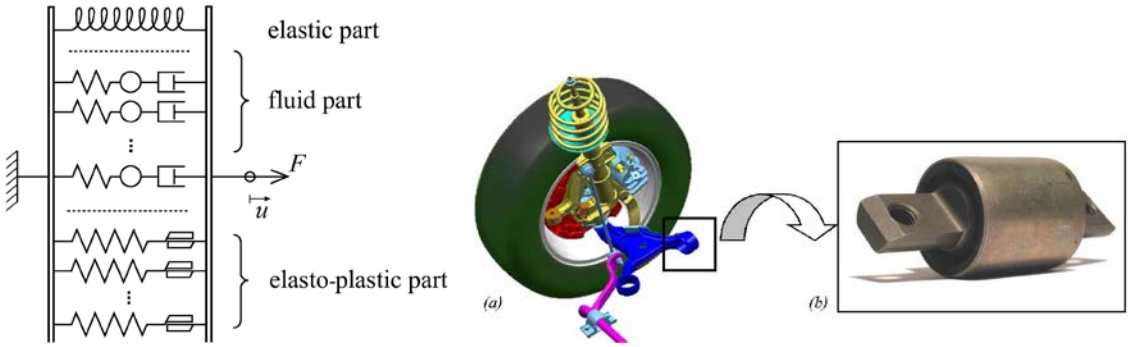

Figure 2.50: Rheological model concept (left) used for the simulation of a hydro bushing (right) **[51]**

The authors propose a concept for an automated parameter fit in conjunction with the physical testing process. General methods for polymer physical testing and data acquisition are outlined below.

2.5.4 Data acquisition for polymer components

Data acquisition is primarily carried out for a frequency band width of up to several kHz **[52], [53]**. In general, the specimen is subjected to a force actuation, where the force and displacement are measured over a frequency sweep. Two main concepts of test rigs are of common practice, (a) a support of the specimen within a rigid frame and alternatively (b), an assembly within a two mass system as shown in Figure 2.51.

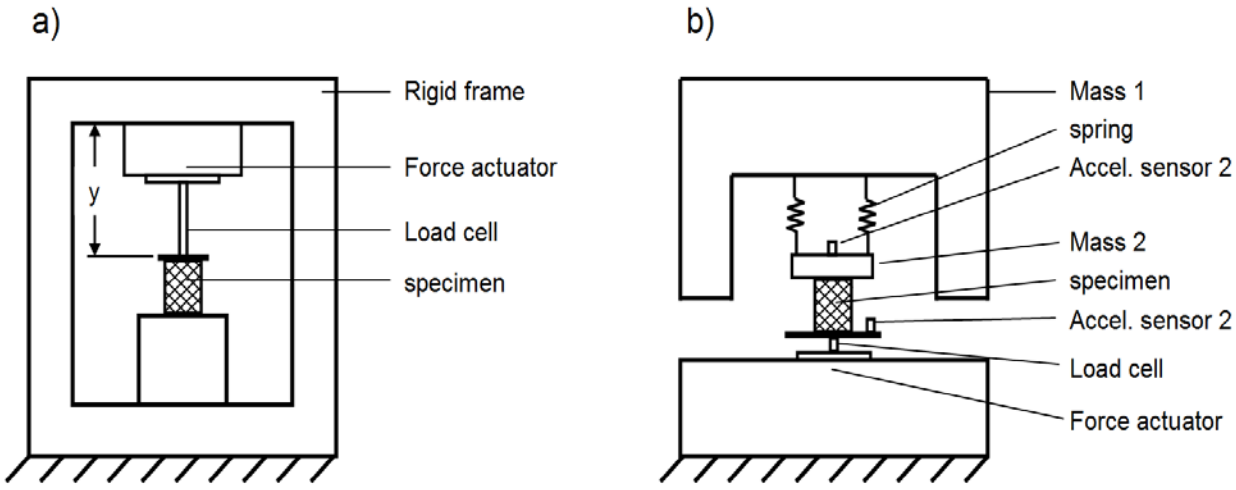

Figure 2.51: Polymer test rig concepts to test polymer elements **[52]**, **[53]**

Using the rig concept a), harmonic force actuation can be performed up to a few hundred Hz. Deformation 'y' and its phase angle to the actuation force are the signals used to establish the dynamic stiffness. The dynamic stiffness is defined by the relation of excitation force-deformation amplitude. The phase angle is used to evaluate damping. At low excitation frequencies also large amplitudes can be tested.

If an extended frequency band is investigated, the rig concept b) is of advantage, where the large mass1 is used as a quasi-static load, linked with mass2 via springs. Mass2 and the springs are adjusted to a low resonance frequency with regards to mass1. The rig is instrumented with two acceleration sensors in conjunction with the actuation force sensor. This enables the analysis of the force-deflection state of the system by post-processing. The achievable frequency range lasts up to several kHz.

Both concepts have in common the specimen displacement as a consequence of the excitation force amplitude and frequency. Thus, it cannot be adjusted directly, apart from very low frequencies that match with a quasi-static load case.

2.5.5 Jounce bumper elements in suspension applications

A fundamental aspect of severe abusive kind vertical driving events is the jounce bumper force transfer in case of impulsive kind actuation. The jounce bumper limits the maximum vertical wheel travel in upward (jounce) direction, whereas the rebound stop defines the lowest position at full hang. In this text, only jounce bumpers are addressed as the maximum vertical loads are experienced in the jounce mode. Location and design of jounce bumpers strongly depend on the suspension architecture. It is a general design concept principle to choose a position of minimal gear ratio with regards to the wheel vertical displacement. This is intended to limit the force level to full jounce position.

2.5.5.1 Jounce bumper in a Mc Pherson strut concept

As an example from a wide range of different suspension architectures, a McPherson type front strut, most commonly used in conventional passenger car applications, is shown in Figure 2.52. The bumper is attached to the body top mount and becomes engaged with the upper end of the damper tube in jounce mode. As illustrated, the free travel to the initial bumper engagement, counted from design position, is rather small compared with the compression range of the bumper. Thus, the bumper is engaged already during 'normal' driving events, not only in an abusive manoeuvre. A smooth

transition from free travel range (linear road spring characteristics) towards the progression caused by the bumper engagement is achieved by a design of relatively thin bumper walls and its wavy contour.

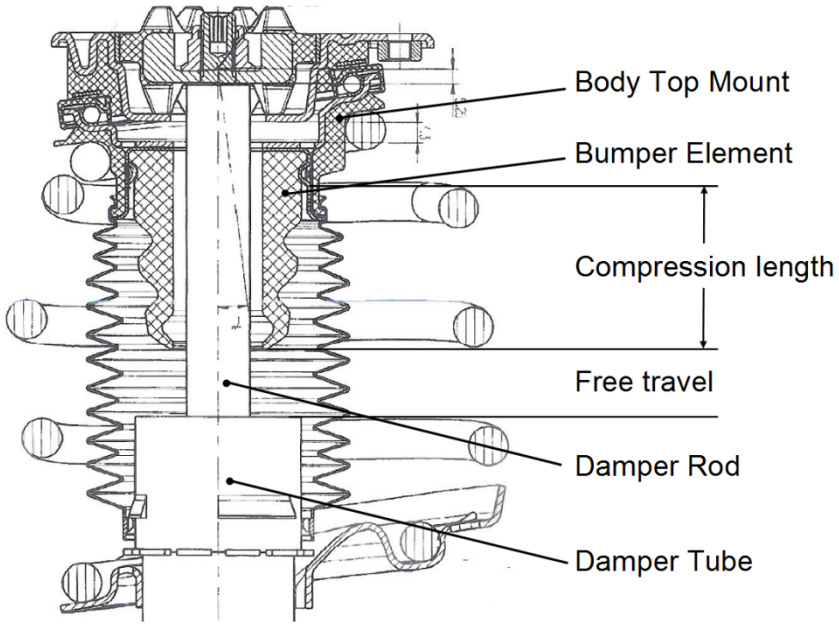

Figure 2.52: Jounce bumper assembly in a Mc Pherson front strut

The consequence of a small gear ratio and the aspect discussed above go along with the need for a large bumper compression length, if a mild progression to jounce is desired. The illustration provided in Figure 2.53 reveals the need for large material compressibility, as the bumper volume in full jounce is condensed to the space available between the lower top mount shell and the upper line of the compression length.

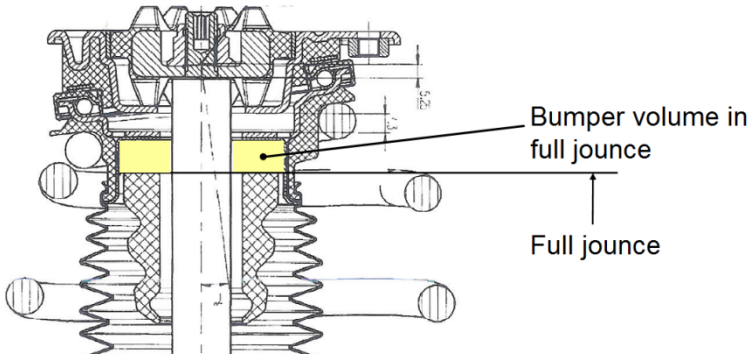

Figure 2.53: Space available for bumper volume in full jounce position

Solid polymer materials are in general almost incompressible with a Poisson's ratio approximately 0.5 **[45]**. An exception is the foam type polymer materials **[54]**, which

most common representative is polyurethane. During the polymerization, polyurethane emits CO2, which blows the volume and is embedded in the format of gas bubbles within the material structure in the final material condition shown in Figure 2.54.

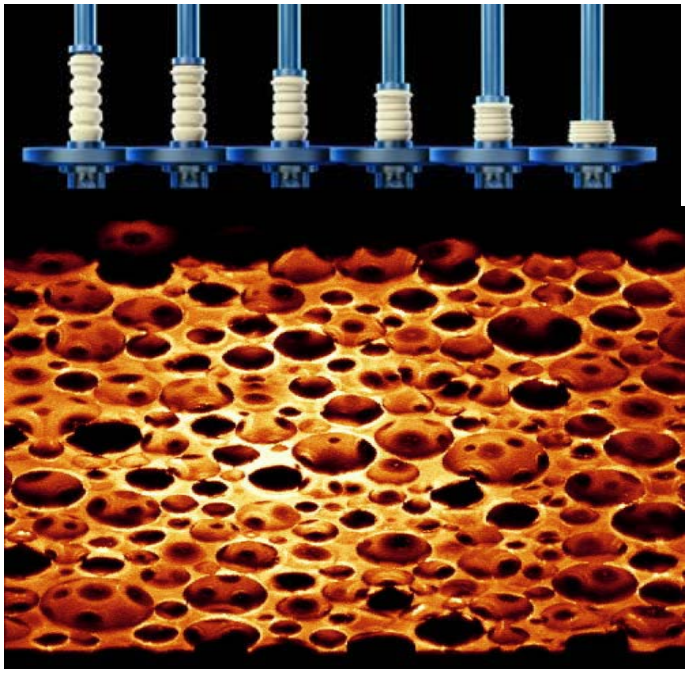

Figure 2.54: Compressibility and material structure of polyurethane **[54]**

Foam type bumpers made of polyurethane are a common standard in automotive industry, because of its cost effectiveness and superior material properties as

- compressible and highly flexible
- easy adjustable stiffness
- high dynamical durability
- low creep
- low cost and weight

2.5.6 Testing of bumper elements

The test rigs described so far are mainly used to generate frequency sweeps intended to investigate the dynamic stiffness and damping properties of polymer materials. In general, these tests are performed for small amplitudes that enable an actuation also at high frequency. In an abusive manoeuvre, the bumper is actuated in an impulsive manner which does not comply with the nature of the rigs described under 2.5.4. An effective

method is seen in the drop test concept, where a specified mass is released at a certain height and hits the bumper element mounted on a grounded force cell.

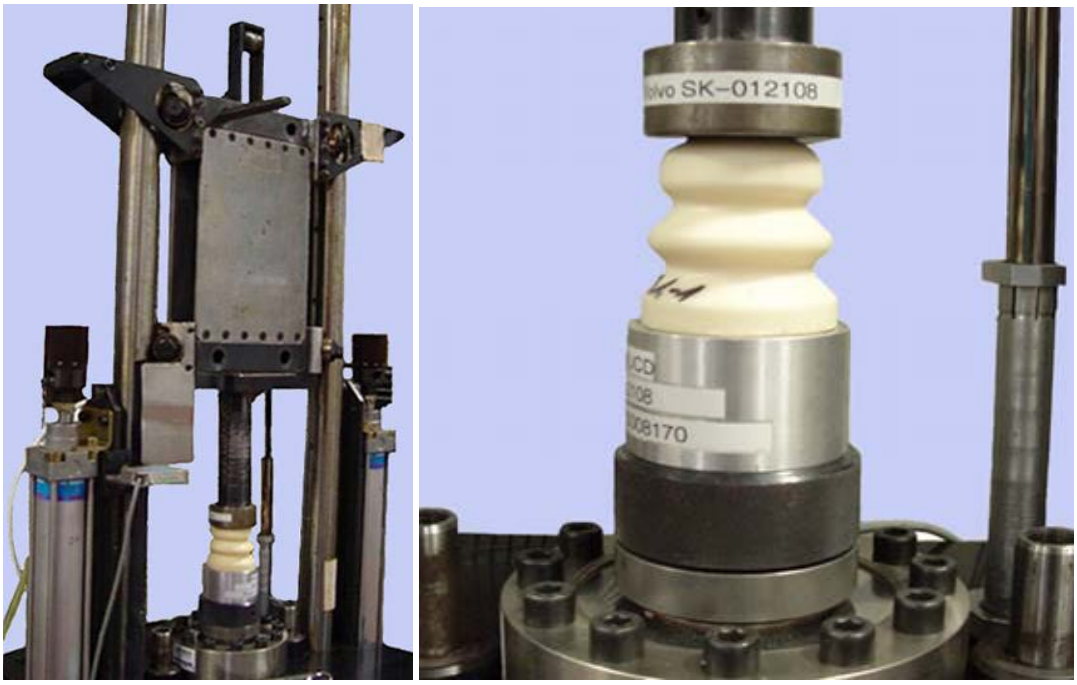

Figure 2.55: Bumper drop test rig **[56]**

The test specification can easily be defined by the potential energy and impulse derived from mass and height.

2.5.7 Dynamic features of foam type polyurethane bumpers

Based on drop test results, Austrell and Wirje **[56]** investigated the difference in static- and dynamic behaviour of polyurethane bumpers. The authors could demonstrate that such bumpers show significant deviation in force transfer to static force response (dashed lines) if applied to impulsive deformation (solid lines) recorded from drop tests shown in Figure 2.56.

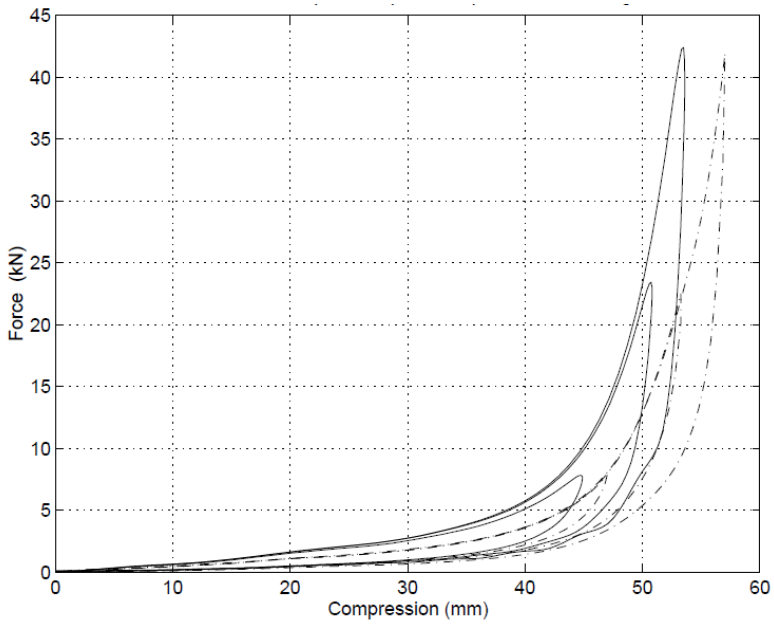

Figure 2.56: First bounce impact data at 96, 189 and 286 J (solid lines), and comparison to corresponding quasi-static loading (dash dotted lines) **[56]**

The authors developed a rheological bumper model based on a Maxwell element intended to simulate the dynamic bumper load curve and to address their typical hysteresis properties. Model validation was performed by comparison with physical drop tests as well as harmonic actuation force response data.

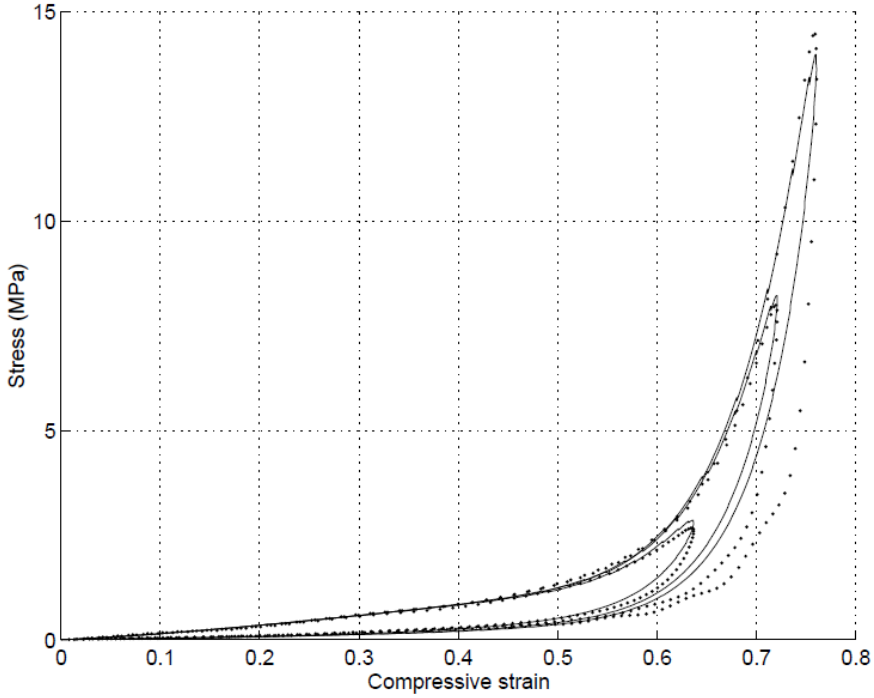

Figure 2.57: Simulation results (dotted line) compared to drop test results (solid) **[56]**

Because of the bumper construction, large displacement and high end force capacity is required for a harmonic actuation. Conventional hydraulic equipment is often terminated to fulfil both requirements simultaneously because the maximum oil volume flow sets the limit for piston velocity.

2.5.8 Summary and conclusions drawn from bumper literature review

In comparison to metal properties, polymer materials are difficult to describe with regards to their physical effects and stress-strain behaviour. Beside pure mathematical models, also rheological models have been discussed, where the latter are seen as the more sophisticated and up to date approach, as these models can easily be included in a MBS structure. An analysis on basis of the FEM is not considered in this thesis, as the numerical effort and complexity involved with this approach does not fit with the strategy of simplicity aimed in this thesis and favoured in industry.

All methods discussed require an element specific data acquisition, mainly gained by means of physical testing. Jounce bumpers, in particular foam-type bumpers, possess a large compression length needed for a smooth engagement. Their dynamic force response in general deviates from static applications. For a physical testing, this aspect has to be taken into account by the feasibility to apply large deformation amplitudes. This necessarily causes high actuation velocity and bumper block force level. The capacity of hydraulic equipment is often limited with regards to this combination of demands. Therefore, the drop test is established as a common standard for the *validation* of foam type bumpers, but less applicable for the *data acquisition* purpose. To overcome the limitations of hydraulic equipment, a mechanical crank was proposed by the author in **[56]** and **[57].** The rig, shown in Figure 2.58 is suitable for large amplitude harmonic actuation and is addressed in chapter 5 and in the appendix B.

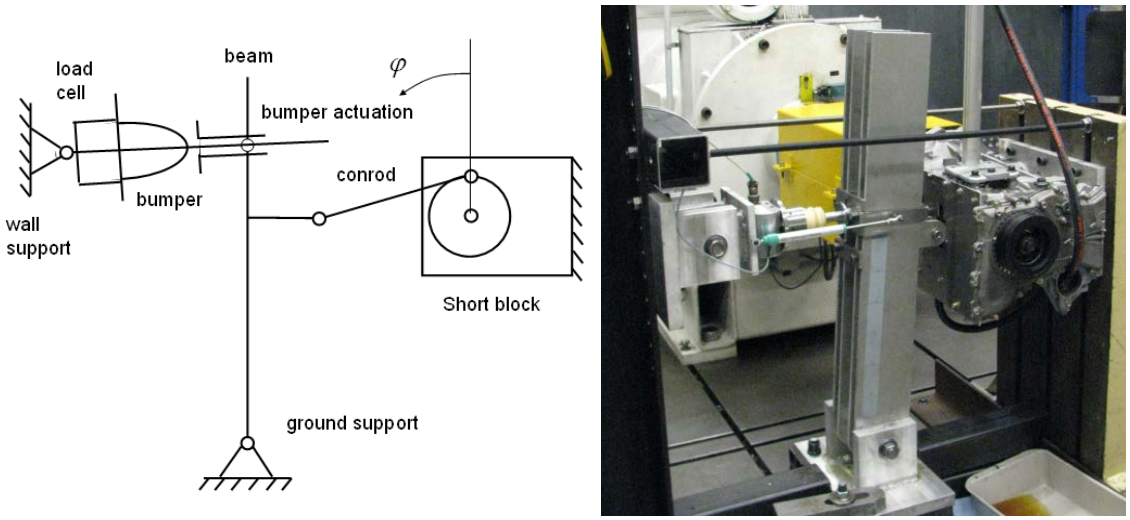

Figure 2.58: Concept of bumper test rig kinematics and physical test set up [**57**, **58**]

The rig recordings are casted into a standardized format of a 3D force response map, tailored to be used as a mathematical model.

2.6 Literature summary and influence on present thesis

The study shows that several kind of vehicle models exist for the purpose to predict wheel centre and component loads with good accuracy derived from abuse kind manoeuvres. This statement can be extended to be valid also for existing tyre- and bumper models. In summary, following findings and conclusions are noted:

1) The concept of Multi Body System (MBS) is confirmed to be the state of the art method applied to set up the mathematical formulation of vehicle simulation models. MBS is preferred to the Finite Element Method (FEM), because of superior numerical efficiency and reduced model complexity.

2) The effort for a model parameterization in general rises with the model complexity level. This awareness explains the advantages of minimal parameter models, if these are tailored to the application of special boundary conditions.

3) A detailed tyre model, that includes the features of a belt to rim clash condition, is required for an abuse kind kerb-strike simulation.

4) A detailed model for the bumper, which limits the vertical wheel travel, addressing the non linearity and dynamic force response features of such components, is obligatory for a decent force prediction.

5) A structure-variant vehicle model architecture is required to cope with the boundary conditions raised in the foregoing items 3 and 4.

A common nature of these models is their high grade of complexity with regards to the number of parameters needed and, in some cases, its complex data acquisition methods, especially in conjunction with tyre- and bumper simulation.
In this thesis, focus is put upon investigation of the macro-scaled structure by using a minimal parameter input set. In the end, the question which should be answered is whether a reasonable load assumption can be made for BiP and DoK manoeuvres on the basis of a minimal parameter model. Thus, all parameters that are assumed to have none or minor effect on the wheel centre- and bumper load level are neglected in the developed model.

2.6.1 Conclusions drawn for the vehicle model requirements

Based on the findings from the foregoing literature study, it can be considered that a decent tyre- and bumper model is an obligatory ingredient, that needs to be included in the vehicle simulation model **[14]**, **[56]**. This necessarily leads to the requirement of a structure-variant model formulation. A one-dimensional concept, as the quarter car suspension model presented in **[21]**, does not include the feature of a body pitch motion, which is seen as a relevant attribute of DoK or BiP driving manoeuvres. As both DoK and BiP event do not cause relevant side forces or roll motion, a planar (bicycle model) was selected for the vehicle model concept, but extended to take fore-aft wheel travel into account (see Figure 2.59). This extension covers the foresight of model upgrade compatibility, intended to match with longitudinal loads expected for BiP manoeuvres, planed for a later stage.
Aligned with this planar model concept, the effects of suspension kinematics, apart from the bumper position relative to the wheel travel, were neglected. These are considered to

be of minor influence on the total force level expected in wheel centre and top mount for a kerb strike. A further aspect is seen in the fact, that a detailed suspension kinematic formulation consequently leads to a spatial model architecture, which is not aligned with the purpose of simplicity.

Due to the moderate velocity level specified for the tests (max 40 km/h), wheel angular momentum effects are not taken into account.

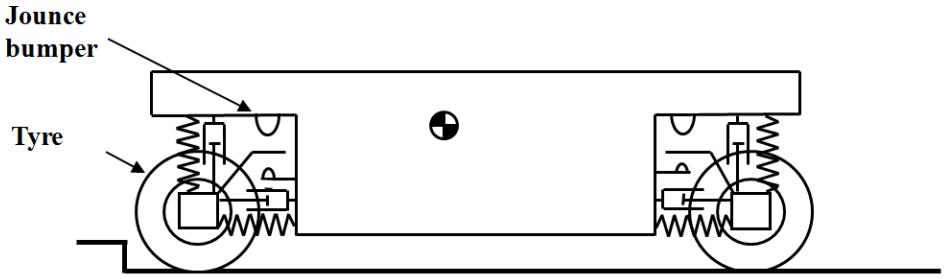

Figure 2.59: Bicycle model concept to simulate DoK and BiP manoeuvre

2.6.2 Conclusions drawn for tyre and bumper model requirements

The literature sources, presented in this study, confirm the impulse-kind nature of kerb strike events **[6]**, **[7]**, **[14]**, **[40]**. Both manoeuvres, BiP and DoK, lead to full-scale jounce bumper and tyre deformation and in general to a belt to rim clash in contact with the kerbstone edge. Because of these observations, emphasis needs to be put upon a thorough modelling of the jounce bumper characteristics to match with the dynamic effects in connection with impulsive kind actuation. In particular, the bumper position relative to bump stop element and its non-linear, viscous-elastic behaviour is seen as a key contributor to vertical load level **[56]**. A map concept, described in chapter 5, was applied to address the bumper non-linear force response and hysteresis for impulse kind-, dynamic actuation expected from a kerb strike manoeuvre.

In line with the aspects discussed for the vehicle model, an in-plane tyre model was used to simulate the kerb-strike. The feasibility to address a belt-to-rim clash during kerb strike is considered to be an essential model feature, needed for an authentic force prediction **[3]**. As discussed for the vehicle model, this requirement implies the need for a structure variant formulation also for the tyre model.

The model can be simplified by addressing the pneumatic radial force response of the tyre only, which neglects its structural stiffness and inertia, as the latter effects are in general of minor importance for conventional tyres, depending on the actual geometry **[21]**. Based on these findings, the tyre vertical load transfer can be simplified by the application of a quasi static approach. The tyre presented in this thesis is defined by four geometric cross sectional parameters and the pneumatic pressure. A tyre belt-to-rim clash condition during kerb strike at full tyre deflection range is addressed by an assumed constant rim stiffness.

Chapter 3: Methodology

3.0 Introduction

In this chapter, the methods used in the thesis are summarized. The numerical methods used to set up and run the different simulation models are presented first, followed by validation methods, where the data acquisition and test conditions are briefly presented. A more detailed description is given in the appropriate subsequent chapters.

3.1 Numerical methods

Here, the numerical methods are described for the modelling approaches used for the vehicle, the tyre and the bumper simulation. Table 3.1 shows a methods overview:

model	structure concept	math. format	method of solution	other detailes
vehicle	MBS of in-plane bicycle model extended to 7 DoF	2nd order differential equations (equations of motion)	numerical integration in the time domain using RUNGE-KUTTA algorithm	fixed time step size Tstep = 1.0E-04 seconds
bumper	two parametric spatial force response map concept	3D matrix containing spline coefficients to describe 3rd order interpolation polynomials	3rd order cubical spline interpolation	twelve spline intervals of width 15° to cover 180 degree phase angle recorded from seven actuation amplitudes 40 - 55 mm
tyre	1) continuous membrane structure for belt and sidewalls	algerbaric function force over deflection	direct analytical solution	derivation based on torus structure analysis **[60]**, **[61]** and hinge bridge analogy **[62]**
	2) discretized chain structure (belt) attached to radial ropes (sidewalls)	algebraic equation derived from virtual work approach	iteration process to establish belt force for equilibrium condition	iteration devided into 5 steps to subsequently adjust the boundary conditions

Table 3.1: Numerical methods overview

3.1.1 Vehicle simulation

The vehicle model is defined by its equations of motion that contain the inertia, stiffness and damping properties of the system. These equations were derived by the application of Lagrange's equation **[14]**. The vehicle model, described in detail in chapter 4, does not incorporate any kinematic constraints, thus the Lagrange approach in the format of equation (2.10) **[17]** addressed in item 2.2.1.2 (c) could be used to derive the equations of motion.

Solutions found for the vehicle trajectories and force responses are derived by numerical integration in the time domain using the Runge-Kutta method. A detailed explanation of this approach is given in appendix A. The simulation models exist in the format of a FORTRAN source code written by the author. Tyre and bumper deflection and their appropriate reaction forces are treated as external forces provided by modular subroutines during the numerical integration.

All results presented in the thesis are derived from a fixed integration time step of 1.0E-04 seconds. The time interval of the impulsive bumper strike event after kerb crossing is about 5.0E-02 seconds, thus a high resolution of 500 data points is provided during the bumper engagement with the time step specified.

3.1.2 Bumper simulation

The bumper force response is gained from interpolation within a two parametric map to establish the force as function of bumper deflection and deformation velocity. Force response traces for the map data set up were recorded from physical harmonic bumper actuation at 10Hz frequency. The force data acquisition was performed for a set of seven actuation amplitudes starting from 40 up to 55 mm as described in chapters 5 and 7. The data recordings in the time domain are post processed to the format of single data points over circular frequency in a resolution of 15 degrees. The appropriate feedback force for a given bumper deflection and velocity state is calculated by numerical cubical spline interpolation which is described in appendix A and in **[23]**, **[64]**. The spline coefficients required for the interpolation are derived in a pre-processing step in advance of the Runge-Kutta numerical integration.

3.1.3 Tyre simulation

Two model approaches are proposed in chapter 6: A full analytical model based on pneumatic pressure and the tyre cross section geometry and secondly a chain model representing the tyre belt structure by discrete chain elements. Whereas the analytical model provides direct solutions for the force response based on the deflection mode, the chain model is combined with the virtual work principle to derive the force response resulting from the belt equilibrium condition. Changes in the boundary conditions are addressed by a numerical iteration process as discussed in chapter 6, item 6.6.2.

3.2 Convergence study

Numerical results in general can vary with the step size specified for the numerical integration. In case of large step sizes, model relevant features in the high frequency range of the analyzed event may be missed. With a transition towards smaller step sizes, higher frequency responses are addressed and the numerical result converges towards the *exact* solution. Such a convergence study shall confirm the specified step size used for the simulation to be appropriate for the specific model application. Numerical robustness can be demonstrated by a step size sensitivity analysis of the response. As mentioned in 3.1.1, all simulation results are derived for a step size of 1.0E-04 seconds. The bumper force response map module revealed to be the most sensitive component in the vehicle model with regards to a step size variation. A deviation of the bumper force was found in the range of only 2% for a step size increase from 1.0E-04 towards 1.0E-03 seconds. Significant deviations (approx. 10%) were observed for a step size of 2.0E-03 seconds, which confirms the robustness of results for the specified step size.

3.3 Validation

The validation of the simulation models was performed separately on both component level (bumper and tyre models) and on system level (vehicle model, incorporating the bumper and tyre models). An overview about the validation methodologies is shown in table 3.2:

model	validation test	measurand	instrumentation	data aquisition
vehicle	Drive over Kerb test at 25 and 40 kph, kerb height 135 mm, 2.0 bar pneumatic tyre pressure	1) Integral top mount force over time	1) force cell GTM, series K, force range 1 - 63 kN	universal analogous signal recording and amplifier system ICM CRONOS series V, sample recodig rate 10 kHz
		2) wheel centre vertical deflection relative to body	2) string potentiometer ASM series WS31, deflection range 1 - 500 mm	ICM CRONOS-V
bumper	1) force response map data recording on sinusoidal displacement actuation rig at 10 Hz circular frequency for 7 amplitudes range 40 - 55 mm	bumper force response over time and sinusoidal bumper displacement over time	force cell produced by FORD machine shop, force range 1 - 80 kN and WAY CON linear potentiometer with line range 0 - 200 mm	ICM CRONOS-V
	2) drop test at fall height 428 mm performed for three masses 23, 45 and 68 kg (96, 189 and 286 J) at ELASTOGRAN **[56]**	bumper force and deflection over time **[56]**	force cell ELASTOGRAN **[56]**, unknown manufacturer	ELASTOGRAN drop test rig data aquisition system **[56]**, unknown manufacturer
tyre	1) comparison of pneumatic pressure induced internal stress to FEA results gained from ABAQUS tyre for three pressure level 1, 2 and 3 bar in absence of external applied deformation	integral circumferential belt force Fg and tyre sidewall line loads Qsb and Qsr at belt and rim edge	ABAQUS finite element analysis	FoE Chassis Engineering ABAQUS tyre models for sizes 205/55-R16 and 235/40-R18
	2) force response measurement against quasi static radial deformation using flat and edge type geometry	radial force response over radial deflection	force cell produced by FORD machine shop, force range 1 - 80 kN	ICM CRONOS-V

Table 3.2: Validation methods overview

3.3.1 Data acquisition

The sensors used for the experimental testing, such as load cells and potentiometers provide an analogous signal to the data acquisition system. This data in general needs to be amplified before the data logging and post-processing can be done in a PC environment. The IMC CRONOS-V data acquisition system as shown in Figure 3.1 was used to record all experimental testing.

Figure 3.1: CRONOS-V data acquisition system

The CRONOS-V combines data recording, amplification of the analogous signal and post processing in a single unit and allows data logging to a sample rate up to 50 kHz for 4 channels. Not just the vehicle testing but all other experimental data from bumper map testing and tyre force response measurements was recorded with this acquisition system.

3.3.2 Vehicle model validation

The validation of the vehicle simulation model was performed by a comparison of top mount force simulation results with measured signals recorded for DoK. A kerb of 135 mm height was negotiated in a free rolling mode with two velocities, 25 and 40 kph as described in chapter 1. The vertical top mount force and the vertical wheel travel relative to body was measured on a FORD vehicle (CD340), equipped with sensors at the front suspension. The DoK event and vehicle instrumentation are shown in Figure 3.2.

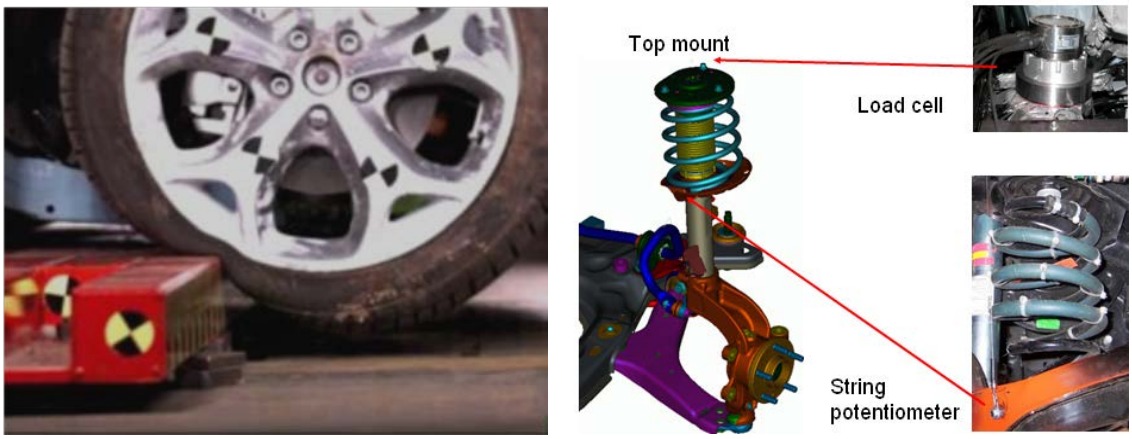

Figure 3.2: DoK event and vehicle instrumentation

The top mount load cell used, GTM (Gassmann Theiss Messtechnik) series K, is specified for a load range up to 63 kN. It was mounted in between the body structure and the McPhesron strut topm mount. Thus, the recording represents the integral vertical force signal combining spring, damper and bumper force.

A string potentiometer ASM model WS31 with a displacement range of 500 mm was used for the wheel displacement measurements. The potentiometer housing was fixed to the strut body tower while the string end was attached to the spring plate of the McPherson strut.

Both signals were recorded in the time domain at a sample rate of 10 kHz.

3.3.3 Bumper model validation

The bumper force response simulation concept is based on a two-dimensional parametric map consisting of measured force response data recorded for harmonic actuation at a circular frequency of 10 Hz. This matches with the conditions of a kerb strike as described in more detail in chapter 5. To generate a harmonic displacement actuation for various amplitudes in the range of 40 – 55 mm, a rig was designed as shown in Figure 3.3:

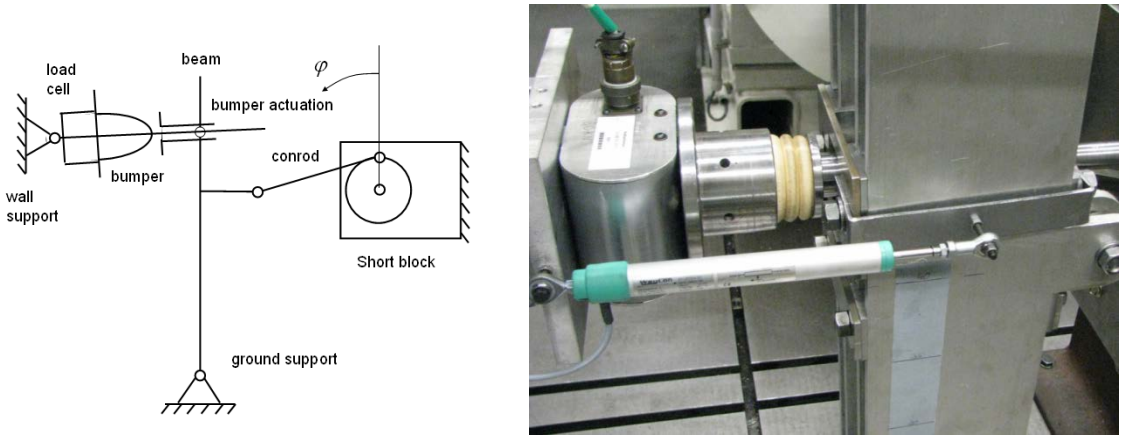

Figure 3.3: Bumper Rig design principle sketch (left) and load cell instrumentation (right)

A FORD manufactured load cell (1- 80 kN) was used in combination with a WayCon linear potentiometer (line range 200 mm) to record force and displacement over time at a frequency of 10 kHz.

To validate the bumper force response map simulation concept presented in chapter 5, a drop test simulation was set up by making use of the recorded map. The results gained from drop test simulation were compared to those gained by experimental data taken from literature published by Austrell and Wirje in **[56]** for validation.

3.3.4 Tyre model validation

The tyre model validation was done on the basis of both numerical comparison to FE results and also physical testing. As a physical testing of the internal tyre stress is considered as a difficult, if not impossible task, FE results were generated by using the FoE Chassis CAE ABAQUS tyre models to confirm the analytical formulas derived for tyre internal stress analysis in chapter 7. These FE models, developed within the FORD Chassis Engineering CAE group, exist for two tyre sizes, 205/55-R16 and 235/40-R18. A detailed description is given in chapter 6.

The physical testing was performed on component level where the tyre force response was recorded for a quasi static radial deformation against both an edge type (blade) and a flat geometry. The test facility representing the set up for an edge geometry is shown in Figure 3.4:

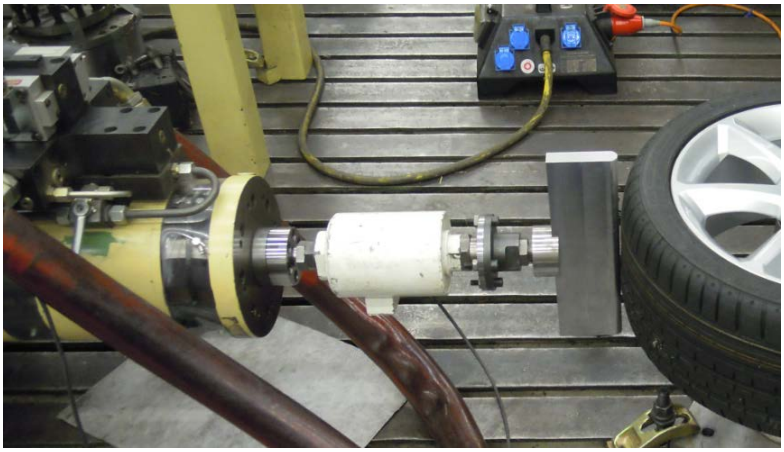

Figure 3.4: Quasi static measurement of radial force response

A FORD manufactured load cell calibrated for the load range up to 80 kN was adjusted in between the hydraulic cylinder and the blade type geometry. Displacement signals were taken from the sensor integrated in the hydraulic cylinder. The recordings were logged in a resolution of 10 force data points per mm radial displacement.

3.4 Closure

A brief overview of the methodology used for the simulation model concepts, numerical algorithms set up and solving has been provided. In addition, the methods of experimental testing for the purpose of validation were presented, in hope that similar work can be performed by the interested reader.

Chapter 4: Minimal Parameter vehicle model

4.0 Introduction

In this chapter the vehicle model concept, its elements and boundary conditions are presented. The model's mathematical formulations, as well as its simplifying assumptions are stated.

4.1 Vehicle Model Concept

As outlined in the literature study, a multi-body approach was chosen for the mathematical formulation of the vehicle model.

As both, DoK and BiP event can be expected not to cause significant side forces or roll motion, a planar (2-dimensional) vehicle model (bicycle model) was selected and extended to take into account fore-aft wheel travel (Figure 4.1). Due to the moderate traverse velocities specified for the tests (max 40 km/h), wheel angular momentum effects are also ignored.

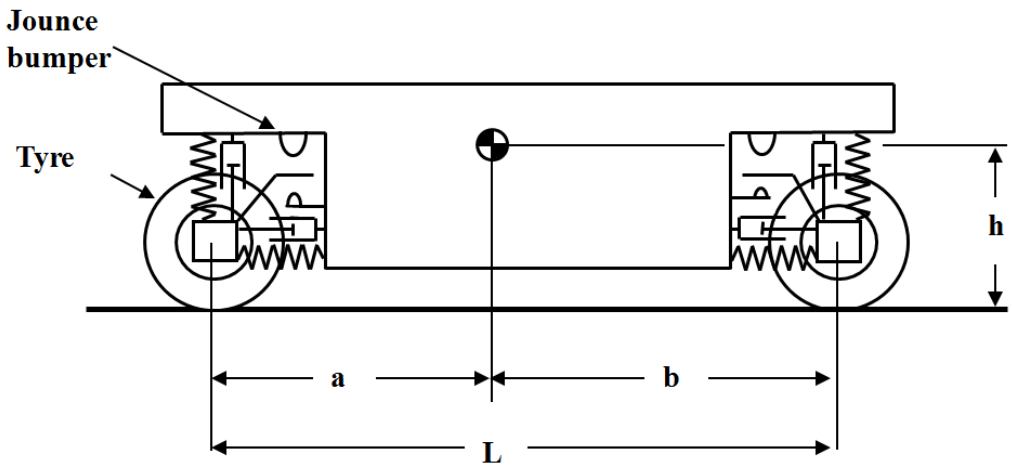

Figure 4.1: Minimum Parameter vehicle model concept to simulate DoK and BiP manoeuvres

As mentioned earlier, the nature of both manoeuvres lead to an impulse-like, full-scale jounce bumper deformation and in general to a tyre belt-to-rim clash during contact with the kerbstone edge. Emphasis is put upon modelling of jounce bumper characteristics

and tyre behaviour under severe impacts. A map concept, outlined in chapter 5, was applied to address the bumper hysteresis, a typical feature for these polymer type components.

The tyre model, which is described in detail in chapter 6, is condensed to address the pneumatic radial force response of the tyre only, neglecting its structural stiffness and inertia.

4.1.1 Model element overview

The individual inertias of the suspension links were combined to a lumped parameter un-sprung wheel mass. The exact suspension geometry, kinematics and individual component stiffness were merged to combined vertical and lateral stiffness elements. Figure 4.2 shows an overview of the vehicle model components listed below:

1. sprung mass and rotational inertia
2. un-sprung masses including wheel, hub, brake, lumped suspension
3. road spring's constant stiffness
4. shock absorber's constant damping
5. jounce bumpers (map concept)
6. rebound stop's non-linear stiffness (no damping)
7. kinematics of free wheel travel and jounce / rebound contacts
8. longitudinal stiffness / damping of wheel centre against body
9. tyre

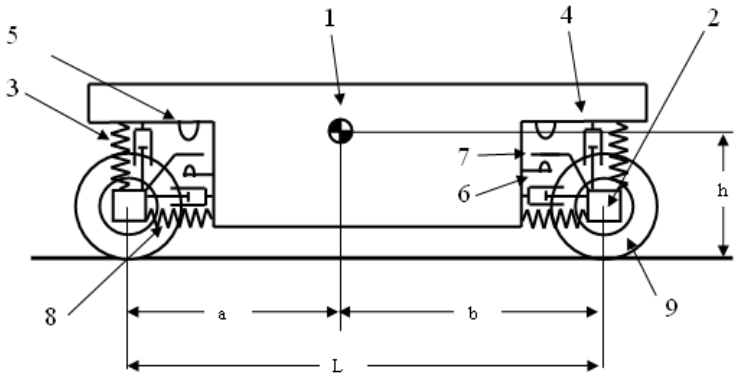

Figure 4.2: Minimum parameter vehicle model

4.2 Derivation of the equations of motion

As the suspension kinematics was reduced to the bump position and engagement, no algebraic equations to define kinematic constraints are required. The model consists of three bodies, **m1** and **m2** representing the un-sprung wheel mass and **m3** for the sprung body. A rotational DoF is considered for the body, addressed by the rotational inertia **J** as shown in the upper image of Figure 4.3. The structure matches with a conventional bicycle model as described in **[17]** and **[20]**, but is extended by three longitudinal DoF X1, X2 and X3 to in total seven system DoF. Forces and moments are indicated as bold arrows in the lower image.

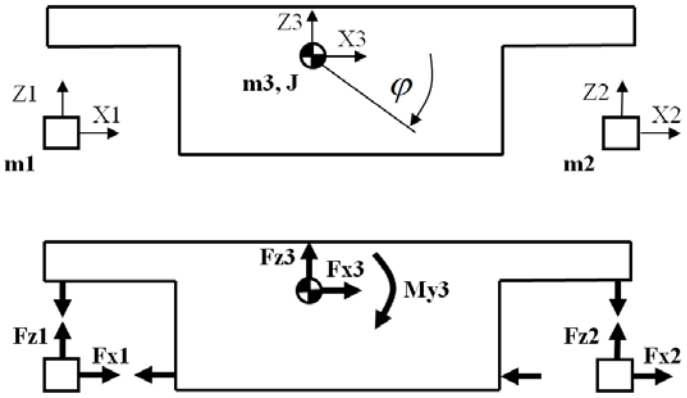

Figure 4.3: Degrees of freedom (upper) and loads shown in a free body diagram

The mathematical formulation of the dynamic force balance to derive the equations of motion can be written in its matrix representation as follows:

$$[M]\cdot\begin{Bmatrix}\ddot{z}_i\\ \ddot{x}_j\\ \ddot{\varphi}_k\end{Bmatrix}+[D]\cdot\begin{Bmatrix}\dot{z}_i\\ \dot{x}_j\\ \dot{\varphi}_k\end{Bmatrix}+[C]\cdot\begin{Bmatrix}z_i\\ x_j\\ \varphi_k\end{Bmatrix}=\begin{Bmatrix}\sum fz_i\\ \sum fx_j\\ \sum my_k\end{Bmatrix} \tag{4.1}$$

Indices i = 1…3 stand for the vertical, j = 1…3 for the longitudinal and k = 1 for the rotational DoF. Indices i, j and k stand for the DoF only and shall not be understood as the mass component indices used for m1, m2 and m3, although these match for the longitudinal and vertical DoF. In particular, the vector multiplied with matrx [C] in equation 4.1 is of the fomat $\{z1,\ z2,\ z3,\ x1,\ x2,\ x3,\ \varphi1\}^T$. As φ is the only rotational DoF, its index k = 1 is dropped out in the following derivations.

The first product (matrix [**M**]) contains the inertial forces, followed by the internal system force responses (matrices [**C**] and [**D**]) and the external forces applied to the system (right side of equation 4.1). To establish the equations of motion, matrices [**M]** for mass and rotational inertia, [**D]** damping and [**C]** stiffness, need to be derived. Lagrange expounded the relationship between energy terms and the equations of motion of a system. As shown in chapter 1, these equations can be derived analytically by partial derivatives with respect to the generalized degrees of freedom q of the system. Lagrange's equation (4.2) was used for the derivation **[14]**.

$$\frac{\partial}{\partial t}\left(\frac{\partial Ekin}{\partial \dot{q}}\right)-\frac{\partial Ekin}{\partial q}+\frac{\partial Epot}{\partial q}=\frac{\partial w}{\partial q} \tag{4.2}$$

In contrast to the classical bicycle model, the system properties of the model will vary for the case of bumper engagement at appropriate vertical wheel displacement states. Three suspension bumper engagement states need to be differentiated, shown in Fig. 4.4:

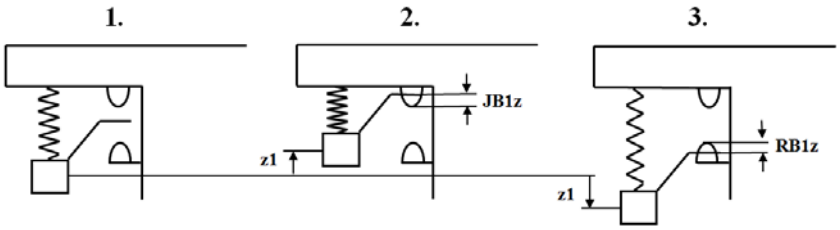

Figure 4.4: Suspension bumper engagement states

1. free wheel travel (no contact to jounce or rebound bumper)
2. wheel travel retainer in contact with jounce bumper
3. wheel travel retainer in contact to rebound stop

4.2.1 Equations of motion for the system in free travel mode

For case 1 above, the system is considered to be free of any wheel travel restrictions; in other words, neither jounce nor rebound occurs. Therefore, the model structure does not change with deflection state; the system structure is invariant.

Equation 4.2 is used to derive the matrices [**M**], [**D**] and [**C**] that describe the equations of motion for the system in free travel mode.

(a) Mass matrix

The formulation of the potential and kinetic energy addressed in equation (4.2) is performed for each degree of freedom. The first two terms contain the kinetic energy and are used to derive the mass matrix [**M**]. For case 1, wheel centres in free travel mode (no bumper engagement), the vertical components z_i lead to the terms:

$$Ekin = \sum \frac{1}{2} m_i \cdot \dot{z}_i^2$$

The longitudinal components x_j reveals:

$$Ekin = \sum \frac{1}{2} m_j \cdot \dot{x}_j^2$$

And for the rotational DoF φ_k gives:

$$Ekin = \sum \frac{1}{2} J_k \cdot \dot{\varphi}_k{}^2$$

Partial derivative with respect to the generalized coordinate $\dot{q}$ and time *t* leads to the terms:

$$\frac{\partial}{\partial t}\left(\frac{\partial Ekin}{\partial \dot{z}_i}\right) = \sum m_i \cdot \ddot{z}_i \tag{4.3}$$

and:

$$\frac{\partial}{\partial t}\left(\frac{\partial Ekin}{\partial \dot{x}_j}\right) = \sum m_j \cdot \ddot{x}_j \tag{4.4}$$

Also:

$$\frac{\partial}{\partial t}\left(\frac{\partial Ekin}{\partial \dot{\varphi}_k}\right) = \sum J_k \cdot \ddot{\varphi}_k \tag{4.5}$$

The second term:

$$\frac{\partial Ekin}{\partial q} = 0$$

for all the DoF, as the kinetic energy, in this case, is not a function of the general coordinate *q*.

Combined equations (4.3) – (4.5) represent the first term of equation (4.1), the mass matrix is established as:

$$\begin{bmatrix} m_1 & & & & & & \\ & m_2 & & & & & \\ & & m_3 & & & & \\ & & & m_1 & & & \\ & & & & m_2 & & \\ & & & & & m_3 & \\ & & & & & & J \end{bmatrix} = [M] \qquad (4.6)$$

(b) Stiffness matrix

The third term in equation (4.2), namely the partial derivatives of the potential energy, lead to the stiffness matrix. In this case, the base geometry a, b, c with respect to the location of body centre of gravity must be taken into account (see Figure 4.5).

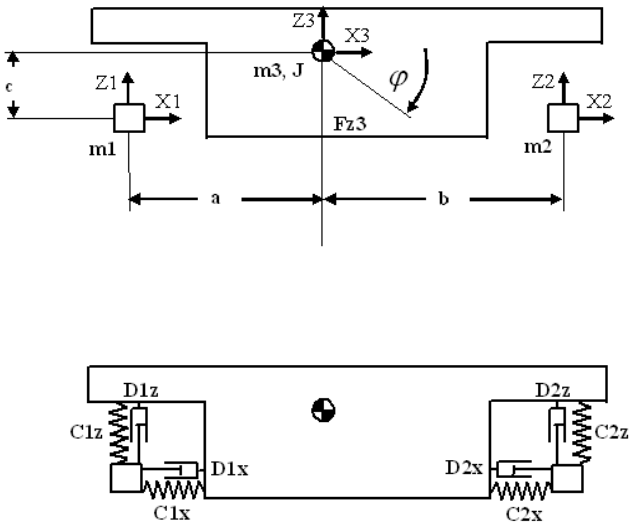

Figure 4.5: Centre of gravity geometry and element overview

For the stiffness and damping configuration as shown in Figure 4.5

Potential energy:

$$\begin{aligned} Epot = & \frac{1}{2}\cdot c_{1z}\cdot\left(z_1-\left(z_3-a\cdot\sin\varphi\right)\right)^2+\frac{1}{2}\cdot c_{2z}\cdot\left(z_2-\left(z_3+b\cdot\sin\varphi\right)\right)^2 \\ & +\frac{1}{2}\cdot c_{1x}\cdot\left(x_1-\left(x_3+c\cdot\sin\varphi\right)\right)^2+\frac{1}{2}\cdot c_{2x}\cdot\left(x_2-\left(x_3+c\cdot\sin\varphi\right)\right)^2 \\ & +m1\cdot g\cdot z_1+m_2\cdot g\cdot z_2+m_3\cdot g\cdot z_3 \end{aligned} \tag{4.7}$$

Considering small deflection angle φ, the expression simplifies to $\sin\varphi \approx \varphi$, $\cos\varphi \approx 1$, leading to the linearized formulation:

$$\begin{aligned} Epot = & \frac{1}{2}\cdot c_{1z}\cdot\left(z_1^2-2z_1z\ +2z_1a\varphi+z_3^2-2z_3a\varphi+a^2\varphi^2\right) \\ & +\frac{1}{2}\cdot c_{2z}\cdot\left(z_2^2-2z_2z_3-2z_2b\varphi+z_3^2+2z_3b\varphi+b^2\varphi^2\right) \\ & +\frac{1}{2}\cdot c_{1x}\cdot\left(x_1^2-2x_1x_3-2x_1c\varphi+x_3^2+2x_3c\varphi+c^2\varphi^2\right) \\ & +\frac{1}{2}\cdot c_{2x}\cdot\left(x_2^2-2x_2x_3-2x_2c\varphi+x_3^2+2x_3c\varphi+c^2\varphi^2\right) \\ & +m_1\cdot g\cdot z_1+m_2\cdot g\cdot z_2+m_3\cdot g\cdot z_3 \end{aligned} \tag{4.8}$$

The partial derivatives with respect to the system degrees of freedom yields:

$$\frac{\partial Epot}{\partial z_1}=c_{1z}\cdot\left(z_1-z_3+a\varphi\right)+m_1g$$

$$\frac{\partial Epot}{\partial z_2}=c_{2z}\cdot\left(z_2-z_3-b\varphi\right)+m_2g$$

$$\frac{\partial Epot}{\partial z_3}=-c_{1z}\cdot\left(z_1-z_3+a\varphi\right)-c_{2z}\cdot\left(z_2-z_3-b\varphi\right)+m_3g$$

$$\frac{\partial Epot}{\partial x_1}=c_{1x}\cdot\left(x_1-x_3-c\varphi\right)$$

$$\frac{\partial Epot}{\partial x_2}=c_{2x}\cdot\left(x_2-x_3-c\varphi\right)$$

$$\frac{\partial Epot}{\partial x_3}=-c_{1x}\cdot\left(x_1-x_3-c\varphi\right)-c_{2x}\cdot\left(x_2-x_3-c\varphi\right)$$

$$\begin{aligned} \frac{\partial Epot}{\partial \varphi} = & c_{1z}\cdot a\cdot\left(z_1-z_3+a\varphi\right)-c_{2z}\cdot b\cdot\left(z_2-z_3-b\varphi\right) \\ & -c_{1x}\cdot c\cdot\left(x_1-x_3-c\varphi\right)-c_{2x}\cdot c\cdot\left(x_2-x_3-c\varphi\right) \end{aligned}$$

Rearranging the terms with respect to the deflections x, z derives the stiffness matrix [**C**] as follows:

$$\begin{bmatrix} c_{1z} & 0 & -c_{1z} & 0 & 0 & 0 & c_{1z}a \\ 0 & c_{2z} & -c_{2z} & 0 & 0 & 0 & -c_{2z}b \\ -c_{1z} & -c_{2z} & c_{1z}+c_{2z} & 0 & 0 & 0 & -c_{1z}a+c_{2z}b \\ 0 & 0 & 0 & c_{1x} & 0 & -c_{1x} & -c_{1x}\cdot c \\ 0 & 0 & 0 & 0 & c_{2x} & -c_{2x} & -c_{2x}\cdot c \\ 0 & 0 & 0 & -c_{1x} & -c_{2x} & c_{1x} & (c_{1x}+c_{2x})c \\ c_{1z}a & -c_{2z}b & -c_{1z}a+c_{2z}b & -c_{1x}\cdot c & -c_{2x}\cdot c & (c_{1x}+c_{2x})c & (c_{1x}+c_{2x})c^2+c_{1z}a^2+c_{2z}b^2 \end{bmatrix} = [C]$$

Equation (4.9)

(c) Damping matrix

Lagrange's equation in the format of equation (4.2) was presented in chapter 2 for the assumption of a conservative system (see equation (1.10)). An analogy is made for the derivation of the damping matrix. The products $[C]\cdot q$ and $[D]\cdot \dot{q}$ in equation (4.1) represent the internal force responses of the system transferred by the spring and damper elements.

In this model, the damper elements are defined as viscous-type and linear in character with regards to velocity. As each damper element is combined with a linear spring in parallel, the damping matrix [**D**] must to be of analogous structure as the stiffness matrix [**C**]. Thus, matrix [**D]** is of identical structure as stiffness matrix [**C]**, but contains the appropriate damping values.

$$\begin{bmatrix} d_{1z} & 0 & -d_{1z} & 0 & 0 & 0 & d_{1z}a \\ 0 & d_{2z} & -d_{2z} & 0 & 0 & 0 & -d_{2z}b \\ -d_{1z} & -d_{2z} & d_{1z}+d_{2z} & 0 & 0 & 0 & -d_{1z}a+d_{2z}b \\ 0 & 0 & 0 & d_{1x} & 0 & -d_{1x} & -d_{1x}c \\ 0 & 0 & 0 & 0 & d_{2x} & -d_{2x} & -d_{2x}c \\ 0 & 0 & 0 & -d_{1x} & -d_{2x} & d_{1x} & (d_{1x}+d_{2x})c \\ d_{1z}a & -d_{2z}b & -d_{1z}a+d_{2z}b & -d_{1x}c & -d_{2x}c & (d_{1x}+d_{2x})c & (d_{1x}+d_{2x})c^2+d_{1z}a^2+d_{2z}b^2 \end{bmatrix} = [D]$$

Equation (4.10)

(d) External forces

The right side of equations (4.1) and (4.2) represent the external force vector **Fe** applied to the system. For the vehicle, it is considered that the external forces beside the gravity only apply to the wheel centre, caused by the kerb strike. The equilibrium condition for the undisturbed vehicle on an even ground (no kerb strike, just vertical equilibrium wheel forces F_{1z}, F_{2z} and gravity) can also be derived using the right side of equation (4.2) as:

$$\begin{aligned} \frac{\partial W}{\partial z_1} &= F_{1z} - m_1 g \\ \frac{\partial W}{\partial z_2} &= F_{2z} - m_2 g \\ \frac{\partial W}{\partial z_3} &= -m_3 g \end{aligned} \qquad (4.11)$$

All other partial derivatives with regards to the coordinates x_1, x_2, x_3 and φ clear out to be zero.

The system deflections are measured from the wheel centre positions related to the un-deformed state. For a static equilibrium position, such as expected for an undisturbed free travel mode on even ground, the gravity of the sprung mass m3 (body) causes a vertical deflection of the road springs. This deformed state, in the following named *design position*, is defined by a set of body CoG coordinates, vertical deflection z3 and pitch angle φ relative to the wheel centres. These initial conditions are derived in section 4.3.

4.2.2 Equations of motion for the system in bumper engaged mode

The matrices [**M**], [**D**] and [**C**] derived so far, represent the system in clearance to bumper and rebound stop contact. All other load transfer components such as springs and dampers are permanently engaged in the load transfer path in absence of any bumper or rebound stop engagement. Thus, matrices [**M**], [**D**] and [**C**] define the vehicle structure in its wheel centre free travel mode.

At a certain level of vertical wheel travel relative to body, the travel will be additionally restricted by the jounce bumper or rebound stop engagement. The structural characteristics, therefore, vary with deflection level. This structure variation is addressed by a bumper-rebound stop engagement analysis as follows:

To solve the system of equations in the time domain, the Runge- Kutta numerical integration method is applied. The results are time functions for the trajectories (state vector for each system component with respect to position and velocity) and the acceleration and internal force response vectors. To analyse the bumper engagement condition, the system deformation state is investigated with respect to the wheel centre position relative to the bumpers for each calculation time step. In the model, the link extending from the unsprung mass to engage with the bumper is considered rigid. Therefore, the front bumper engagement JB1z can be derived from the vertical coordinates z_1 and z_3 in conjunction with the pitch angle φ. Figure 4.6 illustrates the bumper deflection JB1z.

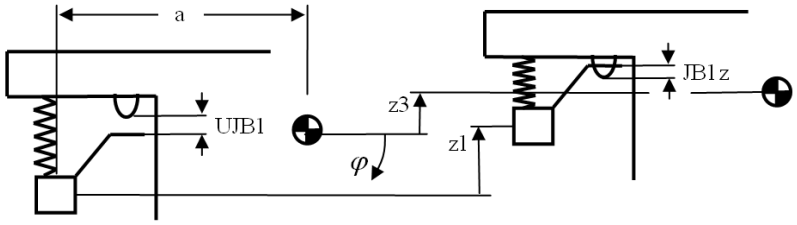

Figure 4.6: Free jounce wheel travel UJB1 and jounce bumper deflection JB1z on a front suspension

With the foregoing, the jounce bumper deflection of the front suspension is defined by:

$$JB1z = z1 - UJB1 - z3 + a \cdot \varphi \tag{4.12}$$

where UJB1 is the free wheel travel to jounce bumper contact, related to the equilibrium condition.

Accordingly, the rear suspension jounce bumper deflection (marked by index 2) becomes:

$$JB2z = z2 - UJB2 - b \cdot \varphi \tag{4.13}$$

For the rebound stop an illustration analogous to Figure 4.5 is shown in Figure 4.7:

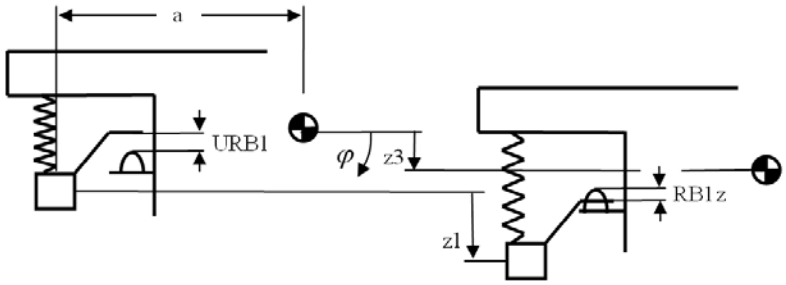

Figure 4.7: Free rebound wheel travel URB1 and rebound stop deflection RB1z on a front suspension

The front suspension rebound stop engagement RB1z is defined by:

$$RB1z = -z1 - URB1 - a \cdot \varphi + z3 \tag{4.14}$$

And for the rear suspension:

$$RB2z = -z2 - URB2 + b \cdot \varphi + z3 \tag{4.15}$$

where, URB1 and URB2 are the free wheel travel to rebound stop contact.

4.2.3 Rearrangement of matrix equation for structure variant system

The derived matrices [**C**], [**D**] represent the *internal* force response, caused by springs and dampers. It is the nature of *internal* forces that they do not change the momentum of the total system as they act in an anti-symmetric manner to the linked components. On the contrary, the external forces in general cause a deviation in the system momentum, except that they do act as an anti- symmetric oriented couple on a common action line.

So far, matrices [**C**], [**D**] are derived for the wheel centres in a free travel mode without jounce bumper or rebound stop engagement (case 1). They represent the *structure invariant* internal forces. In the case of bumper or rebound stop engagement, matrix [**C**] or [**D**] needs to be upgraded by the additional *structure variant* internal forces of these components. However, equation (4.1) can be considered as a general force balance of

inertial, external and internal forces. Therefore, the additional *structure invariant* internal forces, caused by their engagement, can be processed as a couple of *two external* forces of equal magnitude and common action line, but oriented anti-symmetrically. They can, therefore, be balanced with the external force vector **Fe** on the right side of equation (4.1). By doing so, the stiffness matrix derived in equation (4.9) can remain as a structure invariant feature and does not need to be modified.

The external force vector **Fe** is derived for the following cases for front and rear suspensions:

- free travel
- jounce bumper engagement
- rebound stop engagement

Case1: Free wheel travel

No engagement, for front and rear

$$\vec{F}e = \begin{Bmatrix} f_{1z} - m_1 g \\ f_{2z} - m_2 g \\ -m_3 g \\ f_{1x} \\ f_{2x} \\ 0 \\ 0 \end{Bmatrix} \tag{4.16}$$

Case 2: Jounce bumper engagement

For the following derivation, a linear spring characteristic is assumed for the jounce bumper and the rebound stop.

Front the jounce bumper engagement force F_{JB1} , using equation (4.12):

$$\vec{Fe} = \begin{Bmatrix} f_{1z} - m_1 g + CJB1 \cdot (z_3 - z_1 + UJB1 - a\varphi) \\ f_{2z} - m_2 g \\ -m_3 g + CJB1 \cdot (z_1 - z_3 - UJB1 + a\varphi) \\ f_{1x} \\ f_{2x} \\ 0 \\ CJB1 \cdot a \cdot (UJB1 - z_1 + z_3 - a\varphi) \end{Bmatrix} = \begin{Bmatrix} f_{1z} - m_1 g - F_{JB1} \\ f_{2z} - m_2 g \\ -m_3 g + F_{JB1} \\ f_{1x} \\ f_{2x} \\ 0 \\ F_{JB1} \cdot a \end{Bmatrix} \tag{4.17}$$

Rear jounce bumper engagement force F_{JB2}, using equation (4.13), becomes:

$$\vec{Fe} = \begin{Bmatrix} f_{1z} - m_1 g \\ f_{2z} - m_2 g + CJB2 \cdot (z_3 - z_2 + UJB2 + b\varphi) \\ -m_3 g + CJB2 \cdot (z_2 - z_3 - UJB2 - b\varphi) \\ f_{1x} \\ f_{2x} \\ 0 \\ CJB2 \cdot b \cdot (z_2 - z_3 - UJB2 - b\varphi) \end{Bmatrix} = \begin{Bmatrix} f_{1z} - m_1 g \\ f_{2z} - m_2 g - F_{JB2} \\ -m_3 g + F_{JB2} \\ f_{1x} \\ f_{2x} \\ 0 \\ -F_{JB2} \cdot b \end{Bmatrix} \tag{4.18}$$

Case 3: Rebound stop engagement

Front rebound stop engagement force F_{RS1}, using equation (4.14), becomes:

$$\vec{Fe} = \begin{Bmatrix} f_{1z} - m_1 g + CRB1 \cdot (z_3 - z_1 - URB1 - a\varphi) \\ f_{2z} - m_2 g \\ -m_3 g + CRB1 \cdot (z_1 - z_3 + URB1 + a\varphi) \\ f_{1x} \\ f_{2x} \\ 0 \\ -CRB1 \cdot a \cdot (URB1 + z_1 - z_3 + a\varphi) \end{Bmatrix} = \begin{Bmatrix} f_{1z} - m_1 g + F_{RS1} \\ f_{2z} - m_2 g \\ -m_3 g - F_{RS1} \\ f_{1x} \\ f_{2x} \\ 0 \\ F_{RS1} \cdot a \end{Bmatrix} \tag{4.19}$$

Rear rebound stop engagement force F_{RS2}, using equation (4.15), becomes:

$$\vec{F}e = \begin{Bmatrix} f_{1z} - m_1 g \\ f_{2z} - m_2 g + CRB2 \cdot (z_3 - z_2 - URB2 + b\varphi) \\ -m_3 g + CRB2 \cdot (z_2 - z_3 + URB2 - b\varphi) \\ f_{1x} \\ f_{2x} \\ 0 \\ CRB2 \cdot b \cdot (URB2 + z_2 - z_3 - b\varphi) \end{Bmatrix} = \begin{Bmatrix} f_{1z} - m_1 g \\ f_{2z} - m_2 g + F_{RS2} \\ -m_3 g - F_{RS2} \\ f_{1x} \\ f_{2x} \\ 0 \\ -F_{RS2} \cdot b \end{Bmatrix} \qquad (4.20)$$

4.2.4 Jounce bumper force response map application

The above formulations of equations (4.17) to (4.20) represent a linear force response characteristic for the jounce bumper and the rebound stop, addressed by constant stiffness coefficients CJB1, 2 and CRB1, 2. By making use of the jounce bumper map concept previously described, the vehicle model is linked to an external subroutine **map** which feeds back the bumper and rebound forces F_{JB}, F_{RB} relevant to the prevailing initial conditions; z and $\dot{z} = dz/dt$. The map concept takes the nonlinearity and hysteresis of these polymeric-type elements into account. The terms containing CJB and CRB in equations (4.17) to (4.20) are replaced by the jounce / rebound force responses F_{JB} and F_{RB}, obtained from the map subroutine feedback to solver.

4.2.5 External tyre force application

In the case of a kerb strike, the loads applied to the wheel centre are determined by the deformation state caused by the tyre-kerb impact. The concept to establish the tyre force response after a radial deflection *f* against a flat or an edge type contact is described in chapter 4. The reaction force is provided by an external subroutine that feeds back the tyre deformation force vector to the Runge-Kutta solver for each time step of calculations. This is balanced against the external force vector **Fe**.

In Figure 4.8, the force response for a radial tyre deflection is illustrated.

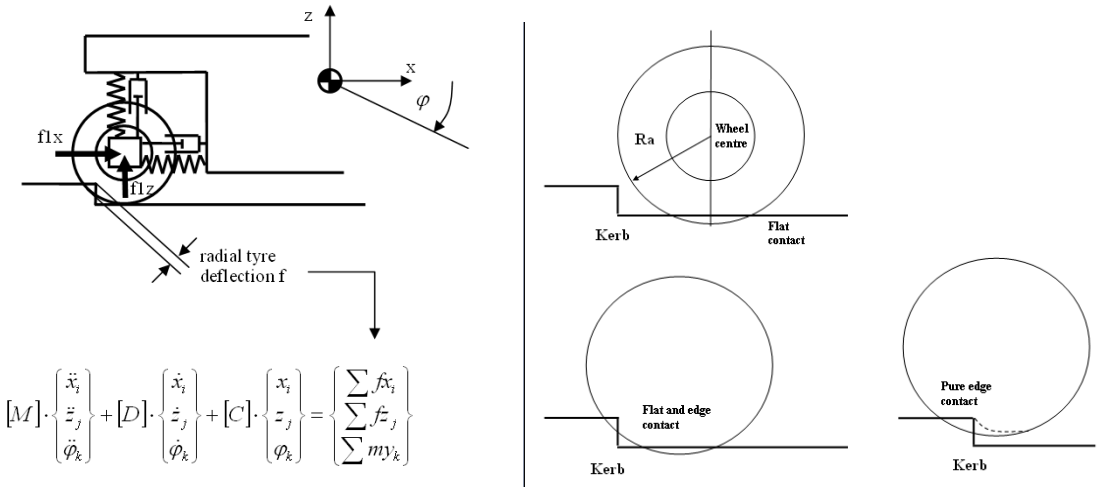

Figure 4.8: Tyre response force feedback to external load vector **Fe** and tyre contact modes

4.2.6 Tyre force analysis in kerb strike mode

Two types of tyre contacts are considered in the model; a flat contact to even (flat) and rigid ground and a purely edge type deformation to simulate the contact with a rigid kerb. In the model, the current deformation state is defined by the belt contour circle interference with the kerb contour or a ground line. The DoK manoeuvre commences in a roll mode towards the tyre rim, where the belt is in pure flat contact to the ground. After the (circular assumed) belt contour enters into contact with the edge of the kerb, a radial deflection is considered at the overlap with the contour. This is the basis of a tyre force response analysis addressed in chapter 6. Consequently, the wheel centre is lifted vertically, causing a shift from a flat contact to ground towards an edge type loading against kerb. During dual contact condition (transition towards pure edge type contact), the tyre force is analysed by a superposition of both flat-type and edge-type contacts as indicated in Figure 4.8 (right).

4.3 Initial conditions set up

In the first stage of both the driving manoeuvres considered in this thesis, the vehicle rolls at a constant speed on a flat ground towards the kerb or a pothole. Rolling resistance is neglected in the model, only vertical wheel centre forces F1z and F2z are

applied to attain the model in equilibrium. The longitudinal components F1x, F2x are set zero.

4.3.1 Equilibrium position parameters

To establish the initial conditions which yield vehicle equilibrium condition, the principle of virtual work has been applied. To attain equilibrium for the undisturbed roll mode only two DoF; z3 and φ need to be addressed:

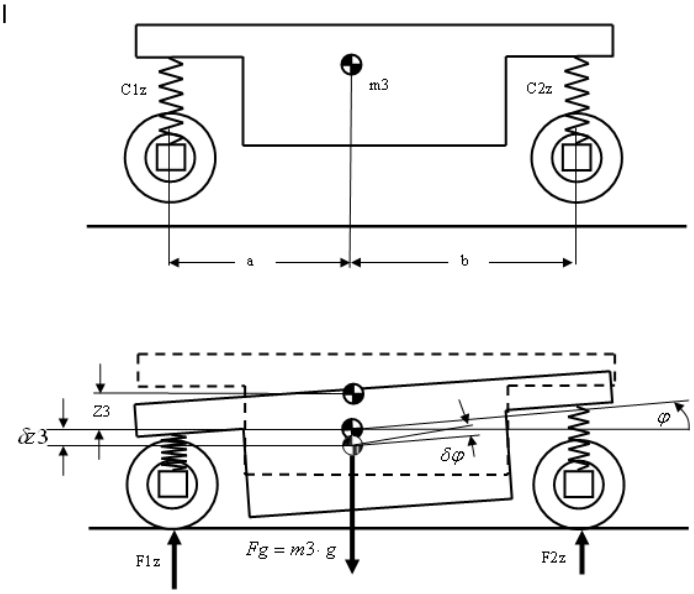

Figure 4.9: System parameters to establish the equilibrium conditions (upper) and infinitesimal deflections from equilibrium (lower sketch)

The upper sketch in Figure 4.9 shows the vehicle model in *full hang* condition. When lowered to the ground, a vertical deflection z3 and the pitch angle φ result from tyre touch down condition, until the final equilibrium position is reached.

To establish z3 and φ, further virtual deflections $\delta z3$ and $\delta\varphi$ are applied in equilibrium condition to cause a virtual work applied to the system. In case of small virtual deflections applied to a system in equilibrium, the virtual work done is known to be zero **[17]**, **[18]**. The virtual work equations for z3 and φ are derived as follows:

$$\begin{aligned} m3g\cdot\delta z3 - F1z\cdot\delta z3 - F2z\cdot\delta z3 &= 0 \qquad z3 \\ -F1z\cdot a\cdot\cos\varphi\cdot\delta\varphi + F2z\cdot b\cdot\cos\varphi\cdot\delta\varphi &= 0 \qquad \varphi \end{aligned} \tag{4.21}$$

Jounce bumper or rebound stop forces do not need to be considered as they are in general not engaged under vehicle static equilibrium condition. Using the system parameters shown in Figure 4.5, the forces F1z and F2z can be expressed by the spring stiffness and system deflections z3 and φ.

$$F1z = C1z \cdot (z3 + a \cdot \varphi)$$
$$F2z = C2z \cdot (z3 - b \cdot \varphi) \tag{4.22}$$

Doing so, the static equilibrium condition is established by equations (2.21) and (2.22):

$$z3 = m3g \cdot \frac{C1z \cdot a^2 + C2z \cdot b^2}{C1z \cdot C2z \cdot (a+b)^2}$$
$$\varphi = -m3g \cdot \frac{C1z \cdot a - C2z \cdot b}{C1z \cdot C2z \cdot (a+b)^2} \tag{4.23}$$

4.3.2 Generic suspension geometry parameters defined for model input

A sketch of the geometrical parameters is provided in Figure 4.10 for a McPherson front suspension. The jounce bumper (JB) and the rebound stop (RBS) engagement, in general, are defined by the upper end of the damper tube. This defines the datum line (zero level) for the vertical wheel centre travel z1.

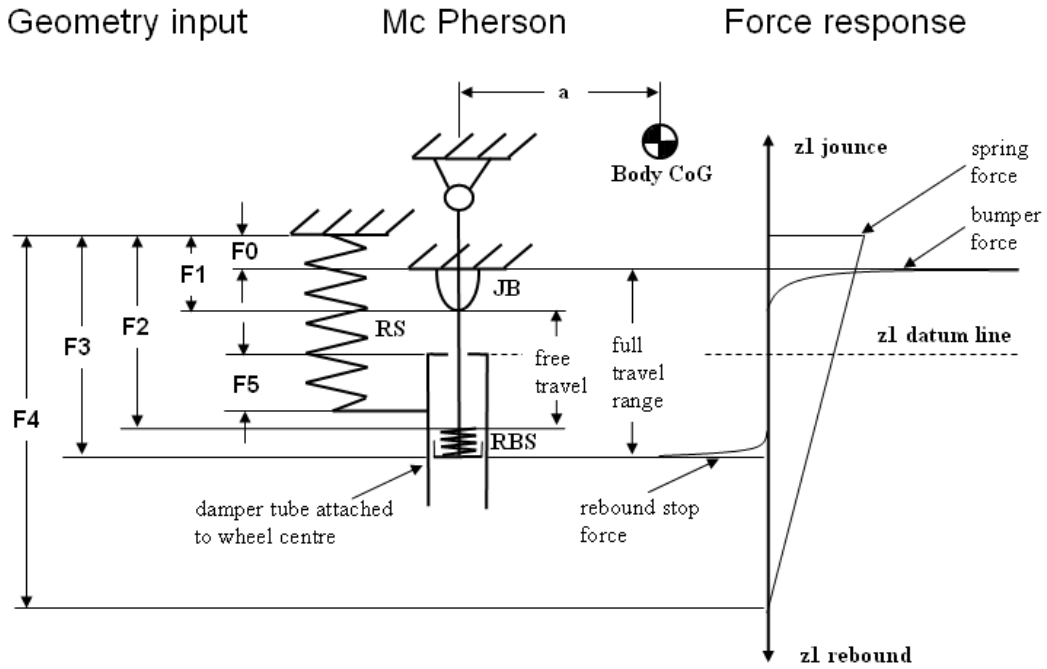

Figure 4.10: Model geometry input parameter for road spring (RS), jounce bumper (JB) and rebound stop (RBS) elements

The positions of the road spring (RS), the jounce bumper (JB) and the rebound stop (RBS) elements are defined relative to the upper spring seat position attached to the sprung mass m3. Vertical dimensions F0 to F5 are used as model input parameters to define the z1 datum line, the free wheel travel, the full operational range and engagement space of the bumper and the rebound stop elements respectively.
The longitudinal dimension 'a' to the CoG is considered to be the common x- component for RS, JB and RBS front suspension elements. It can be seen that the dimensions are general parameters, independent from the actual suspension concept selected for the vehicle.

4.3.3 The method of solution

The model simulation is embedded in a FORTRAN code to have the full flexibility to include specific features such as the map concept and the analytical tyre model, described in chapters 5 and 6. The integration of the coupled differential equations (4.1) is performed in the time domain, using the the Runge – Kutta method. A documentation and description of the numerical method is provided in appendix A.

4.4 Closure

A minimal parameter model is derived for a vehicle tailored for use with the FORD specified extreme driving manoeuvres; drive over kerb (DoK). As the drive events do not cause relevant side forces or roll motion, a planar model is chosen. The known bicycle model is extended to lateral degrees of freedom and linked to external subroutines to include jounce bumper and tyre force responses, based on the concepts described in chapters 5 and 6. The model is set up in the format of a structure-variant architecture to differentiate between free vertical wheel travel and bumper engagement modes.

Chapter 5: The Jounce bumper simulation model

5.0 Introduction

In this chapter, a revised map concept is presented, intended to simulate the response force for large scale jounce bumper deformations. These conditions are typically seen in severe driving manoeuvres such as a kerbstone crossing. The concept was applied to a foam type front suspension jounce bumper made of polyurethane, but is considered to have potential to be used for general simulation of other polymeric elements used in chassis applications, such as engine mounts or hydro-bushings.. It is an integral part of the vehicle model discussed in chapter 4, but can also be linked as an external subroutine and onto a common multi- body simulation environment like ADAMS.

5.1 The Existing concepts

The most common approaches used to simulate the viscoelastic force response / transfer of polymeric elements can be categorized into three main concepts; mathematical, phenomenological and physical models **[47]**:

5.1.1 Mathematical models

Mathematical functions (e.g. polynomials) are derived to describe the force transfer function taken from measurements. The functions approximate the trace of a measured signal **[48]**, **[49]**. They do not distinguish between static and dynamic effects. It is, therefore, difficult to extend simulation studies beyond the scope of the measured boundaries. A unique model must be derived for each element type. Mathematical skills are required to select an appropriate formula, tune the shape of the graph and adapt it to the measured force response trace. In most cases, the advantage is rapid simulations in a multi-body system environment. A typical function can be of the form $F = f(x, \dot{x}, \dots)$.

5.1.2 Phenomenological models

Spring and viscous damper elements can be combined to form a so-called Maxwell or Kelvin – Voigt elements. These elements are described in chapter 2 and are shown in Figure 2.48. Such structure models (called rheological models) can be used to simulate

the viscoelastic behaviour of polymeric elements **[19]**, **[56]**. These models separate the physical effects of stiffness and damping and, therefore, allow usage beyond the measured data. The model must be derived and calibrated uniquely for each element type. Specific MBS modelling skills are required to set up rheological models and in general it is difficult to calibrate the model to fit the entire actuation scale. Compared with mathematical models, the run time for rheological models, in most cases, is longer than the mathematical models in multi-body system environments.

5.1.3 Physical models

The finite element (FE) method replicates the component geometry by a mesh-type structure and, therefore, allows for physical modeling of continuous structures of polymer elements. However, the modelling of a hydro-bush or a foam-type element (e.g. jounce bumpers), requires detailed knowledge of the material properties. The number of meshing elements used correlates to the number of equations to be solved. Hence, detailed FE models can lead to a large system of equations, which increases the solver run time. A further aspect is the observation that the numerical solution procedure tends to divergence problems if the deformation range for a single element exceeds specific limits (often beyond linear viscoelasticity). Special solver strategies, like MARC address some of these shortfalls.

5.1.4 Common features of highlighted concepts

Force response measurements gained from physical component tests are required for the first two of above mentioned approaches for setting up and calibration of the simulation model. In theory, an FE-based physical model does not necessarily depend on component force response tests, with existing high level of confidence regarding material properties. However, these properties need to be tested instead of the actual components.
All the aforementioned models have the common requirement of component-specific tests or determination of material properties prior to model set up.

5.1.5 Current bumper simulation concept in the Ford of Europe (FoE)

Ford of Europe uses a mathematical model concept to simulate the load transfer of polymer structures. The force response trace, in general a non-linear curve gained from a quasi static actuation, is transformed into an interpolation polynomial and embedded into a multi-body system (MBS) environment. Such characteristic curves are used for both, jounce and rebound deflection behaviour. No distinction is made between the jounce and the rebound bumper force responses (hysteresis), typical for polymer components, in this approach. An additional viscous damper element, attached in parallel only allows for a rudimentary curve-fitting, especially in the case of an impulse- like actuation as seen on jounce bumper response during the kerb-stone crossing events.

As known from Ford vehicle test studies and outlined in the literature study (chapter 2), the jounce bumper characteristics are known to be a key feature with regards to the vertical peak load levels. All this explains the effort put towards more realistic representation of bumper force-response under impulsive conditions.

5.1.6 The proposed map concept

The concept is intended to improve the dynamic force response characteristics by taking the velocity-related hysteresis into account, covering the full range of jounce bumper deflections. The idea is to extend the current “universal” parametric static force response function of deflection s, F(s), by a second parameter 'velocity' towards a 3D map F(s, v). This look up table approach would avoid the burden of setting-up an element specific polymer model and takes the influence of actuation velocity into account. Measured force response data gained from harmonic actuations is transferred into a standardised numerical format that would allow an effective solver interaction. The concept follows the idea of a heuristic modelling approach, namely to find a good solution based on limited knowledge within a reasonable time frame.

The aim of the proposed concept can be summarised as follows:

- Extension of the current static force response *curve* towards a force response *map*, appropriate to cover the velocity-relevant hysteresis characteristics of bumper components used in chassis applications.

- Development of a standardised numerical method, applicable for general types of chassis polymeric elements for lateral and rotational degrees of freedom.
- Specification of a standardised test procedure to generate the relevant force response data, applicable for element-specific full deformation range actuation.
- Easy application and fast run-time within existing MBS simulation environments, such as ADAMS.

5.2 Force response map concept

As an introduction to the proposed concept, the process of the map data acquisition and preprocessing are first demonstrated. The data acquisition is discussed for a foam-type jounce bumper used in the MacPherson front suspension of the CD340 (FORD Galaxy) shown in Figure 5.1.

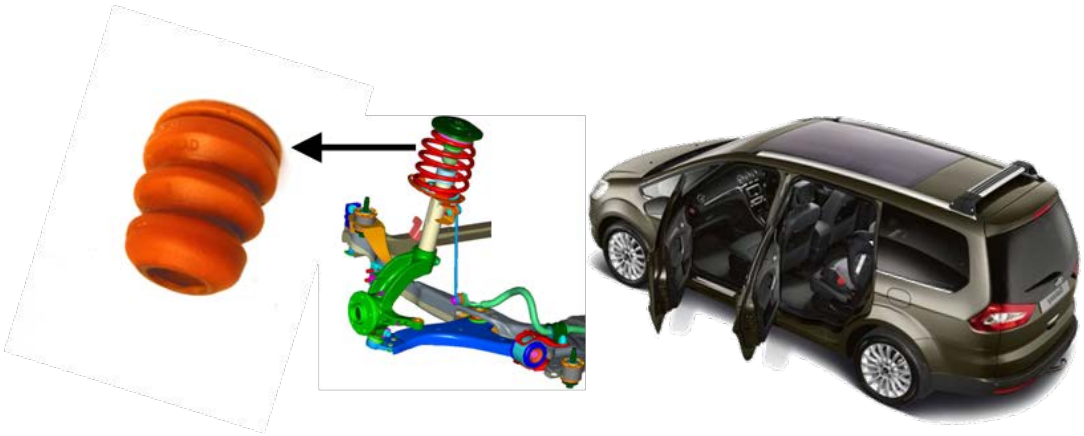

Figure 5.1: Jounce bumper element, MacPherson front suspension for the Ford Galaxy

The bumper is a single degree of freedom vertical compression element which does not transfer any tensile forces. Therefore, the force response (shown in Figure 5.2) for a set of displacement actuation amplitudes (left) remains within the positive range (i.e. in compression). It should be noted that the map concept is generally applicable for lateral and rotational degrees of freedom for both positive and negative deformation ranges.

The bumper map database consists of a set of force response curves gained from harmonic displacement actuation tests as indicated in Figure 5.2. Although the bumper excitation mode during the kerb-crossing event can be of an arbitrary shape and is not necessarily sinusoidal, a harmonic excitation was selected to gain the force response

data. The validity of the approach in simulating an arbitrary motion on basis of map data gained from harmonic actuation is confirmed by a correlation study of map simulation-to-physical drop test results. This is because, in general, a bumper drop test excitation deviates from harmonic motion. The amplitudes and circular frequency need to be specified properly in order to represent the considered load case (in this example the drive over kerb maneouvre) prior to any force response data acquisition.

5.2.1 Specification of operational range

To define the relevant harmonic actuation, firstly the expected operational range with regard to the maximum deflection and velocity (Smax, Vmax) needs to be specified. These values should envelope the worst case driving conditions and can either be gained from measurement of deflection over time recorded during the drive event, or alternatively be interpreted from the boundary conditions of the manoeuvre itself. In the current study, the latter approach is undertaken, as follows:

The CD340 bumper maximum deflection 'Smax' is limited to approximately 60 mm, defined by the bumper block length. The block length is achieved for the condition that the gas inclusions of the foam type material converts into an incompressible form. As the bumper deformation is linked to the damper tube motion, the bumper deflection velocity 'Vmax' is limited by the hydraulic blocking speed of the damper, measured as 3.5m/s.

5.2.2 Specification of related frequency

To specify the event's relevant circular frequency ω for a harmonic actuation, the quotient ω = Vmax / Smax is determined as the data acquisition frequency: $f = \omega/2\pi$. The relevant value for the drive over kerb manoeuvre is approximately 10 Hz.

5.2.3 Generation of the map database

A set of force response curves is recorded from a sinusoidal displacement actuation, performed at the relevant frequency for a set of amplitudes (S1 to S7). The force traces are recorded as functions of time and are subsequently transformed into a function of the harmonic phase angle, φ. The amplitudes should provide a uniform distribution over the

bumper force range as shown in Figure 5.2, which reveals the force response gained from common actuation frequency of 10 Hz.

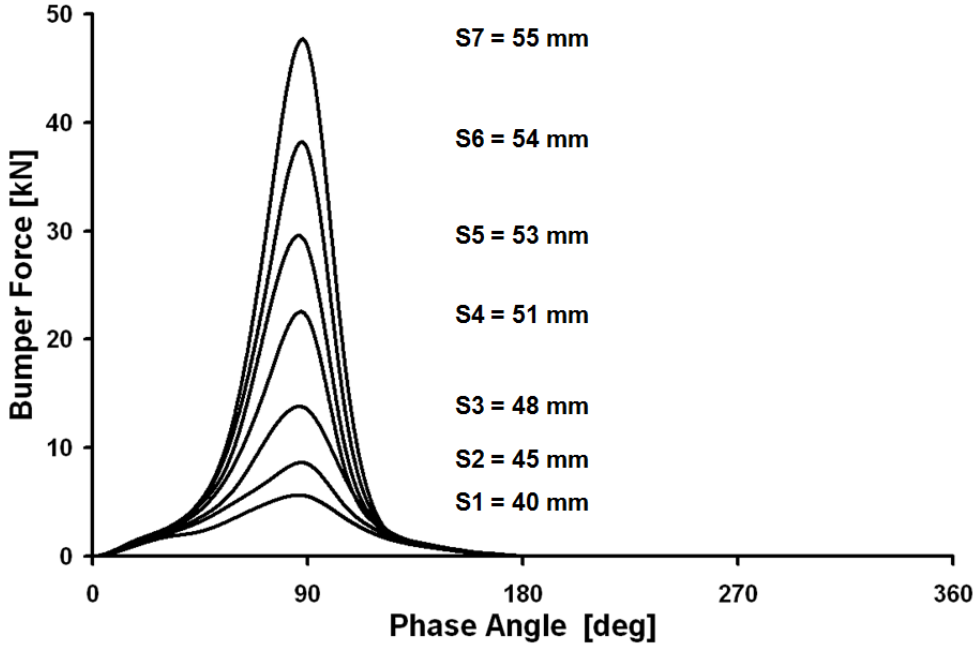

Figure 5.2: Sinusoidal actuation force response
time history of a jounce bumper element

5.2.4 Post-processing of map data

The data in its recorded cannot efficiently be used directly for generation of a map. Post-processing is required to condense the large data quantity. The traces recorded for any given amplitude Si are subdivided into equi-distant angular intervals. Single force values (splines) are selected at each interval border. In Figure 5.3, a phase angle interval of 15° width is applied.

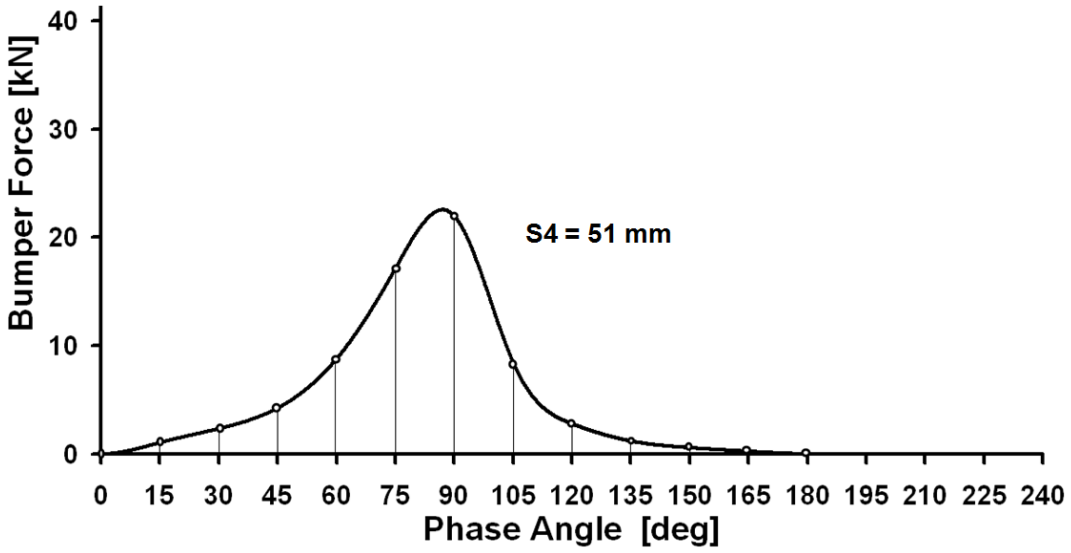

Figure 5.3: Splines gained from a single jounce bumper force response trace at interval width of 15°

A cubic spline interpolation function is used to approximate the trace in between two splines. For the approximation, a third order polynomial is used:

$$F = A_0 + A_1 \cdot z + A_2 \cdot z^2 + A_3 \cdot z^3 \tag{5.1}$$

The variable *z* represents a local coordinate within the current interval in between two neighbouring splines, A0, A1, A2 and A3 are a set of coefficients, specified to fit the curve shape **[23]**.

The coefficients are derived in numerical preprocessing and stored in a three dimensional array (A). The array contains the comprehensive force response information condensed into a compact numerical format. The regular array structure enables fast access and, therefore, an efficient map for solver interaction process discussed in section 5.3.

Figure 5.4 illustrates the data organisation of the array. The coefficients which define the force response trace of number 'k = 4' within the range of interval 'i = 5' are stored in (A) under the corresponding line and register indices.

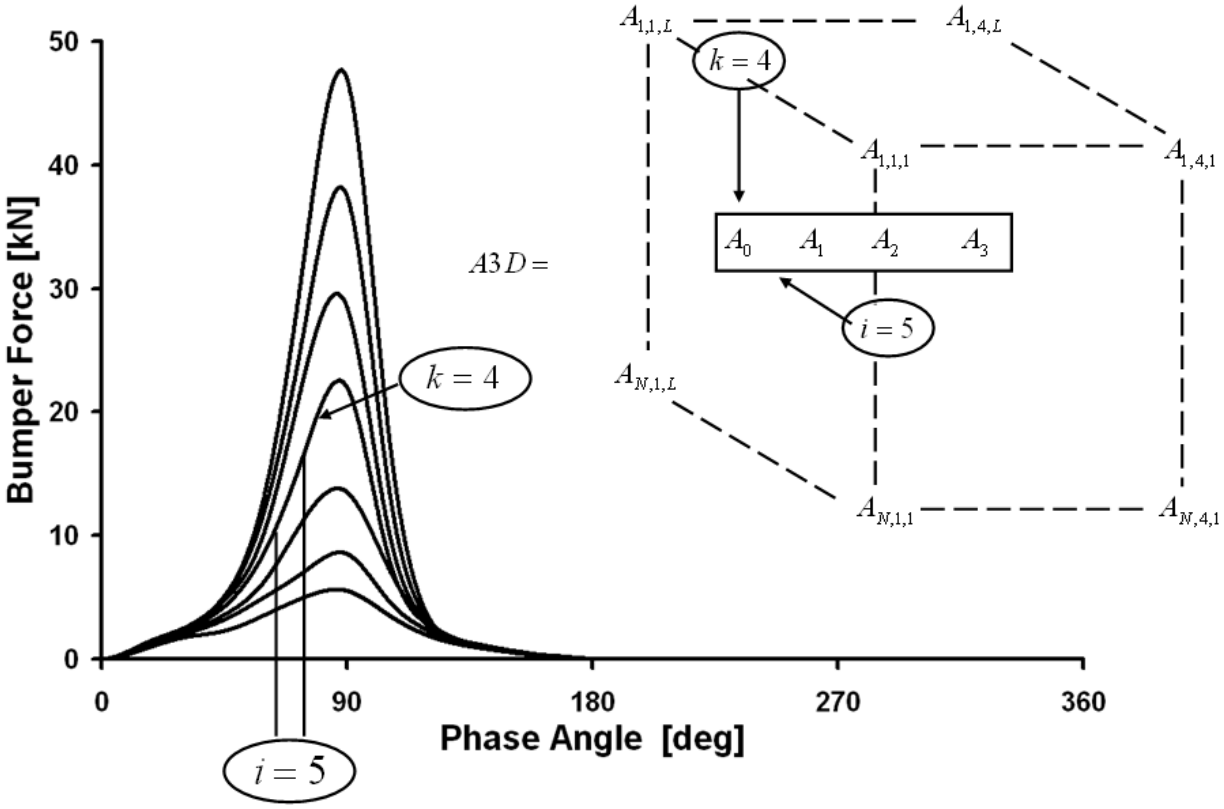

Figure 5.4: Organisation of array 'A' stored by cubic spline coefficients

5.2.5 Map visual interpretation

The following provides a visual interpretation of the 2-parameter map concept, intended to gain a more descriptive insight into the method. The harmonic motion is defined as:

$$s_{(t)} = S_0 \cdot \sin(\omega t)$$
$$v_{(t)} = S_0 \cdot \omega \cdot \cos(\omega t)$$

Both expressions can be presented in a phase diagram *s* over *v*, characterised by an ellipsoidal trace (Figure 5.5).

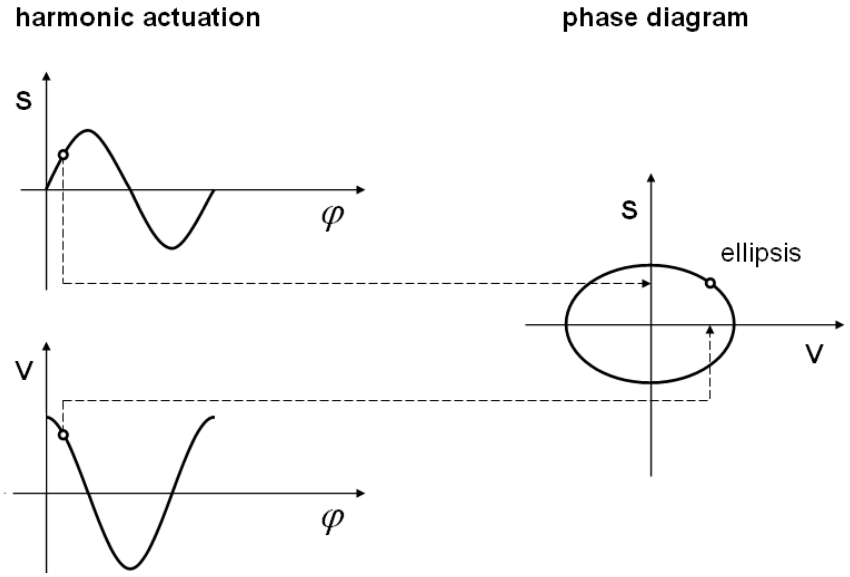

Figure 5.5: Phase diagram *S* over *V* for a harmonic actuation

In conjunction with the expression for the circular frequency phase angle: $\varphi = \omega t$, a generalised velocity $v_{(t)} / \omega$ can be defined as:

$$\begin{aligned} s_{(t)} &= S_0 \cdot \sin(\varphi) \\ \frac{v_{(t)}}{\omega} &= S_0 \cdot \cos(\varphi) \end{aligned} \qquad (5.2)$$

For the generalised velocity, the phase diagram reveals a format of concentric circles in the *xy* plane. Because of the circular shape, also the phase angle φ can be visualized **[17]**.

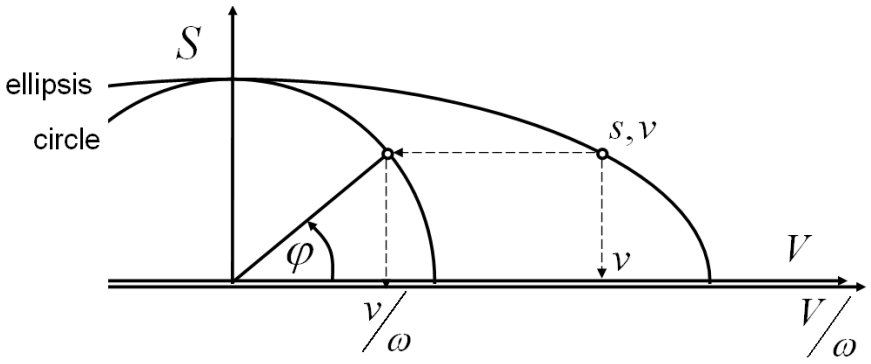

Figure 5.6: Concentric circles found for generalised velocity in a phase diagram

For a compressive element (push), only the phase angle range $0 < \varphi < \pi$ is applicable for the force response as shown in Figure 3.7, whereas push - pull elements (bi-directional) require the full circular range in the phase diagram.

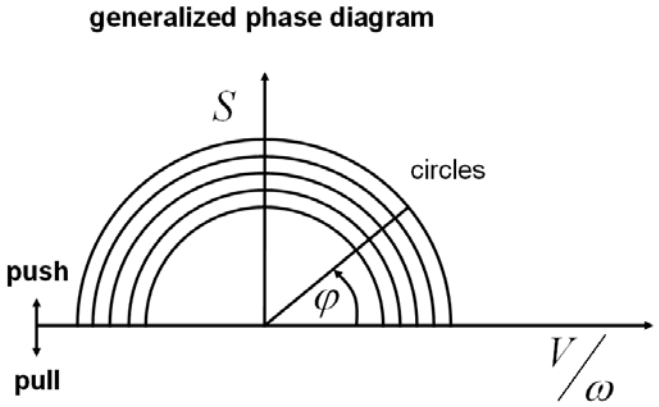

Figure 5.7: Generalised phase diagram for generalised velocity 'V/ω' and phase angle φ for a push element

The three dimensional perspective (Figure 5.8) shows bumper force response traces (red) aligned to the z- axis, whereas the black traces indicate force trace vertical projections to the *xy* plane. The inner trace was recorded for an actuation amplitude S0 = 40 mm. The amplitudes were increased in steps of 5 mm towards the circumfluent traces up to amplitude S4 = 60 mm.

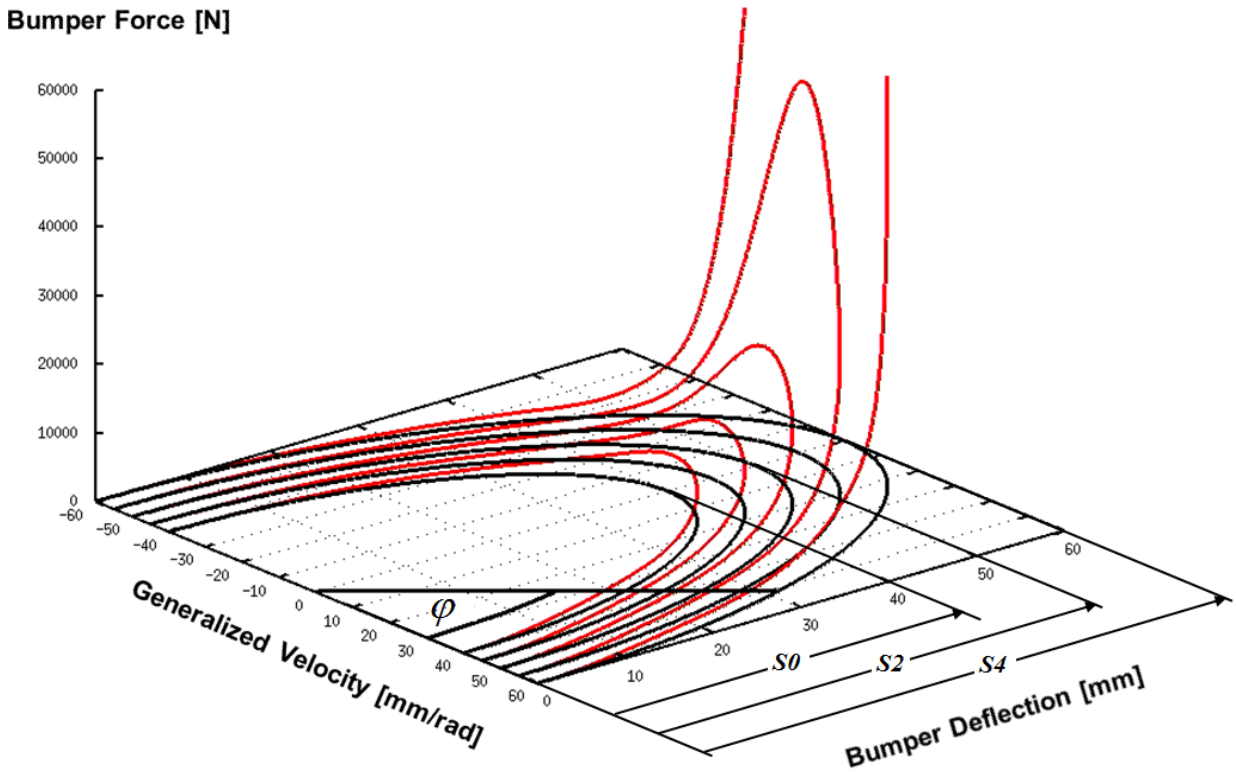

Figure 5.8: Force response traces (red) and their vertical projections (black) into a phase diagram

A side view of the 3D map (Figure 5.9, *zx* plane) illustrates the typical shape known from the hysteresis loops.

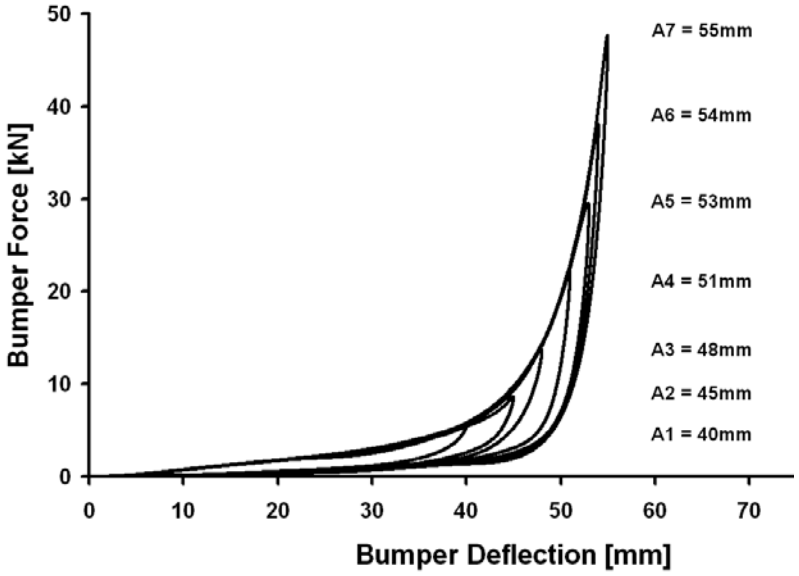

Figure 5.9: Jounce bumper hysteresis loops gained through harmonic actuation

5.3 Map-to-Solver interaction

The following explanation concerns the selection process for a relevant feedback force F(s, v) derived from the map data.

The map concept is embedded into the vehicle multi-body system, presented in chapter 4. Bumper engagement forces are addressed as additional external forces. Therefore, a map force response strategy needs to be integrated as a feedback loop into the numerical environment in order to solve the vehicle's equations of motion. Equations of motion (second order differential equations) can be solved by time marching numerical integration. The integration is performed for discrete time increments, resulting in the system state vectors (displacement, velocity and acceleration of each system degree of freedom at an instant of time). For each time step, a set of initial conditions 's' and 'v' are required in order to calculate the instantaneous state vector. The aim of the map to solver interaction link is to feed back the bumper force, corresponding to the initial conditions at any step of integration.

5.3.1 Definition of Map Datum Point related to initial conditions

All force response curves are gained from harmonic actuation of common (the drive event related) circular frequency ω. To receive a force response from the map, the datum point, corresponding to the initial conditions, must be within the map range defined by the largest circle. The datum point shown in Figure 3.10 is located in between the third and fourth radius (map data array index k = 3, 4), counted outwards from the map centre. It is determined by a polar vector R, aligned to the direction of the angle φ. Therefore, the corresponding phase angle φ and vector R can easily be derived from the current initial conditions S and V as:

$$\tan\varphi = \frac{S}{V/\omega} \qquad R = \sqrt{S^2 + (V/\omega)^2} \tag{5.3}$$

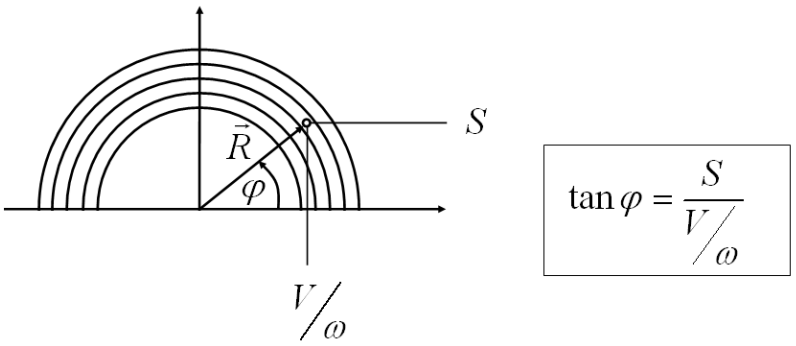

Figure 5.10: Determination of phase angle from initial conditions 'S' and 'V/ω'

5.3.2 Interpolation of the datum force response

The force related to the datum point is approximated by two interpolations; in circumferential and radial directions. For the interpolation in the circumferential direction, the spline coefficients, derived from the pre-processing, are used. An elongation of the polar vector **R** defines three circular intersection points; two inner ones at radii S1 and S2 and an outer point S3. Force values F1, F2 and F3 are related to the intersection points (see Figure 5.11). The forces are commonly located within the same phase angle interval (map data index 'i', see Figure 5.4). If φ_1 and φ_2 are the phase angles that frame the 'i' th interval $\varphi_1 < \varphi < \varphi_2$ and $z = \varphi - \varphi_1$ being the local variable, the forces F1 to F3 can be directly approximated by the spline coefficients stored in the array A as:

$$F1 = A_{i,0,2} + A_{i,1,2} \cdot z + A_{i,2,2} \cdot z^2 + A_{i,3,2} \cdot z^3$$
$$F2 = A_{i,0,3} + A_{i,1,3} \cdot z + A_{i,2,3} \cdot z^2 + A_{i,3,3} \cdot z^3 \qquad (5.4)$$
$$F3 = A_{i,0,4} + A_{i,1,4} \cdot z + A_{i,2,4} \cdot z^2 + A_{i,3,4} \cdot z^3$$

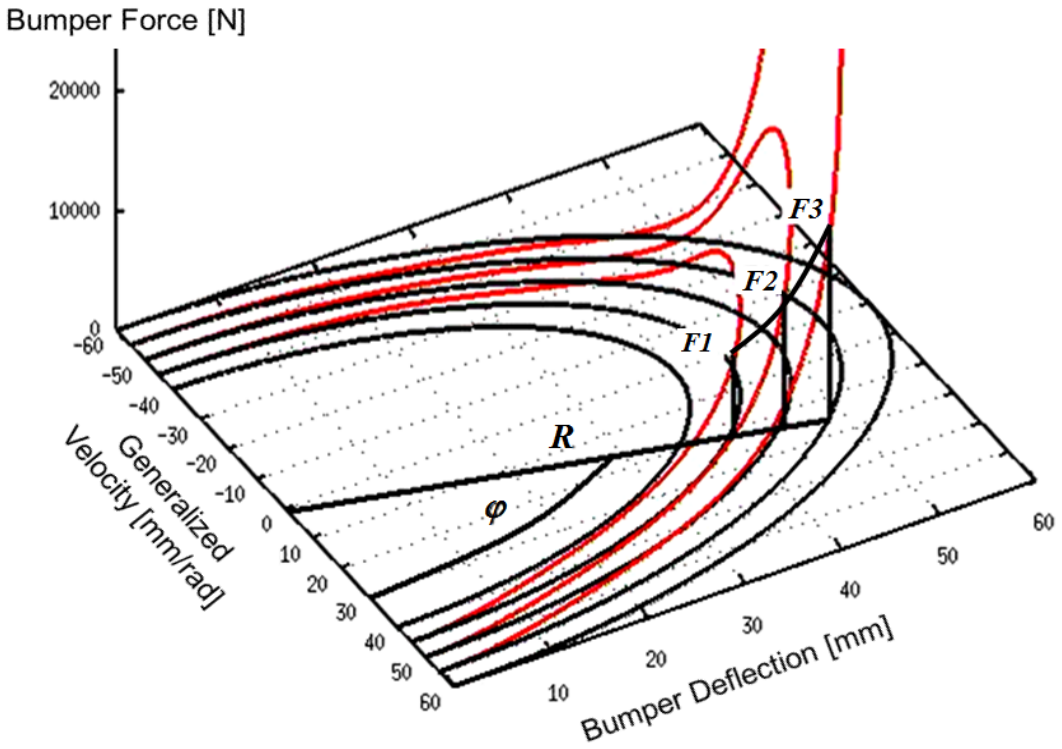

Figure 5.11: Circumferential approximation F1, F2 and F3

In a second operation, the forces F1, F2 and F3 are used to perform a radial interpolation along the datum vector R as shown in Figure 3.10. A polynomial of second order is used as:

$$F_{(S)} = K_0 + K_1 \cdot s + K_2 \cdot s^2 \qquad (5.5)$$

Using the approximations found for F1, F2 and F3, the coefficients Ki are determined by the three equations:

$$F_{(S1)} = F1 = K_0 + K_1 \cdot S1 + K_2 \cdot S1^2$$
$$F_{(S2)} = F2 = K_0 + K_1 \cdot S2 + K_2 \cdot S2^2$$
$$F_{(S3)} = F3 = K_0 + K_1 \cdot S3 + K_2 \cdot S3^2$$

$$\Rightarrow \quad K_0, \quad K_1 \quad and \quad K_2$$

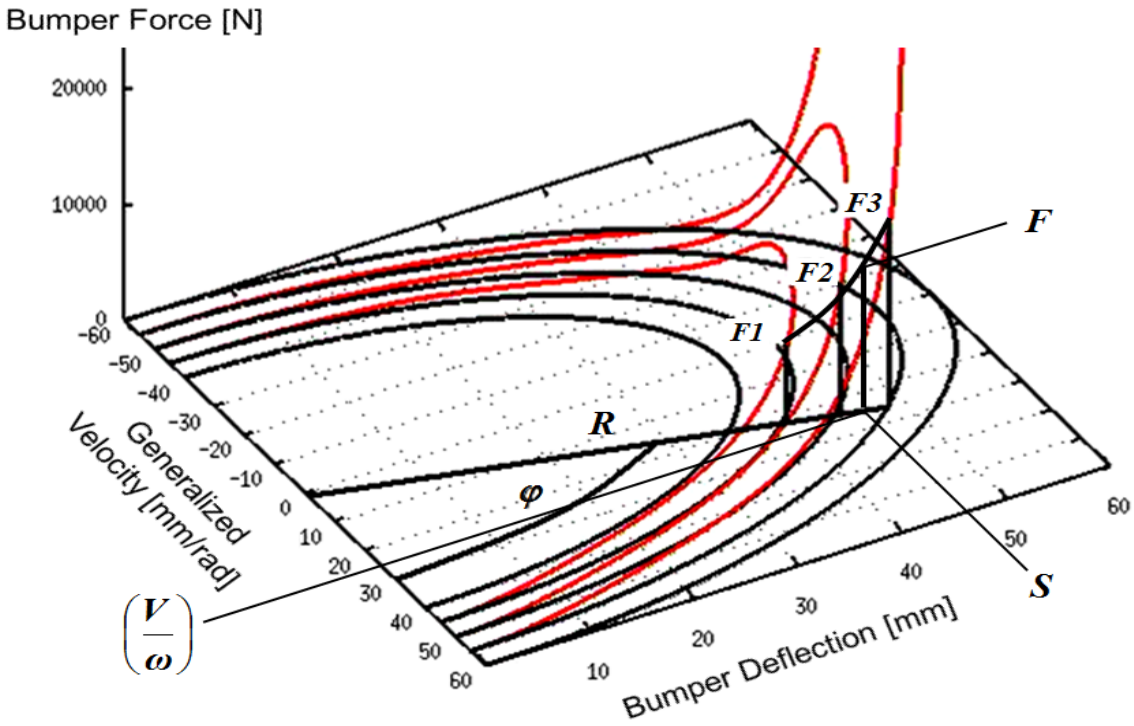

Figure 5.12: Radial approximation *F*

$$F = K_0 + K_1 \cdot R + K_2 \cdot R^2 \qquad (5.6)$$

The two operations directly lead to the map feedback force *F(S, V)*, related to the initial conditions (S, V).

The flow chart, shown in Figure 5.13, summarises the map-to-solver feedback structure:

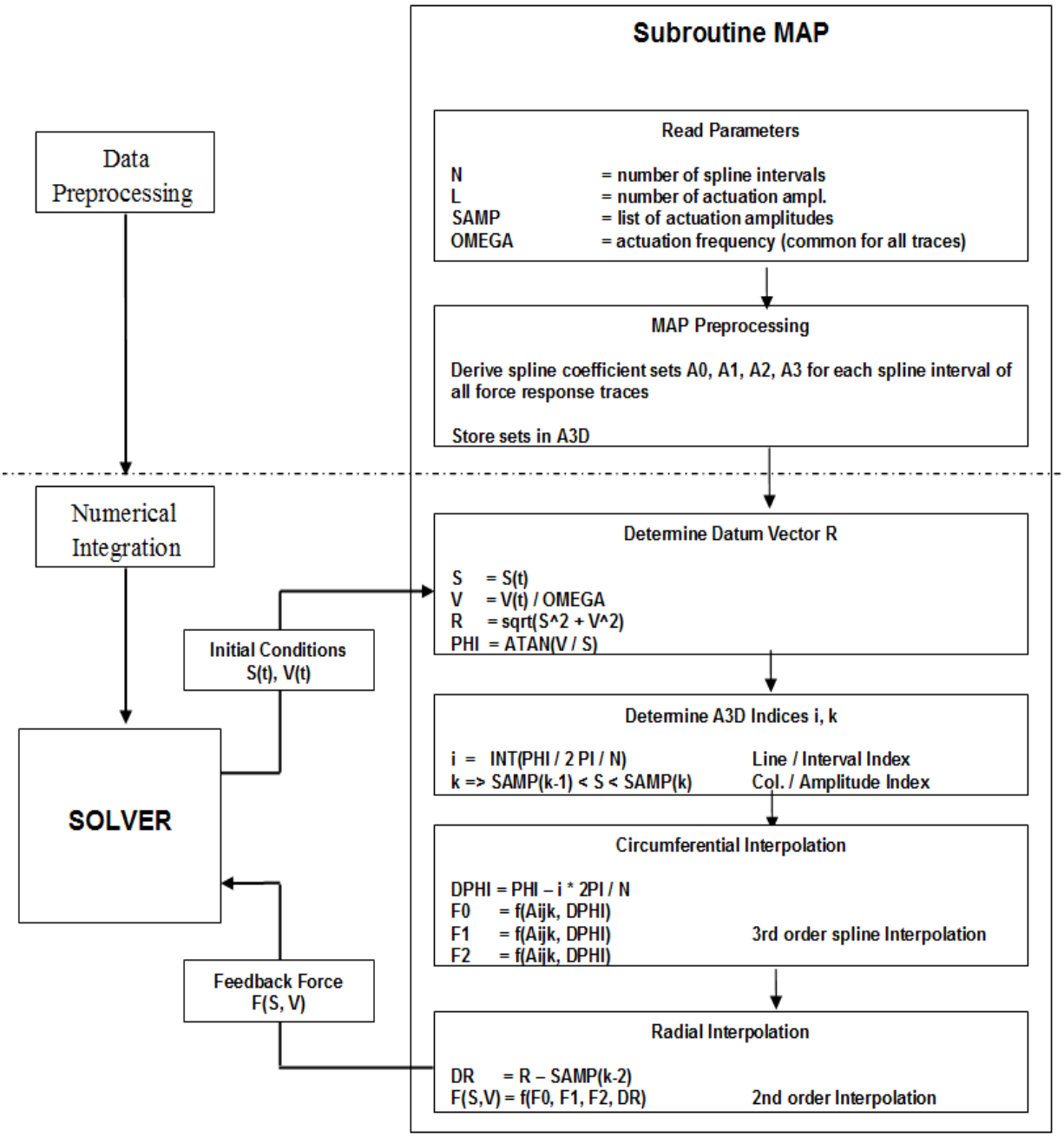

Figure 5.13: Map-to-Solver feedback loop flow chart

In a separate preprocessing action, the three dimensional array A3D is set up with the map spline coefficients prior to the numerical integration of the structural equations of motion. During the solution of the MBS, the force corresponding to the initial conditions S(t), V(t) is retrieved in a feedback loop for each time step.

5.4 Concept potential and limitations

5.4.1 Potential

The map concept is intended for application in simulation of large scale deformations which cover the full range of component deflection. The focus for application is seen in the simulation of severe driving manoeuvres The results, presented in chapter 7, validation, confirm concept applicability for the bumper simulation with good degree of accuracy.

The software developed is a FORTRAN code of modular structure. It can easily be applied as an external subroutine in any MBS environment.

As the map method may be regarded as a standardised process, applicable for lateral and rotational DoFs, an application to other chassis relevant polymeric element types would not require a large effort. Therefore, the vision is to develop further specifications for the actuation parameters discussed in section 5.2.2 to also address the suspension bushings.

In its standardised format, the map force response data generation can be attached to the bushing and bumpers supplier statement of work task list.

5.4.2 Limitations

The following lists the limitations of the expounded map concept:

(a) Superposition effects

Each degree of freedom (lateral or rotational) is addressed individually. Thus, any interaction effects, caused by superposition of multiple DoF is not covered by the map concept.

(b) Frequency

A shortfall of the process is the limitation to only one discrete frequency used for the data acquisition, which is determined by the operational range (Smax, Vmax). The map concept is, therefore by its nature, not valid for a frequency sweep simulation study, which may be considered as a fundamental requirement for NVH investigations. The operational range must be known or estimated prior to the map data acquisition.

(c) Operational range

Contrary to a rheological model, the map concept cannot be extended beyond the operational range defined by the force response data acquisition process. However, the common practice of range extension by data approximation known from 2D static force response curves can also be applied by equally to the three dimensional map concept.

(d) Data acquisition

The data acquisition requires special equipment and in general cannot be provided by means of hydraulic actuation, as the force requirement in conjunction with the velocity demand leads to oil flow rates beyond the scope of ordinary equipment.

The physical force response data acquisition is generally limited in terms of:

- actuation amplitude
- operational range relevant frequency
- maximum force level

If hydraulic cylinders are intended for the harmonic actuation, the limitations are linked to the combination of the three above stated parameters. A maximum force level requires a minimum cylinder cross-section. Frequency and amplitude define the oil volume flow.

To overcome this problem, a mechanical crank concept discussed in chapter 7 is developed and used for the bumper force response map data acquisition.

(e) Memory effects

The concept is valid only for elements that reveal no significant memory effect. The nature of a memory effect is that the force response gained for discrete initial conditions depends on the history of motion that leads to a specific state. The foam-type jounce bumpers used in the current study are proven to have no significant memory effect above the actuation velocity of 0.5 m/s **[56]**.

5.5 Closure

The map concept highlighted in this chapter describes a numerical method to simulate the force transfer function, taking into account the velocity related hysteresis characteristics of a jounce bumper element in chassis applications. Force response measurements performed for harmonic excitation are used as the basis for the simulation. The concept was derived particularly for a polyurethane-type jounce bumper used in the McPherson front suspension used in the CD340 (Ford Galaxy).

The numerical concept is considered to be generally applicable, including for other polymeric type chassis elements, such as conventional or hydro-bushings, for the purpose of impulse-like, full deflection range actuations. A physical validation, as shown for the bumper element, would be required. In doing so, the burden to set up a unique, element-specific model can be avoided.

The force response data set is condensed into a compact numerical format, using cubic spline interpolations to enable an effective solver interaction, linked to MBS. The force response data acquisition method is simple, but in conjunction with the bumpers it can exceed the limitations of conventional hydraulic equipment.

The database is generated for a discrete operational frequency only. The frequency response scope is therefore limited and cannot be extended beyond the measured range. The method is neither applicable for NVH investigations nor for elements that reveal significant memory effects.

The map concept, including data acquisition, data transformation to map format and integration with an MBS solver can be incorporated into a standardised process.

Chapter 6: Minimal parameter in-plane static tyre model

6.0 Introduction

The model discussed here is intended to approximate the static contact force response of a conventional belt tyre used for passenger cars for the case of radial penetration in contact with a rigid body. The rigid body contact geometry is assumed to be a straight line (edge contact) or plane surface (flat contact), acting over the complete width of the belt. Force response traces obtained for the above mentioned tyre deflections typically reveal an almost linear character **[21].** Therefore, the radial tyre force response is often simulated by using a linear spring model **[28]**. In general, experimental testing or other efforts are required to derive the spring stiffness for such a model. The aim of the model proposed here is to avoid such experimental efforts and instead derive the force response analytically from a minimum set of geometrical parameters and the pneumatic pressure. The model will be shown to match the static force response with reasonable accuracy for flat and edge contact. It will be used for an in-plane kerb strike simulation DoK as defined in chapters 1 and 2 to evaluate the maximum vertical load level. An edge-type kerb-to-rim clash is the intended nature of this test in order to cause a radial deflection over the full tyre deformation range. The maximum wheel force level is expected for the clash condition (Figure 6.1 right), followed by a roll-over motion to climb the kerb. The post-clash belt contact will necessarily transform from an edge-type to a flat geometry. To adhere to the principle of simplicity, this contact transition is not considered to be a part of the simulation model. The kerb geometry is, therefore, defined as a blade-type obstacle as shown in Figure 6.1 left.

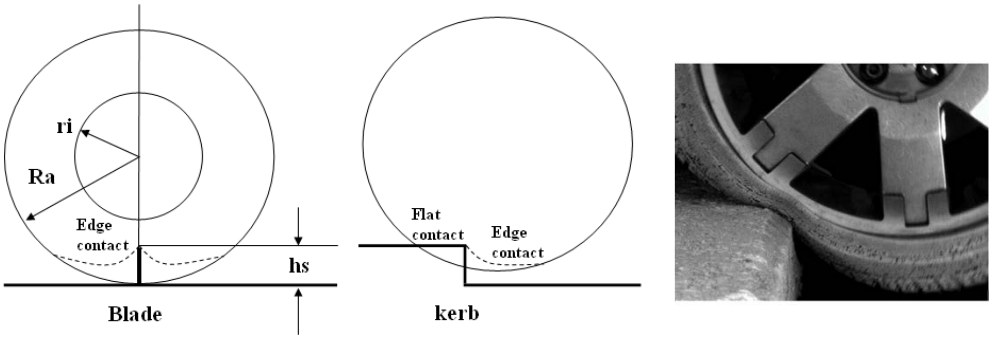

Figure 6.1: Simplified kerb simulation and real kerb strike

6.1 Structural components of conventional passenger car belt tyres

The tyre structural components are shown in Figure 6.2. Item (1) shows the tyre protector (tread), comprising pure rubber material, underlay by bandages (2). Two steel layers (3) are weaved from cables (steel belt), supported by shoulder elements (4) in its transition to the rubber made sidewalls (5). The tyre carcass consists of two nylon cord layers (body ply; item 6). These radially oriented nylon cords (6) are wrapped around a ring made from a steel wire bundle (bead; item 7) and the bead profile (8). The bead is surrounded by a linen textile (9) guided by the shafer elements (10), which protect the sidewall cord structure attached to the bead. A thin rubber coating (liner; 11) surrounds the carcass cord layers and protects the tyre from pneumatic pressure loss. During the vulcanization process, the rubber components are melted to form a compound structure with the other elements.

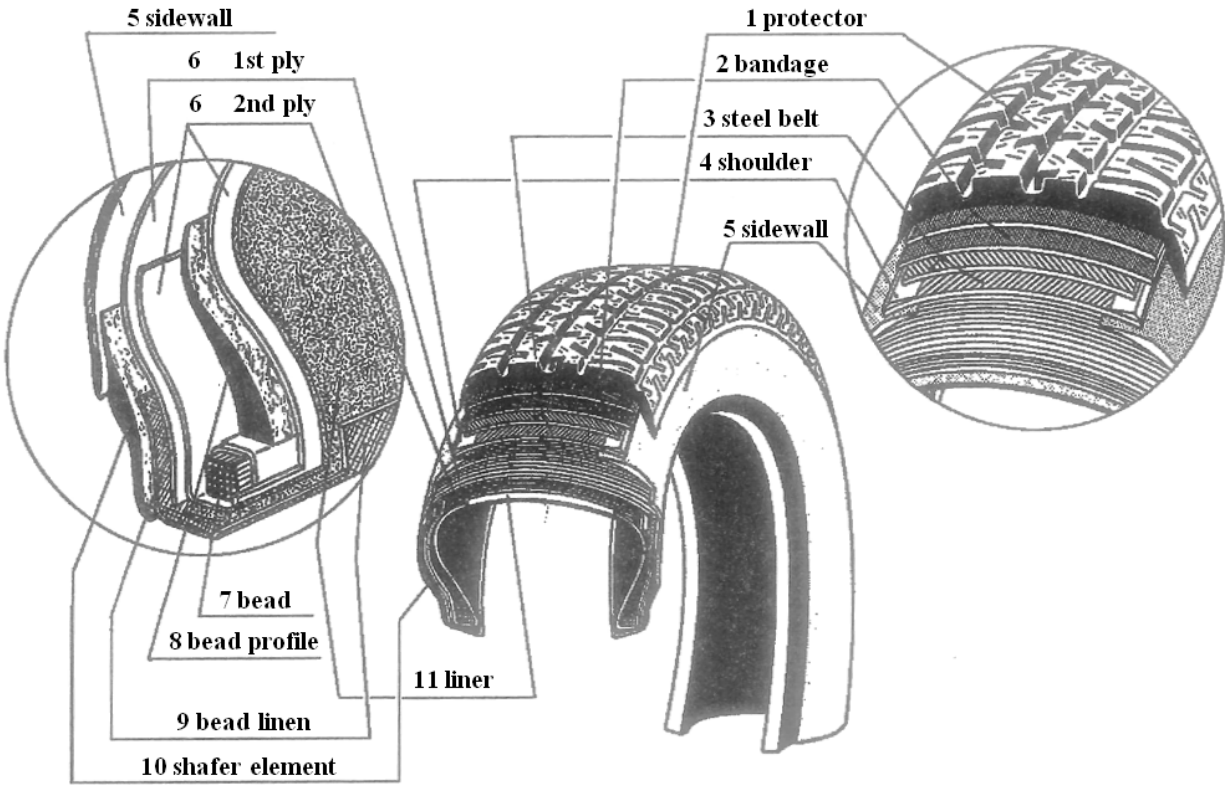

Figure 6.2: Belt tyre structure components [**21**]

In the following, the combined structure consisting of components 1 to 4 is addressed as the *belt*, whereas components 5 to 10 are specified as *sidewall*. Components 4 and 7 are considered to act as a revolute joint that link the sidewall to the belt and to the rim structure.

6.2 General assumptions for physical properties of conventional passenger car tyres

These are:

- The mass of the tyre structure is approximately 20% of the total un-sprung mass, attached to the wheel centre. Only a small portion of the tyre mass is appreciably deformed during a radial kerb strike. It is, therefore, assumed that the inertial forces caused by tyre deformation are small compared with the total inertial force of the un-sprung mass resulting from the 'Drive over Kerb' event.
- Static measurements revealed that the force required for radial deformation of the tyre structure to be smaller than 10 % compared with the total force.
- The increase in tyre pneumatic pressure during radial deformation was measured against that of the flat contact to rim and remained within 10%.

The following assumptions were made with respect to the tyre structure:

- The belt inlay (steel wire) causes a high circumferential stiffness, but it is designed to be flexible in bending.
- Radially-oriented nylon cords within the sidewall structure provide large longitudinal stiffness in the radial direction, but also a high degree of bending flexibility.
- The circumferential stiffness of the sidewall structure is considered to be small in comparison with the circumferential stiffness of the belt.

6.3 Definition of the Tyre model

As a consequence of the above assumptions, the simulation task was reduced to the calculation of the in-plane pneumatic induced force, where stiffness caused by the deformation of the rubber structure and its inertial effects are neglected in the model. The tyre structure is condensed down to two elements, the belt and the sidewalls as shown in Figure 6.3. Both elements are simplified in respect of geometry, inertia and stiffness.

(a) Geometry:

- The steel belt geometry is assumed to be cylindrical for an un-deformed tyre (free of external loads).
- The sidewall geometry is assumed as an ideal torus section, attached to the belt and the bead (see Figure 6.4).

(b) Inertia:

- Both elements; the belt and the sidewall, are considered to be massless.

(c) Stiffness:

- The belt is considered to behave as an inextensible ring, rigid in the circumferential and axial directions. It is considered to behave like an ideal membrane with regards to bending stiffness in circumferential direction.

- The sidewall cords are considered as rigid in its longitudinal (along the cords centre line) direction. The sidewall structural stiffness perpendicular to the cords but in-plane with the sidewall (in its circumferential direction) is considered to be of negligible stiffness and with no resistance against shear deformation. The wall is also assumed to behave membrane like, ideally flexible in bending.

(d) Pneumatic pressure:

- This is assumed to remain constant during any radial deformation.

6.3.1 Geometrical parameters of the tyre model

Four geometrical parameters taken from the real cross-section, indicated in the right half-section of Figure 6.3 are defined so as to describe an idealised tyre model.

- Ra, belt outer radius
- ri, rim radius
- bt, belt width
- fc, height of sidewall arc

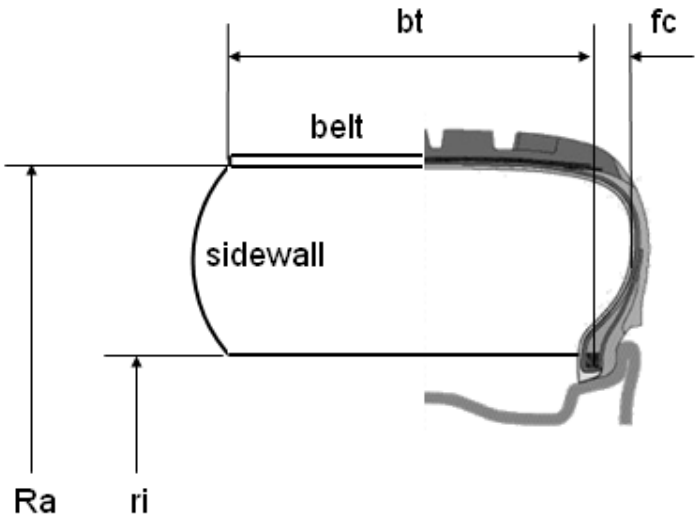

Figure 6.3: Tyre model geometrical parameters taken from the real cross-section

The sidewall structure is simplified as a radial membrane in shape of an *xz* in-plane toroidal section (see Figure 6.4). All the following derivations are based on the above simplifications and assumptions.

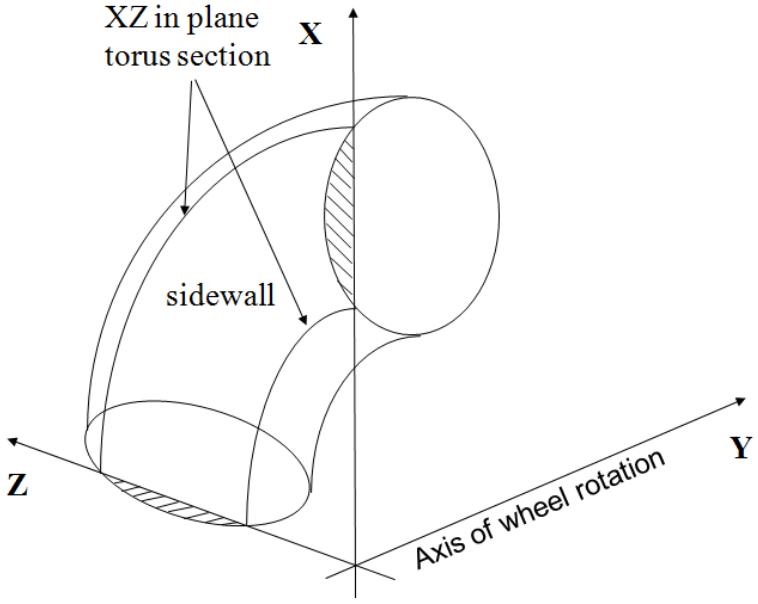

Figure 6.4: The sidewall model structure considered as toroidal membrane section

6.4 Full analytical tyre model based on shell theory

Based on the tyre structure assumptions made above, full analytical formulas are derived for the pneumatic caused internal stress and the force response against radial deformation is provided in the next items by making use of the membrane theory.

6.4.1 Derivation of analytical model properties for an un-deformed tyre

The internal stress applied to the tyre model elements is analysed for the tyre in its un-deformed state. In this case, the belt contour is assumed to be an ideal right circular cylinder linked to the sidewalls, considered as a toroidal membrane section as shown in Figure 6.4. In particular, the internal radial stress σ1 at the sidewall-to-belt link and the circumferential belt force Fg are derived (see Figure 6.7).

(a) Derivation of torus membrane stress

Timoshenko **[59]** derived a general in-plane stress relationship for a doubly-curved element of a thin-walled vessel structure subjected to an internal pressure *p*, as shown in the shaded element of Figure 6.5.

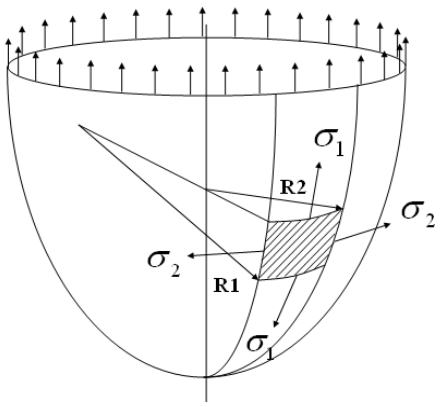

Figure 6.5: In-plane stress on double curved thin walled vessel at constant pressure **[59]**

With R1 and R2 being the vessel radii of curvature, the equilibrium condition in the radial direction applied for the shaded membrane element reveals:

$$\frac{\sigma_1}{R1}+\frac{\sigma_2}{R2}=\frac{p}{tc} \tag{6.1}$$

where *tc* is the wall thickness of the vessel shell element.

When applied to a torus structure, shown in Figure 6.6, R1 is considered as the radius of the torus cross-section in the *xy* plane, whilst R2 stands for the outer contour radius in the planar section *xz* plane.

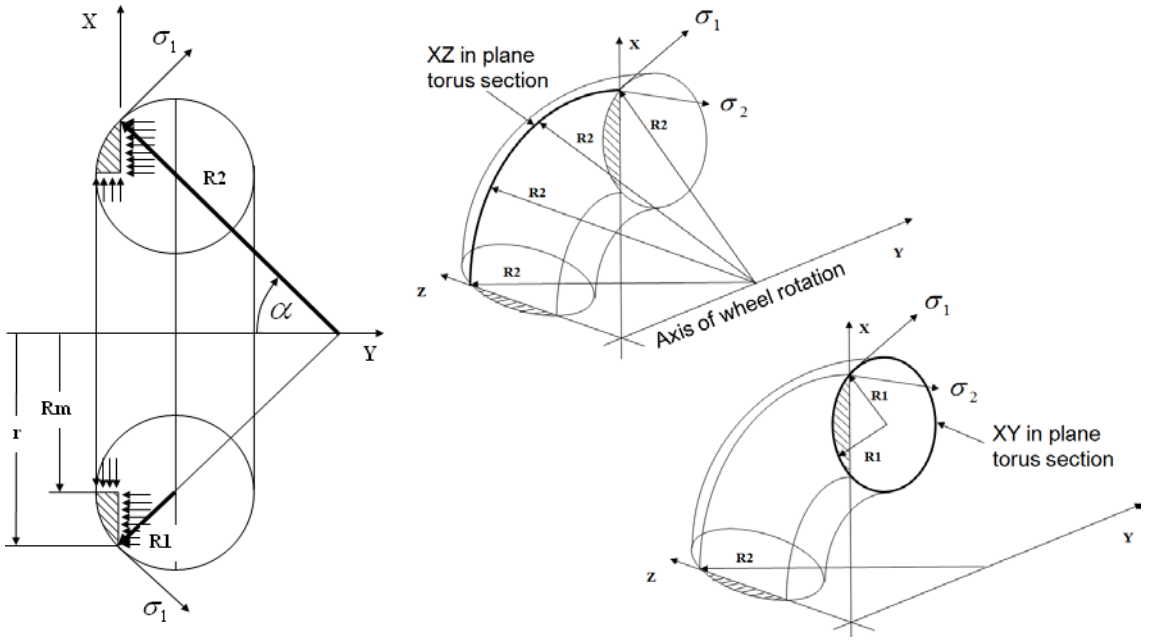

Figure 6.6: Curvature radii R1, R2 and membrane stresses σ_1, σ_2 in a torus section

For *tc* being the wall thickness of the membrane and *p* the pneumatic pressure, the equilibrium condition in the *y*-direction leads to the radial stress, σ_1:

$$2\pi \cdot r \cdot tc \cdot \sigma_1 \sin\alpha = p \cdot \pi \cdot \left(r^2 - Rm^2\right) \tag{6.2}$$

Using the first part of the geometrical relationship: $\sin\alpha = \frac{r - Rm}{R1} = \frac{r}{R2}$, the radial stress of the sidewall can be derived as a function of radius *r*:

$$\sigma_1 = p \cdot \frac{R1}{2tc} \cdot \left(1 + \frac{Rm}{r}\right) \tag{6.3}$$

In combination with equation (6.1), the circumferential stress σ_2 reveals to be constant all over the toroidal section *xy*, thus:

$$\sigma_2 = p \cdot \frac{R1}{2tc} = const \tag{6.4}$$

(b) Application of the shell theory to derive belt and sidewall stresses

Equations (6.3) and (6.4) represent the toroidal membrane stress for an ideal isotropic elastic material. When applied to a tyre structure, it must be noted that the material elasticity is no longer isotropic as the belt structure is almost rigid in the circumferential direction, whereas the sidewalls are quite flexible. Therefore, the circumferential stress σ_2 would mainly transfer through the belt structure, resulting in *Fg* (see Figure 6.7). In line with the model assumptions with regard to stiffness, listed under section 6.3 c, the sidewall circumferential stress σ_2 can be assumed to be zero in the deviation of equation (6.4). A deviation of σ_2 does also change the radial balance to σ_1 , according to equation (6.1).

Despite these deviations, equation (6.3) can be applied to calculate the tyre sidewall stress σ_1 which defines the line load *Qsg* linked to the belt edges:

$$Qsg = \sigma_{1(r=Ra)} \cdot tc = p \cdot \frac{R1}{2} \cdot (1 + \frac{Rm}{Ra}) \tag{6.5}$$

Similarly, the sidewall line load *Qsr* at the rim contact can be found as:

$$Qsr = \sigma_{1(r=ri)} \cdot tc = p \cdot \frac{R1}{2} \cdot (1 + \frac{Rm}{ri}) \tag{6.6}$$

The equilibrium condition in the *z*- direction, shown in Figure 6.7, was used for the derivation of the belt force *Fg*. A cylindrical shell element representing the belt is applied to the sidewall stress σ_1 and the circumferential belt force *Fg*. Both loads hold the shell in equilibrium against the pneumatic force in the *z*- direction, caused by pressure *p* applied to the projected shell area (see Figure 6.7).

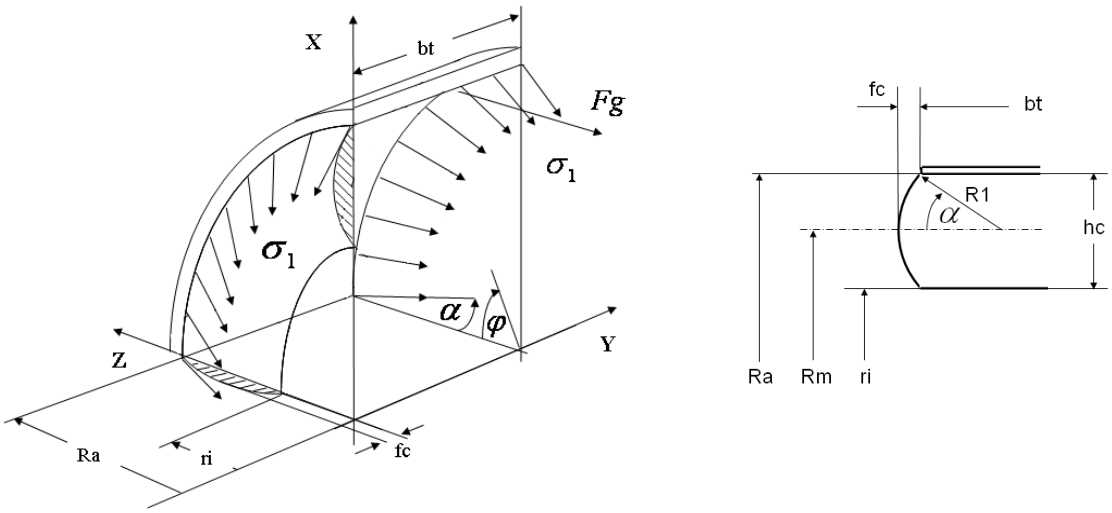

Figure 6.7: Belt shell structure applied to sidewall stress and belt force *Fg*. Right: the tyre cross-sectional geometry

$$Fg = p \cdot Ra \cdot bt - 2 \cdot \sigma_1 \cdot \cos\alpha \cdot Ra \cdot tc \int_{\varphi=0}^{\pi/2} \cos\varphi \cdot d\varphi$$

By using equation (6.3) and the four geometrical relations:

$$Rm = \frac{Ra + ri}{2} \qquad hc = Ra - ri \qquad R1 = \frac{hc^2 + 4\,fc^2}{8\,fc} \qquad \cos\alpha = \frac{R1 - fc}{R1}$$

the integration leads to the circumferential belt force *Fg* as:

$$Fg = p \cdot \left[Ra \cdot bt - (Ra + Rm) \cdot (R1 - fc) \right] \tag{6.7}$$

6.4.2 Assessment of analytical method versus FEM results

To validate equations (6.5), (6.6) and (6.7), their predictions were compared with results from an FE analysis as shown in Figure (6.8). The FE results were provided by the FORD Chassis CAE group in FoE. Chassis CAE makes use of an ABAQUS tyre model. It is based on the standard ABAQUS TYRE described in **[42]**, but parameterized and validated by Chassis CAE.

The comparison was done for two tyre sizes 235/40-R18 and 205/55-R16 (see chart 6.1).

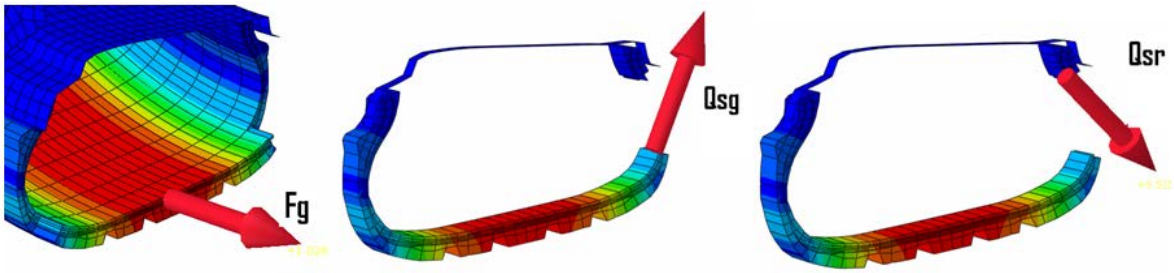

Figure 6.8: Intersection load analysis based on ABAQUS FE tyre simulation

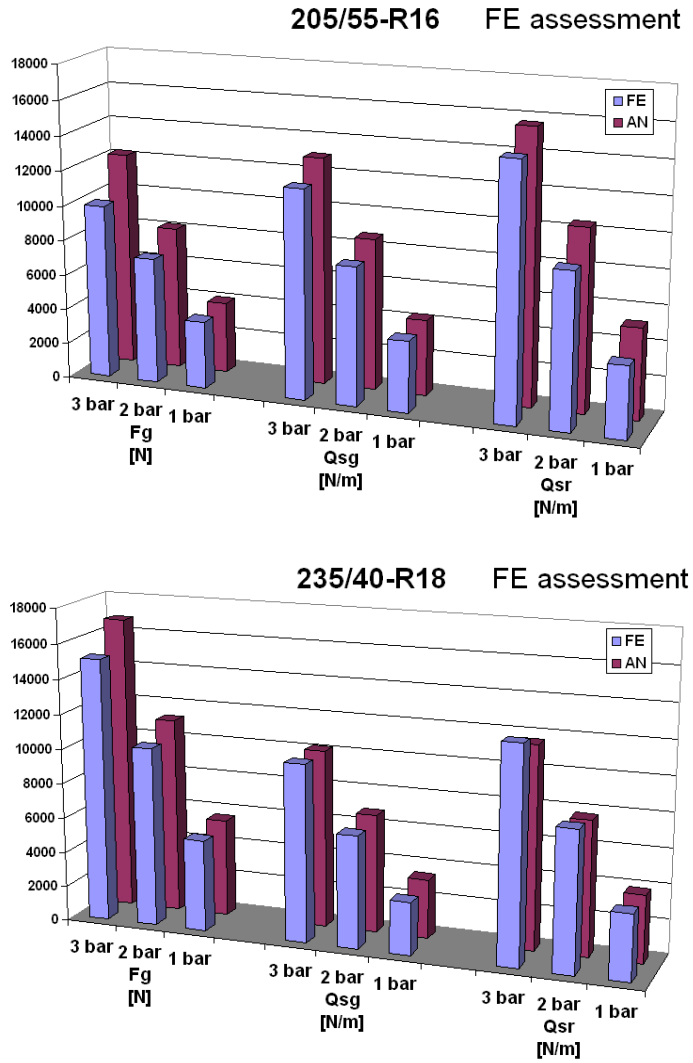

Chart 6.1: Overview of internal load validation results for 205/55-R16 and 235/40-R18

The deviations found between analytical and FE results for the belt force *Fg*, sidewall line loads *Qsg* to the belt and *Qsr* to the rim are on average smaller than 10% for an un-deformed tyre stress analysis.

6.4.3 The tyre model to simulate force response against radial deformation

When the tyre is loaded in contact with even ground or forms an edge contact with a kerbstone, a local radial penetration occurs. The local radial deformation causes a global belt and sidewall deformation, and therefore, affects the entire tyre structure. Hence, in general a comprehensive structural analysis is required to calculate the force response. This approach is addressed by the chain model in section 6.5. Nevertheless, the simple model concept derived in this section can replace a detailed tyre structural analysis by simple geometrical assumptions for the belt deformation state.

Two patch geometries are outlined; a flat contact with the ground and an edge-type contact.

For a flat contact, the maximum belt contact length to ground is approximated by the tangent section shown in Figure 6.9, left. A circular shape is assumed for the residual belt, which is not in contact with the ground. Because of its simplicity, it is acknowledged that this approach violates the assumption of a constant belt length (imcompressibility of the rubber compound). Tyre force response curves obtained from the flat contact deformation are known to be of almost linear character with a slight progression **[14]**, **[21]**, **[26]**. Therefore, the maximum force required to deform the belt into rim contact position is analysed and subsequently linearised over the radial belt deflection range.

To analyse the edge contact, an analogy to a hinge bridge structural analysis **[61]** is made, which is used in civil engineering. The belt length affected by radial deformation (effective length Le) is approximated by the span width of a hinge bridge as shown in Figure 6.10. To validate the simplified approaches, the results are assessed against an ABAQUS FE tyre model.

(a) Flat contact model

The analysis is based on a membrane assumption, where the flexible belt is considered to transfer the effect of internal pressure to an ideal planar and rigid ground by neglecting the structural effects. The maximum contact patch length can be approximated by a horizontal line tangential to the rim at the deflection level *fmax*, where the belt contacts the contour of the rim of radius ri (Figure 6.9).

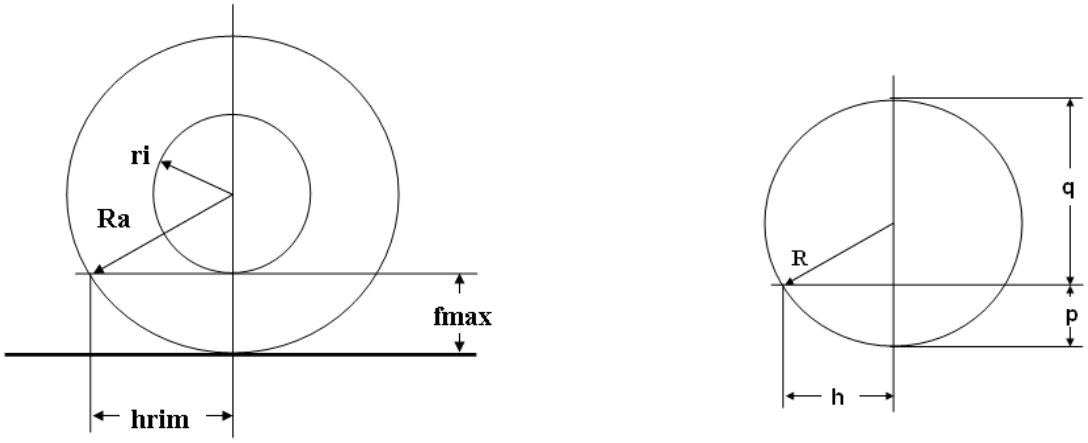

Figure 6.9: Flat contact of a simplified tyre and a Euclidean circular geometry

Using the Euclidean law: $h^2 = p \cdot q$ (Figure 6.9, right), the maximum length of the contact patch hrim becomes:

$$hrim = \sqrt{(Ra - ri) \cdot (2Ra - (Ra - ri))}$$

Thus, linearisation leads to the tyre patch contact length hp as:

$$hp_{(f)} = 2 \cdot \frac{hrim}{Ra - ri} \cdot f$$

Hence, the contact force against flat ground can be approximated by equation (6.8):

$$Fc = p \cdot hp_{(f)} \cdot bt \tag{6.8}$$

(b) Edge contact model

The contacting profile is assumed to be a blade-type obstacle in an allusion to a hinge bridge pylon. It represents an idealised line contact over the belt width as shown in Figure 6.10. The hinge bridge span width Le is considered to behave analogous to the belt radian length *Le* (effective length) subjected to radial deformation.

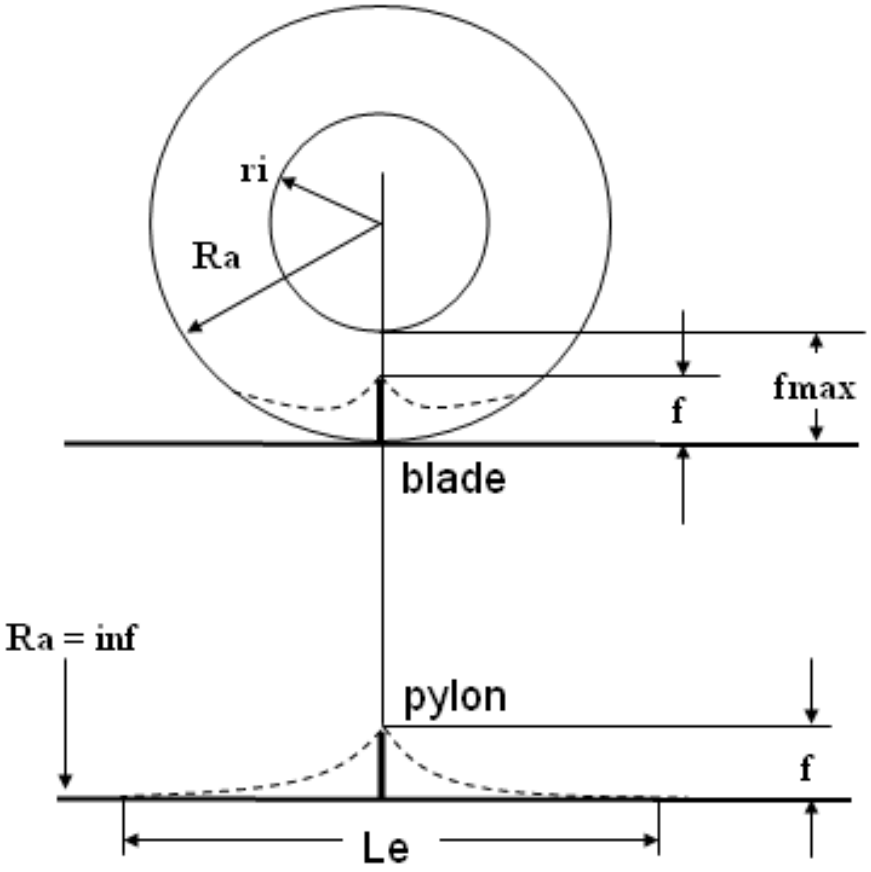

Figure 6.10: Edge contact for a simplified tyre geometry

Circumferential forces *Fg* hold the belt structure in equilibrium against the pneumatic force applied to the projected area 2Ra*bt and the sidewall line stress σ1 (Figure 6.7). With an increasing radial deflection *f* (Figure 6.11, right), the projected belt area and hence the belt force *Fg* decreases. This effect is recognised by the correction of the belt force *Fg* in equation (6.9):

$$Fg_{corr} = Fg \cdot \frac{2Ra - f}{2Ra} \tag{6.9}$$

With the assumption of a common belt force magnitude at the upper and lower belt ends and an analogy to the hinge bridge rope equations (6.10) **[61]** derived for constant line load *q* (see Figure 6.11 left), this leads to equation (6.11).

Rope equations:

$$H = \frac{q \cdot Le^2}{8f} \qquad and \qquad \tan\beta = 4 \cdot \frac{f}{Le} = \frac{V}{H} \tag{6.10}$$

Analogy:

$$H = \frac{q \cdot Le^2}{8f} = p \cdot \left[Ra \cdot bt - (Ra + Rm) \cdot (R1 - fc)\right] \cdot \frac{2Ra - f}{2Ra} = Fg_{corr} \tag{6.11}$$

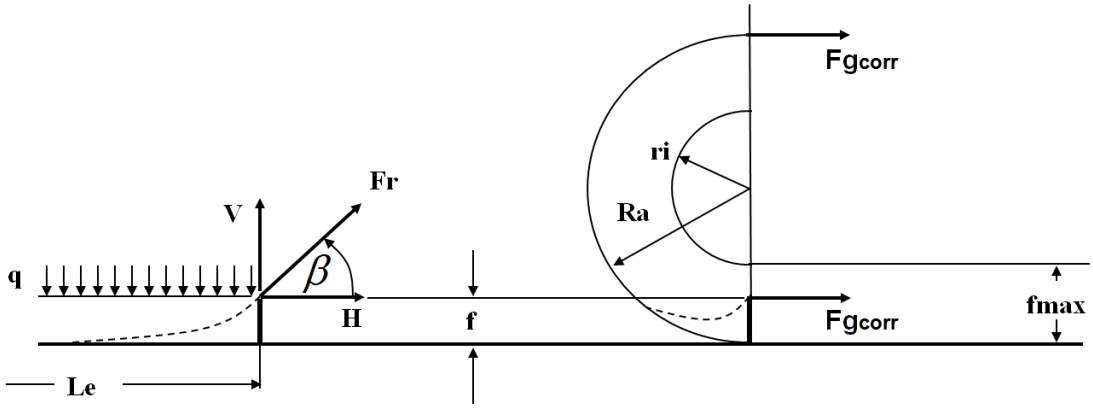

Figure 6.11: Belt load analogy to equations for a rope

The left hand side of Figure 6.11 shows the hinge bridge rope (dashed line), attached to the horizontal equilibrium force *H*. The rope is shown for half its span-width (effective length *Le*). On the right hand side of Figure 4.11, the half tyre is attached to the horizontal belt forces. For an edge contact, the belt is considered to act analogous to a simply supported rope ($H = Fg_{corr}$). Based on the analogy assumption (6.11) the horizontal belt force *H* can be estimated by using the equations (6.7) and (6.9) derived from shell theory, whereas the vertical component $V = H \tan\beta$ preliminary remains unknown in absence of the rope angle β. A view on the rope equation (6.10) reveals that this angle is related to the effective length *Le*. Rearranging equation (6.11) by taking into account $q = p \cdot bt$ and $hc = Ra - ri = f_{\max}$, the effective length *Le* for a full range of radial deflection to rim contact can be estimated by equation (6.12).

$$Le = 2 \cdot \sqrt{2 \cdot hc \cdot \left[Ra - \frac{(Ra + Rm) \cdot (R1 - fc)}{bt}\right] \cdot \frac{2Ra - hc}{2Ra}} \tag{6.12}$$

Now, equations (6.10) and (6.12) are used to analyse the tangent angle β of the rope (Figure 6.11) for the case of maximum deflection $f_{\max}$:

$$\tan \beta_{\max} = \frac{4 f_{\max}}{Le} \tag{6.13}$$

Strictly speaking, both effective length *Le* and the tangential angle β are non-linear functions of the radial deflection *f*. However, the agreement to physical testing and FE results was improved by a linearization of β over deflection *f* and by neglecting the correction factor *(2Ra – f) / 2Ra* used for the derivation of constant length *Le*, which simplifies equation 6.12:

$$Le = 2 \cdot \sqrt{2 \cdot hc \cdot \left[Ra - \frac{(Ra + Rm) \cdot (R1 - fc)}{bt} \right]} \tag{6.12-a}$$

With the assumptions made above, equations (6.9) to (6.12-a), the radial belt force *Fc* for an edge contact can be approximated by:

$$\begin{aligned} Fc = 2 \cdot V &= 2 \cdot H \cdot \tan \beta_{\max} \cdot \frac{f}{f_{\max}} \\ &= 8 \cdot \frac{f}{Le} \cdot Fg_{corr} = 2 p \cdot bt \cdot f \cdot \frac{(2Ra - f) \cdot \sqrt{Ra - (Ra + Rm) \cdot (R1 - fc)/bt}}{Ra \cdot \sqrt{2 \cdot (Ra - ri)}} \end{aligned} \tag{6.14}$$

Beside the deflection *f*, equation (6.14) is reduced to the pneumatic pressure *p* and four geometrical parameters taken from the tyre cross-section.

6.4.4 Numerical results assessment to FE model

An assessment of the force response (*Fc*) of the numerical results for the flat contact's simple model (linear membrane) was made against ABAQUS FE structural analysis. Results gained for flat contact are shown in chart 6.2:

(a) Flat contact

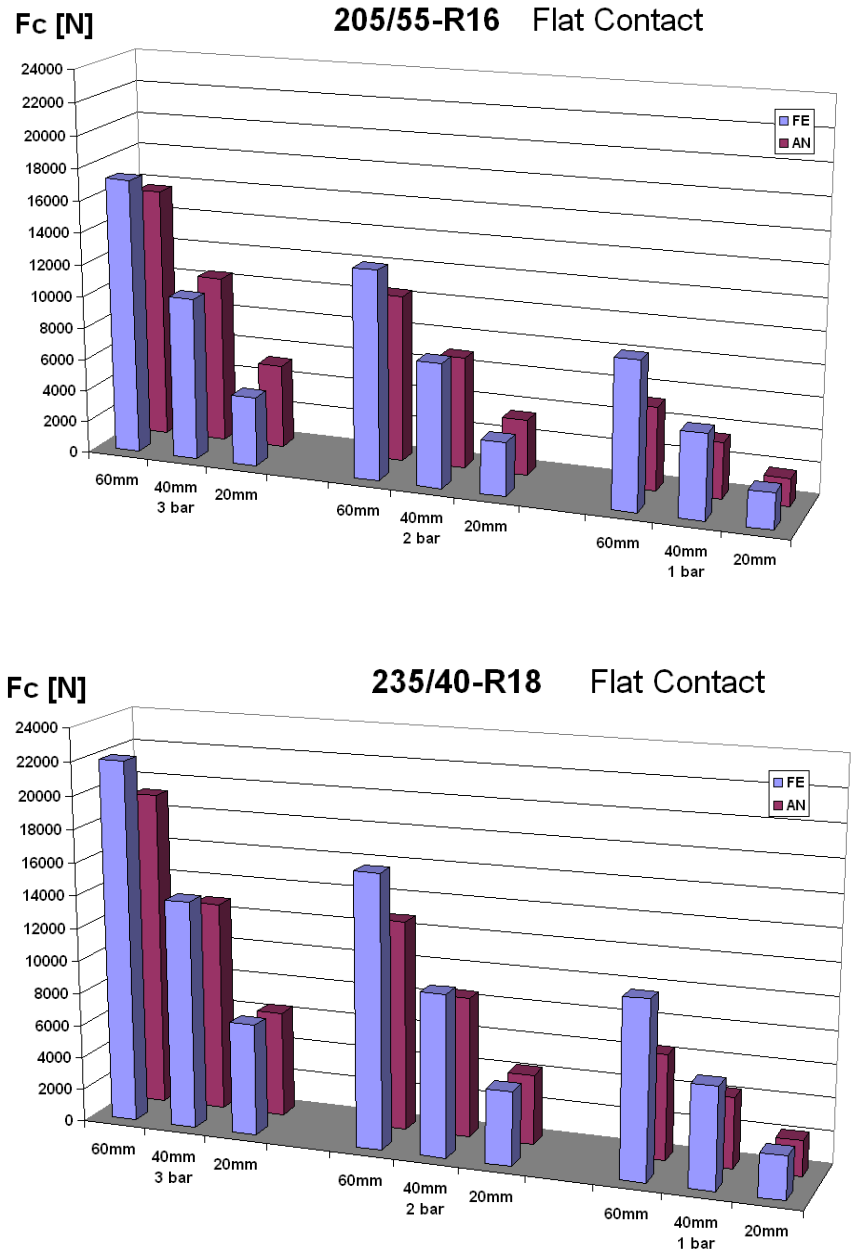

Chart 6.2: Flat contact vertical force for linear membrane and those of ABAQUS FE model

The results reveal a good fit for small deflections (20mm) only. The deviations increase with rising deformation and decreasing pressure. The reason for the difference is considered to be due to the omission of the tyre structural stiffness and sidewall effects.

(b) Edge contact

An assessment of the numerical results for edge-type contact for the simple model (rope analogy) is made against the FE structural analysis. These are shown in chart 6.3.

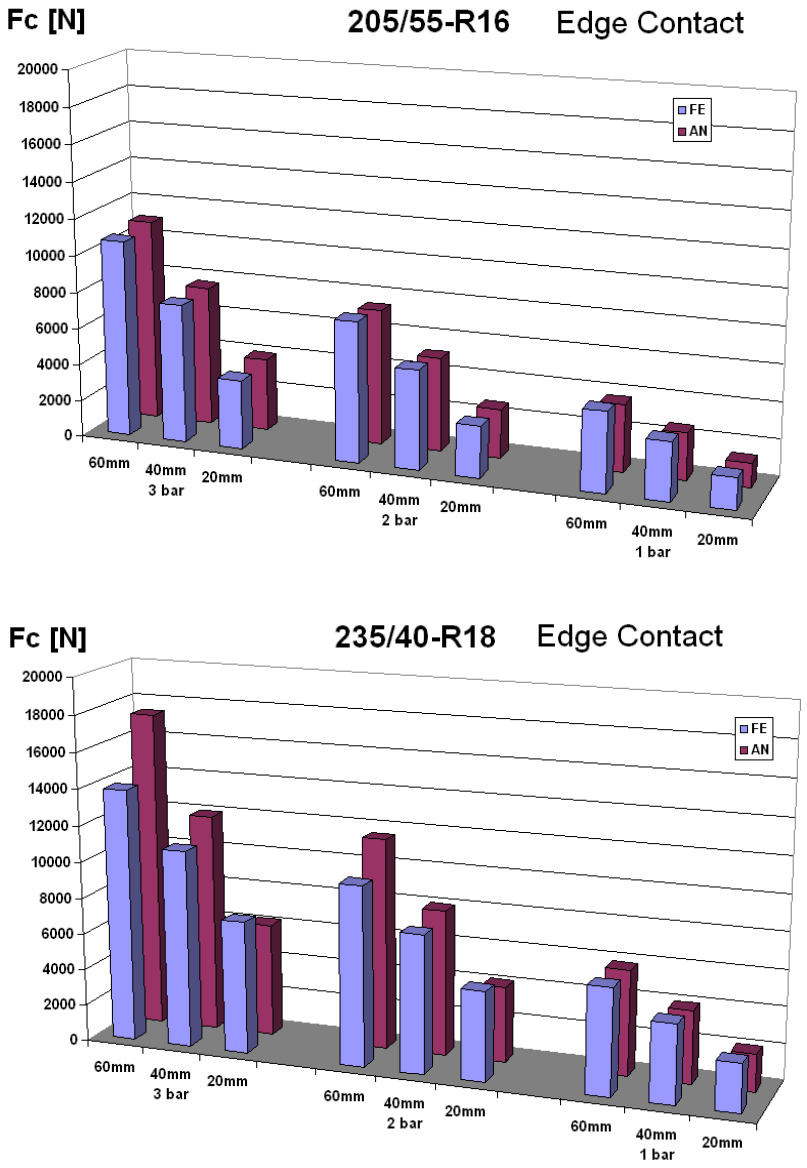

Chart 6.3: Edge contact vertical Force for the linear membrane model versus the FE model for tyre types 205/55-R16, 235/40-R18

Deviation less 10% is noted for the tyre size 205/55-R16. In contrast to the flat contact, the edge contact simple model over-predicts the force level for tyre size 235/40-R18. The deviations increase with rising deformation and pressure, but even for 3bar and 60mm deflection (conditions for close to rim contact) the deviation does not exceed 20%.

6.5 Physical tyre model based on chain type structure

One feature that both the simple models presented above have in common is that the belt contour shape is determined by the definition of the contact patch length hrim (for the flat contact model, see Figure 6.9) and by the equivalent length definition Le for the edge-type contact. In both cases, the belt contour is a consequence of these definitions, which does not necessarily fulfil the physical equilibrium condition. Furthermore, the effect of belt-to-sidewall deformation and its interaction with the sidewall forces is neglected in the simple model approach. To confirm the validity of these simplified conditions, a physical chain model, based on the virtual work principle is derived for the edge-type contact problem. The aim is to find the edge contact force that matches with the desired radial deformation and simultaneously fulfils the belt equilibrium condition.

(a) Chain model structure

The continuous belt structure is divided into discrete rigid bar elements of tyre axial length 'bt' and in-plane length 'cl', (see Figure 6.12). The bars are oriented in the wheel's axial direction and linked by revolute joints at their side edges to form a roller chain-like ring structure of radius Ra. The bar elements' in-plane length 'cl' corresponds to a one degree geometrical resolution of the in-plane angle α_t, resulting in 360 elements, representing the full circular belt. Rope forces Fsw derived from the sidewall membrane stress are attached to the bar ends. The belt circumferential force Fg, as well as the sidewall forces Fsw are transferred by the assumed revolute joints.

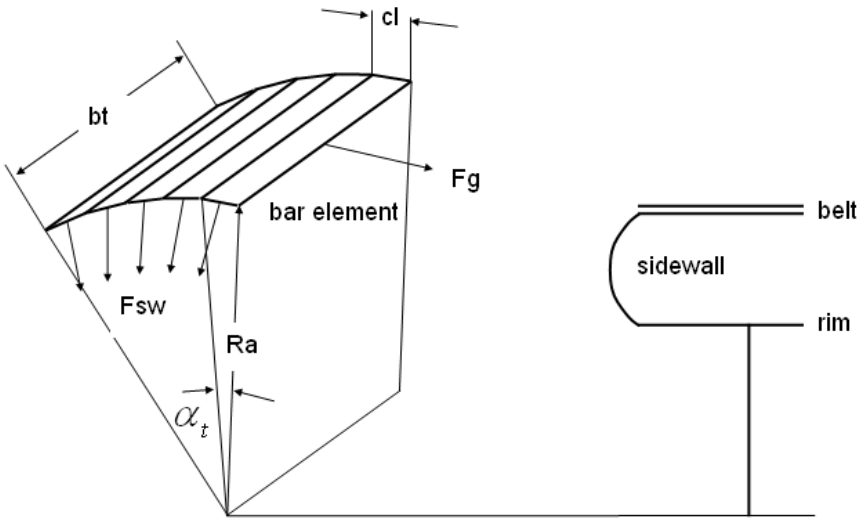

Figure 6.12: Chain structure of tyre belt (left) and cross section (right)

The above model structure is used to investigate the static force response of a radial deformed tyre belt shown in Figure 6.13. Using equation (6.5) the sidewall force Fsw at the bar ends, shown in Figure 4.12, is:

$$Fsw = Qsg \cdot Ra \cdot \alpha_t = p \cdot \frac{R1}{2} \cdot (Ra + Rm) \cdot \alpha_t \tag{6.15}$$

Similarly, the sidewall force at the rim is:

$$Fri = Qsr \cdot ri \cdot \alpha_t = p \cdot \frac{R1}{2} \cdot (ri + Rm) \cdot \alpha_t$$

(b) Derivation of radial force response

For static radial deformation, the tyre belt must be in equilibrium with the radial applied external force Px (Figure 6.13).

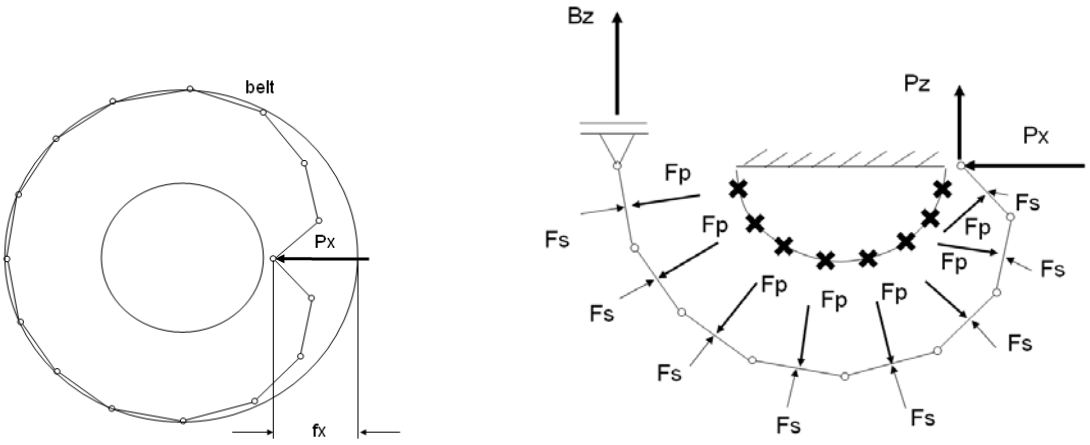

Figure 6.13: Tyre belt chain model in radial deformation state

Considering a symmetric deformation (Figure 6.13 left), the analysis can be reduced to that of the lower half belt. In-plane sidewall forces Fs and pneumatic forces Fp are attached to each belt bar element. The pneumatic forces are directed perpendicular to each bar element and are of constant magnitude, whereas the sidewall forces Fs are directed towards their attachment points (crosses in Figure 6.13 right), fixed to the rim and vary in magnitude.

6.5.1 Model simplifications, boundary and initial conditions

(a) Shear stress

A consequence of the radial belt deflection is the occurrence of shear deformations in the sidewalls (Figure 6.14).

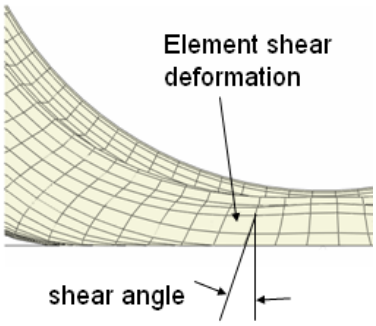

Figure 6.14: Element shear deformation caused by the radial tyre deflection

The shear stress, caused by the sidewall shear deformation, is neglected in the current model.

(b) Boundary support condition

In the case of a radial load Px, applied to the belt's free-end, only a small deflection in the *x*- direction is expected at the supported end of the belt, linked to the floating bearing shown in Figure 6.15 (left). Hence, the bearing force Bx can be considered to be small in relation to the external force Px at the belt free-end for the case of a fixed bearing as shown in the right hand sketch. A simplification is achieved for the support configuration shown in right hand sketch, as it retains a deformation of the belt relative to the rim.

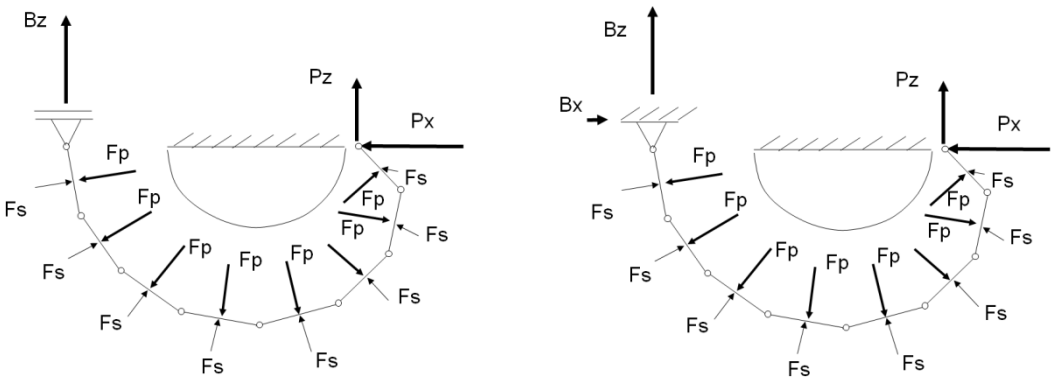

Figure 6.15: Simplified boundary conditions for tyre belt model

(c) Element forces at initial condition

A circular contour is defined for the polygonal belt structure in case that the radial force Px becomes zero and all the other forces; Fs and Fp attached to the elements are directed radially and would be of a constant magnitude as shown in Figure 6.16 (left).

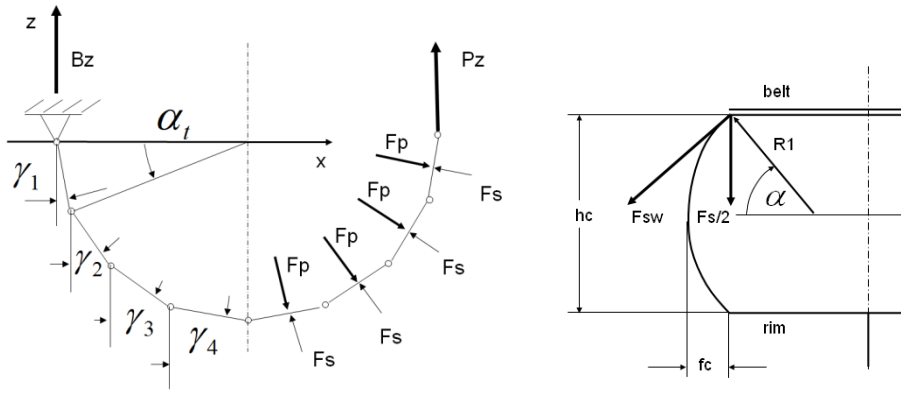

Figure 6.16: Circular tyre belt contour and tyre cross section in initial condition

In this case, the in-plane radial component Fs of the sidewall force Fsw is derived from equation (6.15) as:

$$\begin{aligned} Fs &= 2Fsw \cdot \cos\alpha \\ &= p \cdot R1 \cdot \alpha_t \cdot (Ra + Rm) \cdot \cos\alpha \end{aligned} \tag{6.16}$$

and the pneumatic force Fp remains

$$Fp = p \cdot bt \cdot Ra \cdot \alpha_t$$

The forces to maintain equilibrium at the free belt end are:

$$Px = 0$$
$$Pz = Fg = p \cdot [Ra \cdot bt - (Ra + bt) \cdot (R1 - fc)]$$

6.5.2 Sidewall force to belt interaction

It is the nature of pneumatic forces (Fpi) to act perpendicular to the surface. Therefore, their directions always correspond to the element angles γi as shown in Figure 6.16. They are of constant magnitude, whereas the sidewall forces (Fsi), shown in Figure 6.15 (right) vary in magnitude as a function of belt deformation and are always directed towards their attachment points fixed to the rim.

The sidewall force Fsw, acting on the belt bar element ends, is derived for the un-deformed circular tyre (initial condition) under section 6.5, equation (6.15). Its magnitude depends on pressure p, the span length hc and the sidewall slack hang fc, shown for the initial condition in Figure 6.17 (left). The span length is defined by the position of the belt bar ends and the invariant rope attachment point to the rim.

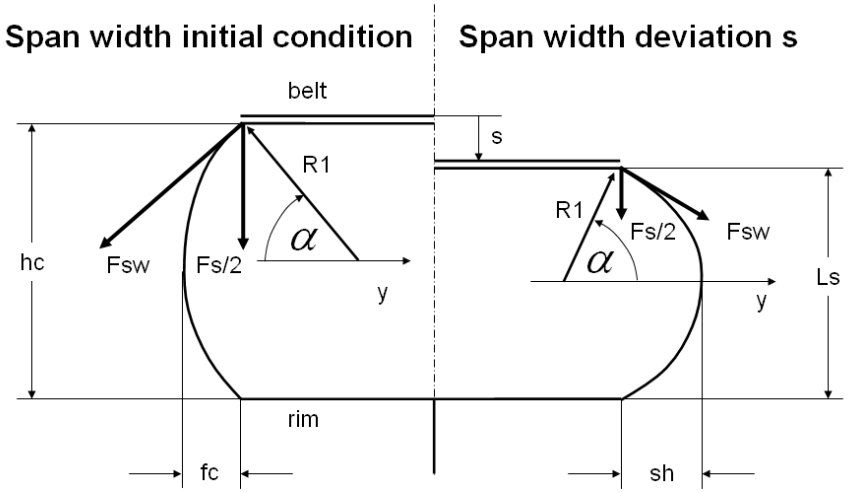

Figure 6.17: Element sidewall force Fs for initial condition and radial belt deflection

In the case of a span width deviation 's' (Figure 6.17, right), the slack hang 'sh' increases whereas span width 'Ls' and the sidewall force Fs decrease with the rising deviation 's'. For the loaded tyre, the span width 'Ls' is not necessarily directed radially, but is a function of the belt deflection state. The span width deviation 's', caused by the belt deformation, is used as a variable to define the sidewall force Fsw. Four cases are discussed as follows:

Case 1:

The maximum span width is limited by the sidewall radian 'bc' at zero slack hang 'sh'. This condition defines a singularity as it results in the sidewall force Fsw becoming infinite (case 1, Figure 6.18). In this case, the span width deviation 's' is defined as negative and achieves its maximum magnitude 'ac' for the sidewall contour in full stretch.

$$s = -ac$$
$$Fsw = \infty$$

Case 2:

For the unloaded tyre (circular belt shape), the span width corresponds to the radial tyre width 'hc' against the rim (s = 0). For the span width deviation 's' to become zero, the sidewall force Fsw is defined in equation (6.15) as:

$$s = 0$$
$$Fsw = p \cdot R1/2 \cdot (Ra + Rm) \cdot \alpha_t = Fsw1$$

Case 3:

For a positive span width deviation (s > 0) towards the rim attachment, the sidewall force decreases as the slack hang 'sh' increases, hence:

$$0 < s < hc$$
$$Fsw < Fsw1$$

Case 4:

For the belt contact to the rim condition, the sidewall force is approximated by equation (6.17); the formula for the circumferential stress of a cylindrical vessel of radius Rk:

$$s = hc$$
$$Rk = bc/2\pi \qquad (6.17)$$
$$Fsw = p \cdot Rk \cdot Ra \cdot \alpha_t = Fsw2$$

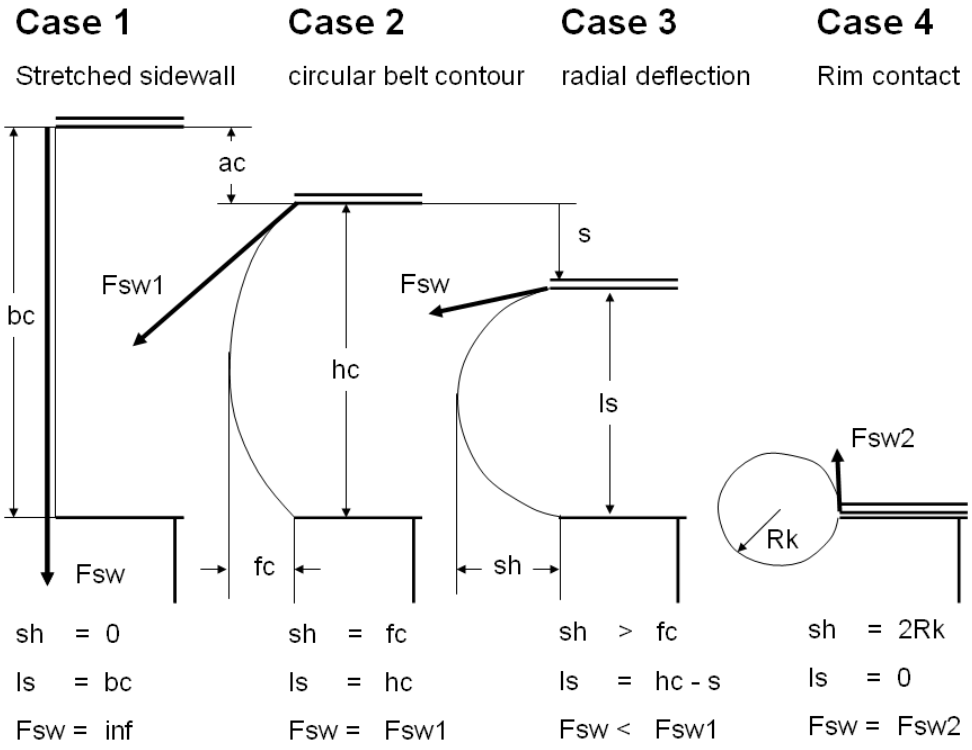

Figure 6.18: Analysis of sidewall force Fsw

The graph in Figure 6.19 shows an approximation curve considered for the sidewall force Fsw as a function of span width deviation s. The origin of the axis system is defined by the unloaded tyre condition.

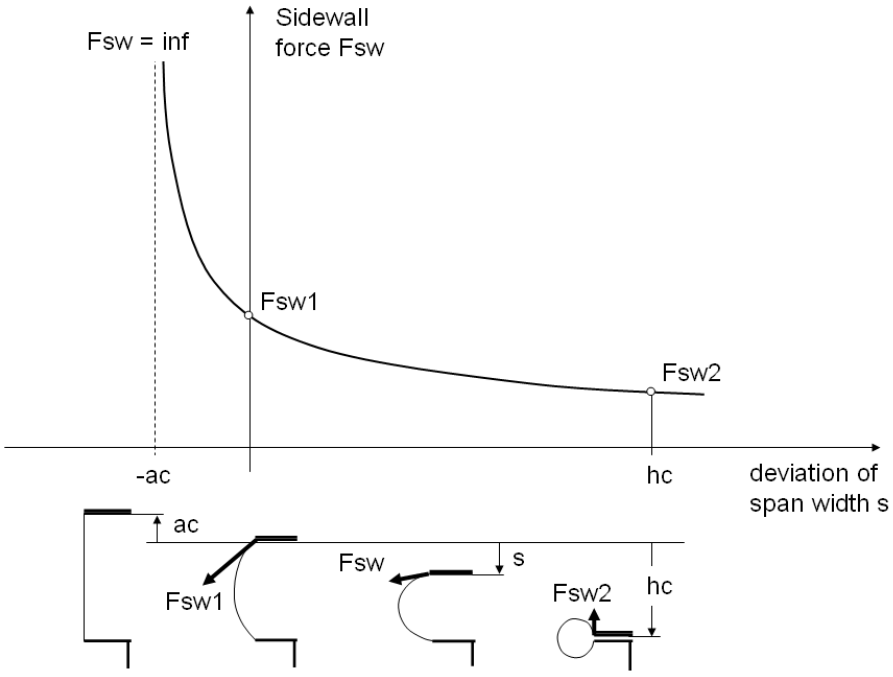

Figure 6.19: Approximation of sidewall force Fsw as function of span width deviation *s*

Equation (4.18) is used to approximate the curve shown in Figure 4.19:

$$Fsw(s) = \frac{g}{(ac + s)^u} \tag{6.18}$$

Approximation parameters g and u were derived by using the discrete solutions defined for the span width deviation s = 0 and s = hc:

$$Fsw(s = 0) = \frac{g}{ac^u} = Fsw1 \tag{6.19}$$

$$Fsw(s = hc) = \frac{g}{(ac + hc)^u} = Fsw2 \tag{6.20}$$

Rearranging equations (6.19) and (6.20) leads to:

$$g = ac^u \cdot Fsw1$$
$$g = (ac + hc)^u \cdot Fsw2$$

Equating the above equations reveals that for the first parameter u:

$$\left(\frac{ac}{ac + hc}\right)^u = \frac{Fsw2}{Fsw1}$$
$$u = \log_{\left(\frac{ac}{ac+hc}\right)} \cdot \frac{Fsw2}{Fsw1}$$

$$u = \frac{\ln\left(\frac{Fsw2}{Fsw1}\right)}{\ln\left(\frac{ac}{ac + hc}\right)} \tag{6.21}$$

Equation (6.21) is substituted into (6.19) leading to the second parameter g as:

$$g = Fsw1 \cdot ac^u \tag{6.22}$$

6.5.3 The derivation of sidewall deformation state

(a) Span width belt- to rim attachment points.

The span width Ls is defined by the sidewall-rim connector points (xi, zi) on the rim contour and (xa, za) on the belt bar elements marked with cross symbols in Figure 6.20. The rim connector attachment points are defined by the geometry pitch angle α_t , whereas the belt connector positions are a function of the deflection element angles γi .

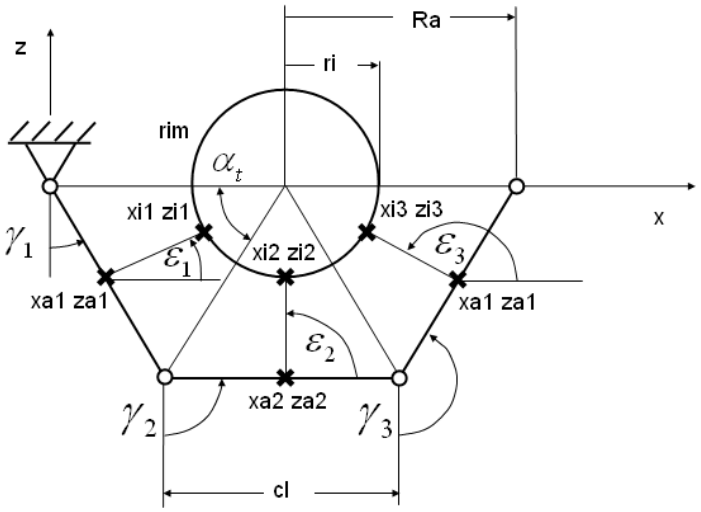

Figure 6.20: Sidewall force connector points xi, zi and xa, za on rim and belt elements

Directions of the sidewall forces Fsw are aligned along the two line points (xa, za), (xi, zi) on the belt and rim. The coordinates are derived as follows:

Rim connector points:

$$xi_{(i)} = Ra - ri \cdot \cos\left(\frac{2i-1}{2} \cdot \alpha_t\right)$$
$$zi_{(i)} = -ri \cdot \sin\left(\frac{2i-1}{2} \cdot \alpha_t\right) \qquad (6.23)$$

Belt connector points:

$$xa_{(i)} = \sum_{j=1}^{i-1} cl \cdot \sin\gamma_j + \frac{cl}{2} \cdot sin\gamma_i$$
$$za_{(i)} = -\left[\sum_{j=1}^{i-1} cl \cdot \cos\gamma_j + \frac{cl}{2} \cdot \cos\gamma_i\right] \qquad (6.24)$$

The attitude angles εi and the span width lengths 'Lsi ' can be derived with respect to the coordinates obtained using equations (6.23) and (6.24). Thus:

$$\tan \varepsilon_i = \frac{zi_i - za_i}{xi_i - xa_i}$$
$$ls_i = \sqrt{(xi_i - xa_i)^2 + (zi_i - za_i)^2} \tag{6.25}$$

b) Direction of the sidewall force

Only the in-plane (*x*-*z* plane) component Fs of the sidewall force Fsw is relevant to simulate the belt deformation as the tyre axial components (*y*-direction) cancel each other. The in-plane component is defined by the cosine of the sidewall tangent angle α shown in Figure 6.21.

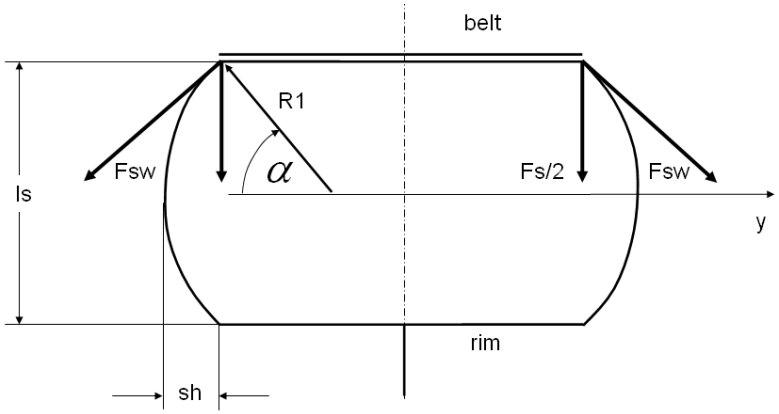

Figure 6.21: Tyre cross-section showing the sidewall tangent angle α

For 'bc' being the radian length of the membrane cross-sectional contour, direction angle α is defined by the geometric relations:

$$R1 \cdot 2\alpha = bc$$
$$R1 \cdot \sin \alpha = \frac{ls}{2}$$

Combining the above equations leads to:

$$\frac{\sin\alpha}{\alpha} = \frac{ls}{bc} \tag{6.26}$$

For discrete relations of the span widths lsi with the arc length bc, the reference angles α_i can be determined by analysis of the function derived in equation (6.26). The graph of the function f(α) = $\sin\alpha / \alpha$ is illustrated in Figure 6.22.

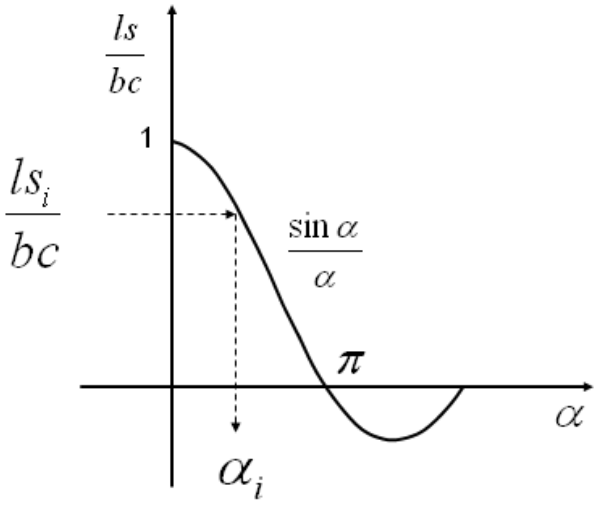

Figure 6.22: Graph for the function f(α) = $\sin\alpha / \alpha$ to determine discrete sidewall force angle

Combining equations (6.17) to (6.26), the in-plane sidewall force Fs, acting on a belt bar element in equation (6.16) can be determined.

6.6 The Mathematical concept for modeling the radial belt deformation

A common method used to analyze a static equilibrium condition for a multi-body system is to formulate the force balance for each single element. In conjunction with compatibility conditions defined by the element constraints, a linear equation set can be obtained. Solution can then be obtained using Gaussian algorithm or through matrix inversion. For a chain type structure representing the half belt modeled with a 1° elemental resolution, there are 180 equations. Adding the constraint formulations, solution for a matrix of 360 by 360 is required. To avoid this large computational burden, the principle of virtual work is used as an alternative analytical concept. As this concept delivers direct solutions for all system degrees of freedom, the need for matrix inversion becomes obsolete. The external loads Fsi and Fpi applied to the system components (chain elements) are functions of the system degrees of freedom (element angles γi) in this approach. Thus, a set of solutions found for a given instantaneous equilibrium condition needs correction of the applied external forces. This feedback loop needs to be embedded in the solver algorithm, shown in item 6.6.2. In item 6.6.1, the derivation of the virtual work equations applied to the belt chain structure is discussed.

6.6.1 Virtual work principle applied to in-plane belt deformation

The boundaries described in 6.5.1 c represent an equilibrium condition for the belt chain structure considered (Figure 6.23). A virtual deflection $\delta\gamma_j$ applied to any single element j, compatible with the element constraints, causes a virtual work applied to the system. According to the principle, this work should be zero for a system in static equilibrium state **[17]**.

$$\delta W = \sum_j \vec{F}_j \cdot \delta\vec{r}_j = 0 \tag{6.27}$$

It is noted that the principle is effectively applicable for systems only that are free of energy dissipation, which applies to the model properties outlined in item 6.5 (a). The vector $\vec{r}$ describes the local deflection of an external force application point.

(a) Virtual work derived for the first single belt element

The principle of virtual work is applied to the belt contour represented by the in-plane element angles γi for a given load Px, Pz attached to the free right belt element shown in Figure 6.23 (left).

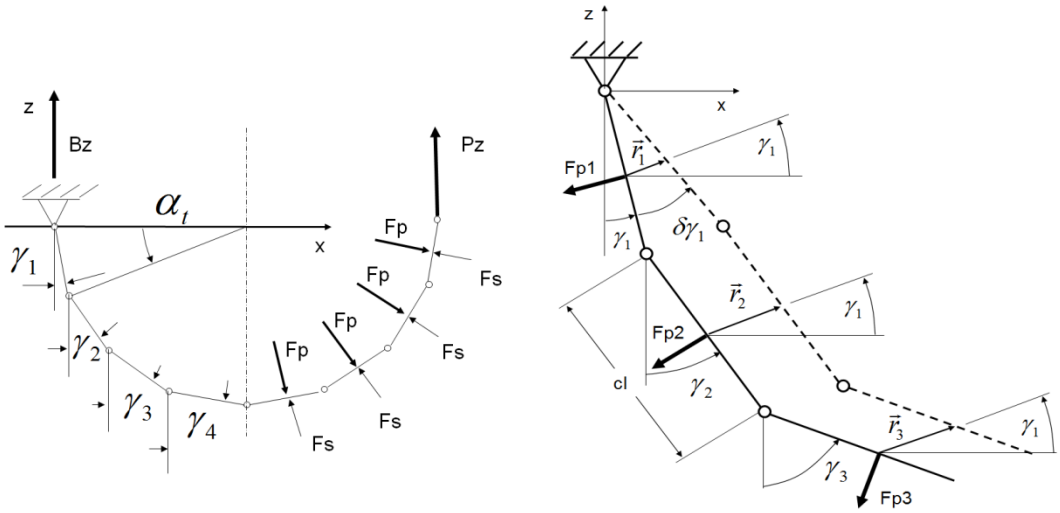

Figure 6.23: Belt structure to derive virtual work equation

A virtual deflection $\delta\gamma_1$ applied to the first degree of freedom γ_1 transfers the chain structure into the dashed shape shown in Figure 6.23 (right). All other angles γi (i = 2, n) are assumed to remain unchanged. The transfer of the force application points is defined by the vectors $\vec{r}_i$, commonly aligned by γ_1 against x- axis. The magnitude of $\vec{r}_1$ is defined by $cl/2 \cdot \delta\gamma_1$, the other deflections $\vec{r}_i,\ i = 2,n$ are of common magnitude $cl \cdot \delta\gamma_1$. With the aforementioned, the virtual work applied to the system of the 'n' elements caused by Fpi and Fsi becomes:

$$
\begin{aligned}
\delta W_1 = {} & (Fpz_1 + Fsz_1)\cdot\sin\gamma_1 \cdot \frac{cl}{2}\delta\gamma_1 + (Fpx_1 + Fsx_1)\cdot\cos\gamma_1 \cdot \frac{cl}{2}\delta\gamma_1 && first\ \ element \\
& + (Fpz_2 + Fsz_2)\cdot\sin\gamma_1 \cdot cl\delta\gamma_1 + (Fpx_2 + Fsx_2)\cdot\cos\gamma_1 \cdot cl\delta\gamma_1 && \sec ond\ \ element \\
& + (Fpz_3 + Fsz_3)\cdot\sin\gamma_1 \cdot cl\delta\gamma_1 + (Fpx_3 + Fsx_3)\cdot\cos\gamma_1 \cdot cl\delta\gamma_1 && third\ \ element \\
& + \quad ... \\
& + (Fpz_n + Fsz_n)\cdot\sin\gamma_1 \cdot cl\delta\gamma_1 + (Fpx_n + Fsx_n)\cdot\cos\gamma_1 \cdot cl\delta\gamma_1 && n'th\ \ element \\
& + Pz\cdot\sin\gamma_1 \cdot cl\delta\gamma_1 + Px\cdot\cos\gamma_1 \cdot cl\delta\gamma_1 && external\ \ force \\
= {} & 0
\end{aligned}
\qquad (6.28\text{-}1)
$$

The term that sums up the virtual work found for the second element is:

$$\begin{aligned}\delta W_2 = {} & (Fpz_2 + Fsz_2)\cdot\sin\gamma_2\cdot\frac{cl}{2}\delta\gamma_2 + (Fpx_2 + Fsx_2)\cdot\cos\gamma_2\cdot\frac{cl}{2}\delta\gamma_2 && \text{second element}\\ & + (Fpz_3 + Fsz_3)\cdot\sin\gamma_2\cdot cl\delta\gamma_2 + (Fpx_3 + Fsx_3)\cdot\cos\gamma_2\cdot cl\delta\gamma_2 && \text{third element}\\ & + (Fpz_4 + Fsz_4)\cdot\sin\gamma_2\cdot cl\delta\gamma_2 + (Fpx_4 + Fsx_4)\cdot\cos\gamma_2\cdot cl\delta\gamma_2 && \text{fourth element}\\ & + \quad ... \\ & + (Fpz_n + Fsz_n)\cdot\sin\gamma_2\cdot cl\delta\gamma_2 + (Fpx_n + Fsx_n)\cdot\cos\gamma_2\cdot cl\delta\gamma_2 && \text{n'th element}\\ & + Pz\cdot\sin\gamma_2\cdot cl\delta\gamma_2 + Px\cdot\cos\gamma_2\cdot cl\delta\gamma_2 && \text{external force}\\ = {} & 0\end{aligned} \tag{6.28-2}$$

(b) General formulation of virtual work for plane chain structures

After rearranging (6.28-1, 2), the generalized formulation for the first (*n*-1) elements can be written as:

$$i = 1,\quad n-1$$

$$\tan\gamma_i = -\frac{\frac{1}{2}\cdot(Fpx_i + Fsx_i) + \sum_{j=i+1}^{n}(Fpx_j + Fsx_j) + Px}{\frac{1}{2}\cdot(Fpz_i + Fsz_i) + \sum_{j=i+1}^{n}(Fpz_j + Fsz_j) + Pz} \tag{6.29}$$

And for the last (i.e. the *n*th) element:

$$i = n$$

$$\tan\gamma_n = -\frac{\frac{1}{2}\cdot(Fpx_n + Fsx_n) + Px}{\frac{1}{2}\cdot(Fpz_n + Fsz_n) + Pz} \tag{6.30}$$

where

$$Fpx_i = -Fp\cdot\cos\gamma_i$$

$$Fsx_i = Fs\cdot\cos\varepsilon_i$$

and

$$Fpz_i = -Fp\cdot\sin\gamma_i$$

$$Fsz_i = Fs\cdot\sin\varepsilon_i$$

Angles ε_i describe the sidewall attitudes (Fig. 6.20) derived from equations (6.23–25).

A simple example consisting of three elements subjected to pneumatic pressure as shown in Figure 6.23 is chosen to confirm the equilibrium condition for the angles defined in equations (6.29) and (6.30). Case #1 and #3 show pneumatic forces Fp, perpendicular to γi. Pneumatic force directions taken from case #1 are copied to case #2. Simple static analysis confirms that for all the three cases, the structure is in equilibrium for the external load Px and Pz attached to the free end of the chain.

Case1: Case 2: Case 3:

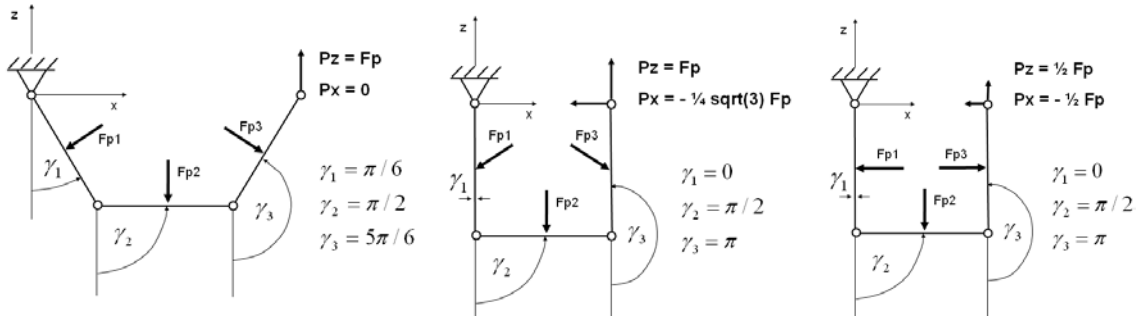

Figure 6.23: Example for three elements applied to pneumatic force Fp and the external load P

For pressure forces Fpi and the external force Px,z applied to the structure in direction and magnitude as shown in Figure 6.23, equation (6.29) is used to determine γ_1 and γ_2, and (6.30) for γ_3, confirming the results for the equilibrium angles γi.

6.6.2 Method of Iteration

The above mentioned example is used as an introduction to the iteration concept:

In an analogy to tyre structure, case #1 represents the circular polygon contour of a radial unloaded belt (Px = 0) in equilibrium. A variation of the external load vector P, such as that exhibited for case #2, results in a radial deflection (-x direction) of the belt structure for magnitude of a unit elemental length. It is noted that in case #2, although in equilibrium, the forces Fpi do not act perpendicular to the 1st and 3rd element anymore and, therefore, violate the nature of a pneumatic force. For a radial load Px = -½ Fp and the vertical load Pz = ½ Fp, applied as shown in equilibrium case #3, the orthogonality condition is fulfilled. Thus, case #3 represents a physically valid load case for the tyre model defined as a chain structure.

The aim of the iteration process is to find a static equilibrium force vector P which corresponds to a specified in-plane deformation of the tyre belt. The variation of P applied to the belt free end defines a new deformation state of the system. Thus, a specified deformation fx, fz can be achieved by a displacement controlled iteration loop applied to the components Px and Pz, using equations (6.29) and (6.30) until the specified deformation fx, fz is achieved for the free belt end with reasonable accuracy (see Figure 6.24, left).

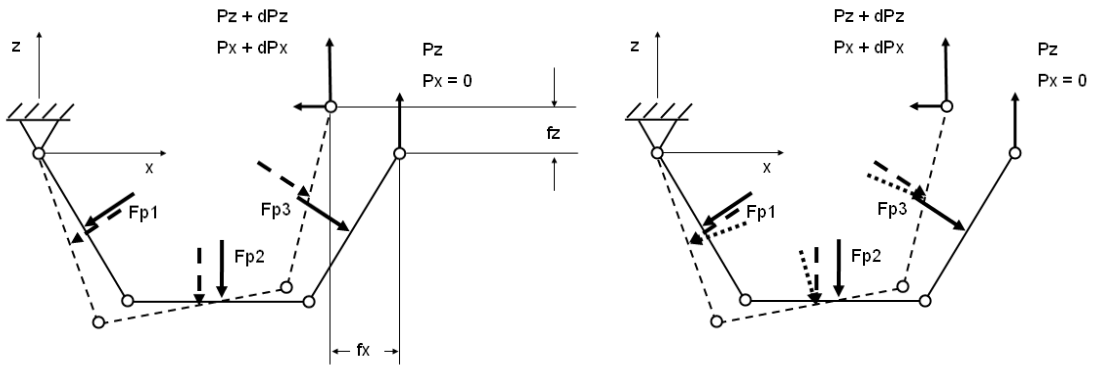

Figure 6.24: Deflections fx, fz of the tyre belt structure (left) and alignment of pneumatic force direction (right)

For the case fz being zero, the radial component Px represents the tyre contact force which induces the radial deflection fx. It is noted, that each iteration step changes all the belt elemental angles γi. Thus, the pneumatic force vectors Fpi, by definition

perpendicular to the elements, are functions of the structural degrees of freedom. Directional alignment is sought for pneumatic and sidewall forces (Fpi, Fsi) after each iteration step as indicated for the pneumatic forces in Figure 6.24 (right). The solid force is displaced to the position indicated by the dashed force vector, but remains unchanged in direction and magnitude. Subsequently, the dotted force is aligned perpendicular to the displaced element (dashed chain geometry).

(a) Definitions

The position angles of the belt elements are defined by γi , measured from the negative z-axis (see Figure 6.25). Pneumatic force directions are defined by the angles φ_i measured from the x- axis. Angles ε_i define the sidewall forces Fsi, also measured from the positive x-axis.

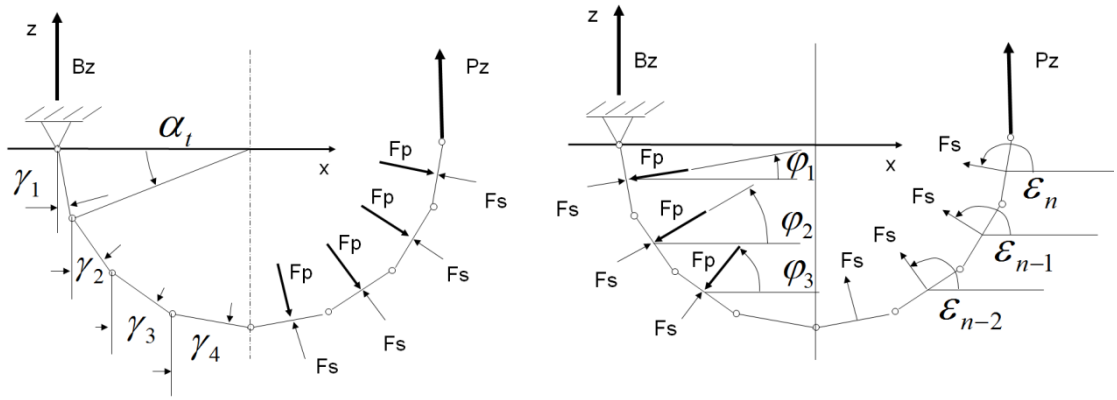

Figure 6.25: Angle definitions and x, z coordinate system

(b) Initial condition

The initial condition for the iteration process is defined by the circular contour of the belt. For this geometry the internal elemental forces (sidewall Fsi and pneumatic forces Fpi) are defined in magnitude and direction by the geometric pitch angle α_t as:

$$\gamma_i = \frac{\alpha_t}{2} + (i-1)\cdot\alpha_t = \varphi_i = \varepsilon_i \tag{6.31}$$

The initial values for the magnitudes of the sidewall forces are set by equation (6.16), the magnitude of the pneumatic pressure remains constant during the iteration.

6.6.3 Iteration subdivision

The chain contour, representing the geometry equilibrium condition of a tyre belt model is considered to remain within the fourth quadrant, defined by the x, z coordinate system defined in Figure 6.26. For the case that the force P applied to the free end extends stability limits, solutions are found also in other quadrants. In this case, the chain geometry can flip into a folded condition and the iteration concept does not converge towards a tyre belt appropriate solution.

To avoid such buckling problems, the iteration was subdivided into a number of steps.

(a) Stage 1: adjustment of initial position

To control the iteration of the external force P, the position Sx and Sz of the free belt end attached to P is analyzed after each iteration step by the elemental angle sum of γi as:

$$Sx = \sum_{i=1}^{n} cl \cdot \sin \gamma_i$$
$$Sz = \sum_{i=1}^{n} cl \cdot \cos \gamma_i \qquad (6.32)$$

where *cl* stands for the width of a chain element (Figure 6.26).

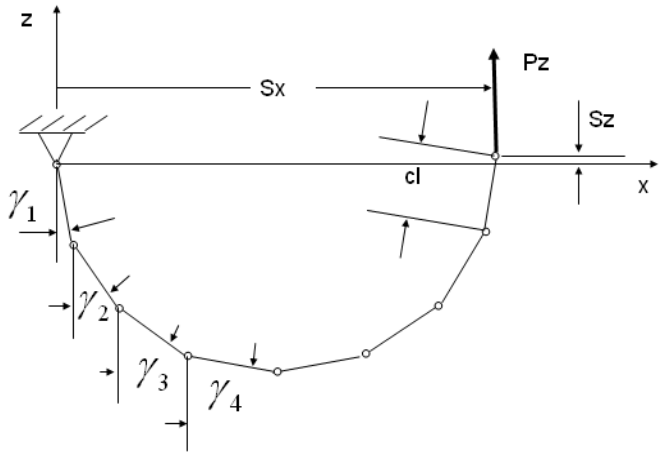

Figure 6.26: Belt free end position Sx after first iteration step

For the position vector Sx = 2Ra (wheel radius) and Sz = 0, the circular belt contour is achieved. Under this condition, Pz corresponds to the belt force Fg, derived from equation (6.7), and Px is zero. These values can preferably be set as default initial values to speed up the iteration process for P. A correction of the pneumatic and sidewall force

directions φ_i, ε_i is obsolete as they were initially set to match the ideal radial geometry by equation (6.31).

(b) Stage 2: application of specified deformation 'f'

During the second P iteration, the position vector S is modified with regard to the specified deformation fx, fz.

$$\begin{aligned} Sx &= 2Ra - fx \\ Sz &= fz \end{aligned} \tag{6.33}$$

All direction angles φ_i aligning the pneumatic forces and ε_i, the direction of sidewall forces, as well as the force magnitudes remain unchanged during the iteration for P until the specified position vector S is confirmed using equation (6.32).

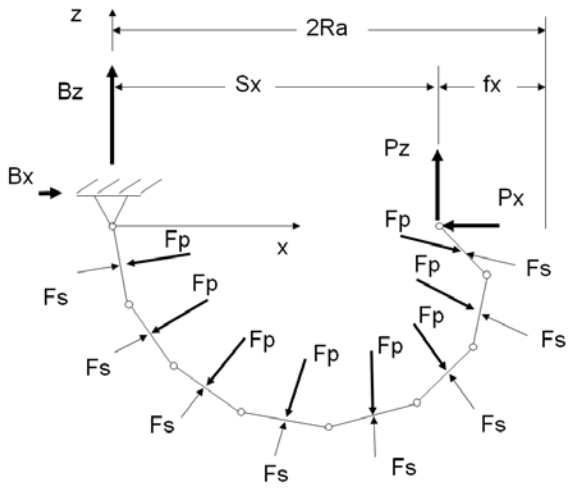

Figure 6.27: Belt free end position after second part of the iteration process

(c) Stage 3: correct the pressure force direction φ_i

As mentioned in the iteration concept, the alignment of the pneumatic force direction to achieve orthogonality with the belt bar elements is performed during the third iteration stage. The alignment of force direction angles φ_i to the elemental position angles γi is performed in ten steps:

$$\Delta\varphi_i = \gamma_i - \varphi_i$$

For ten alignment steps

$$\varphi_{i\ corr} = \varphi_i + \frac{i}{10} \cdot \Delta\varphi_i$$

As each alignment step changes the end position vector S, a subsequent correction is performed by an iteration of P to refit the specified belt deformation.

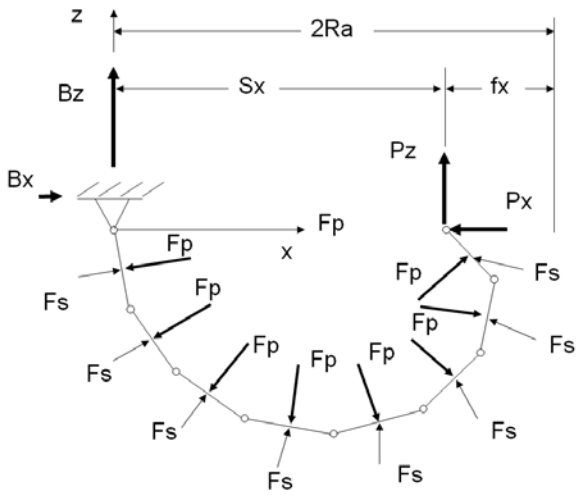

Figure 6.28: Alignment of pneumatic force Fp direction perpendicular to belt elements

(d) Stage 4: correct sidewall force direction ε_i

In an analogy to stage 3, the alignment of the sidewall force directions to match with the rim connecting points is performed in ten steps. Equations (6.29), (6.30) and (6.31) are used to calculate the sidewall force angles ε_i:

$$\Delta\varepsilon_i = \gamma_i - \varepsilon_i$$

For ten alignment steps

$$\varepsilon_{i\ corr} = \varepsilon_i + \frac{i}{10} \cdot \Delta\varepsilon_i$$

It is noted that a simultaneous alignment of the pneumatic force directions is continued during the iterative process for the sidewall forces in the stage 4.

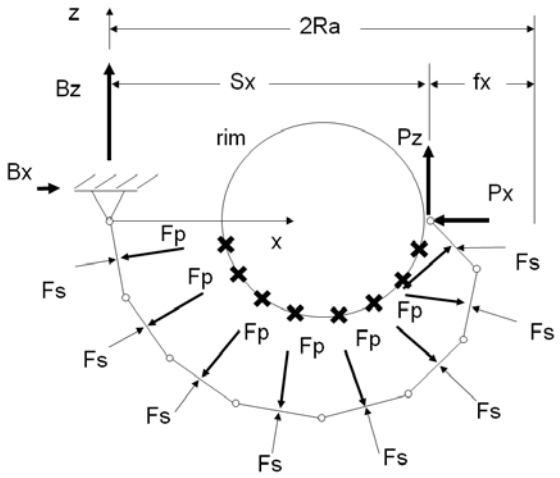

Figure 6.29: Alignment of sidewall forces Fs directions with rim connecting points

(e) Stage 5: correct sidewall force magnitude Fs

The deformed belt geometry results in a span width deviation 's' of the sidewall membrane between an element and its rim connection point. Thus, the sidewall force magnitude (see **6.5.2**) needs to be adopted. The reduced sidewall force magnitude is indicated in Figure 6.30 at the right hand side of the belt structure. Correction is performed in 10 steps analogous to the stages 3 and 4 of the iteration process. As in stage 4, the correction of pneumatic and sidewall force directions continues simultaneously with the correction of the sidewall force magnitude.

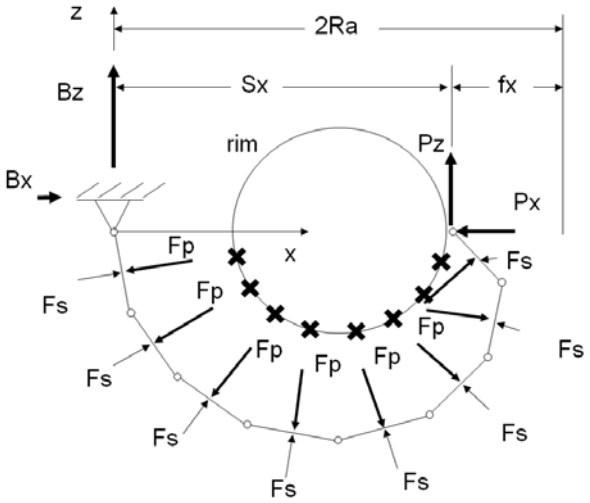

Figure 6.30: Complete alignment of pneumatic- and sidewall forces

6.6.4 Numerical results for iteration stages 1 to 5

Figure 6.31 provides a visual impression to demonstrate the impact of the individual iteration parts on the belt contour shape of tyre size 205/55-R16, with 2 bar pneumatic pressure. The red contour trace represents the final shape after each iteration stage. Px and Pz are the equilibrium forces at the right-sided belt free end. The final contour is shown in Figure 6.31 down right.

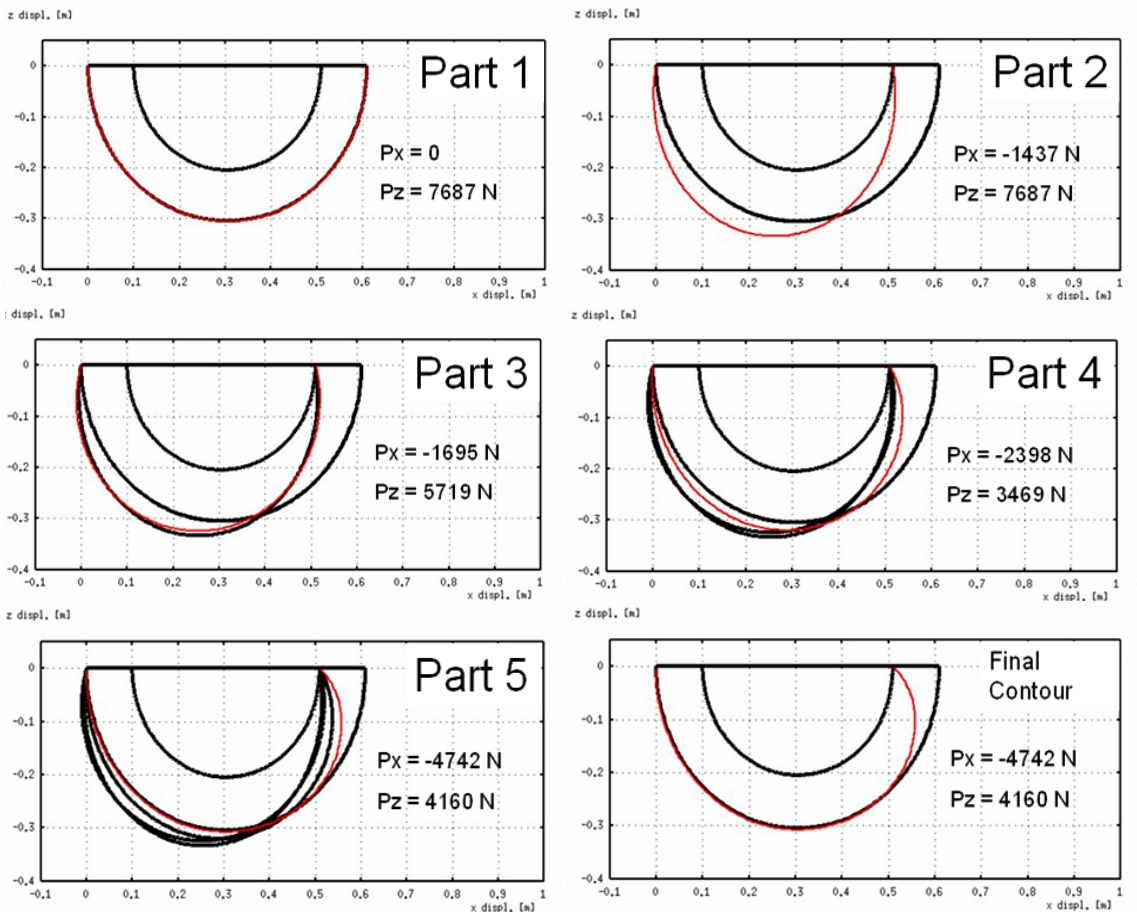

Figure 6.31: Final belt contour after iterations stages 1 to 5

Part 1 of the iteration is intended to adjust the belt contour in its initial position Sx = 2Ra and Sz = 0 at the chain end. The belt shape reveals a perfect circular contour as would be expected for purely tangential loading Pz. The radial force at the right sided chain free end Px is zero, Pz represents the circumferential belt force of the unloaded tyre.

After a deflection in the negative x-direction to the rim contact position (part 2) the belt contour becomes symmetrical with respect to the z- axis as the pneumatic and sidewall

forces remain constant in magnitude and direction. Thus, the vertical force magnitude Pz remains unchanged.

The symmetrical state is maintained with perpendicular alignment of the pneumatic forces against the belt contour, performed in part 3, which affects both the radial and vertical forces. With the alignment of the sidewall force directions in part 4, the belt contour reveals a non-symmetric shape. This action causes a significant increase in the radial force magnitude.

Finally, an adjustment of the sidewall force magnitudes reveals the final belt contour. It is noted that the radial force almost doubles in magnitude during the last iteration step. A final contour plot displays the belt shape, being close to a circular contour until it deviates in the last quarter towards its free end.

Figure 6.32 illustrates the shape history recorded for 15 mm deformation steps of radial deformation.

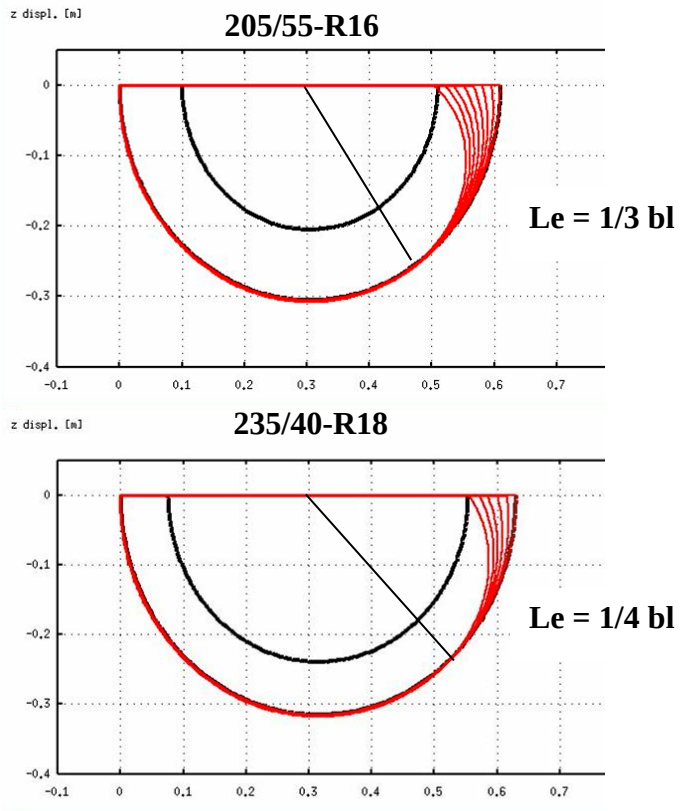

Figure 6.32: Belt deflection traces against edge type radial deformation

A visual analysis indicates the belt length Le affected by the radial deformation to be approximately 1/3 and 1/4 of the total belt lengths 'bl' respectively. This corresponds to 0,67m for the 205/55-R16 and 0,5m for the 235/40-R18 sized tyres. The comparison to the effective length calculated on the basis of equation (4.12) shows 0,25m (205/55-R16) and 0,35m (235/40-R18) respectively. These results reveal an underestimation for Le with the assumptions made for the simple edge contact model approach in section 6.2.

6.6.5 The chain model applied to edge and flat tyre patch contact geometries

The belt deformation profile is related to the geometry of the penetrating body. External forces P that act as a contact line on a single element as indicated in Figure 6.10, are considered to be an edge-type contact. As long as the penetrating structure deviates from the tyre curvature, the initial plane deformation would always start from a contact line.

For a blade-type structure deforming the tyre, the contact line remains valid for the full deformation range to the rim contact as shown for the upper half belt in Figure 6.33 (left).

In the case of a flat contact geometry (plate), the belt element at the free end is limited in deformation when it forms a planar contact with the penetrating body as shown for the lower half belt in Figure 6.33 (left).

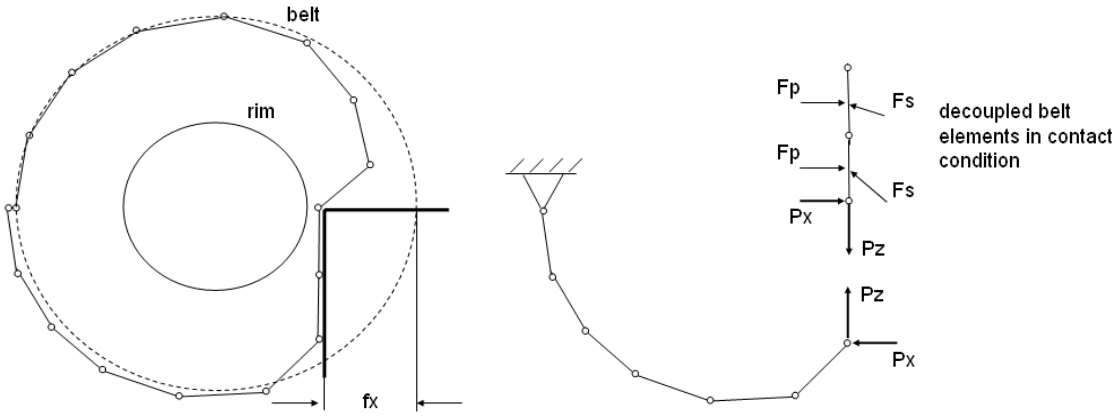

Figure 6.33: Flat and edge type tyre patch contact

To analyze the lower half belt, the elements in flat contact with the penetrating structure can be decoupled and handled separately from the iteration process as shown in Figure 6.33, right-hand side. Superposition of both the structure parts finally reveals the contact

force by combining the free belt elements with the decoupled elements in a planar contact.

As only a half the tyre belt structure is considered, two independent iterations need to be performed for a combined, edge and flat type contact, to simulate the belt deformation caused by a kerb stone impact as indicated in Figure 6.33.

6.7 Numerical results

The results listed in section 6.6.4 were performed on the basis of the tyre size 205/55-R16 with a 2 bar inflation pressure against an edge-type radial deformation. The analysis was performed for 180 elements, resulting in a one degree resolution for the half belt contour. In the following sections, numerical force response results for the simple model (equations (6.8) and (6.14)) as well as the chain model discussed in items 6.5 and 6.6 are presented for flat and edge contact exemplarily for two tyre sizes 205/55-R16 and 235/40-R18.

6.7.1- Numerical results for simple model force response

The numerical results for the simple model force response against a flat (equation (6.8)) and an edge-type contact (equation (6.14)) are shown in Figure 6.34.

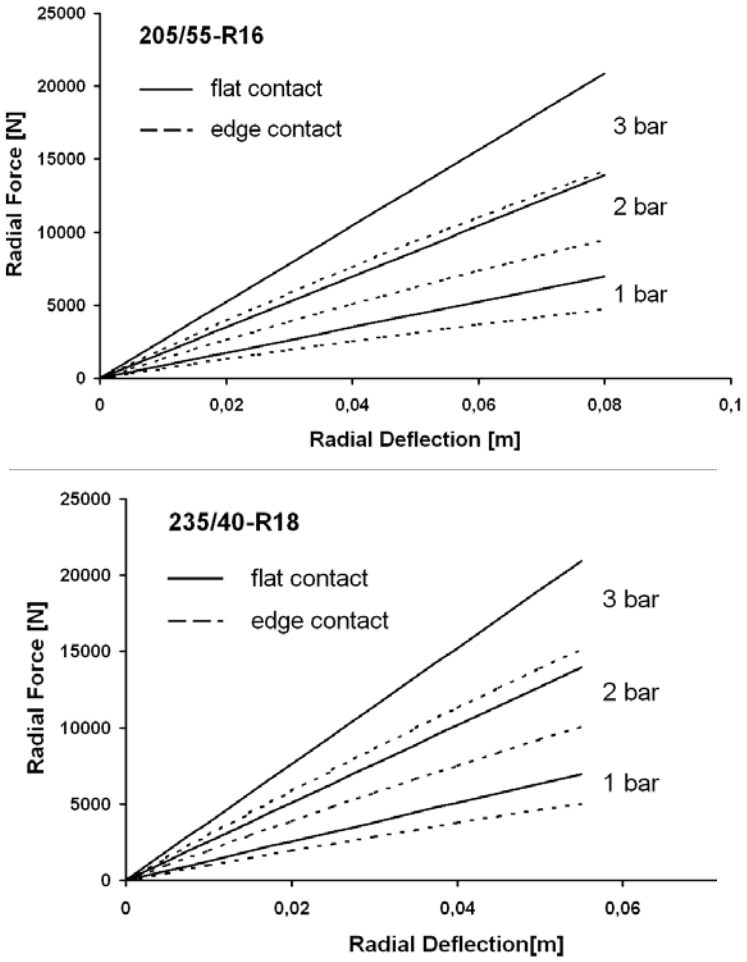

Figure 6.34: Numerical results for simple model flat and edge contact force response

The force response magnitude, gained from the flat contact exceeds the edge-type force level. This is expected as the deformed tyre volume, caused by the flat contact deformation is necessarily larger compared with the edge deformation. In contrast to the linear flat contact force traces, the edge contact results show a slight regression.

6.7.2- Numerical results for chain model force response against edge contact

An overview of force – deflection traces calculated for the two sizes of tyre; 205/55-R16 and 235/40-R18 analyzed for 1, 2 and 3 bar inflation pressures are shown in Figure 6.35. For both tyre sizes, deflections are obtained up to the rim contact condition. As only the half belt was analyzed, the radial reaction force Px was corrected by a factor of two to represent the wheel force level.

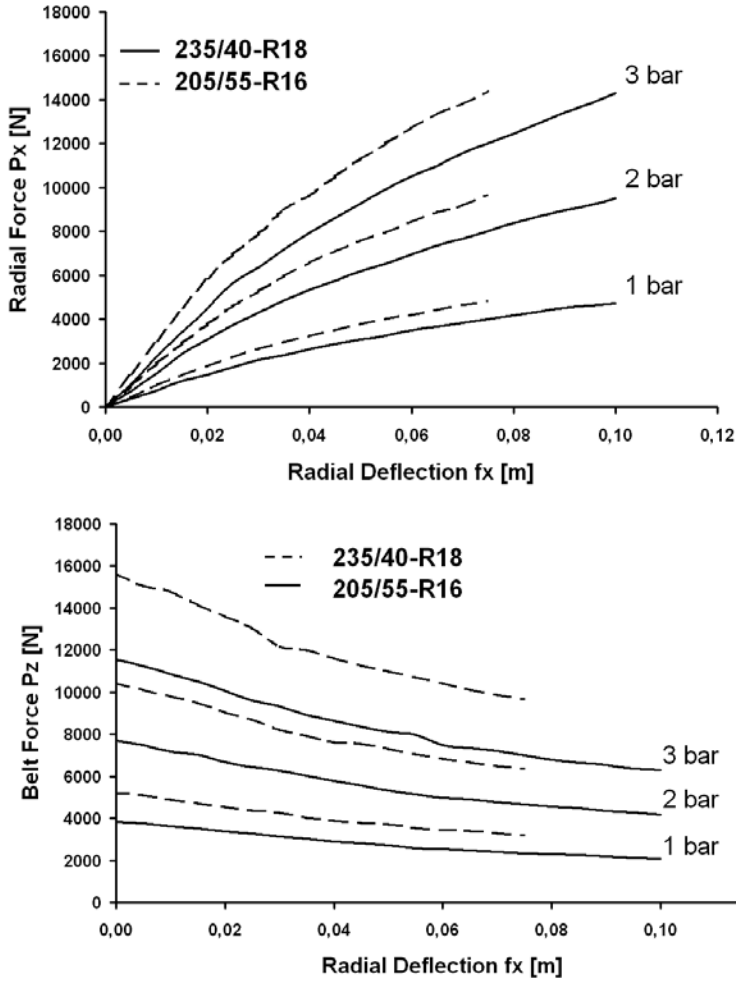

Figure 6.35: Chain model results for Radial Force Px and Belt Force Pz over radial deflection against an edge-type contact

The traces calculated for the radial force Px have a regressive characteristic, typical of edge-type deformation and are confirmed by experimental data shown in chapter 7. A decrease in the belt force magnitude Pz with an increasing deformation confirms the assumption made for the simple edge-type contact model discussed in section 6.4.3 b.

6.7.3- Assessment of simple and chain edge-type contact model force responses

A direct assessment of the results obtained from simple full analytical approach and the chain model iteration is shown in Figure 6.36. For both tyre sizes, a regression trace characteristic is visible, but it is more pronounced with the chain model.

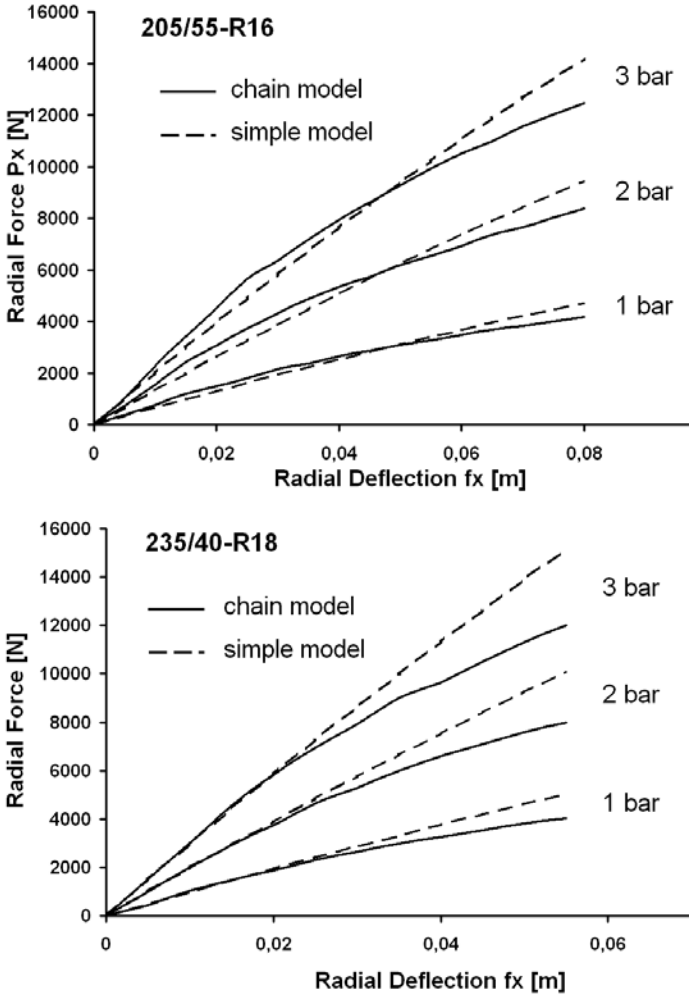

Figure 6.36: Edge force response assessment for simple- and chain model

6.8 Closure

In this chapter, an in plane static tyre model was derived based on internal stress analysis derived from membrane theory. Simple analytical models were developed to predict the force response against radial belt deformation in contact to a blade type edge- and a flat geometry to represent a kerb stone and flat ground. Beside the pneumatic pressure, the model parameters are condensed to four geometry parameters taken from the tyre cross section. The simple models are based on assumptions made for the belt deformation mode.

A more detailed model, where the belt is subdivided into a chain like structure of single bar elements attached to sidewall ropes, was set up for the edge type contact to confirm the assumptions made for the simple model. Virtual work principle in conjunction with a force iteration process was used to derive solutions in static equilibrium to external applied radial loads. The model was used to analyze the sidewall impact on belt deformation contour; radial force response was assessed to results gained from simple model.

Chapter 7: Model Validation

7.0 Introduction

The numerical results are verified by experimental measurements. The measurements were obtained at both component level, as well as system level (full vehicle test drive over kerb). All the test work was initiated and guided by the author in conjunction with the test facilities in FoE, namely the structural testing and crash test laboratories. For those components, which were considered as being particularly relevant for the vertical force response addressed in chapter 4, force response data was recorded as function of deformation (static tyre test) and deformation velocity (dynamic bumper test).

7.1 Static tyre Test

Force response trace records were obtained under quasi-static conditions, as the tyre simulation model concept does not include any structural inertial effects. The radial deformation was performed for a flat and edge-type geometries (plate and blade tests) as shown in Figure 7.1. The traces were recorded for two tyre sizes; 205/55-R16 and 235/40-R18. In contrast to force response against a plate (flat geometry representing a rigid even ground) widely documented in the literature (e.g. **[21]**, **[26]**, **[33]**, **[36])**, data representing an edge-type contact is not so common. The blade geometry shown in Figure 7.1 was chosen to represent contact with an edge-type obstacle such as a kerb stone.

Figure 7.1: Plate and blade geometry force response test set up

Tests were conducted for three nominal pneumatic pressure levels; 1, 2 and 3 bars. Nominal pressure was applied as initial condition at circular belt contour in the absence of any external load. The pressure level was monitored during the entire deformation range, commencing with a circular belt contour and up to the belt-to-rim contact. A further test with an open valve was used to measure the pure structural component of the force response.

7.1.1 Assessment to measurements

The measured force response traces, shown in Figure 7.3 were obtained from the plate deformation (flat ground). They reveal the typical progressive shape in contrast to the regressive characteristics seen against the blade penetration (edge-type contact).

The pneumatic pressure level is related to the tyre volume deviation ratio. It depends on the gas volume ratio of the unloaded tyre (circular belt contour) and the volume in the deformed state. It is obvious that this ratio is linked to the tyre cross-section and the geometry of the penetrating body.

The largest increase in the pneumatic pressure was found to be for the 205/55R16 during deformation against a plate as shown in Figure 7.2. Its deviation remained within 10 % of the nominal pressure level.

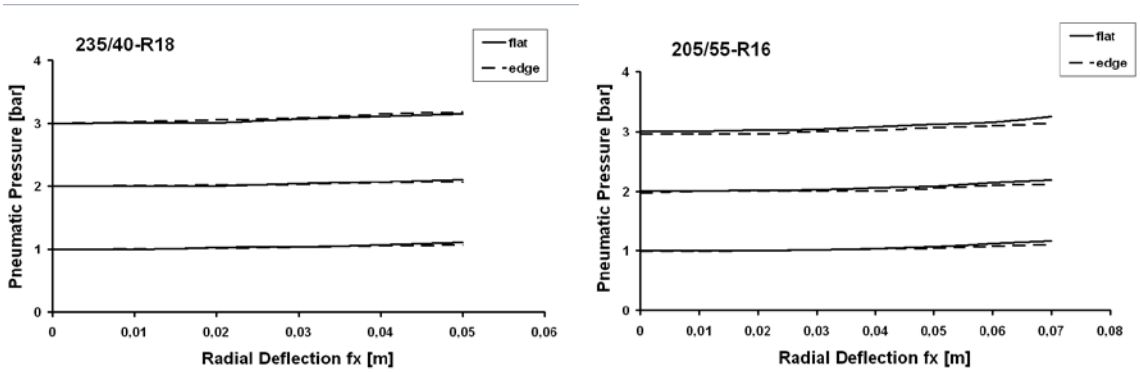

Figure 7.2: Pneumatic pressure over radial deflection against plate

The graphs in Figure 7.3 show the total force response recorded and compared with those predicted numerically. These are for blade contact deformation performed for the tyre sizes 235/40-R18 and 205/55-R16

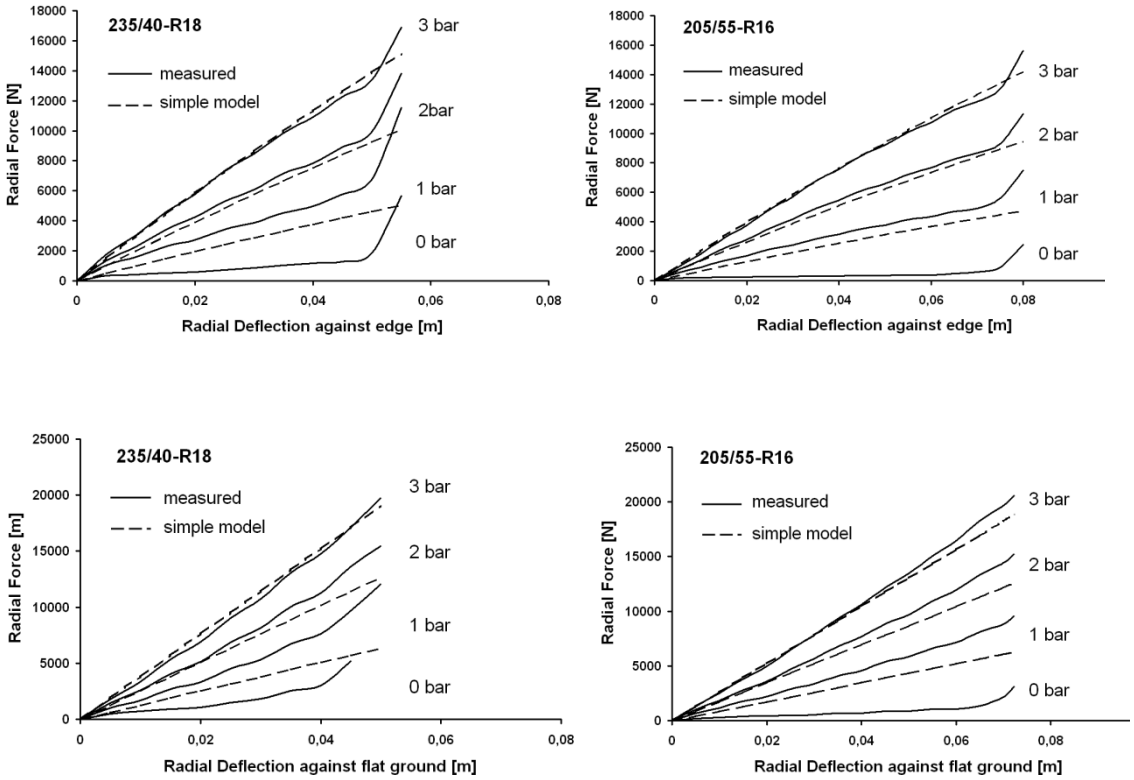

Figure 7.3: Measured edge- and flat contact force response compared with simple model results

The recordings are compared with the simple model approach (Figure 7.3) and to the chain model, virtual work approach (Figure 7.4).

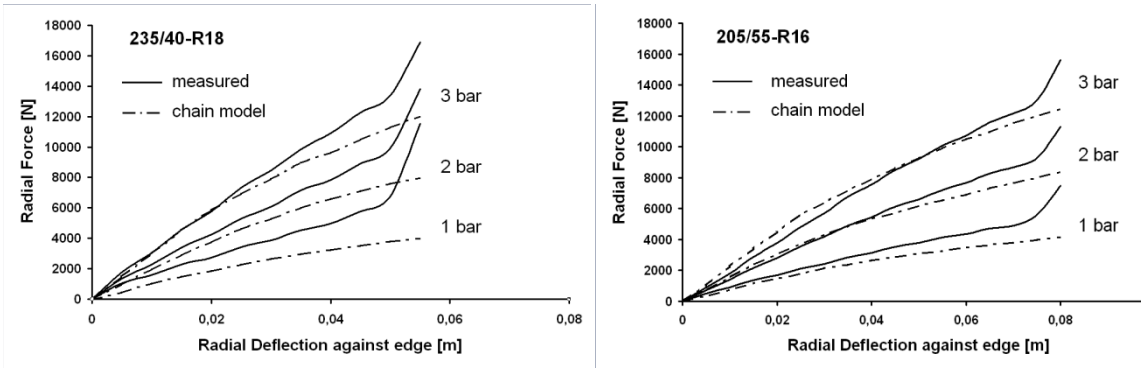

Figure 7.4: Measured edge contact force response compared with chain model results

7.1.2 Conclusion

Although the simple analytical model, proposed in section 6.2, is intended to cover the pneumatic force component only, the comparison with the experimental data which also includes the structural force deformation component still shows good correlation. Simulation results found for the chain model seem to over-estimate the regressive character of the force response trace.

7.2 Dynamic Bumper Test

As explained in chapter 5, the bumper visco-elastic behaviour and hysteresis is considered to be of significant effect for the vertical load level. Therefore, dynamic testing was applied to take into account these properties in the force response map. In contrast to NVH related measurements that cover a wide frequency range **[52]**, **[53]**, the bumper map data was obtained from harmonic displacement actuation, performed for a single frequency only, this being the drive over kerb relevant frequency of 10 Hz. Whereas NVH data do not necessarily cover the full component deflection range, this feature is required for the bumper actuation to be relevant for the drive over kerb impact simulation.

A sinusoidal actuation of amplitude 60 mm at 10 Hz frequency with a maximum force level of 40kN, as required to fulfill the CD340 bumper boundary conditions, in general exceeds the limits of conventional hydraulic equipment used in the OEM's. To overcome this shortfall, a mechanical crank actuation concept was designed as shown in Figure 7.5.

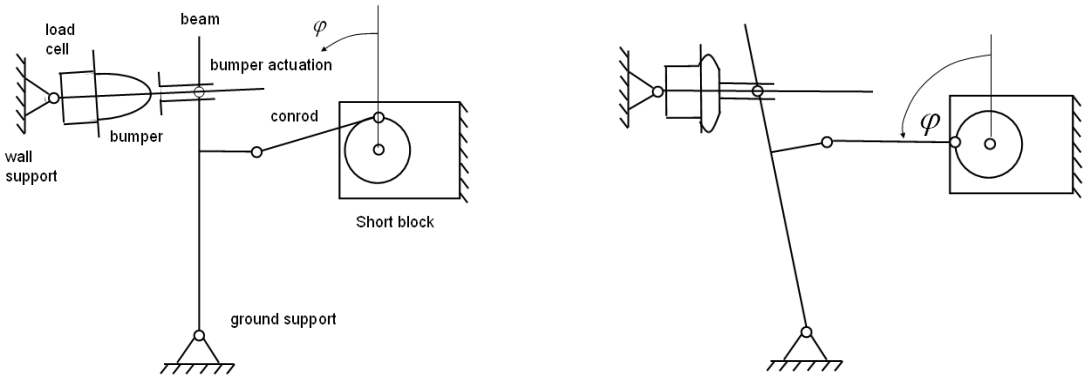

Figure 7.5: Concept of bumper test rig kinematics (left) and in compression mode for $\varphi = \pi / 2$

A short block taken from a 2l combustion engine was linked via the engine connecting rod to a vertical beam. The beam is supported to the ground by a revolute joint. The crankshaft of the short block is driven y an eddy current dynamometer at a constant speed of 600 rpm in order to cause an in-plane rotational oscillation of the beam around the ground support joint at 10 Hz. The beam is linked to the bumper element by a bumper actuation mechanism that transfers the rotational beam motion into a translational bumper actuation without violating the beam kinematic constraints.

The force response is measured by a load cell mounted on the wall support. The vertical wall support position and the bumper actuation mechanism on the beam are of adjustable height to allow positioning for various deformation amplitudes applied to the bumper. The lateral bumper position is set for a bumper engagement during the first half of the harmonic period only (compression phase). The system initial condition is defined for the beam vertical position in contact with the bumper at crank angle $\varphi = 0$. This adjustment leads to a bumper contact at the maximum actuation velocity, desired to simulate a kerb strike impact. For a counter clockwise crank rotation, the jounce bumper becomes compressed as shown in Figure 5.5 for the crank position $\varphi = \pi / 2$.

The bumper is in compression mode for crank angles $\varphi = 0$ and π, it loses contact in between $\varphi = \pi$ and 2π. An illustration of the bumper rig is shown in Figure 7.6.

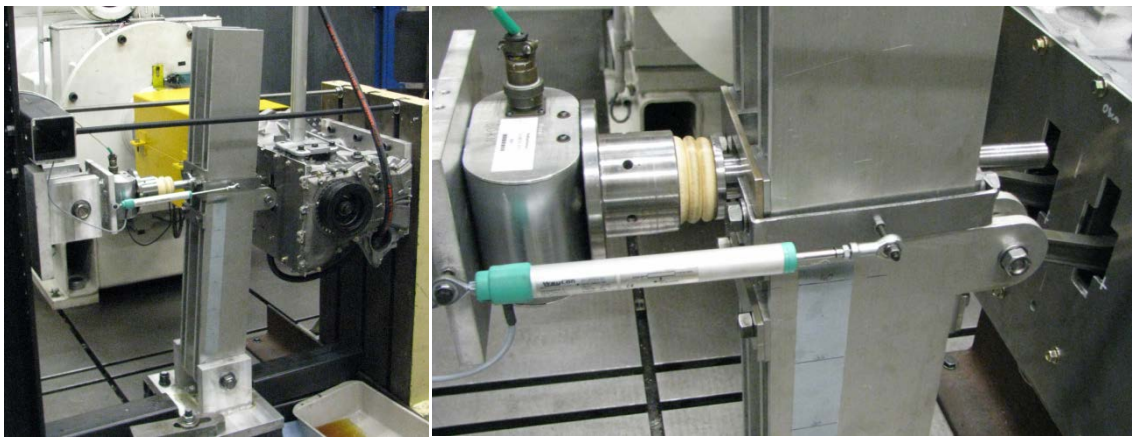

Figure 7.6: Bumper test rig

It is noted that the beam displacement is not of a pure harmonic characteristic as the analysis of the exact crank kinematics reveals components of second order that cause a deviation from pure sinusoidal motion **[14]**.

However, the trace of the displacement over time shown in Figure 7.7 demonstrates a quasi-harmonic character. It is considered, that the deviation from an exact sinusoidal actuation remains small and is of minor consequence for the purpose of the force response map.

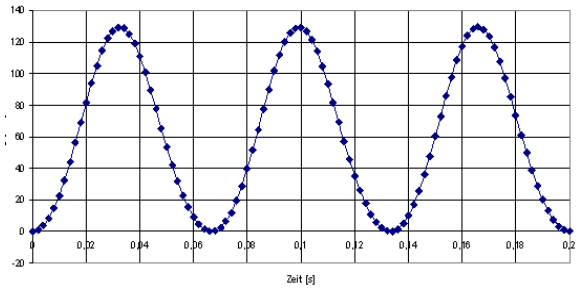

Figure 7.7: Displacement for jounce bumper actuation over time

The rig was used to generate a set of force response curves recorded from sinusoidal actuation with the relevant frequency for a set of amplitudes (S1 to S7) as described in section 5.2. These amplitudes account for the range of operational compression range as shown in Figure 7.8.

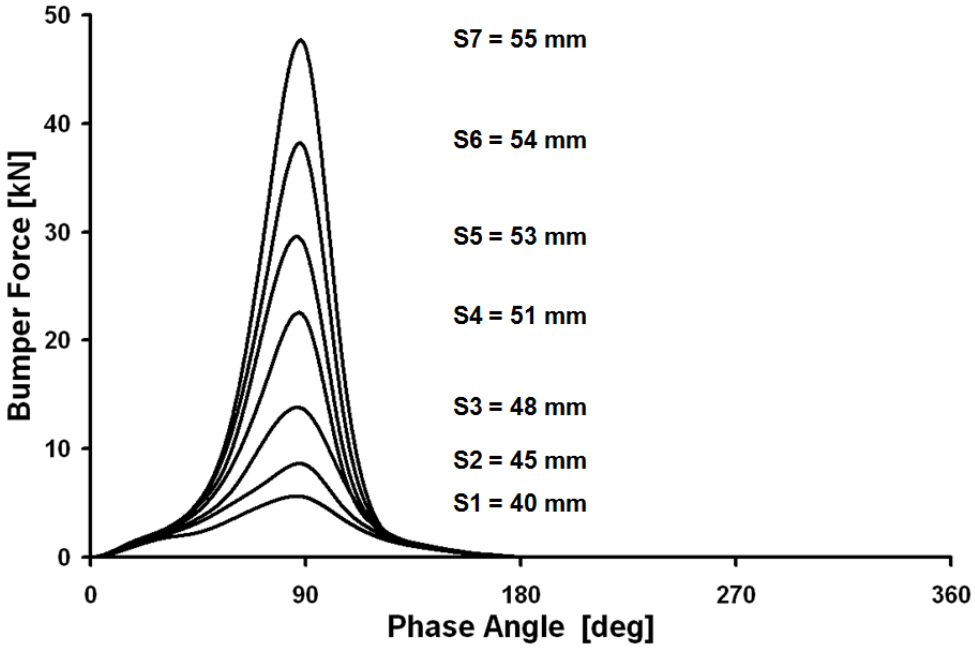

Figure 7.8: Bumper force response after sinusoidal displacement actuation

7.2.1 Map validation concept

As already mentioned, the force response map is generated on the basis of harmonic actuation. A kerb strike event cannot be considered to cause a sinusoidal actuation to the bumper in compression mode. To validate the concept's functionality, the simulation must provide reasonable force responses also for any arbitrary actuation that would deviate from harmonic motion. Although the drive over kerb test is intended to be repeatable with regard to its boundary condition, a direct measurement of the bumper forces in a full vehicle test remains difficult. A simple alternative is a drop test **[54]**, **[55]**.

7.2.2 Drop test

A drop test, as indicated in Figure 7.9, consists of a single mass, rested at a specified vertical height above the bumper element. The mass is released freely under the influence of gravity, falling down guided by rods and causes an applied impulse onto the bumper. The rig can be considered to be free of significant damping. The force response is measured over time by using a load cell installed beneath the bumper.

The drop test rig and a table of test parameters are shown in Figure 7.9.

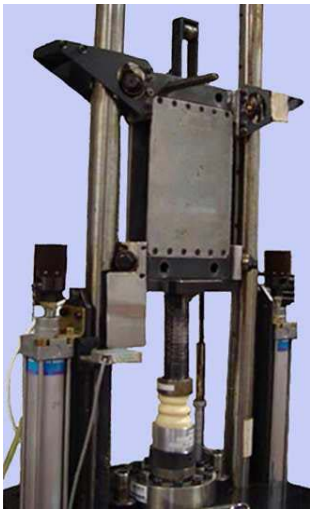

Impact velocity (m/s)	Fall height (mm)	Kinetic energy (J)	Fall weight (kg)
2.9	428	286	68
2.9	429	189	45
2.9	425	96	23

Figure 7.9: Drop test rig and test table. Source **[55]**

Such a test causes a harmonic state of motion for the special case of a linear spring characteristics only **[63]**. As the bumper element behaves in a non-linear manner, the

displacement gained from a drop test is accordingly non-harmonic. Thus, the drop test concept fulfills the requirement of a non-harmonic motion.

For the validation of the proposed map concept, a numerical drop test simulation model (single mass subjected to gravity) was set up and combined with a map force response subroutine, described in chapter 5. The simulation results were compared with the force response measured traces from the physical tests published in **[55]**. Simulation and measured data were gained for three energy levels, 96, 189 and 286 Joules, corresponding to a fall height of 0.43 m yielding a 2.9 m/s impact velocity.

7.2.3 Simulation results

Force response measurements from sinusoidal actuations were generated on the bumper test rig shown in Figure 7.6. The recorded data was post-processed and transformed into the standardised map format as discussed in section 5.3. To obtain a visual impression of the drop simulation results, the blue drop force response trace is shown in a 3D chart (Figure 7.10) in conjunction with the red force traces recorded from sinusoidal actuation.

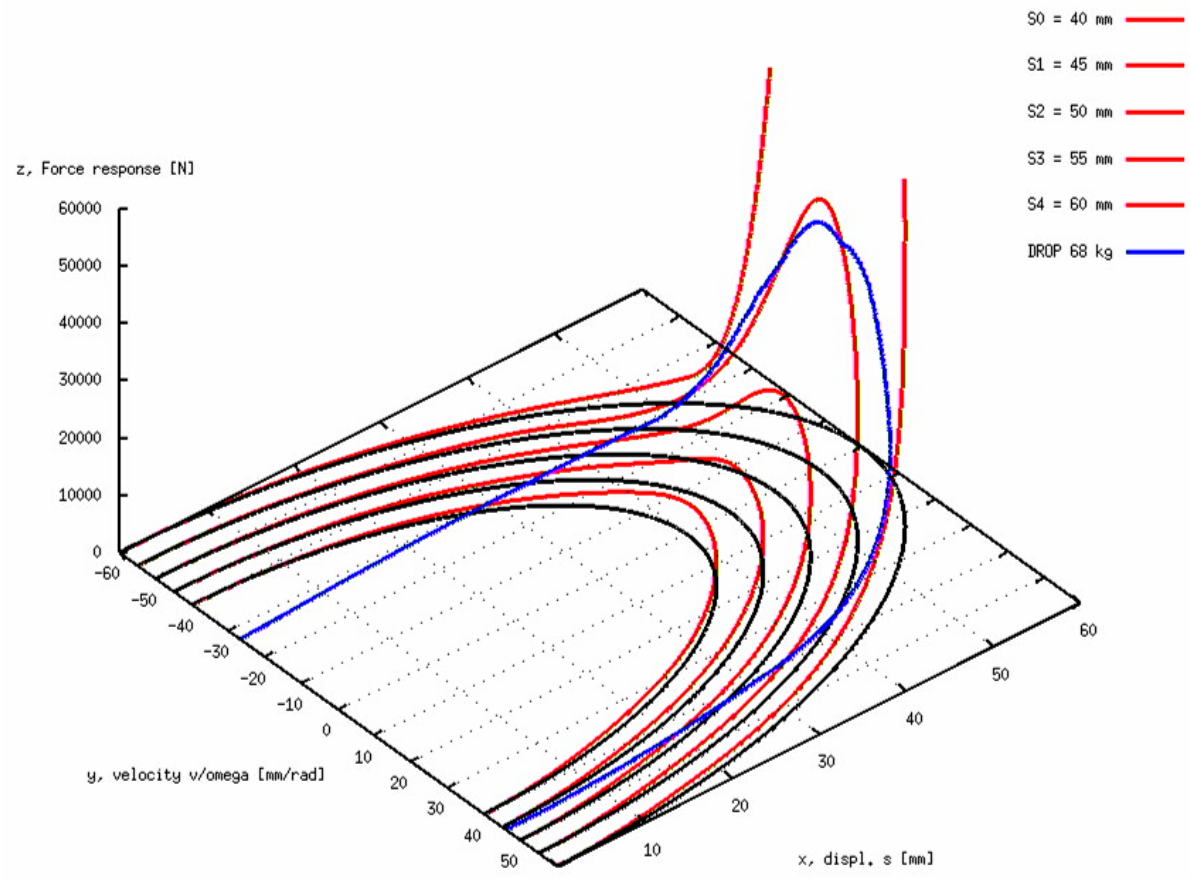

Figure 7.10: Drop test force response trace simulation result (blue) for 286 J (68 kg)

A vertical projection of the force response trace down to the x- y- plane (Figure 7.11) proves the deviation of the drop motion in bumper contact (blue trace) from the harmonic motion of the map input force traces (red).

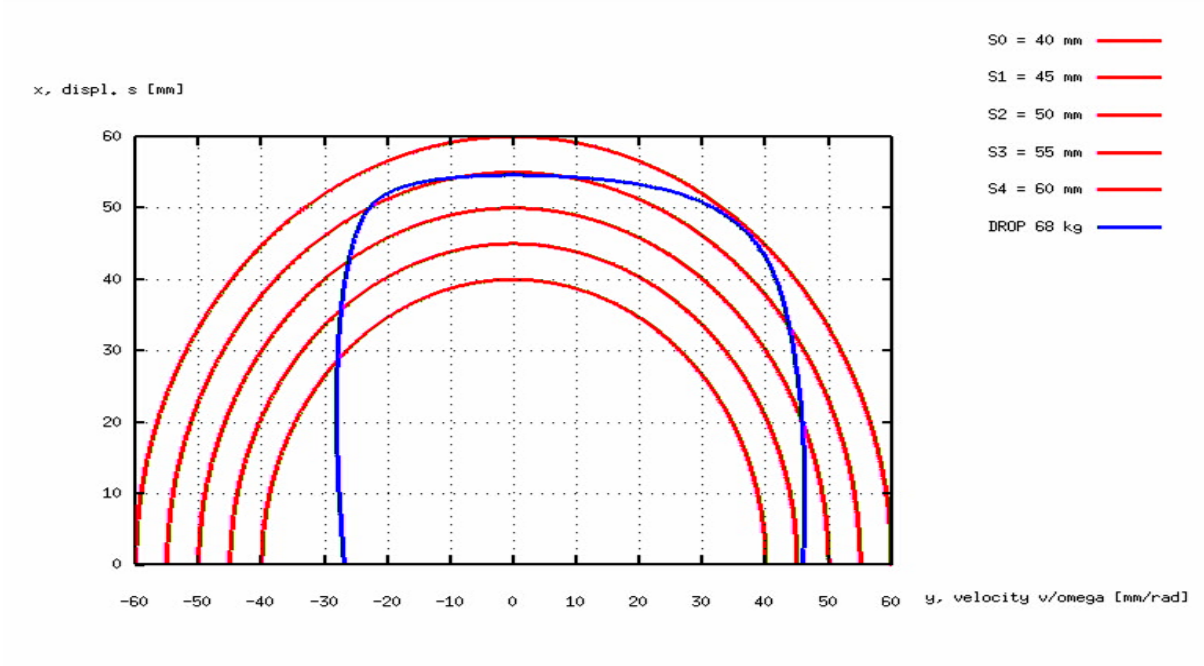

Figure 7.11: Drop motion trace simulation result for 286 J (68 kg drop test) during jounce bumper contact

The simulation results are compared with the physical measurements taken from **[55]**. Figure 7.12 demonstrates good correlation found for hysteresis loop shape and the peak force magnitudes.

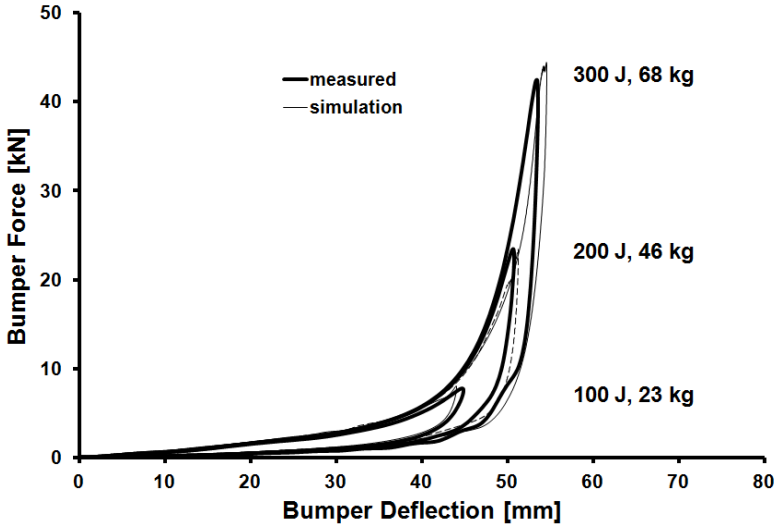

Figure 7.12: Assessment of force simulation (light) and measured drop test forces (bold)

To demonstrate the improvements of the map concept methodology, a drop test simulation was performed on the basis of a non-linear bumper force response curve, taken from a quasi-static jounce trace. As no damping was considered in the drop test simulation for the non-linear spring characteristics, the force response trace, shown in Figure 7.13, does not reveal any hysteresis. Contrary to the peak load of about 40 kN being close to the measured value, the conventional non-linear model predicts about 60 kN for the 300 joule drop test simulation.

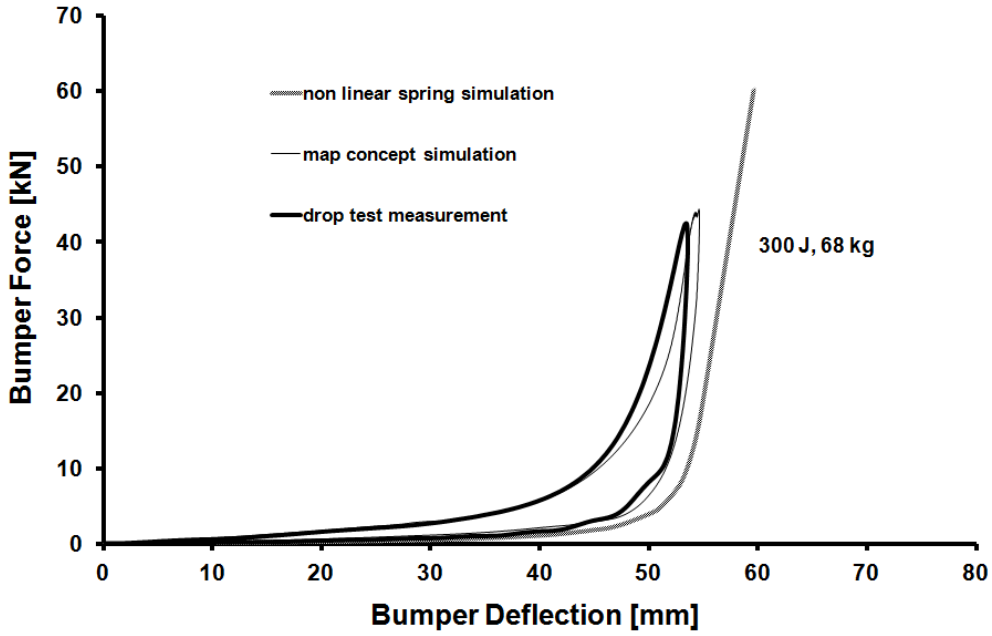

Figure 7.13: Drop test assessment for un-damped non linear spring, map concept and physical test

7.2.4 Conclusions

Based on the assessment of numerical predictions made here, it can be concluded that for the case of the polyurethane jounce bumper investigated, the assumption could be confirmed that the map concept is applicable for the purpose of simulation of the bumper force response gained from arbitrary shape of impulsive motion with reasonable accuracy.

7.3 Full vehicle Test

A drive over kerb test as described in the introduction was performed for a CD340 (FORD Galaxy). Two speed levels; 25 and 40 km/h were tested for a kerb strike event, crossing a beam of rectangular cross-section adjusted to 135 mm height shown in Figure 7.14. The crossing was performed in the direction normal to the beam with the intention of a simultaneous strike for both wheels. The vehicle crosses the bar in a free rolling mode, with no braking or acceleration.

Figure 7.14: Drive over kerb test set up

The vehicle was equipped with tyres of size 235/40-R18, adjusted to a pneumatic pressure of 2 bar. The vehicle was loaded according to the FORD specification standards determined for passenger cars.

7.3.1 Instrumentation

To record the vertical suspension force, a load cell was installed at the top mount position. As the top mount consolidates the load path of the road spring, damper and the bumper, the recording reveals an integral signal of all the three resistive components and, therefore, represents the total vertical suspension force.

A string potentiometer was attached to the spring plate and grounded at the body structure to measure the vertical wheel displacement relative to the vehicle body. An overview of the sensor and load cell application is shown in Figure 7.15.

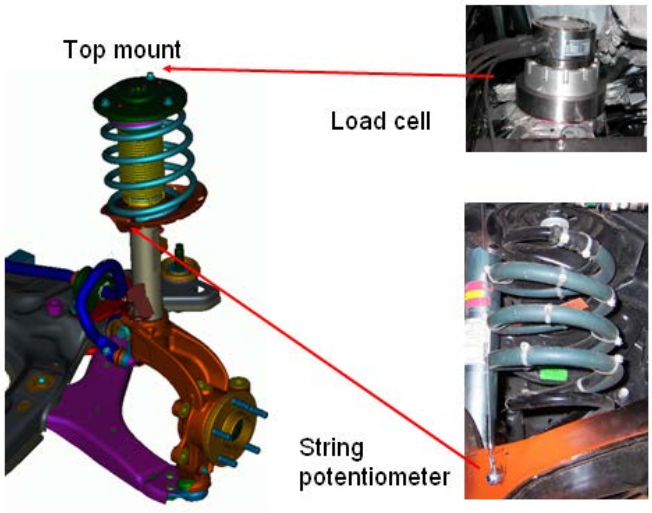

Figure 7.15: Load cell and string potentiometer instrumentation

7.3.2 Assessment of simulation and measured results

The assessment is based on the measured force over time traces gained for the top mount force and the vertical wheel displacements compared with simulation results. Simulation results are obtained by implementation of equations 4.1, 4.9-4.11, 4.16-4.20 and 4.22 (vehicle), 5.1, 5.3, 5.5-5-6 (jounce bumper) and 6.12a, 6.14 (tyre). The model input parameters are shown in table 8.1 on page 186.

7.3.2.1 Top mount force

A comparison of the recorded vertical suspension top mount force time history (signal) with the predictive simulation results is shown in Figure 7.16:

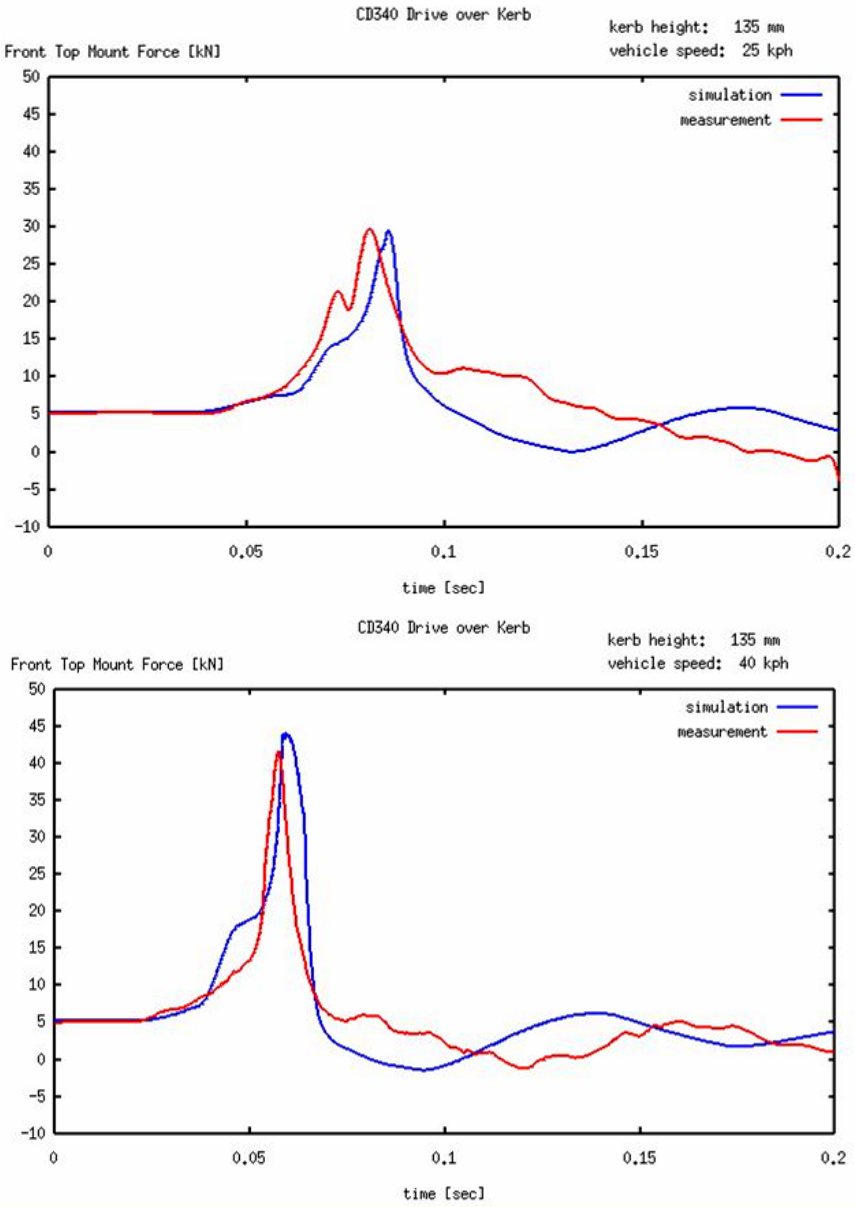

Figure 7.16: Top mount force and vertical wheel centre deflection over time for drive over kerb test

The results show good correlation for the vertical suspension force level, whereas the shape of the signal does not match the characteristic of the measured trace. The simulation reveals that the bumper force component has a larger magnitude in the load path compared to that of the spring, damper and bumper vertical suspension force as shown in Figure 7.17.

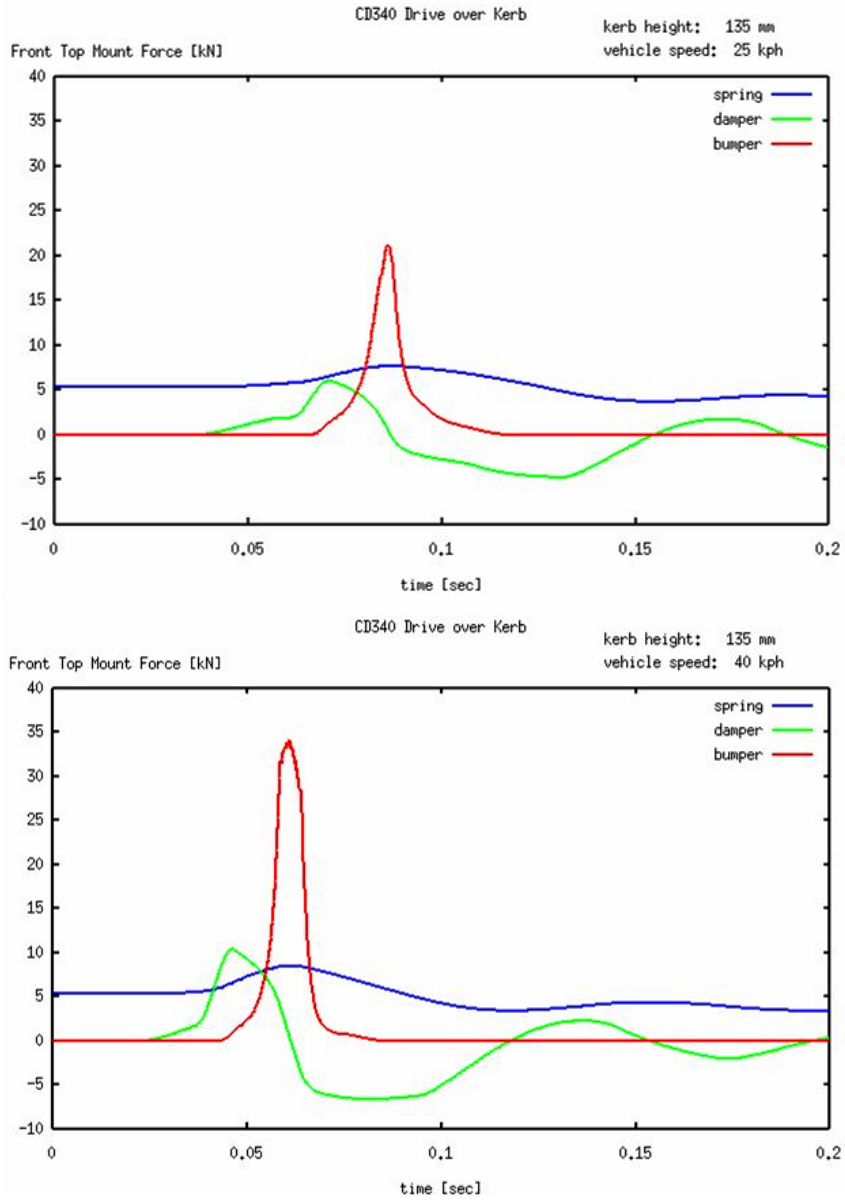

Figure 7.17: Simulation of spring, damper and bumper force component of top mount force during kerb strike

The results shown in Figures 7.16 and 7.17 were achieved after an implementation of a linear spring element into the model to simulate the body stiffness. Figure 7.18 shows the spring element representing the body stiffness linked to the bumper element in a series connection in order to account for the transfer of the full bumper force.

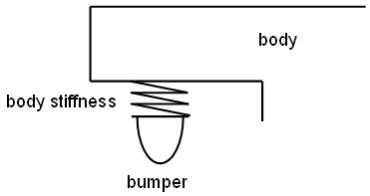

Figure 7.18: Accounting for the vehicle body stiffness

For the case where the vehicle model is set up with the assumption of a rigid body (as described in chapter 4), the jounce bumper attachment to the body is assumed to be rigid as well. With this assumption, the predicted bumper force becomes excessive as shown clearly in Figure 7.19 and does not match that measured, especially at higher vehicle speeds (40km/h). The reason is the impulsive nature of the force response, typical for jounce bumpers at large deformations.

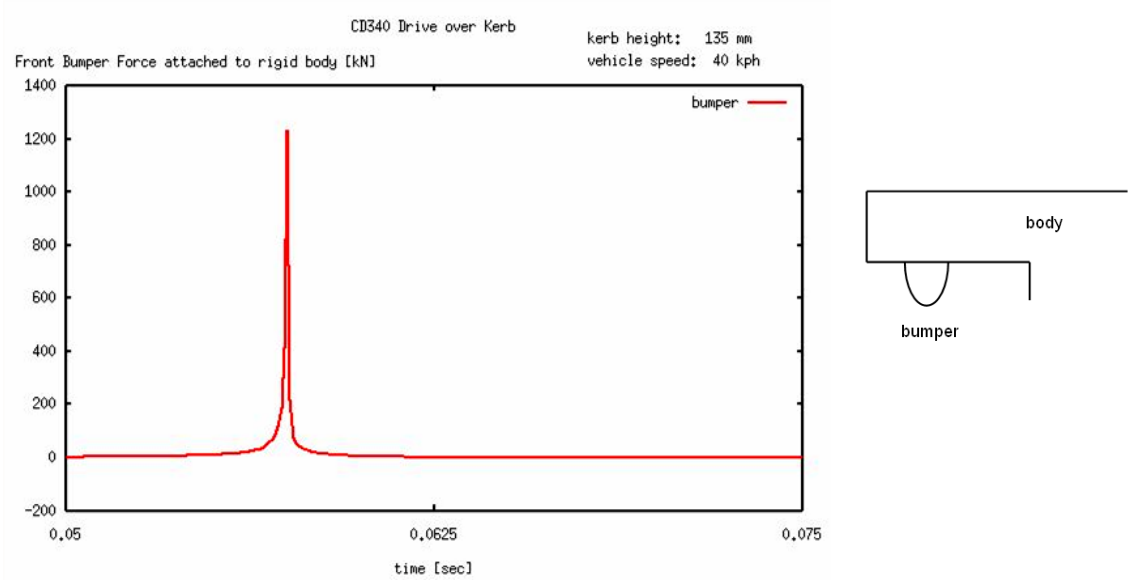

Figure 7.19: Simulation of bumper kerb strike force for rigid attachment to the vehicle body assumption

An iteration method described here is intended to approximate the load reduction expected as a result of body top mount compliance. Figure 7.20 shows a linear spring, representing the top mount body stiffness **CBO1z** in combination with a (non linear) bumper stiffness **C(s).** The force response of both elements is shown as a function of deflection for bumper **F**(**s**) and body **F**(**u**). In general the body stiffness is of higher magnitude compared with the bumper within its initial deflection range, visualized by the slopes of the curves in Figure 7.20.

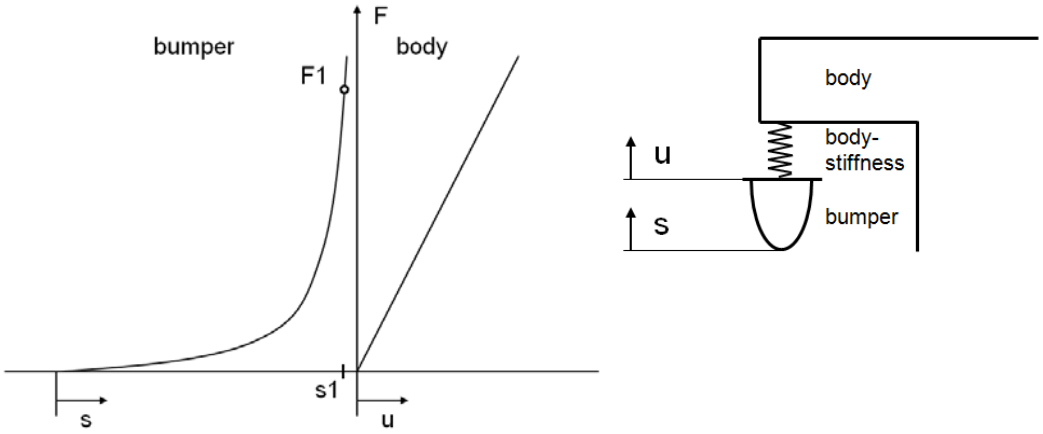

Figure 7.20: Non linear bumper- and linear vehicle body force response.

The iteration starts with an impact against the bumper, which is assumed to be in a rigid attachment mode. The initial peak force **F1** in conjunction with bumper deflection **s1** is not considered to be affected by body compliance in absence of body deformation **(u = 0)**. The first iteration is based on the assumption that the bumper deflection **s1** will decrease in the case of elastic body deformation. Thus, **F1** would cause a body deflection of **u1 = F1/CBO1z** and the bumper deformation would relax by the amount of the body deflection **u1,** down to **s2 = s1 – u1** (Figure 7.21). With this assumption, a revised bumper force **F2** can be determined.

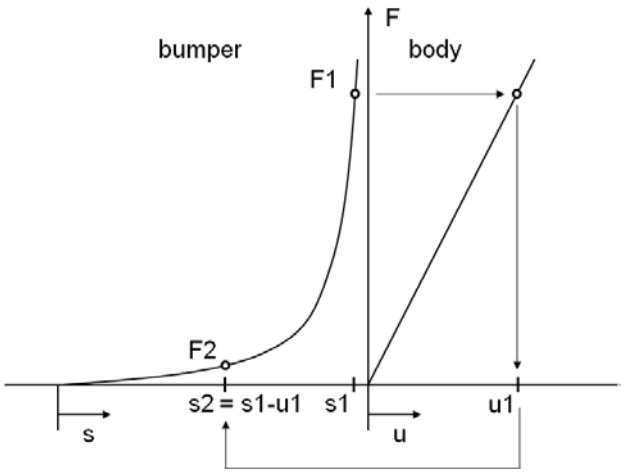

Figure 7.21: Bumper force F2 and deflection s2 after first iteration.

Whereas **F1** (rigid attachment) can be considered to exceed the real top mount force **F**, a relaxation of the bumper element by **u1** will result in an exacerbated effect of body compliance. Thus, the real force **F** is expected to be within the interval **[F1, F2]**, where

F2 < F < F1. An equivalent top mount deflection **u2 = F2/CBO1z** can be derived analogous to **u1.** Subsequent iterations refine the interval as illustrated in Figure 7.22.

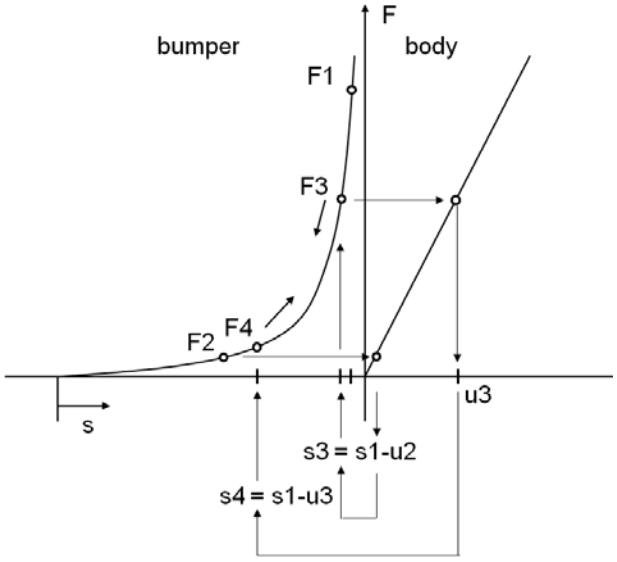

Figure 7.22: Bumper force F3 and deflection s3 after second iteration.

The iteration stops when a specified small difference **abs(Fi+1 – Fi)** is achieved.
It is evident that the bumper peak load cutback depends on the body stiffness **COB1z** and the initial force response **F1** against rigid body. The cutback is marginal within the initial bumper deformation range as long as the bumper stiffness **C(s)** does not exceed the body stiffness **COB1z**. A limitation is set for **F1** if the related body deflection **u1** exceeds the initial bumper deflection **s1** which leads to the condition **u2 < 0**.

7.3.2.2 Wheel displacement

An assessment of the vertical wheel displacement reveals unsatisfactory correlation between the measured signal and simulation results (Figure 7.23). This can be explained considering the limited ability of the simulation to deal with combined edge and flat contact as roll over the kerb progresses. The missing component here is the transition from the initial edge type tyre contact towards a flat contact to kerb in the later stage during the roll over mode. A combined edge and flat type contact was indicated in Figure 6.33 as an optional feature of the chain type simulation model, but not yet implemented in the simulation.

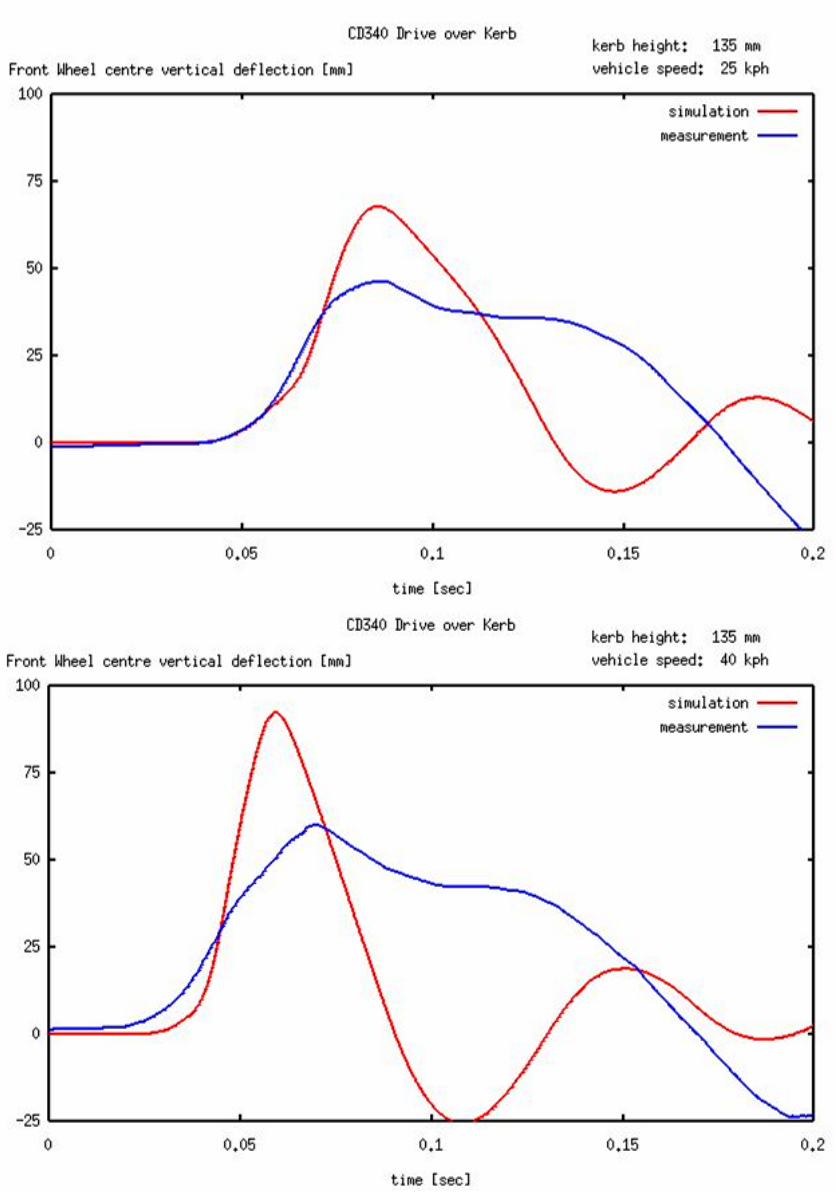

Figure 7.23: Vertical wheel displacement relative to body

Another aspect addressed with the deviations seen in the wheel travel results is that the stiffness and damping properties are modelled as linear, whereas for the system (beside the road spring) a non-linear behaviour is considered. The simulation model does address non-linearity for the bumper and tyre only, whereas the damper, rim and the body stiffness are modelled as linear elements.

However, the order of the force peaks fits well to that expected in a kerb strike event as shown in Figure 7.24.

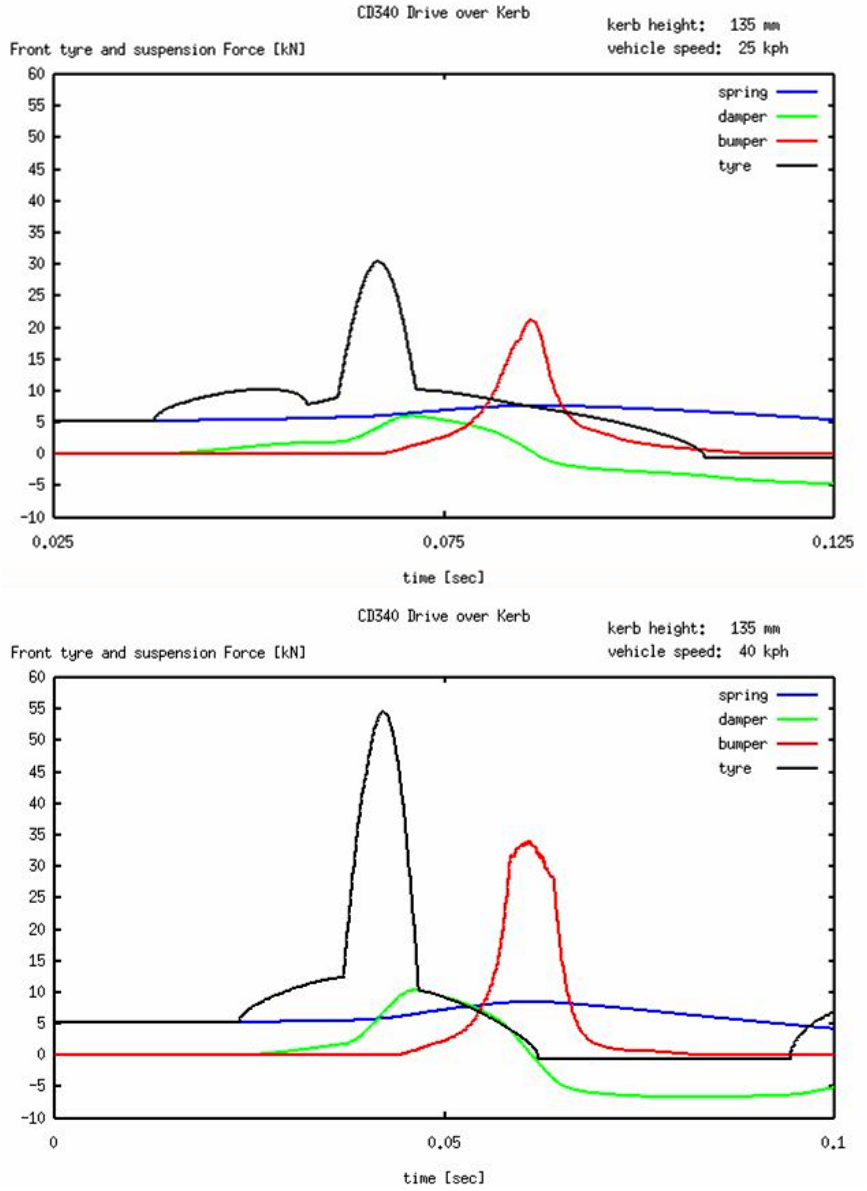

Figure 7.24: Subsequence of peak force during kerb strike event

The tyre peak load achieves a magnitude of approx. 30 kN after kerb crossing at 25 kph (upper window in Fig. 7.24), which is in good agreement to the load level reported in **[7]**. It can be observed that the peak force applied to the tyre (black) occurs in advance of the maximum bumper force (red). Thus, the tyre loads cannot directly be related to the bumper peak force, such as in a quasi static case. Furthermore, the shape of the force trace also reveals the transition from pneumatic radial belt force to that of a rim contact force at a load level of approximately 10kN. This contact force level is also confirmed by the experimental data shown in Figure 7.3, found for tyre size 235/40-R18 under rim contact condition against a blade shape with a pneumatic pressure of 2 bar. In contrast to

the pneumatic force, the rim force component increases in significance for the vertical velocity state of the wheel after the kerb strike.

7.3.3 Plausibility study for tyre force response in the kerb contact mode

The following demonstrates the plausibility of the wheel force signals resulting from the DoK simulation. Figure 7.25 illustrates the time signal of the vertical force F1z applied to the wheel in traversing over the kerb mode. Besides the force F1z, characterised by discontinuities numbered (1) to (6), traces for vertical wheel centre position z1 and radial tyre deflection f1 are also shown.

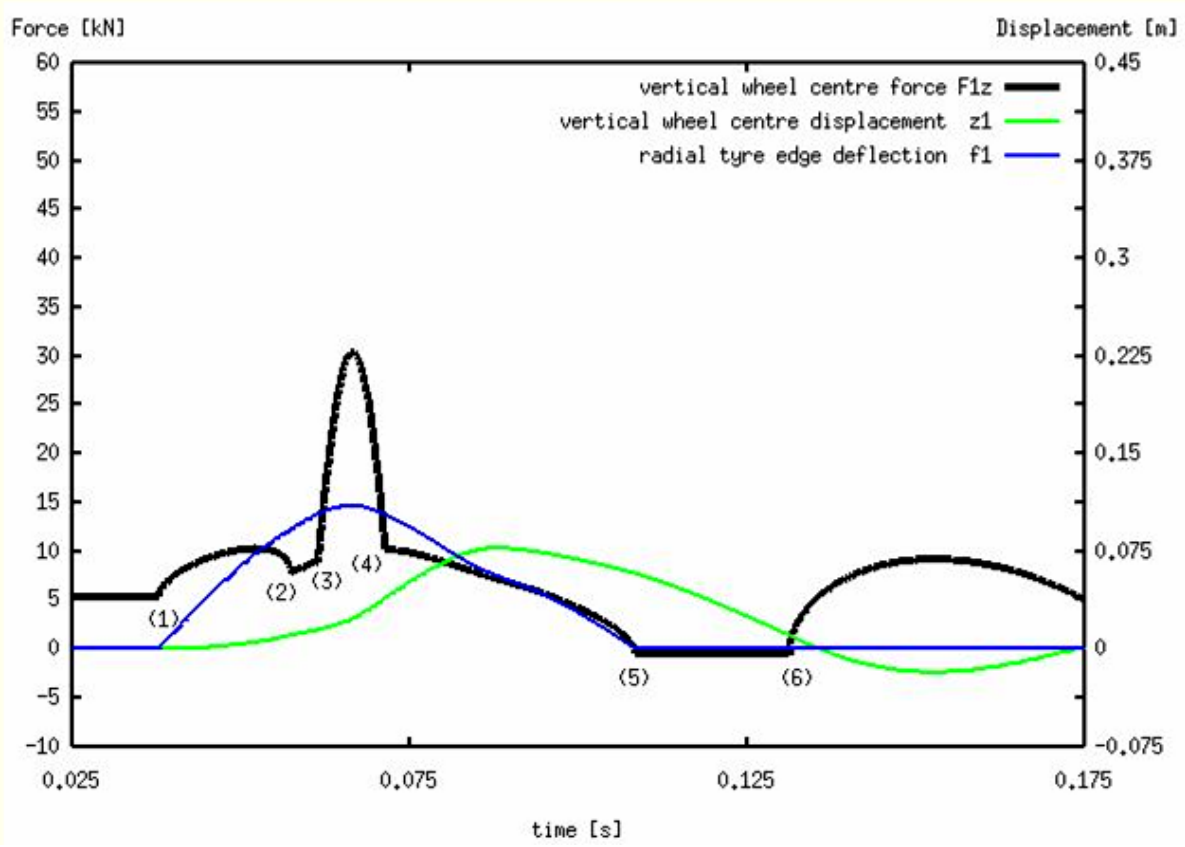

Figure 7.25: Plausibility plot for kerb climbing mode

The vertical force, caused by a purely flat type contact to the ground remains constant until the tyre belt strikes the rim at (1) as also shown in Figure 7.26. Thereafter; from (1) to (2), the total force is a superposition of flat and edge-type contact force and ramps up the wheel centre vertical position z1. The transfer from flat to purely edge-type load is complete at point (2), where z1 achieves the level of the initial flat contact patch radial deflection (see Figure 7.26).

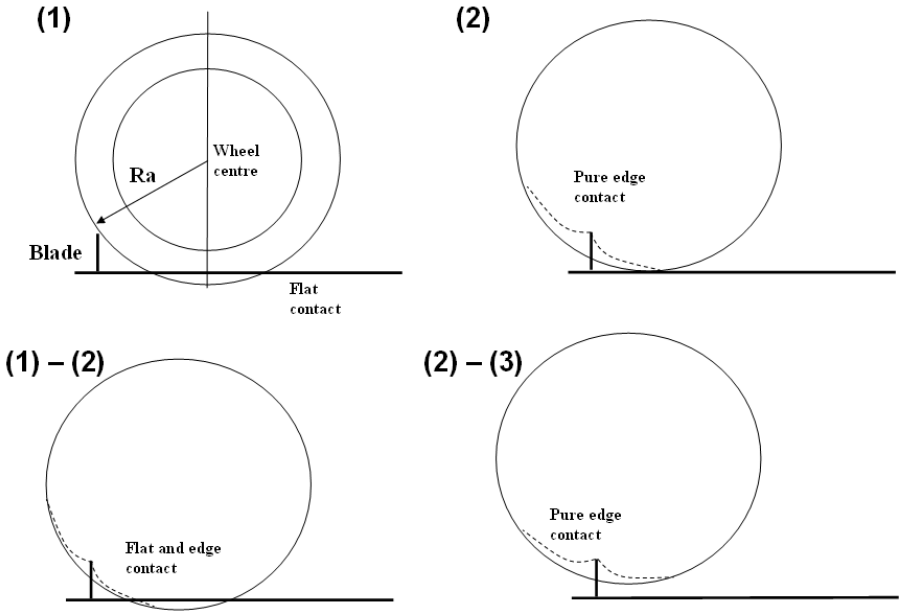

Figure 7.26: Illustration of tyre contact modes (1) to (3)

At point (3), the radial deflection f1 is limited by the rim radius ri, causing a rim clash condition until position (4) is reached. The drastic force increase is caused by the radial contact stiffness of the rim against the kerb edge and leads to the maximum gradient seen for z1. After point (4), the contact remains in pure edge-type contact mode until point (5), where the wheel loses contact and bounces to the flat ground at point (6) as shown in Figure 7.27.

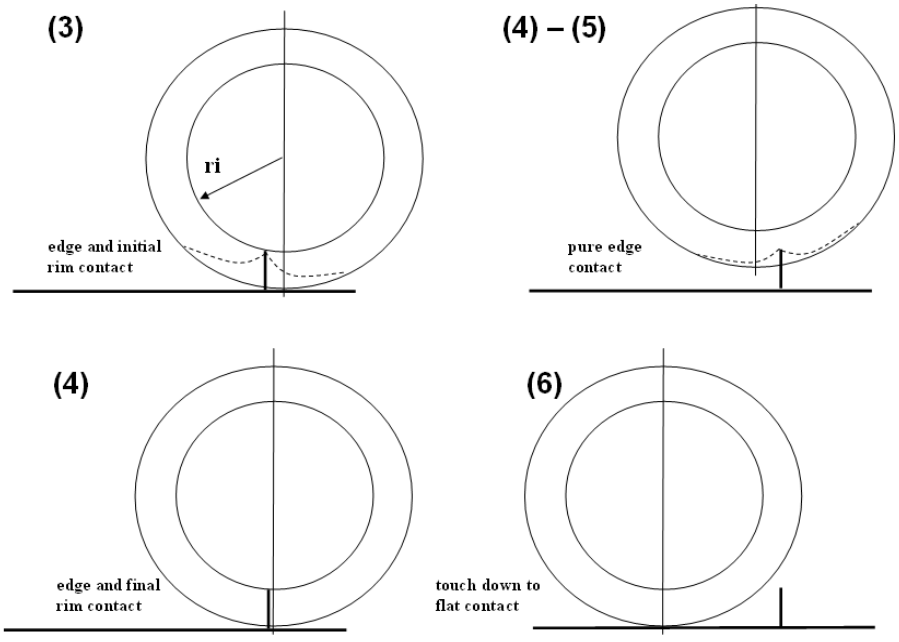

Figure 7.27: Illustration of tyre contact modes (3) to (6)

7.3.4 Conclusion

Although attributes that are considered to be key contributors to the vertical load level, such as a proper simulation of the dynamic bumper engagement and tyre force response characteristics are addressed in the vehicle model, the physical testing revealed that body vertical stiffness should not be neglected. This is important in order to match the predictions with the measured top mount forces, especially for the abusive test operation performed at higher speed level of 40 kph at kerb height 135mm.

7.4 Closure

In this chapter vehicle model validation was performed by comparison with measurements on component and system levels. The results confirm that the tyre force response against a static, in-plane radial deformation can be approximated by simple analytical formulae, as derived in chapter 6, with reasonable accuracy. The results obtained from an edge-type simple model show a better correlation with the measurements compared with the data obtained from the more complex chain model.

The validation of the map approach applied to the foam type jounce bumper demonstrates good correlation with the results obtained for drop testing published in **[55]**. The assessment shows that the map approach, based on sinusoidal actuation, is also applicable to simulate non-sinusoidal motions such as those resulting from drop tests.

A vehicle (CD340 FORD Galaxy) was instrumented with load cells to record the vertical front suspension top mount load during DoK. The assessment of the integral signal traced for spring, bumper and damper loads could be calibrated with reasonable accuracy after a further linear spring element was added to the model to represent body vertical stiffness. This indicates that the model can effectively be used for parametric studies as discussed in chapter 6 subject to minimal calibration of the model. Load prediction in total absence of a validated reference remains quite uncertain.

Chapter 8: Parameter study

8.0 Introduction

The aim of the minimal parameter model presented in the previous items is to predict the effect of a loading scenario in the early design phase and to perform relevant parametric studies in order to assess different system concepts. A parametric study is intended to investigate the influence of system parameters upon a specific system attribute of interest. In general, it can be performed in various ways, for example through physical testing, where a given attribute is measured for several sets of parameter stack ups. In many cases, the effort can be reduced by using a parametric simulation model instead of physical prototype testing. The study can also demonstrate the plausibility of the model used. The following study is addressed to investigate the vertical suspension force level in conjunction with the drive over kerb test, described in chapter 7, section 7.3.

8.1 Conceptual study

In this chapter, the model parameters are altered to investigate the trend with regards to the vertical suspension load level. The study is confined to the front suspension response. The set of model parameters is divided into two main parts addressing geometry and kinetic attributes separately. The scope of the study includes the front suspension relevant geometric and kinetic vehicle parameters, influenced by the drive over kerb test boundary conditions for the kerb height and vehicle velocity. In table 8.1 and Figure 8.1, an overview of the comprehensive set of vehicle model parameters is listed for CD340:

Geometry parameters

Wheel base & CoG [m]		
a = 1,379		longitudinal dist CoG to front WC
b = 1,471		longitudinal dist CoG to rear WC
h = 6,89E-1		CoG height to ground
Suspension Front / Rear [m]		
F0 = 6,485E-2	**R0** = 1,131E-1	upper spring seat to jounce bumper mount
F1 = 1,3485E-1	**R1** = 1,831E-1	upper spring seat to jounce bumper tip
F2 = 2,75E-1	**R2** = 2,9E-1	upper spring seat to rebound stop tip
F3 = 2,8E-1	**R3** = 2,95E-1	upper spring seat to rebound stop mount
F4 = 3,8E-1	**R4** = 4,5E-1	unloaded spring length
F5 = 5,785E-2	**R5** = 1,131E-1	lower spring seat to travel lock
Tyre [m]		
Ra = 3,15E-1		belt outer radius
ri = 2,12E-1		rim radius
bt = 1,95E-1		belt width
fc = 1,5E-2		sidewall concavity
p = 2,0E5 N/m^2		pneumatic pressure

Kinetic parameters

Masses [kg]	
m1 = 51,5	front wheel unsprung mass
m2 = 40	rear wheel unsprung mass
m3 = 1051	(body + load) / 2 sprung mass
J = 3938 kgm^2	rotational inertia
Stiffness [N/m]	
C1z = 3,2E04	front road spring stiffness
C2z = 2,6E04	rear road spring stiffness
C1x = 2,8E06	front longitudinal WC. stiffness
C2x = 4,8E06	rear long. WC. stiffness
CBO1z = 1,4E06	body front top mount vert. stiffness
CBO2z = 1,2E06	body rear top mount vert. stiffness
Crim = 3,2E06	rim radial edge stiffness
Damping [Ns/m]	
D1z = 2,57E03	front vertical damping
D2z = 1,71E03	rear vertical damping
D1x = 2,23E03	front longitudinal damping
D2x = 2,52E03	rear longitudinal damping

Table 8.1: CD340 vehicle model input parameter list

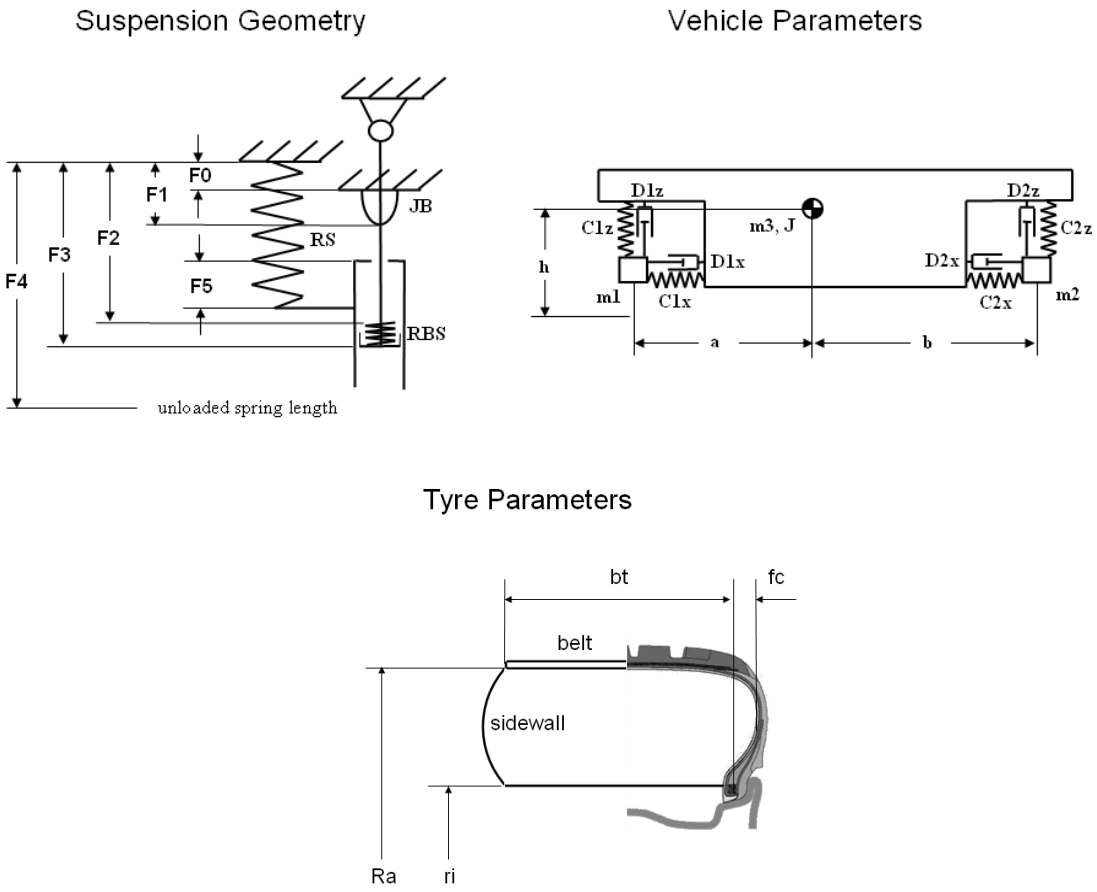

Figure 8.1: Vehicle model input parameters

Geometry data listed in table 8.1 are gathered from the FORD CAD system, the kinetic parameters were extracted from the vehicle dynamics ADAMS models, developed and validated by the FORD Chassis Engineering department. On particular the stiffness values were measured under quasi static conditions on the FORD K&C rig (kinematics & compliance).

In chapter 7, the model was validated by comparing its predictions with measured data obtained from DoK for two distinct velocities, 25 and 40 kph. The operational condition tested at 25kph was used as a datum base line in conjunction with a set of suspension parameters, adjusted to the nominal dimensions specified for the FORD Galaxy (CD340). Figure 8.2 shows the traces calculated for the wheel and top mount vertical force components, resulting from the vehicle model for the baseline parameter set up. The responses reveal a difference in the force level and a time shift for the maxima. The parameter study, therefore, was conducted individually for the vertical components of the wheel and the top mount forces.

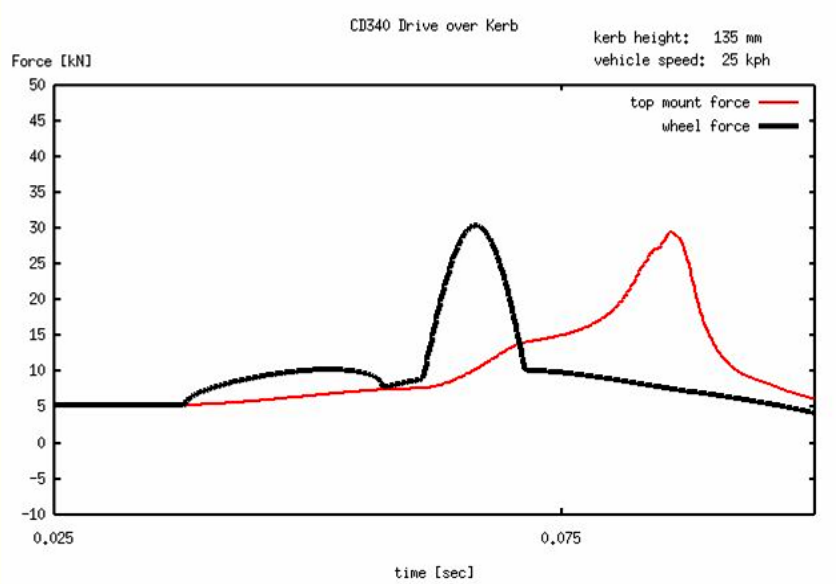

Figure 8.2: Vertical wheel- and top mount force DoK simulation results for baseline model set up

The relevant individual parameters are varied whilst the others are kept at their base line values, representing the vehicle nominal design condition. The nominal condition of the investigated parameter is related to the initial value on the variational factor axis.

8.2 Geometrical parameters

The geometrical parameters are subdivided into three categories, defining:

- the main vehicle dimensions related to the wheel base and the CoG position
- suspension geometry, defining the free travel to the bump event
- tyre cross-sectional geometry

8.2.1 The main vehicle dimensions

For this case, the influence of the centre of gravity (CoG) position is ascertained by a variation of the parameters a, b and h as shown in Figure 8.3. The sum a + b specifies the wheel base, whereas the individual parameters 'a' and 'b' determine the relative position of the CoG with respect to the wheel centres. Therefore, the influence of the wheel base and the CoG's relative position on vertical load was determined separately. Results are shown in Figure 8.4.

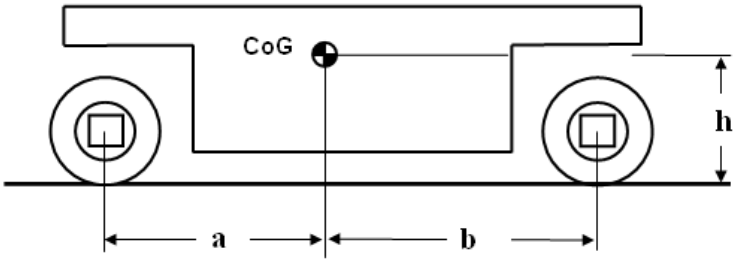

Figure 8.3: Vehicle main dimensions wheel base (a+b) and CoG height (h)

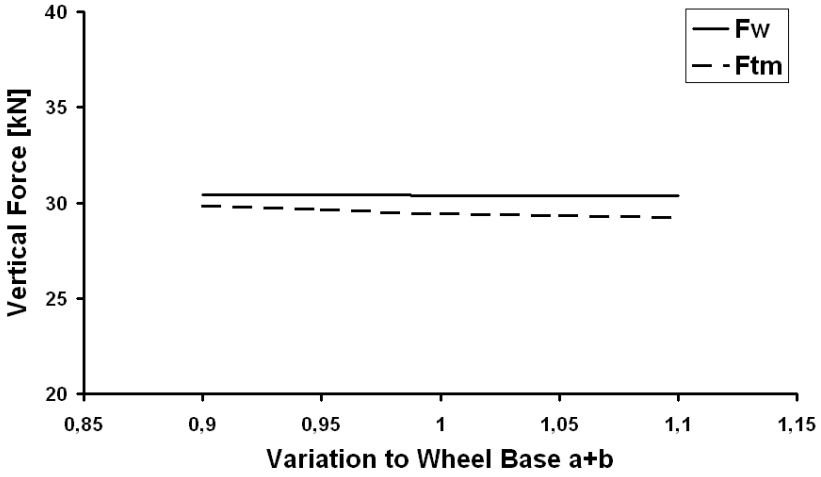

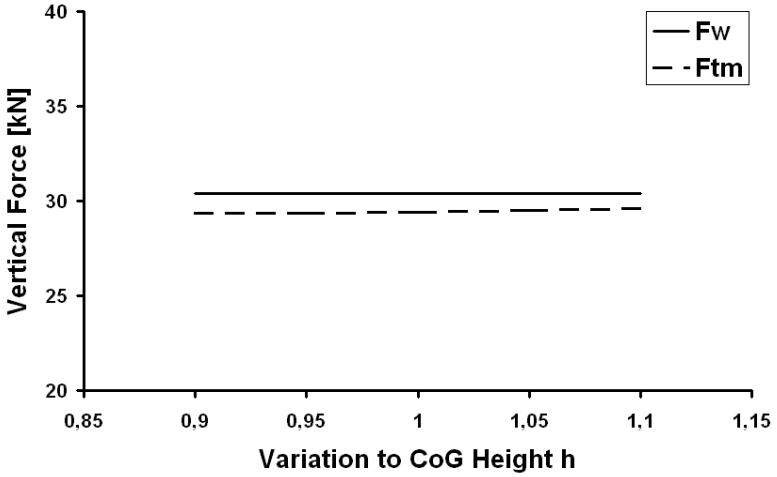

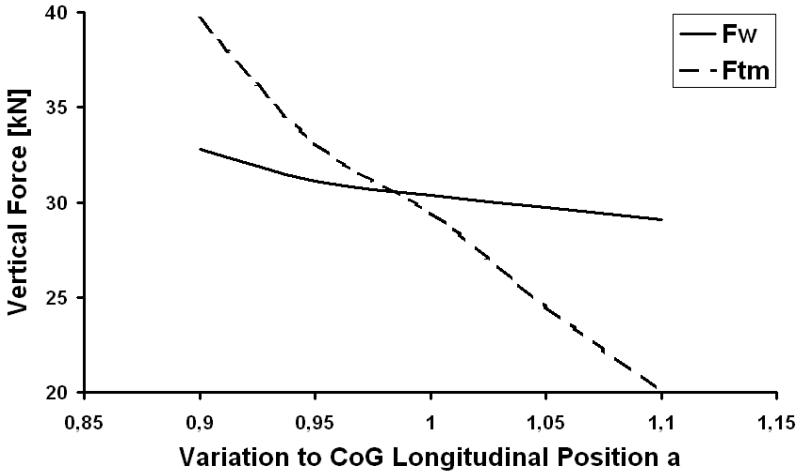

Figure 8.4: Impact of wheel base (a+b) and CoG position a, h on wheel - and top mount load

The effect of wheelbase and CoG height variations on the vertical generated force level remains almost neutral for both the wheel and the top mount (i.e. negligible differences). This indicates that the influence of the sprung mass rotational inertia is not significant in conjunction with the lever arms a, and the height h.

A CoG position variation relative to the wheel centres increases the load level for the case that its position is more proximate to the front suspension with a marked influence upon the top mount force. This would be expected, as the resistance of the top mount against vertical shift increases with the CoG balance towards the vehicle front end. The same effect can be considered for the wheel, but attenuated by the suspension vertical elasticity.

8.2.2 Suspension geometry

The suspension geometry, defined in the model, consists of six parameters F0 – F5. These parameters are not independent of interaction and do not represent a minimal parameter set. The parameter set configuration is intended to allow for an easy model set up, based on the component dimensions. Figure 8.5 shows the front suspension geometry under static equilibrium condition; in undisturbed roll mode towards the kerb.

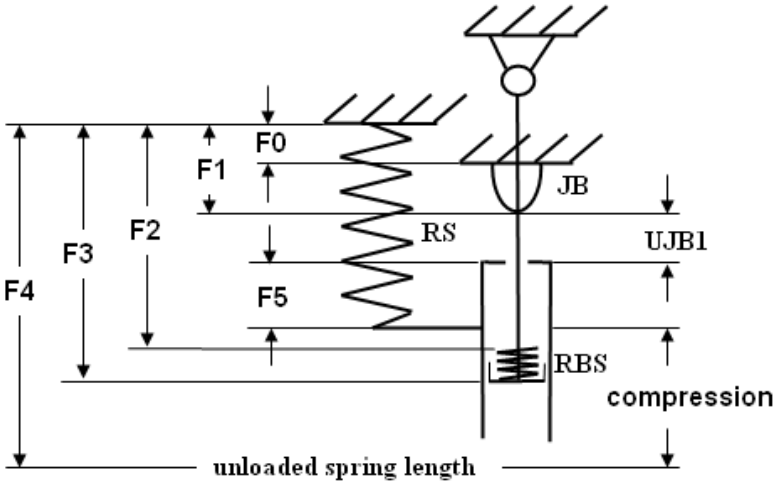

Figure 8.5: Suspension geometry parameters

The dimension considered to be relevant for vertical DoK loads is the free wheel jounce travel UJB1 to bumper engagement. It is defined by the bumper engagement position F1 relative to the upper spring seat on the one hand, and the spring compression in vehicle equilibrium condition on the other hand. There is, therefore, no single geometrical feature, as the configuration is a result of the equilibrium condition, thus depending on the spring rate as well. The bumper length itself, (F1 – F0), could not be varied in this study, because it is an integral attribute of the force response map described in chapter 3. A variation of bumper length would require individual map data sets, not readily available. Each dimension F0, F1, F4 or F5 can be used to vary the free travel UJB1. The variation was adjusted within 10% of its nominal value; i.e. relative to the vehicle design condition UJB1 = 21 mm (CD340, FORD Galaxy). Dimensions F2 and F3 determine the rebound engagement, post jounce stroke and, therefore, are not considered in this study. Results are shown in Figure 8.6.

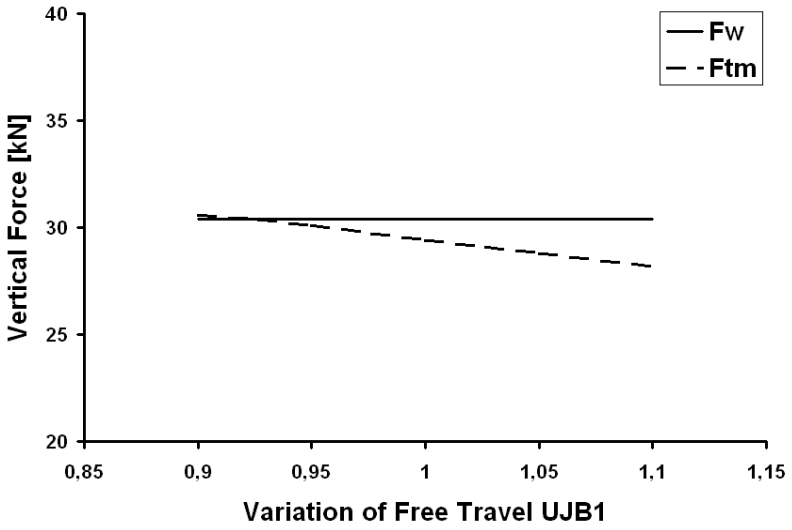

Figure 8.6: Impact of vertical free travel on wheel- and top mount vertical peak load

The wheel peak force occurs in advance of the bumper full engagement, this is the reason why the wheel peak load level remains unaffected by a marginal change in the free travel, whereas the top mount peak load shows a decreasing trend with an increasing UJB1 travel. This is in line with the fact that the system dissipates more energy through viscous damping with an increased free travel. Therefore, the bumper becomes engaged at a reduced system energy level.

8.2.3 Tyre geometry

As described in chapter 6, besides the pneumatic pressure, tyre geometry has also an influence on the belt circumferential force and thus determines the tyre radial reaction force characteristics. In this study, the belt width bt, the belt and rim radii, Ra and ri, as well as the sidewall lateral deflection fc, as shown in Figure 6.7, are investigated.

The tyre size 205/55-R16 is used as the baseline with a 2 bar inflation pressure.

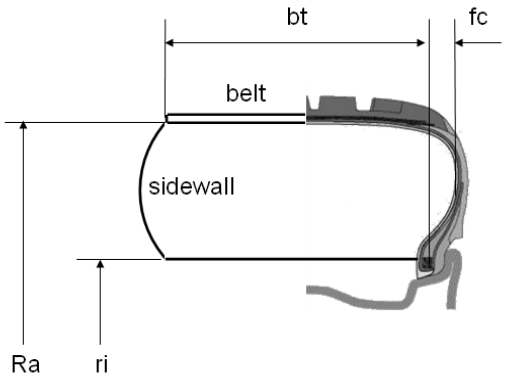

Figure 8.7: Tyre geometry parameters

The radii Ra and ri also influence the wheel roll characteristics whilst climbing over a kerb. The roll effect is investigated by a combined variation of Ra and ri in order to maintain the sidewall geometry, height (hc = Ra – ri) and lateral deflection fc, at the baseline condition. Thus, the influence of the roll radius R on the vertical force level can be analysed with a minimal effect on the tyre force response characteristics. In a separate variation of the single parameter Ra, the effect of a sidewall height variation hc is also investigated. Some results shown in Figure 8.8 reveal non-linear response behaviour. To obtain a better understanding about the cause and effect, time signals for variation level 0.9, datum level 1.0 and 1.1 are supplemented to the variation diagrams.

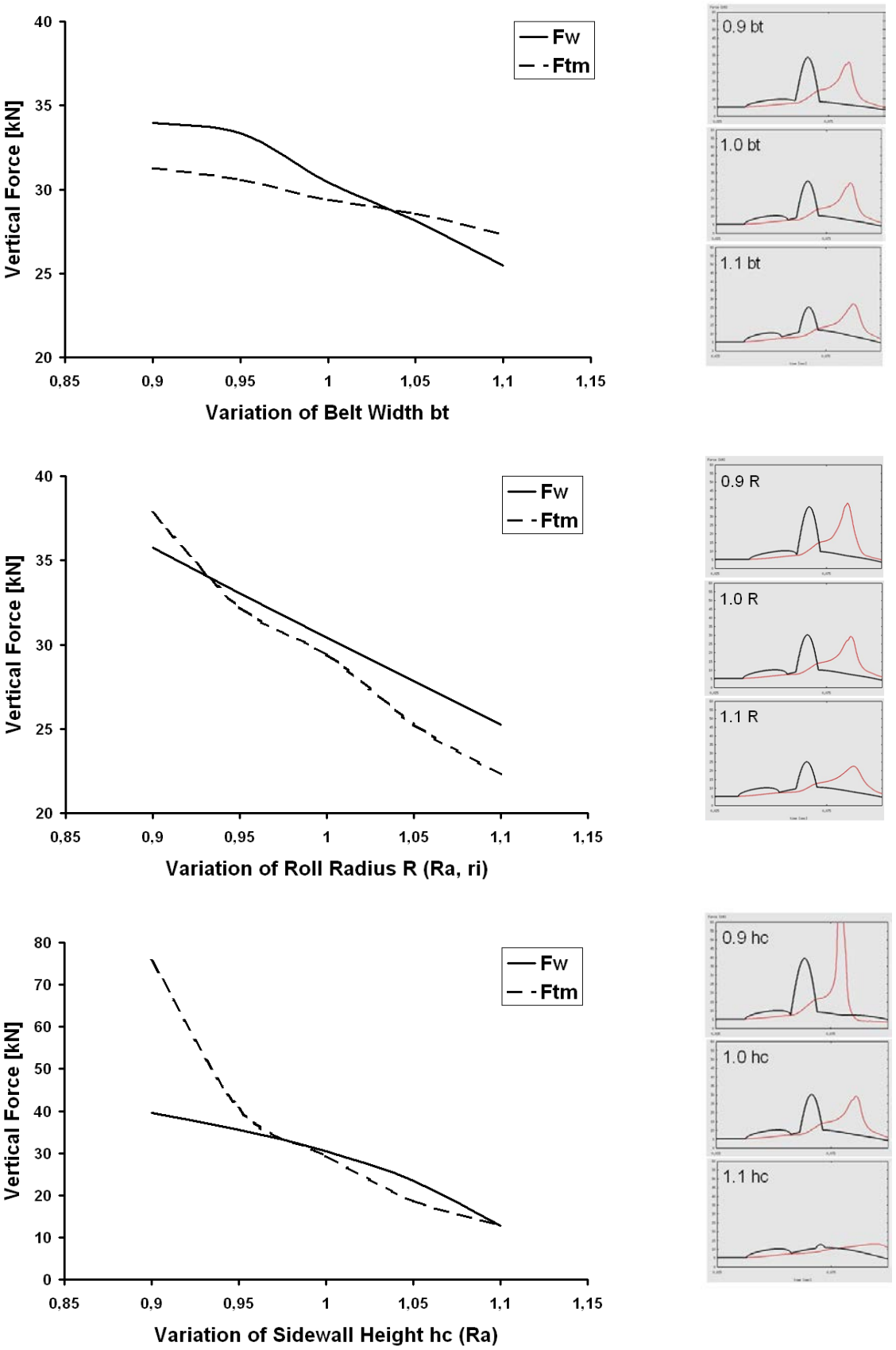

Figure 8.8: Impact of tyre cross section geometry on vertical load level during DoK

A common feature seen for all the variations is the advanced timing of the wheel maximum force with respect to the top mount peak load. The maximum wheel force level and impulse contribution occurs for the rim under the kerb clash condition in all the cases shown. The top mount force can be considered as a reaction to the system impulse of the unsprung mass, imparted during the kerb clash. The wheel and the top mount force levels are increased with the harshness of the clash condition. The wheel impulse magnitude determines the delay in the top mount response.

A wide tyre (bt) has more resistance against radial deformation. The kerb clash appears later in time and is less pronounced and the top mount force peak occurs later in time.
A similar trend is seen for the variation of the roll radius R (variation of Ra and ri). Beside the fact, that a large wheel radius is of advantage for a smooth roll mode on an uneven ground, a larger belt radius leads to an increase in the circumferential belt force as shown in equation 6.7. The latter is in line with the radial tyre stiffness and thus confirms the trend as seen for the belt width.

The variation of the sidewall height (hc) directly determines the belt-to-kerb contact radial travel towards the rim clash condition. Thus, an increase of hc relieves the rim clash and also leads to a delay of the top mount peak load. This parameter shows the strongest influence compared with the other tyre geometrical parameters, namely roll radius and width, recognized through the revised vertical force scope scale adjusted to 0 – 80 kN.

A tyre geometry parameter that is not within the automotive industry scope of control is the sidewall lateral deflection fc, as it is a given feature designed by the tyre manufacturer. Nevertheless, its influence was monitored in this study as shown in Figure 8.9.

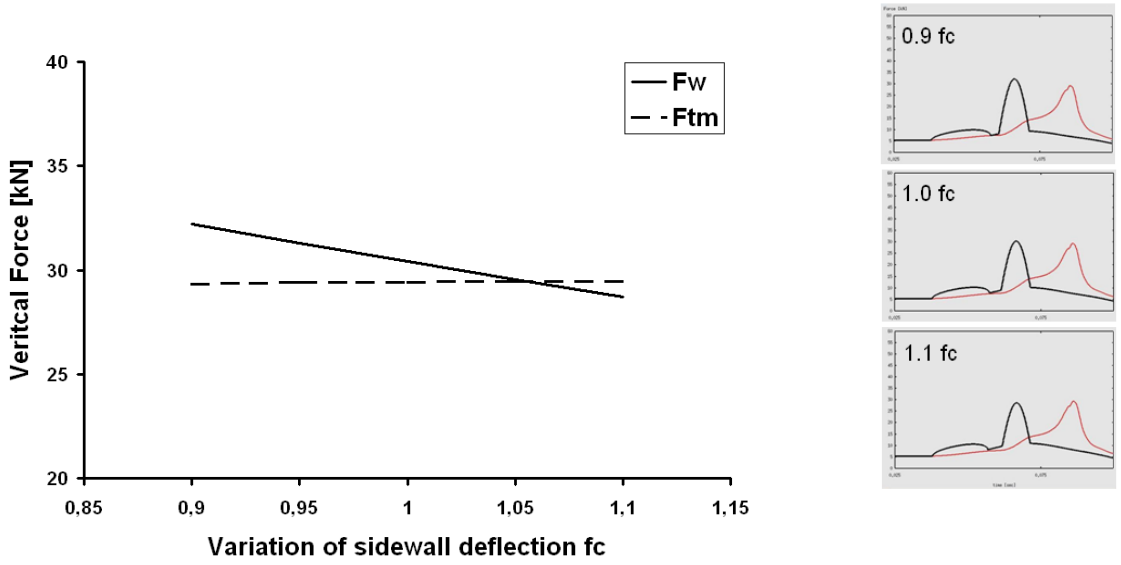

Figure 6.9: Variation of sidewall lateral deflection fc

As shown by equation (6.14), the radial belt contact force against an edge tyre penetration decreases for small sidewall slack hang fc. The tyre behaves less stiff against radial deformation. Thus, a rim clash to kerb occurs advanced and harsh in case of small corrugated tyre sidewalls (see time history for variation level 0.9) compared to large sidewall warpage (level 1.1). This explains the higher wheel forces for variations smaller one, whereas the top mount load remains almost unaffected. Although fc has no significant impact on vertical loads, it strongly affects the internal sidewall stress as shown by equations (6.5) and (6.6) in chapter 4.

8.3 Kinetic parameters

The system parameters which describe those elements that contribute to the dissipative kinetic energy, such as mass, stiffness and damping are considered as kinetic parameters in this study. Another parameter, tyre pneumatic pressure p, is also addressed in this category as it is relevant for the tyre radial stiffness. An overview of the kinetic parameters is shown in Figure 8.10.

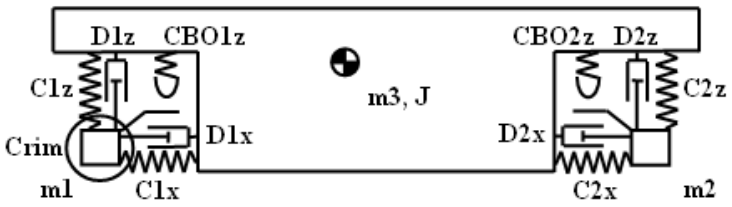

Figure 8.10: An overview of kinetic model parameters

8.3.1 Discrete vehicle masses and rotational inertia

For the front suspension analysis, the unsprung mass m1, sprung mass m3 and rotational inertia J are varied. Results are shown in Figure 8.11.

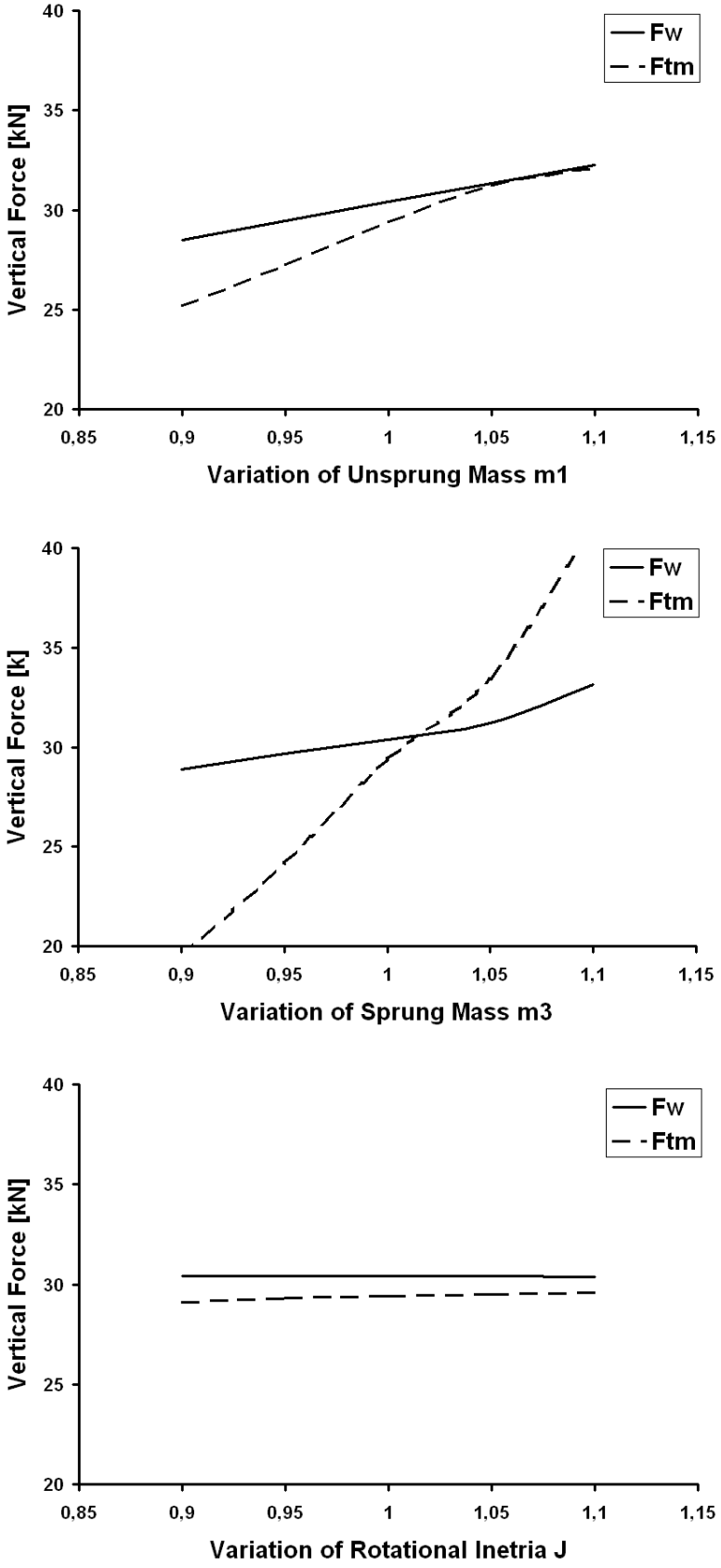

Figure 8.11: Variation of sprung – and un-sprung mass m1, m3 and rotational inertia J

A rise in the wheel unsprung mass increases both the top mount and wheel force levels. The increase in force is evenly balanced for the top mount and the wheel, whereas a variation of the sprung mass m3 reveals concentrated effect on the top mount. In contrast to the influence of mass, the rotational inertial effect on the force level appears to be negligible. This indicates a small body resistance against rotation for a force applied via the relatively long lever arm a, which confirms the conclusions made for the wheel base.

8.3.2 Suspension, rim and body stiffness

The spring stiffness C1z determines the spring compression in the usual design position as shown in Figure 8.5. A variation of C1z would cause a simultaneous deviation in the free travel UJB1. To investigate the effect of stiffness, the bumper position F1 is adjusted in parallel to keep the free travel adjusted to its nominal condition. Results are shown in Figures 8.12 and 8.13.

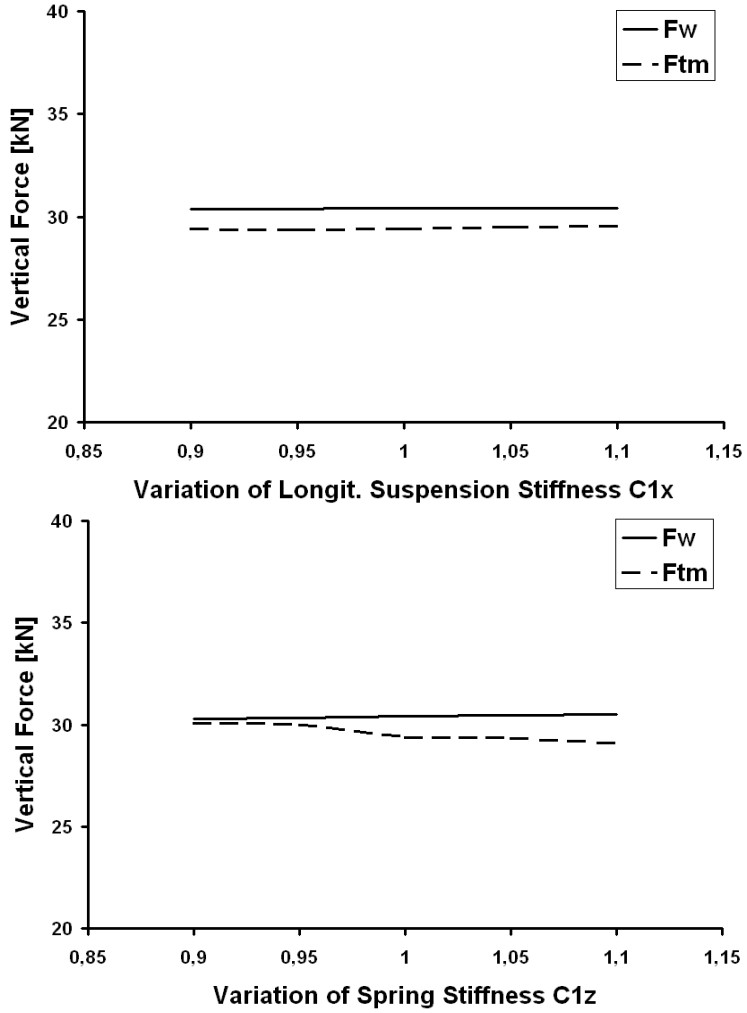

Figure 8.12: Variation of vertical and longitudinal suspension stiffness

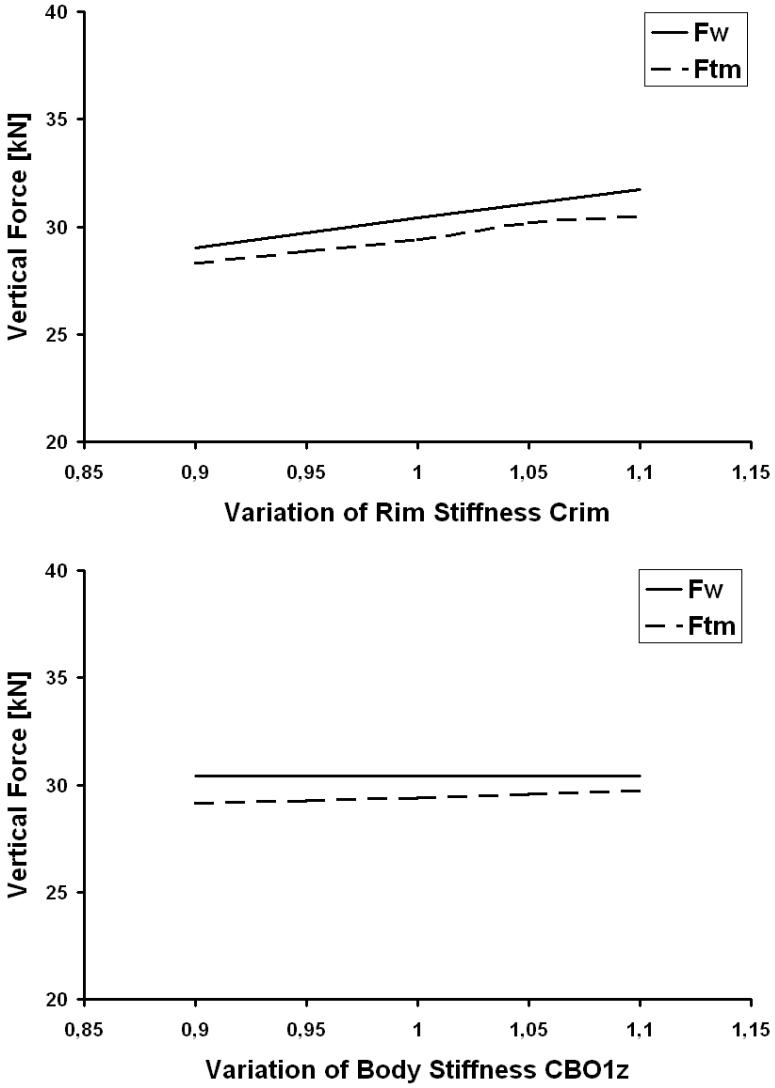

Figure 8.13: Variation of rim- and body stiffness

A variation in stiffness within the 10% range does not reveal any change in the vertical force level of similar significance as seen for the mass variation. An exception is observed for the rim stiffness that mainly drives the impulse as discussed for the tyre geometry in section 8.2.3.

The wheel peak load occurs in advance of bumper full range engagement. Therefore, the variation of the body stiffness has no effect on the wheel force level, whereas a rising trend can be seen for the top mount loads as would be expected.

8.3.3 Suspension damping

The model is set up with viscous type damping elements. A variation of damping parameter is performed for the longitudinal and vertical damping coefficients D1x and D1z. Results are shown in Figure 8.14.

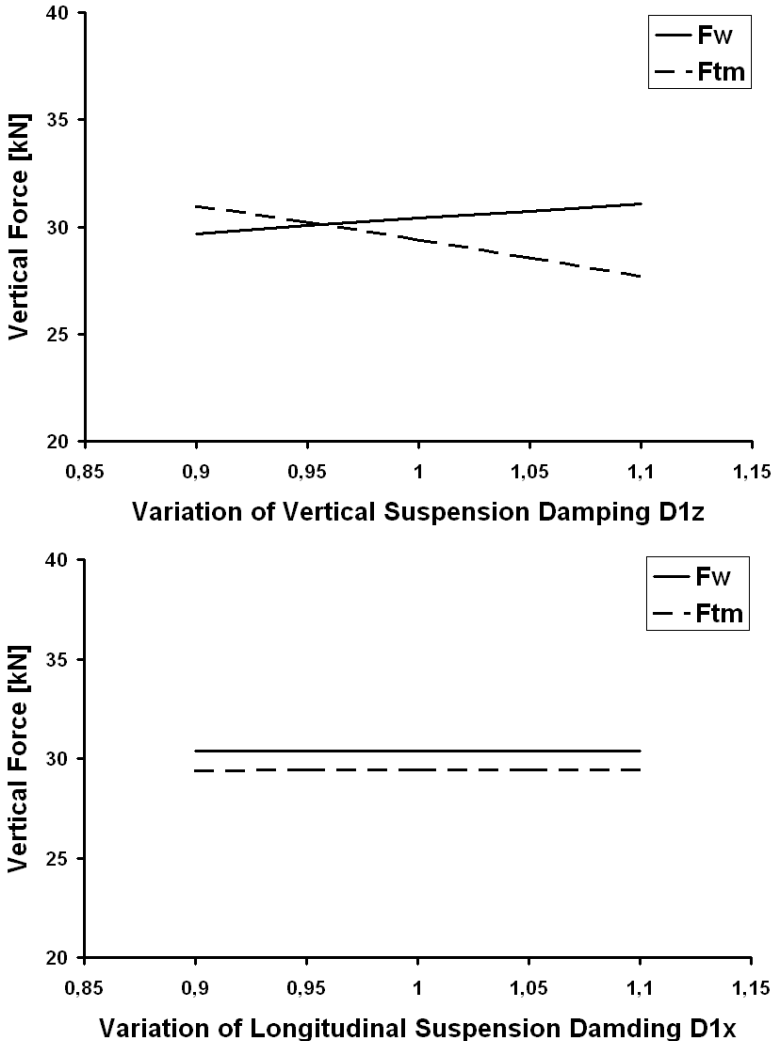

Figure 8.14: Variation of suspension damping

The results found for the variation of the vertical damping show an inverse trend against each other. This can be explained by the fact that an increased damper rate D1z would tend to ramp up the wheel resistance against jounce. As a consequence, the force level rises with the damping rate. On the other hand, the damper dissipates kinetic energy of the un-sprung mass. This is why the bumper engagement occurs at a lower energy level. This condition is equivalent to a reduced fall height of a drop test (see chapter 5, section 5.2) which explains the decreasing trend shown for the top mount force in the upper plot of Figure 8.14.

8.4 DoK test parameters

In sections 8.2 and 8.3, the parameters which describe the vehicle physical properties are discussed. Here the two parameters that describe the boundary conditions for the drive over kerb test, namely step height hs and vehicle speed Vx are investigated. The influence of parameter hs is strongly non-linear. This is the reason why the diagrams are supplemented by the force traces to show the effects in a more descriptive manner (Figure 8.15).

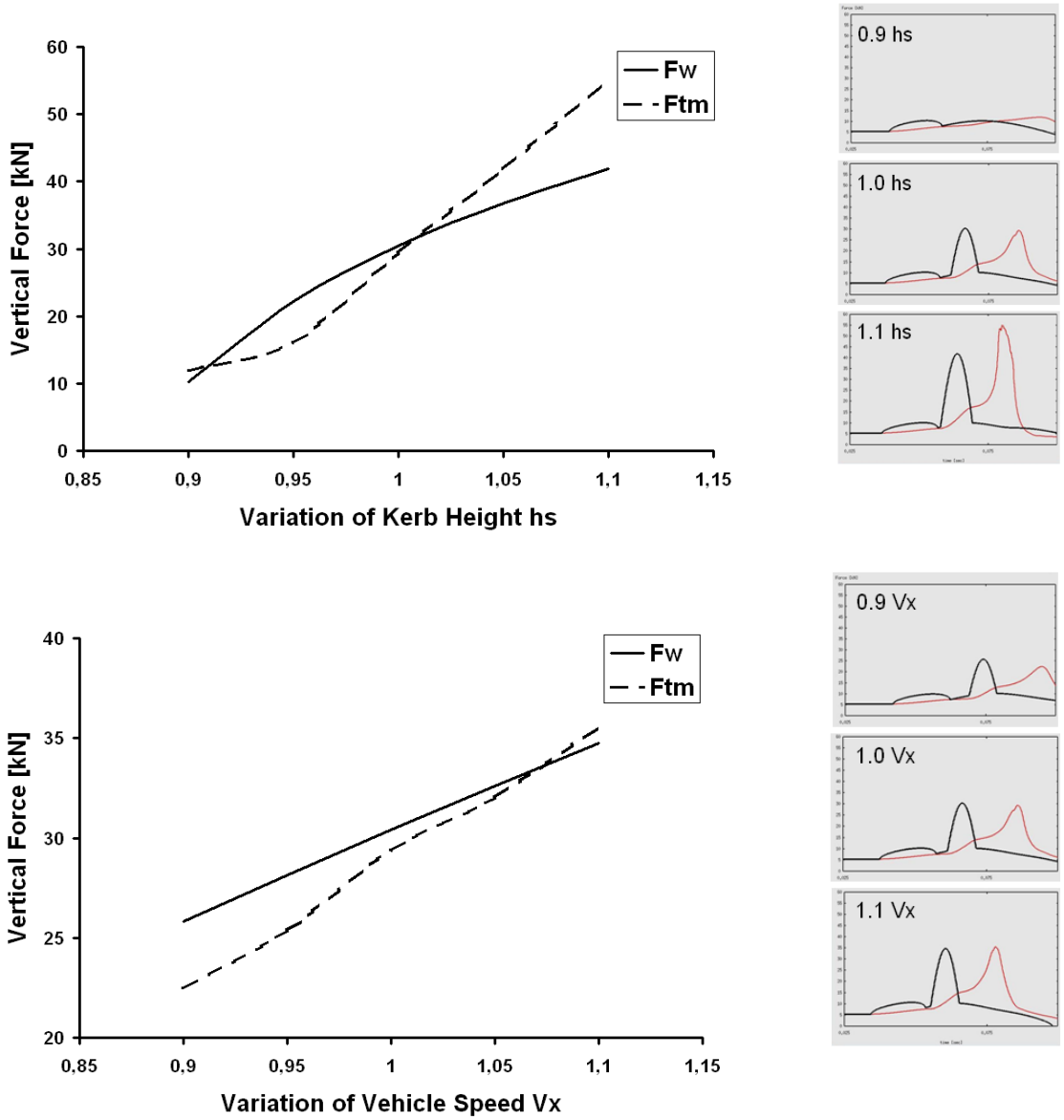

Figure 8.15: Variation of DoK manoeuvre boundary conditions step height (hs) and vehicle speed (Vx)

Results obtained from the kerb height variation show a significant increase in the peak load for the maximum kerb height (note the enlarged scale on the vertical axis). This indicates that the specified kerb height (hs = 135mm) is already at a critical level for the vehicle parameter set configuration, considering a load level beyond 50 kN. On the other hand, the reduced kerb height does not even cause a rim-to-kerb clash, as shown in the time trace plots for 0,9 hs.

The results found for the variation of vehicle speed Vx confirm the assumption that the load level is expected to increase for a rise in vehicle velocity. For the vehicle parameter set up investigated, the load increase is balanced towards the top mount force, but starts at a lower level. The trace character for wheel and the top mount of course depend on the individual component stiffness of the rim contact and the jounce bumper.

8.5 Parameter assessment

Finally, the influence of the parameters discussed in this study are assessed with regards to their individual effect intensity upon the vertical load level on the wheel (Fw) and on the top mount (Ftm). To simplify the analysis, the traces of the variation graphs are linearized within the variation range performed (in between 0.9 to 1.1). The slopes of the linearized graphs, namely the force deviation over the variation band width, are taken as a measure to indicate the significance of a given parameter. A ranking of the normalized slopes is shown in Figure 8.16. Positive sign indicates a rising force level for a given parameter's increasing value from the nominal vehicle condition. The ranking is evaluated by the sum of normalized slope magnitudes for both Fw and Ftm for each of the used parameters.

It can be noted that the ranking shown in chart 8.1 is representative for the specific vehicle model set up concerned in this study. It cannot be interpreted as a general pattern for all passenger cars, as the weighting of parameters depend on the individual values set.

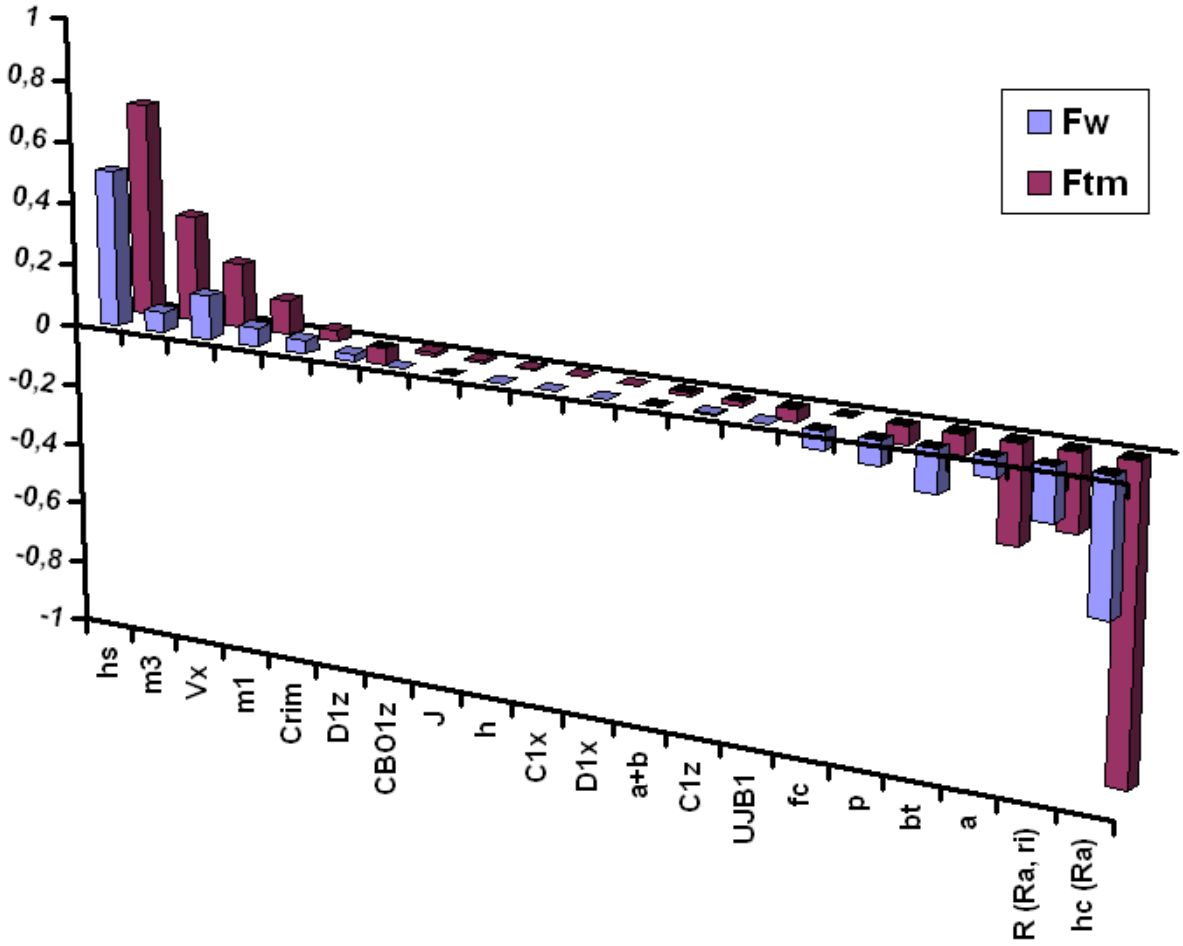

Chart 8.1: Ranking of model parameters

The ranking chart reveals the tyre sidewall height **hc** as the dominant parameter and, therefore, defined by the ranking level (-1) with respect to its influence on the top mount load. This was chosen as a datum for the normalized ranking illustration. For the case, that the top mount load would need to be reduced to cope with design targets, the most efficient modification of the parameter set up would be an increase of the tyre sidewall height. This parameter of course is an integral property of standardized tyre architecture and can only be varied in conjunction with a tyre geometry set up of a revised tyre size. Doing so, the parameter influence of tyre roll radius **R**, width **bt** and sidewall lateral deflection **fc** would also need to be taken into account.

Step size **hs** and vehicle speed **Vx** are test boundary conditions, specified as sign off requirements and should not be varied, other than for the purpose of a test evaluation.

An alternative to the tyre modification is given by a reduction of sprung mass **m3**, and shifting the CoG position (variation of **a)**. Subsequent in ranking, the un-sprung mass

m1, tyre pneumatic pressure **p**, free jounce travel **UJB1** and last, not least the wheel radial stiffness **Crim** and vertical damping **D1z** are metrics expected to have potential to relieve or worsen the top mount load level. The remaining parameters are considered to be of negligible influence. Surprisingly this can be seen for the influence of the suspension spring stiffness **C1z**. The conclusion is, that the bumpers, typically featuring a distinctive progression, dominate the vertical loads. In this context, it is a surprising model outcome that the body stiffness **CBO1z** does not have a strong influence upon the top mount level. This was not expected, as the model validation discussed in chapter 7, indicated this parameter as being essential for a successful calibration. The reason is assumed to be the low speed level (25km/h) used to conduct the study. The low speed test condition does not induce excessive loads such as those seen for higher speeds (40km/h), thus body stiffness in this case is less significant.

A similar discussion can be conducted to address the parameters affecting the wheel force level. To obtain a more general overview about the influence of the parameters, a decision matrix shown in table 8.2 provides a parameter evaluation for the model set up.

	Parameter	Fw	Ftm	
Geometry				
Wheel base & CoG	a	(-)	(- -)	longitudinal dist CoG to front WC
	h	( )	( )	CoG height to ground
Suspension	UJB1	( )	(-)	wheel free jounce travel
Tyre	R (Ra, ri)	(- -)	(- -)	wheel roll radius
	hc (Ra)	(- - -)	(- - - -)	carcass height
	bt	(- -)	(-)	belt width
	fc	(-)	( )	sidewall concavity
Kinetic				
Masses and Inertia	m1	(+)	(+)	front wheel unsprung mass
	m3	(+)	(+ + +)	(body + load) / 2 sprung mass
	J	( )	( )	rotational inertia
Tyre	p	(-)	(-)	pneumatic pressure
Stiffness	C1z	( )	( )	front road spring stiffness
	C1x	( )	( )	front longitudinal WC. stiffness
	CBO1z	( )	( )	body front top mount vert. stiffness
	Crim	(+)	(+)	rim radial edge stiffness
Damping	D1z	(+)	(-)	front vertical damping
	D1x	( )	( )	front longitudinal damping
DoK Test				
	Vx	(+)	(+ +)	vehicle speed
	hs	(+ + +)	(+ + + +)	kerb height

Table 8.2: Parametric evaluation for CD340 front suspension, effect on vertical load

The chart shows signs (+) for an increase and (-) for a decrease in the vertical load with a rising magnitude for a parameter value, an empty bracket ( ) indicates a neutral effect.

8.6 Closure

A parametric study is conducted to evaluate the influence of model parameters upon the vertical wheel and top mount loads and to evaluate the model consistency. The parameters were varied within a 10% range of a baseline, defined by the nominal conditions for a FORD Galaxy (CD340). The study was performed for the comprehensive front suspension model parameter set up. The influence of various parameters was evaluated individually, followed by an interpretation with regards to the physics of the system response. The study results are summarized in a ranking chart and a decision matrix to assess and evaluate the influence of model parameters.

Chapter 9: Source Code structure

9.0 Introduction

The entire software used to set up the vehicle model, bumper force transfer simulation and the tyre force response is comprehensively developed on basis of author's written FORTRAN tools. This includes also numeric applications, such as solver and interpolation methods described in appendix A. No commercial software was used. A reason for avoiding commercial codes is that new approaches, like the map concept routine or the tyre chain model can be developed and tested in a fully controlled software environment, without the need to fulfil boundary conditions specified in a commercial code. Furthermore, numerical effects generated from a 'black box' do not need to be considered. The FORTRAN source code is, therefore, a stand-alone document and is seen as an integral part of this thesis.

As the code is of modular structure, single elements, such as the bumper force response module, can be linked to commercial MBS solvers as external subroutines.

In this chapter, the code module structure and its input / output files are presented.

9.1 Code Modular Structure

An overview about the source code modules is shown in Figure 9.1.

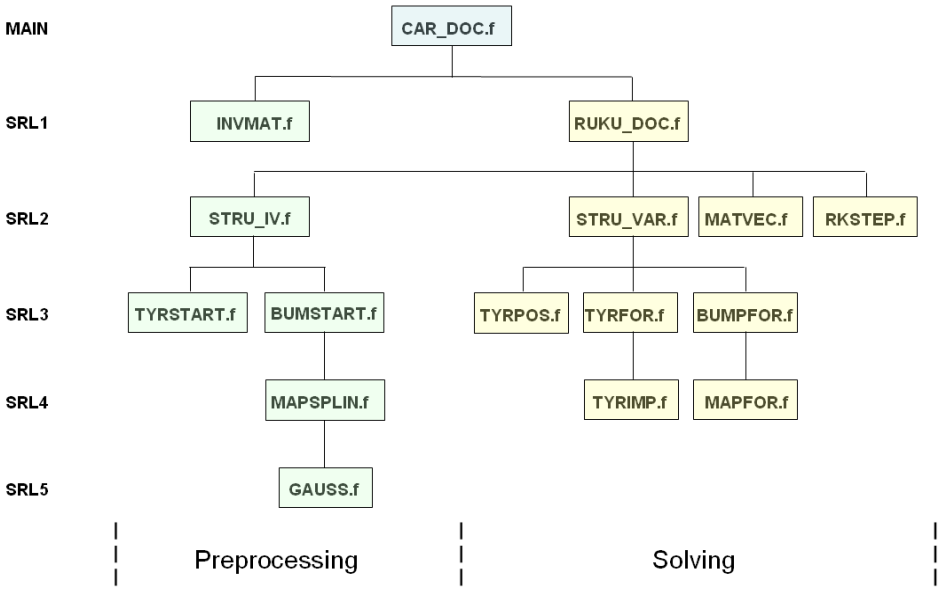

Figure 9.1: Code structure overview

The left column reveals the source code hierarchy on top the main program followed by subroutine levels SRL1 – SRL5. The hierarchy describes the subsequence of the call-, respectively feedback relation between the modules. Below the main program CAR_DOC, the modules are divided into two groups to sort the pre-processing of the structure invariant system properties on the left, and the solving of the structure variant system in the time domain on the right side.

9.2 Source code modules

The main program CAR_DOC reads in all the structure invariant system parameters described in the parameter study, chapter 8. A first pre-processing is initiated by the call of INVMAT to generate the inverse mass matrix. This allows use of the mathematical expressions of the form shown in the appendix A, equation A.4:

$$\{\ddot{X}\} = [M]^{-1}\left(\{FE\} - [D]\cdot\{\dot{X}\} - [C]\cdot\{X\}\right) \tag{9.1}$$

It is noted that also non-diagonal, full set matrices (dynamical coupled structures) are inverted by INVMAT. The module RUKU_DOC can be seen as the central executive unit. It continues the pre-processing (left) and initiates the solving in the time domain, shown on the right. The following items provide the module specific input and output for pre-processing and solving.

9.2.1 Pre-processing

Based on the vehicle speed specified for the DoC event, module STRU_IV sets up initial values x_i and $\dot{x}_i$, z_i and $\dot{z}_i$ in longitudinal and vertical directions, beside the body pitch angle φ and $\dot{\varphi}$, for all system degrees of freedom (see Figure 9.2). The initial condition is defined by a free roll on an even ground towards the kerb. Thus, it describes a quasi-static condition in z and a constant velocity in x- direction. The vehicle remains in design position, where vertical velocities $\dot{z}_i$ are commonly zero. All longitudinal velocities $\dot{x}_i$ are of constant magnitude as specified for the DoC event.

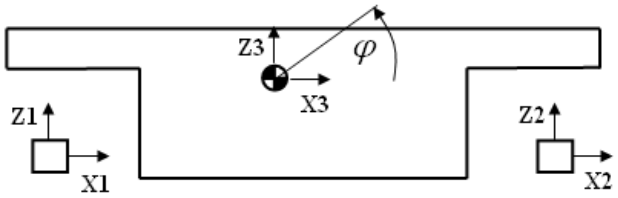

Figure 9.2: STRU_IV initial value set up

For further pre-processing, STRU_IV calls the modules TYRSTART and BUMSTART. TYRSTART is used to derive initial tyre patch deformation values tpx and tpz, caused by the static equilibrium loads in vehicle design position and the initial wheel centre distance towards the kerb (see Figure 9.3). Index 1, 2 defines the front / rear wheel.

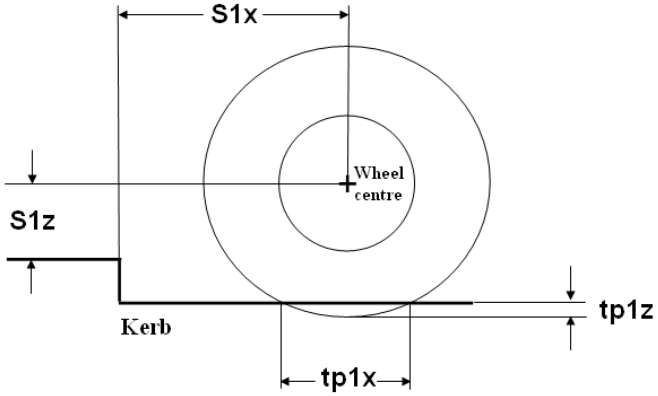

Figure 9.3: TYRSTART, initial tyre patch deformation and WC distance to kerb

BUMSTART analyses the initial suspension free travel UJB and URB to jounce bumper and rebound stop engagement for the vehicle in design position.

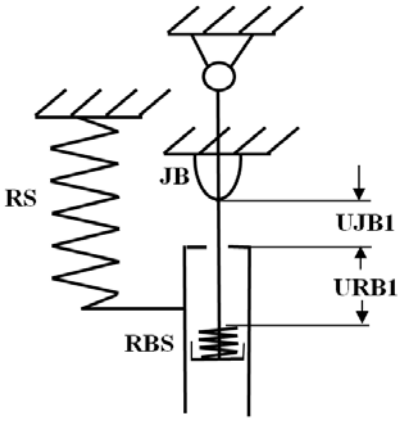

Figure 9.4: BUMSTART, initial jounce- and rebound free travel UJB1,2 and URB1,2 front and rear suspension

The pre-processing operation is finalized by BUMSTART which also delivers spline coefficients for the force response map, based on recorded traces gained from sinusoidal actuation. To do so, this module transfers the discrete spline points to MAPSPLIN, where the equation system is set up and solved in conjunction with module GAUSS.

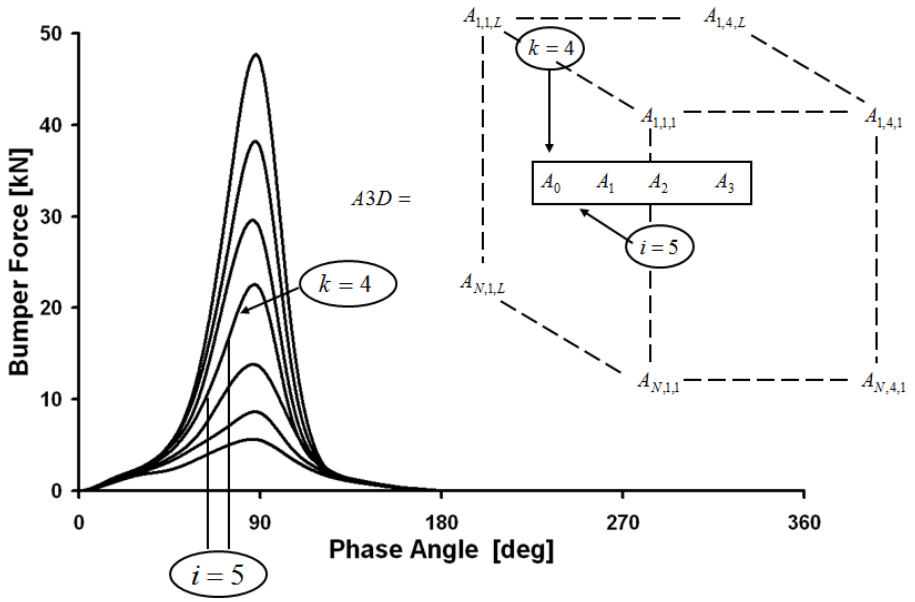

Figure 9.5: MAPSPLIN, spline coefficients to set up three dimensional bumper map array A

9.2.2 Solving

In contrast to the pre-processing, dealing with the structure invariant parameters, the modules organized in the solving block deal with the structure variant attributes that change over time.

The solving operation in the time domain is centrally organized by the RUKU_DOC module. As indicated by the module name, it is based on a conventional Runge-Kutta integration presented in appendix A. For each single time step, RUKU_DOC performs a comprehensive structure analysis with regards to the time variant system parameters. It is also used as the main source for the output files listed in item 9.3.

Depending on the current vehicle deflection- and velocity state, as well as the wheel position relative to the kerb, additional forces, caused by bumper engagement and belt-to-kerb contact, are applied as external forces, defined in module STRU_VAR (see also chapter 4, item 4.2). STRU_VAR separates between tyre- (TYRPOS, TYRFOR) and bumper forces (BUMFOR) in subordinated level SRL3.

(a) Tyre response

Before the tyre force response can be derived by TYRFOR, the module TYRPOS is used to detect the current wheel position relative to the kerb and to analyse a possible contour geometry intersection in between the belt and the kerb as shown in Figure 9.6.

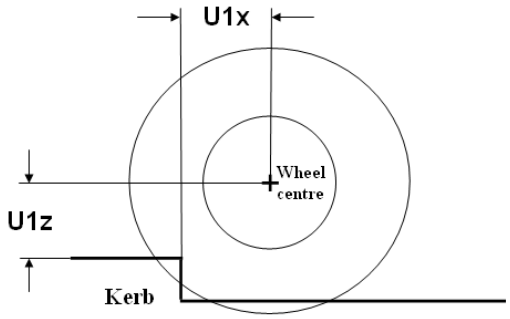

Figure 9.6: TYRPOS, wheel centre position relative to kerb at current time step.

In case of an intersection with the rigid assumed kerb (contact condition), module TYRFOR is called to quantify the radial belt deformation f1 against edge and to calculate the response force in conjunction with TYRIMP.

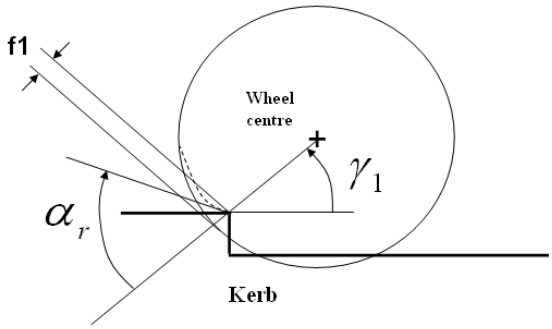

Figure 9.7: TYRFOR, wheel centre position relative to kerb at a current time step

After a differentiation is performed for pure flat, combined flat, edge and pure edge contact, the actual force response is provided by module TYRIMP. This is the interface to the actual tyre model, linked to the pure analytical equations 6.9 to 6.14 derived in chapter 6, item 6.4.3. Alternatively, the chain iteration model, item 6.5, can be linked here. The chain model would additionally need to be equipped with the five separate iteration steps addressed in chapter 6, item 6.6.3.

(b) Bumper response

In a first step, BUMFOR analyses the current bumper engagement status, shown for a front jounce bumper in Figure 9.8:

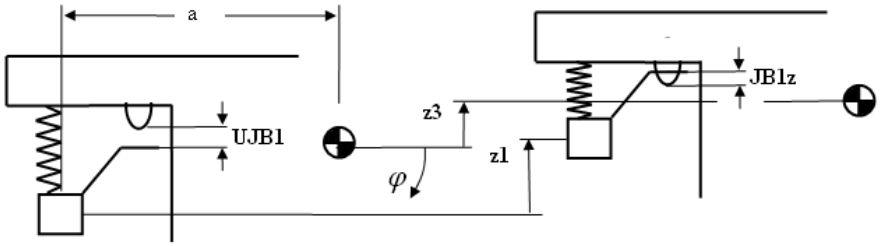

Figure 9.8: BUMFOR, bumper engagement at a current time step

In case of engagement, the current deformation state, displacement 'S' and deflection speed 'V', is transferred to MAPFOR to generate the bumper force response. The map to solver interaction concept was derived in chapter 5, section 5.3. An illustration of the map concept that shows the force response Fdatum as a function of 'S' and 'V' is given in Figure 9.9:

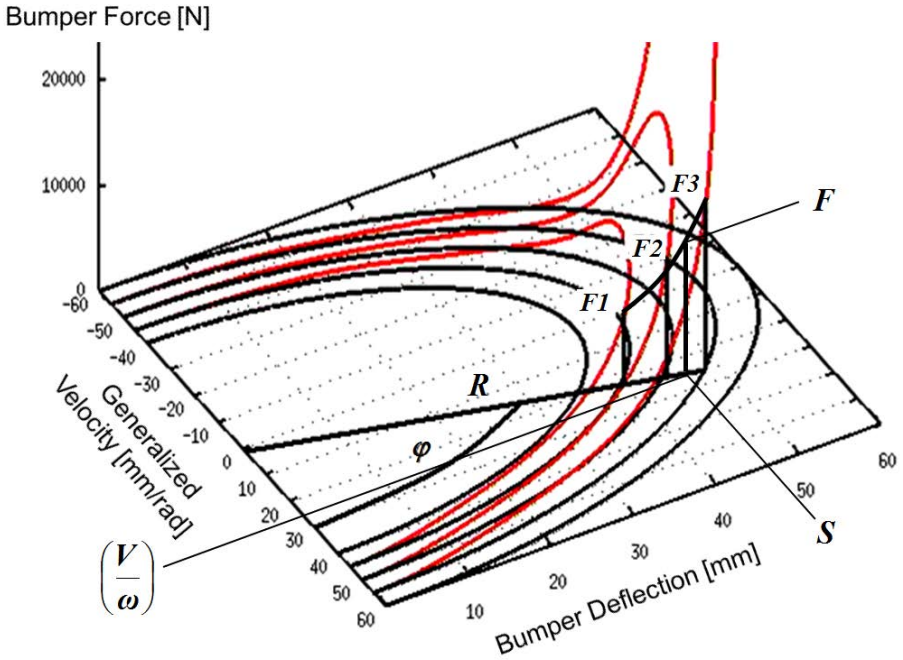

Figure 9.9: MAPFOR, force response **F**, function of displacement **S** and deflection velocity **V**

MAPFOR represents the final step in the process chain of structure variant system analysis under the central module STRU_VAR. The solution continues by module MATVEC to perform the matrix – vector multiplications:

$$\{F_C\} = [C] \cdot \{X\}$$
$$\{F_D\} = [D] \cdot \{\dot{X}\} \qquad (9.2)$$

These vectors represent the internal reaction forces found for spring and damper elements addressed in equation 7.3, used to calculate the accelerations in module RKSTEP, where all four Runge-Kutta steps are performed.

$$\{\ddot{X}\} = [M]^{-1}\left(\{FE\} - [D] \cdot \{\dot{X}\} - [C] \cdot \{X\}\right) \qquad (9.3)$$

9.3 Output files and formats

Table 9.1 shows a list of standardized output files of CAR_DOC. All output files (.TMP) are in ASCII format.

UNIT	FILENAME	OUTPUT	COMMENT
40	STATEVEC.TMP	$T, \{X\}, \quad T, \{\dot{X}\}, \quad T, \{\ddot{X}\}$	state vector
300	SPRIFOR.TMP	$T, \quad FS1z, \quad FS2z, \quad FS1x, \quad FS2x$	Spring forces
301	DAMPFOR.TMP	$T, \quad FD1z, \quad FD2z, \quad FD1x, \quad FD2x$	Damper forces
302	TMFOR.TMP	$T, \quad FTM1z, \quad FTM2z$	Top mount total forces
303	WCFOR.TMP	$T, \quad FWC1z, \quad FWC2z, \quad FWC1x, \quad FWC2x$	Wheel center forces
304	BUMFOR.TMP	$T, \quad FJB1, \quad FRB1, \quad FJB2, \quad FRB2$	Bumper- / rebound stop forces

Table 9.1: Standard output files of CAR_DOC

The output files defined by units 40, 300, 301 and 304 can directly be derived from the solver operations, whereas the top mount total forces (302) and the wheel centre forces (303) are derived separately.

9.3.1 Top mount forces

The top mount combines three separate load path

- road spring
- suspension damper and
- jounce bumper

in a single component. The principle is depicted in Figure 9.10:

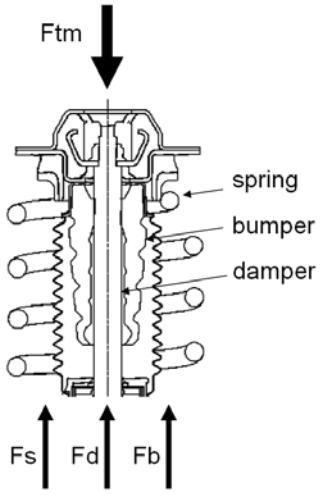

Figure 9.10: Top mount force components spring Fs, damper Fd and bumper Fb

The total top mount force applied to the body structure is derived by the sum of (300), (301) and (304).

9.3.2 Wheel centre forces

For the evaluation of the spindle loads, two options are discussed. On the one hand, the force can be quantified by the external tyre forces reduced by the inertia terms determined by the wheel acceleration. On the other hand, the complete dynamic equilibrium is assembled by the additional spring, damper and, in case of engagement, bumper forces.

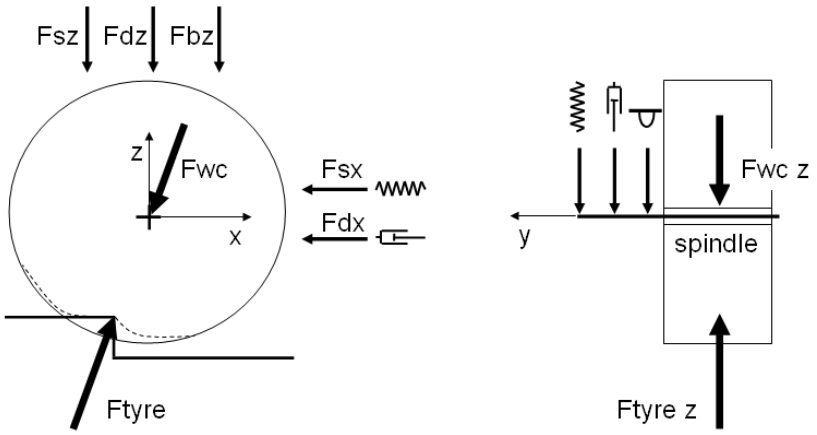

Figure 9.11: Top mount force components spring Fs, damper Fd and bumper Fb

For the front wheel, this assumption leads to:

$$\begin{aligned} F_{WC\_x} &= F_{tyre\_x} - m_1 \cdot \ddot{x}_1 && = F_{sx} + F_{dx} \\ F_{WC\_z} &= F_{tyre\_z} - m_1 \cdot (\ddot{z}_1 + g) && = F_{sz} + F_{dz} + F_b \\ F_{WC} &= \sqrt{F^2{}_{WC\_x} + F^2{}_{WC\_z}} \end{aligned} \qquad (9.4)$$

9.4 Closure

In this chapter an overview about the source code structure and its in- and output files is given. The software is a FORTRAN code of modular structure, subdivided into main- and subroutine units. The individual modules, such as bumper force response map or the tyre chain model, can be used as stand alone items also. Thus, these modules enable upgrade compatibility for a BiP event simulation and also can be linked as external subroutines to commercial multi body solvers like ADAMS.

Chapter 10: Thesis summary and outlook

10.1 Conclusions and contribution to knowledge

Based on the results provided in this thesis, the following overall conclusions can be drawn.

- It is important to develop an accurate model for the jounce bumper to include its hysteretic behaviour when subjected to loading, particularly of impulsive nature such as kerb strike or pot-hole braking. Under these conditions the bumper undergoes dynamic contact forces which act over its full deflection range. In case of a simplified model, based on a static force response curve only, the hysteresis and thus, the dissipation of energy, would be neglected. This would typically lead to an over-estimation of the peak load. An assessment to drop test measurements has revealed deviations of up to 30% as shown in Figure 7.13.

- The bumper force response map simulation concept, based on data derived from harmonic bumper actuation is also applicable to analyse force response gained from non-harmonic actuation, such as that typically expected after a kerb strike. This was confirmed by assessment of response to drop tests (Figures 7.11, 7.12).

- In general, conventional hydraulic test equipment is not suitable for recording the force response traces which are required for the map input. This is particularly true in case of large bumper deformation range which consequently demands for large actuation amplitudes, combined with high end bumper force levels of the order of 40 kN. In conjunction with a kerb strike, the relevant actuation frequency (in this case 10 Hz) and the flow capacity limit the feasibility for conduct such tests. A mechanical crank was developed to overcome this shortcoming.

- A simple mathematical tyre model (equation (6.14)), based on the input of a few geometrical parameters and pneumatic pressure suffices to model the static force response against kerb edge radial contact deformation in the deflection range up

to a rim clash. The tyre structural compliance contribution to the overall force response does not normally exceed a range of 10% for a flat contact with the ground. This statement, already addressed in literature **[21]** (Figure 2.42) remains also valid for an edge type contact. This was confirmed by an assessment of static measurements performed for a pneumatic pressure of 2 bar (Figure 7.3).

- The tyre pneumatic pressure level can be considered to remain almost constant in case of flat and edge type radial penetrations up to the full deflection range extending to a rim contact (Figure 7.2). Thus, a constant pressure approach used in both mathematical and chain type tyre models is justified.

- For the FORD specified kerb strike event, the force level caused by the belt to rim contact clash significantly exceeds the pneumatic force response of full tyre deflection. Thus, a thorough specification of the rim stiffness is obligatory for the wheel force analysis (Figures 7.24, 7.25).

- At “high” speed impact (40 km/h) the top mount force simulation drastically exceeds those measured form a vehicle. This mismatch could be attenuated by the introduction of a stiffness element to represent the vehicle body compliance. This observation confirms the importance of considering the vehicle body structural behaviour in kerb strike events and other abusive boundary conditions.

10.2 Achievement of aims

The objectives of the research, set in the introduction chapter have been achieved. These are addressed below.

Objective 1: Develop a minimal parameter vehicle model, tailored for the simulation of the vertical suspension load after kerb strike. It shall be adapted to the FORD specified boundary conditions for DoK and shall also protect upgrade compatibility to simulate the BiP event at a later stage.

In chapter 4, a conventional in-plane bicycle model concept was extended to 7 degrees of freedom to take into account the fore- aft wheel centre suspension movement. The model is tailored to simulate DoK and includes a mathematical tyre model. Wheel travel is limited by a non-linear jounce bumper model and a rebound stop element. In all, a total number of 35 parameters define the entire vehicle model. Upgrade compatibility to BiP is arranged through the modular code structure.

Objective 2: Generate a valid alternative to a rheological approach for a bumper model that takes the velocity induced hysteresis into account.

A spatial map concept is described in chapter 5 to address the energy dissipation effects in the force response under impulsive conditions for the full range of jounce bumper deformation range. The concept, including data acquisition, transformation to map format and integration to a solver can be incorporated into a standardized process. This methodology is considered as a novel, enabling an easy simulation of velocity- related hysteresis of polymeric elements. The concept is considered to be applicable also to conventional and hydro-bushings.

Objective 3: Derive a tyre model to simulate the pneumatic induced static force response against flat and edge type radial deformation.

In chapter 6, a mathematical static force response model was derived for both flat and edge type contact. The model simulates the pneumatic force response and neglects the structural compliance for simplicity reasons. It is defined by four geometrical parameters besides the pneumatic pressure. Tyre structural assumptions made for the mathematical model are confirmed by a detailed truss-type physical model and physical testing.

Objective 4: Validate the bumper and tyre models by an assessment to appropriate physical testing on component level.

A drop test simulation assessment correlation with physical measurements is performed to validate the jounce bumper force response map results in chapter 7. A comparison

with a simplified analysis based on a static force response curve shown in Fig. 7.13 reveals some shortcomings, if the hysteresis effects are neglected.
Tyre model validation is performed against physical static tests for two sizes, 205/40-R16 and 235/55-R18 and at various pressure levels as shown in Fig. 7.3 and 7.4. The dynamic behaviour was addressed in a plausibility study (Figure 7.25).

> *Objective 5: Validate the vehicle model equipped with the bumper and tyre simulation approaches on system level by a full vehicle DoK testing.*

In chapter 7, a physical full DoK test is reported with an instrumented vehicle. Recordings of the top mount force and wheel centre deflection are compared with the simulation results in Fig. 7.16 and show good conformance.

> *Objective 6: Carry out a parameter study to verify the plausibility of the vehicle model on basis of a specific FORD vehicle.*

A full parametric study for 20 independent vehicle parameters is carried out in chapter 8, based upon the FORD vehicle CD340. The study is supplemented by a plausibility discussion and chart 8.1 for a parameter ranking with regards to vehicle-specific impact with different vertical load levels.

10.3 Critical assessment of approach and suggestions for future work

An analysis of the vehicle simulation results gained for the top mount forces shows reasonable conformance with physical tests for velocity range up to 25 km/h, but reveals a significant over-estimation for a crossing speed of 40 km/h (Figure 7.19). This deviation is because of the rigid attachment of the jounce bumper to the vehicle body. An additional linear stiffness element was used to correlate the simulation results to the measured force signal. This observation confirms that vehicle body structural stiffness is a significant parameter which needs to be taken into account, especially for higher vehicle velocities in kerb strike. This aspect requires a detailed vehicle body structural analysis to determine the load path for a vertical top mount force directed via the body structure towards the attachment points. Such investigation can be performed by means

of an inertial relief analysis, a standard method in FEM. Detailed body structure models are in general not at hand in the beginning of a development program, thus carry over experience must be used instead.

The data acquisition for the jounce bumper force response map was performed via a mechanical crank. Force response traces were gained when the crank rotational speed achieved a level equivalent to the specified frequency. During the rig rotational ramp up operation towards the specified frequency, the bumper element is subjected to an actuation and hence, a bumper preconditioning cannot be avoided. Therefore, it is intended to update the bumper rig to allow decoupling of the bumper engagement during the ramp up process.

The mathematical tyre model is set up to analyse radial force response against either an edge or a flat type contact. A combination of both modes, as expected to occur during a kerb roll over mode, where the initial edge contact is considered to become a combined edge and flat type contact (Figure 6.33). This transition is not currently addressed by the developed model. In principle, the chain type truss model is suitable to be applied to such a combined form of contact as described under paragraph 6.4.

With the DoK minimal parameter model, it is intended to predict the vertical suspension load envelope. This represents a first milestone of the overall vision of a comprehensive loading model. The model is compatible for an upgrade to a Brake into Pothole (BiP) simulation, as it is of a modular structure with key features, such as the tyre and bumper simulation concepts. The model can be extended to perform a longitudinal load analysis as well. As the nature of a lateral force impact would induce roll of the vehicle, the existing model tailored to the DoK event cannot easily be adapted to analyse such manoeuvres. A completely different model may be required.

To cope with BiP, the tyre modelling should preferably be extended to the chain type physical truss model, proposed in this thesis. This would allow a combined flat and edge contact, as well as having the potential to take the brake-induced circumferential force component into account. The proposed model would need to be extended for this purpose.

A key feature required to model BiP is the suspension longitudinal stiffness characteristics. On a front McPherson suspension geometry, this is mainly determined by the linking elements (conventional and hydro-bushings) to the vehicle body structure. The map concept is considered to be applicable to these chassis polymer elements in its standardized format, but would need to be validated by further physical testing. As for the jounce bumper, relevant actuation frequencies for the data acquisition would need to be defined for the specific bushing positions and applications.

List of references

[1] **Rai, N. S., Solomon, A. R.**, Computer Simulation of Suspension Abuse Tests Using ADAMS, International Congress & Exposition, Detroit, Michigan, SAE 820079, 1982.

[2] **Gallrein, A., Bäcker, M.**, CDTire: a tire model for comfort and durability applications, Fraunhofer- Institut für Betriebsfestigkeit und Systemzuverlässigkeit LBF, 2008.

[3] **Gipser, M.**, ADAMS/FTire- A Tire Model for Ride & Durability simulations. International ADAMS User's Conference, Tokyo 2000.

[4] **Haga, H.**, Evaluation of tyre models for durability loads prediction using a suspension-on-a-drum environment, Vehicle System Dynamics Vol. 43, Supplement 281-296, 2005.

[5] **Haga, H.**, Simulating very large Tire Deformations withCD tire, SAE 2009-01-0577, 2009.

[6] **Gallrein, A, Bäcker, M.**, A tire model for very large tire deformations and its application in very severe events, SAE 2010-10M-0059, 2010.

[7] **Yoon, J., Kye, K.**, Suspension Abuse Test Simulation using model stress recovery, SAE 2004-01-0776, 2004.

[8] **Gipser, M.**, FTire, a New Fast Tire Model for Ride Comfort Simulations. International ADAMS User's Conference Berlin, 1999.

[9] **Holzweißig, F., Dresig, H.**, Lehrbuch der Maschinendynamik, 4. Auflage, Fv Leipzig, 1994

[10] **Girkmann, K.**, Flächentragwerke, Springer Verlag, sechste Auflage, 1986

[11] **Timoshenko, S.**, Theory of elasticity, Mc Graw-Hill, 1934

[12] **Timoshenko, S.**, Schwingungsprobleme der Technik. Springer Verlag, 1962.

[13] **Bathe, K. J.**, Finite Elemente Methoden, Springer Verlag, 1990

[14] **Rahnejat, H.**, Multibody dynamics, Vehicles, Machines and Mechanisms, Arrowsmith Ltd, UK, 1998.

[15] **Schiehlen, W., Popp, K.**, Eine Einführung in die Dynamik des Systems Fahrzeug – Fahrweg, Vieweg und Teubner, 1993.

[16] **Corves, B.**, Lecture Multi Body Dynamics, Department of Mechanism Theory and Dynamics of Machines, RWTH Aachen University, 2011.

[17] **Thomson, T.**, Theory of vibrations with applications, fourth edition, Stanley Thornes Ltd, 1993.

[18] **Pestel, E.**, Technische Mechanik Band 3, Kinematik und Kinetik, Hochschultaschenbuch-Verlag, 1969.

[19] **Gross, D, Hauger, W., Wriggers, P.**, Technische Mechanik 4, Hydromechanik, Elemente der Höheren Mechanik, Numerische Methode, 7. Auflage, Springer Verlag, 2009.

[20] **Magnus, K.**, Schwingungen, Teubner Verlag, 1964.

[21] **Willumeit, H. P.**, Modelle und Modellierungsverfahren in der Fahrzeugdynamik, Teubner Verlag Stuttgart – Leipzig, 1998.

[22] **Zurmühl, R.**, Praktische Mathematik für Ingenieure, Springer Verlag, 1960.

[23] **Feldmann, D.**, Repetitorium der numerischen Mathematik, Binomi Verlag Hannover, 2001.

[24] **Rill, G.** Instationäre Fahrzeugschwingungen bei stochastischer Erregung, Diss., Univ. Stuttgart, 1983.

[25] **Müller, P. C., Popp, K. u. Schiehlen, W.O.**, Berechnungsverfahren für stochastische Fahrzeugschwingungen, Ing.- Arch., 49, 235-254, 1980.

[26] **Ammon, D.**, Modellbildung und Systementwicklung in der Fahrzeugdynamik, Habitilationsschrift, Universität Karlsruhe, 1996

[27] **Bestle, D.**, Analyse und Optimierung von Mehrkörpersystemen, Springer Verlag, 1994.

[28] **Ammon, D.**, Gipser, M., Rauh, J., Wimmer, J., Effiziente Simulation der Gesamtsystemdynamik Reifen-Achse-Fahrwerk, High Performance Simulation of Tire, Suspension and steering System Dynamics, VDI Berichte Nr. 1224, 1995.

[29] **Göldner, H.**, Leitfaden der Technischen Mechanik, Fv Leipzig, 1966

[30] **Kobetz, C.**, Modellbasierte Fahrdynamikanalyse durch ein an Fahrmanövern parameteridentifiziertes querdynamisches Simulationsmodell, Dissertation Universität Wien, 2003.

[31] **Ruf, E.**, Theoretische Untersuchungen des Federungsverhaltens von Vierrad-Straßenfahrzeugen (Theoretical investigations into the suspension behaviour

of four wheel road vehicles). Fortschr. –Ber. VDI-Z., Reihe 12, Nr44, 104-105, Düsseldorf, 1983

[32] **Bakker, E. and H.-B. Pacejka**: A new tire model with an application in vehicle dynamics studies. SAE- P. 89 00 87, Society of Automotive Engineers Inc., 1989.

[33] **Pacejka, H. B.**: Tire and Vehicle Dynamics, Butterworth-Heinemann, Oxford, 2002.

[34] **Koettgen, V.**, LMS Conference Europe. 2006.

[35] **Schmeitz, A.J.C.**, 'A semi-empirical three dimensional model of the pneumatic tyre rolling over arbitrarily uneven road surfaces', dissertation, Delft University of techniology, Delft, The Netherlands, 2004.

[36] **Böhm, F.**, Zur Mechanik des Luftreifens, Habilitationsschrift Stuttgart, 1965.

[37] **Soedel, W.**, Vibration of shells and plates, Marcel Dekker, 1981.

[38] **Geng, Z., Popov, A. A., Cole, D. J.**, Measurement, identification and modeling of damping in pneumatic tyres, International Journal of Mechanical Sciences 49, page 1077 – 1094, 2007.

[39] **Tsotras, A., Mavros, G.**, The simulation of in plane tyre modal behaviour: a broad modal range comparison between analytical and discretised modelling approaches, Aeronautical and Automotive Engineering Department, Loughborough University, 2009.

[40] **Bäcker, M., Gallrein, A.**, A method to combine a tyre model with a flexible rim model in a hybrid MBS/FEM simulation setup, 2011.

[41] **Herkt, S.**, Model Reduction of nonlinear problems in structural mechanics: Towards a Finite Element Tyre Model for Multibody Simulation, 2008.

[42] **Zamzamzadeh, M., Negarestani, M.**, A 3D Tire/Road Interaction Simulation by a developed model (ABAQUS code), Chiang Mai, Thailand, ASIMMOD, 2007.

[43] **Zegelaar, P.W.A. and Pacejka, H.P.**, Dynamic tyre responses to brake torque vibrations. Vehicle System Dynamics, vol. 27, supplement 1, 1997.

[44] **Bohrmann, S**., Grundbegriffe zum Nachschlagen, Vibracoustic Firmenschrift, Schwingungstechnik für Automobile, 2002

[45] **Ward, I. M., Sweeney, J.**, The Mechanical Properties of Solid Polymers, second edition, John Wiley & Sons, Ltd, 2004

[46] **Lion, A.**, Phenomenological modelling of strain induced structural changes in filler reinforced elastomers: a time domain formulation of the Kraus model, Kautsch. Gummi Kunst., 4, 2005

[47] **Jöckel, M., Bruder, F., Franz, T.**, Charakterisierung und Modellierung des dynamischen Übertragungsverhaltens von Elastomerlagern für die Lastdatenberechnung,Fraunhofer Institut, LBF, Darmstadt, 2008.

[48] **Berg, M.**, A non linear rubber spring model for rail vehicle dynamics analysis, Vehicle Systems Dynamics, Band 30/1998 Heft 3-4, 197-212, 1998

[49] **Dronka, S. Rauh, J.**, Co-Simulations Interface for User-Force-Elements, Vortrag zum SIMPACK-User-Meeting, Baden Baden, 2006

[50] **Steinweger, T., Weltin, U.**, Mehrdimensionale Beschreibung elastischer Lager in MKS-Simulationen. VDI Berichte NR 1416, 1998

[51] **Svensson, M., Hakansson, M.**, Hyrobushing model for Multi-Body Simulations, Master's dissertation Lund University Sweden, printed by KFS I Lund AB, 2004

[52] **Kessler, J.**, Erfassung dynamischer Kennwerte von Gummi-Metall-Elementen und anderen elastischen Elementen. Haus der technik e.V. Tagung, 1983

[53] **Wick, A.**, Ermittlung dynamischer Kennwerte an Gummi-Metall-Elementen. Automobiltechnische Zeitschrift (ATZ) 88, Nr. 4, Franck'sche Verlagshandlung Stuttgart, 1986

[54] **Schranz, S.**, Cellasto: Grundlagen, Mechanische Eigenschaften & Bauteilsimulation, Vortrag Lemförde, 07.11.2006

[55] **Austrell, P. E., Wirje, A.**, A viscoelastic bump stop model for multi-body simulations based on impact test data, fifth european conference on Constitutive Models for Rubber (ECCMR), France, 2007

[56] **v. Chappuis, H.**, Simulation of impulsive vertical suspension bumper response subjected to abuse manoeuvers, DVM workshop, Darmstadt, 2011.

[57] **v. Chappuis, H., Mavros, G., King, P., Rahnejat, H.**, Prediction of impulsive tyre- suspension response subjected to kerb strike, ECCMAS Multibody Dynamics thematic conference, Brussels, 2011

[58] **Girkmann, K.**, Flächentragwerke, Springer Verlag, sechste Auflage, 1986.

[59] **Timoshenko, S.**, Strength of materials, part II, advanced problems, second edition,Van Nostrand Comp., 1962.

[60] **Szabo, I.**, Höhere Technische Mechanik, Springer Verlag, 1964.

[61] **Beer, G.**, Baustatik 2, Seilstatik, Theorie zweiter Ordnung, Skript Universität Graz, 2004.

[62] **Collatz, L.**, Numerische Behandlung von Differentialgleichungen, Springer Verlag, 1951.

[63] **Niemmann, G.**, Maschinenelemente Band II, Springer Verlag, 1960.

[64] **Faires, J. D., Burden, R. L.**, Numerische Methoden, Spektrum Akademischer Verlag Heidelberg, Berlin , Oxford, 1994.

Appendix A: Numerical methods used

A.0 Introduction

Analytical solutions of equations of motion, in general deliver precise results or closed form solutions, but usually embody various assumptions. Numerical methods are often used as an alternative, if an analytical solutions cannot be obtained and are usually approximate, but with lesser degree of assumptions. In such cases, an approximation derived from numerical methods is accepted as a substitute for the exact analytical solution. Analytical mathematical results can be derived directly from algebraic terms, whereas solutions derived from numerical methods are in general the result of an approximation process. An example is applying Newton integral calculus to find the area below the graph of a function. An approximation for the area can also be found by summing up the rectangular areas below the stepped polygon in the graph. Deviations from the exact analytical solution can be minimized by increasing the number of elements, thus the computational effort. This is effected by increasing the number of polygon edges or by using rectangular trapezoids instead of rectangles for a better curve fit. This describes a common nature of numerical methods; its precision is linked to the numerical effort expended and the method used.

Here, those numerical methods are described which are relevant to the subject matter of this thesis. The scope includes two main topics:

- Numerical integration of coupled, second order ordinary differential equations in the time domain.
- Curve interpolation, using third order spline functions.

The first topic is concerned with the solution of equations of motion derived in chapter 2 for the vehicle simulation model, whilst the second topic is used to derive the data condensation of the map approach, described in chapter 5.

A.1 Numerical integration of differential equations

Beside a variable x, differential equations also contain expressions of derivatives of x, such as $y' = dy/dx$, $y'' = d2y/dx^2$ and so forth. It can generally be expressed as $y^{(n)} = f(x, y, y', y'', \ ... \ , y^{(n-1)})$. To obtain a solution, the equations needs to be integrated with respect to x for n times. Analytical mathematics provides several, to some extend creative methods in order to solve the differential equations. Unfortunately, the number of equations, that can be solved analytically, is limited to a few special cases only, whereas a graphical or numerical solution can be provided in almost every case.
From the wide range of this subject, this appendix is limited to the application methods for equations of motion. Initially, the structure and properties of such equations are presented, followed by a discussion of the general features known for first order equations, intended to explain the method of numerical integration. Finally, the detailed Runge-Kutta process and its application to solve a set of coupled differential equations is described.

A.1.1 Structure and attributes of coupled equations of motion

The differential equations discussed in this thesis are functions of time. Thus, they are of the general form: $y^{(n)} = f(t, y, \dot{y}, \ddot{y}, \ ... \ , y^{(n-1)})$, where $\dot{y} = dy/dt$. Multi-body dynamics applications, such as the vehicle model discussed in chapter 2, are limited to second order equations: $\ddot{y} = f(t, y, \dot{y})$ and contain multiple degrees of freedom. Each individual degree of freedom is expressed mathematically by an ordinary differential equation, also known as the equation of motion. The mathematical formulation derived for the assembled system, therefore, forms a set of coupled equations. In this context, the term coupled expresses the fact, that the single equation structure takes into account the physical interactions with the other degrees. The mathematical formulation of the set of equations can be organised in the form of a matrix structure as shown below:

$$[M] \cdot \{\ddot{X}\} + [D] \cdot \{\dot{X}\} + [C] \cdot \{X\} = \{FE\} \qquad \text{(A.1)}$$

The matrices M, D and C were derived in chapter 4, in which the vectors $\ddot{X}$, $\dot{X}$ and X represent the system motion and deformation state (i.e. the state vectors), FE stands for

the external force vector. Matrix sizes conform to the systems number of degrees of freedom and contain coefficients m, d and c which are multiplied with the vector components $\ddot{x}$, $\dot{x}$ and x. The term 'ordinary' is used in cases where the coefficients are constants (they are no functions of time) and addresses the fact that they only contain the derivatives with respect to a single parameter (time in this case). This is in contrast to partial differential equations, which contain derivatives of more than one variable, for example time and temperature gradients used in a heat transfer problem. The largest order derivative ($\ddot{x}$) defines the 'order'.

The equation of motion for a single degree of freedom system can be rearranged to the highest order derivative as shown in (A.2), representing a function of x, $\dot{x}$ and t in the format of a so-called initial value problem.

$$\ddot{x} = \frac{1}{m} \cdot \left[fe_{(t)} - d \cdot \dot{x} - c \cdot x \right] = f(t, x, \dot{x}) \tag{A.2}$$

In terms of physics, it means, that for an instant time t and a discrete set of initial values for x and $\dot{x}$, a discrete solution for the instantaneous acceleration $\ddot{x}$ can be determined. A two step subsequent integration of equation (A.2) leads to the system time history for x and $\dot{x}$. It can be shown that a single equation of second order (A.2) can always be separated into two equations of first order (A.3) by substituting $\dot{x} = y$ **[17]**, **[22]**.

$$\begin{aligned} \dot{x} &= y = f(t, x) \\ \ddot{x} &= \dot{y} = \frac{1}{m} \cdot [\, fe_{(t)} - d \cdot y - c \cdot x] = f(t, x, y) \end{aligned} \tag{A.3}$$

This format can also be derived starting from a vector equation (A.1), as follows:

$$\{\ddot{X}\} = \left[M\right]^{-1} \left(\{FE\} - [D] \cdot \{\dot{X}\} - [C] \cdot \{X\} \right)$$

In case of a system with two degrees of freedom, the outlined format would be:

$$\begin{Bmatrix} \ddot{x}_1 \\ \ddot{x}_2 \end{Bmatrix} = \begin{bmatrix} m_{11} & m_{12} \\ m_{21} & m_{22} \end{bmatrix}^{-1} \cdot \left(\begin{Bmatrix} fe_1 \\ fe_2 \end{Bmatrix} - \begin{bmatrix} d_{11} & d_{12} \\ d_{21} & d_{22} \end{bmatrix} \cdot \begin{Bmatrix} \dot{x}_1 \\ \dot{x}_2 \end{Bmatrix} - \begin{bmatrix} c_{11} & c_{12} \\ c_{21} & c_{22} \end{bmatrix} \cdot \begin{Bmatrix} x_1 \\ x_2 \end{Bmatrix} \right) \tag{A.4}$$

The matrix format can be expanded to twice the number of equations, transformed to first order forms. To do so, coupled vectors combining $\dot{x}$, $\ddot{x}$, are transformed to x, $\dot{x}$ on both sides of the equation. For simplicity reasons, the mass matrix shall be considered to be diagonal: $m_{12} = m_{21} = 0$. Thus, the inversion of M leads to:

$$\begin{Bmatrix} \dot{x}_1 \\ \dot{x}_2 \\ \ddot{x}_1 \\ \ddot{x}_2 \end{Bmatrix} = \begin{bmatrix} 0 & 0 & 0 & 0 \\ 0 & 0 & 0 & 0 \\ 0 & 0 & 1/m_{11} & 0 \\ 0 & 0 & 0 & 1/m_{22} \end{bmatrix} \cdot \begin{Bmatrix} 0 \\ 0 \\ fe_1 \\ fe_2 \end{Bmatrix} - \begin{bmatrix} 0 & 0 & 1 & 0 \\ 0 & 0 & 0 & 1 \\ c_{11}/m_1 & c_{12}/m_1 & d_{11}/m_1 & d_{12}/m_1 \\ c_{21}/m_2 & c_{22}/m_2 & d_{21}/m_2 & d_{22}/m_2 \end{bmatrix} \cdot \begin{Bmatrix} x_1 \\ x_2 \\ \dot{x}_1 \\ \dot{x}_2 \end{Bmatrix} \tag{A.5}$$

A matrix - vector multiplication and rearranging of x, $\dot{x}$, $\ddot{x}$ proves the equivalence of equations (A.4) and (A.5). For the substitutions:

$$\begin{Bmatrix} \dot{x}_1 \\ \dot{x}_2 \\ \ddot{x}_1 \\ \ddot{x}_2 \end{Bmatrix} = \begin{Bmatrix} \dot{y}_1 \\ \dot{y}_2 \\ \dot{y}_3 \\ \dot{y}_4 \end{Bmatrix} = \{\dot{Y}\} \quad \textit{and} \quad \begin{Bmatrix} x_1 \\ x_2 \\ \dot{x}_1 \\ \dot{x}_2 \end{Bmatrix} = \begin{Bmatrix} y_1 \\ y_2 \\ y_3 \\ y_4 \end{Bmatrix} = \{Y\} \tag{A.6}$$

equation (A.4) can finally be transformed into first order, also known in the state variable format as:

$$\begin{Bmatrix} \dot{y}_1 \\ \dot{y}_2 \\ \dot{y}_3 \\ \dot{y}_4 \end{Bmatrix} = - \begin{bmatrix} 0 & 0 & 1 & 0 \\ 0 & 0 & 0 & 1 \\ c_{11}/m_1 & c_{12}/m_1 & d_{11}/m_1 & d_{12}/m_1 \\ c_{21}/m_2 & c_{22}/m_2 & d_{21}/m_2 & d_{22}/m_2 \end{bmatrix} \cdot \begin{Bmatrix} y_1 \\ y_2 \\ y_3 \\ y_4 \end{Bmatrix} + \begin{bmatrix} 0 & 0 & 0 & 0 \\ 0 & 0 & 0 & 0 \\ 0 & 0 & 1/m_{11} & 0 \\ 0 & 0 & 0 & 1/m_{22} \end{bmatrix} \cdot \begin{Bmatrix} 0 \\ 0 \\ fe_1 \\ fe_2 \end{Bmatrix}$$

A more general format of (A.5) is expressed as:

$$\{\dot{Y}\} = \begin{bmatrix} 0 & I \\ -M^{-1} \cdot C & -M^{-1} \cdot D \end{bmatrix} \cdot \{Y\} + \begin{bmatrix} 0 & 0 \\ 0 & M^{-1} \end{bmatrix} \cdot \{FE\} \qquad \text{(A.7)}$$

The first order state variable format is the standard condition to apply the Runge-Kutta integration used in this thesis. Before the operational sequence of the integration method is described, a visual insight into the nature of the first order differential equations is provided.

A.1.2 General features of ordinary first order differential equations

In contrast to a 'conventional' function $y = f(x)$, a first order differential equation $y' = f(x, y)$ depends on two parameters x and y. In visual sense, the equation can be interpreted as the gradient at a given point on a map defined by coordinates x and y. For a given equation $y' = f(x, y)$, a discrete solution can be developed graphically by sketching line elements of slope y', calculated for any point (x, y) according to the given equation, into a gradient map shown in Figure A.1. Starting from an arbitrary set of initial values x_0, y_0, a discrete solution $y = f(x)$ can be developed stepwise by following the gradients on the map. Three discrete solutions found for initial values $y_0 = 0$, $x = x_0$, x_1 and x_2 are exemplary as indicated by the bold dashes.

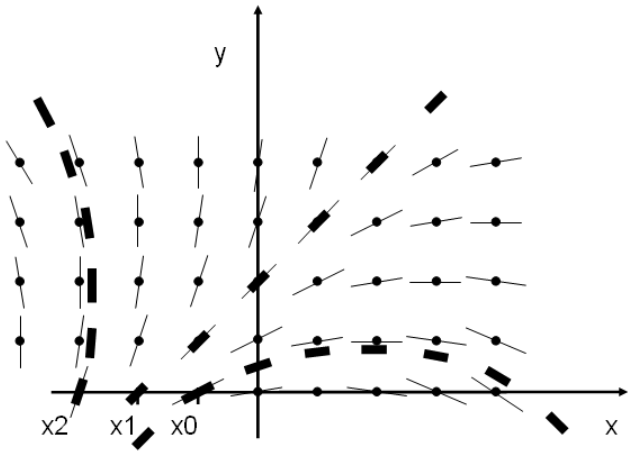

Figure A.1: Gradient map and discrete solutions for the first order differential equation $y' = f(x, y)$

It is obvious, that discrete solutions depend on the initial value set **[12]** (for instance, the initial values $y = 0$, $x = x_1$ deliver the discrete solution indicated by the bold dashed

straight line, whereas the solutions for $x = x_0$, $x = x_2$ reveal curved traces in this case). For the purpose of a better visualization, points with gradients of common magnitude can be linked to form a curve; the so-called isoclines. These curves are not necessarily linear traces, but in this example the isoclines are defined by parallel diagonals of the gradient one. A focus on line elements at a discrete value of x exhibits a gradient variation along the vertical y-direction. For the special case that the gradient map reveals vertical isoclines only, it can be concluded that all line element gradients remain constant in the y- direction. In other words, y' is not a function of y. This feature marks the character of 'conventional' functions $y' = f(x)$ in contrast to differential equations $y' = f(x, y)$ and indicates that 'conventional' functions can also be seen as a special case of differential equation. The feature, gradient being a function of *y* as well, is one reason for numerical inaccuracy caused by a 'gradient error' during integration. This is discussed next.

A.1.3 Numerical integration method and deviation order to analytical solution

As mentioned in the introduction (A.0), a numerical integration can be interpreted as a summation of the area enclosed between the abscissa and the graph of a function. On the other hand, the derivative y' quantifies the slope of the graph $y(x)$ at an instant value of x. The process of numerical integration will be first demonstrated on the basis of the Euler - Cauchy method, shown for a 'conventional' function $y' = f(x)$ in Figure A.2:

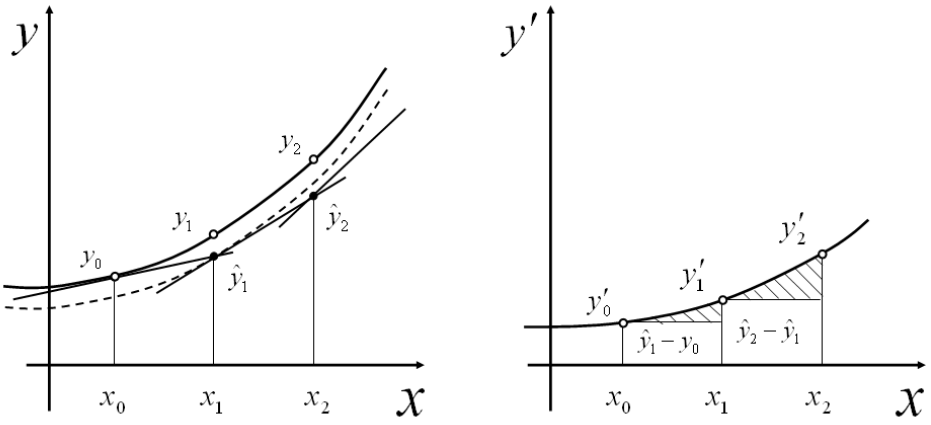

Figure A.2: Graphical illustration of Euler – Cauchy numerical integration and quadrature error

The right hand side figure shows the function $y' = f(x)$ to be integrated with respect to x. Circles indicate the accurate analytical solutions, bold points show approximated values. As the solution depends on the initial values, also known as initial conditions, the numerical integration process is commenced by defining x_0, y_0 shown in the left hand figure. The derivative is illustrated by a tangent. Its slope is quantified by the function value $y'_0 = f(x_0)$ shown on the right figure. A new integral value $\hat{y}_1 = f(x_1)$ can be approximated by adding the rectangle $y'_0 \cdot (x_1 - x_0)$ to the initial value y_0. For $h = x_1 - x_0$, the approximation law for this approach is:

$$\hat{y}_1 = f(x_1) = y_0 + y'_0 \cdot h \approx y_1$$

It is noted that the approximation $\hat{y}_1$ does not precisely with the exact analytical value y_1, thus, the bold illustration. The deviation $\Delta y = y_1 - \hat{y}_1$, known as quadrature error, is caused by neglecting the shaded area on top of rectangle $\hat{y}_1 - y_0$. The error necessarily increases with the step size $t_1 - t_0$, as well as the number of integration steps. Despite the fact that the approximations found for the integral values $\hat{y}_1$, $\hat{y}_2$ etc, deviate from the analytical solutions y_1, y_2, the values calculated for the derivatives y'_1, y'_2 remain accurate (circles), as the gradients in y_1 and $\hat{y}_1$ $\dot{y}$ are of common magnitude.

This changes in case of a differential equation $y' = f(x, y)$, where the derivative y' is now a function in *y*- direction too, as illustrated in the gradient map in Figure A1.1. The quadrature error will then be superimposed by a deviation of the tangent gradients in y_1 and $\hat{y}_1$, known as gradient error. This is indicated by the bold dots in the right hand side graph of Figure A.3, and further increases the numerical deviation.

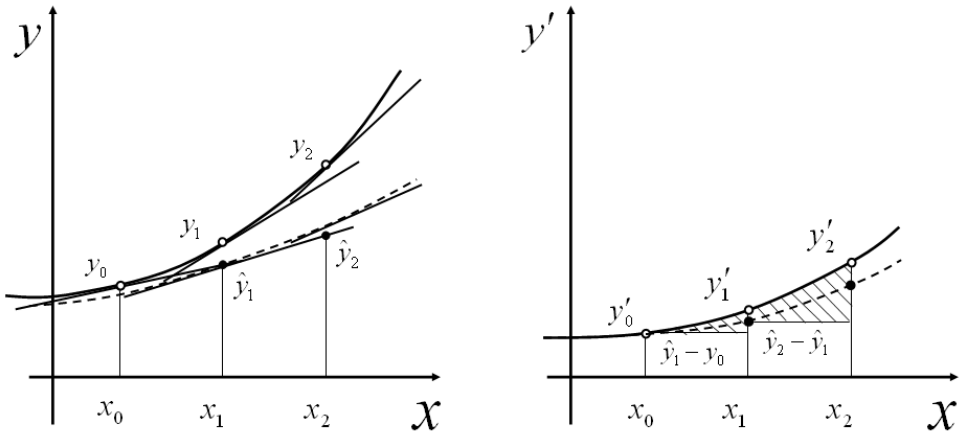

Figure A.3: Graphical illustration of numerical gradient error

The gradient error by its nature is a specific feature of the individual differential equation and can hardly be avoided **[22]**, whereas the quadrature error depends on the numerical method used to approximate the integral increment ΔY for the next time step. To assess the accuracy of different approximation methods, the increment derived from Taylor Series is used as a scale. At an instant point $y_0 = f(x_0)$ of a steady function $y = f(x)$, the Taylor Series can be used to approximate $y_1 = f(x_0 + h)$ next to x_0 by the term

$$y_1 = f(x_0 + h) = y_0 + y_0' h + y_0'' \frac{h^2}{2!} + y_0''' \frac{h^3}{3!} + y_0{}^{IV} \frac{h^4}{4!} + \ \ldots \ + y_0^{(n)} \cdot \frac{h^n}{n!}$$

A formal integration of the series delivers the most accurate solution possible to tune the integral towards the analytical result for $n \to \infty$.

$$Y_1 = Y_0 + \int_{x_0}^{x_0+h} y(x) = \left| y_0 x + \frac{1}{2} y_0' x^2 + \frac{1}{3} y_0'' \frac{x^3}{2!} + \frac{1}{4} y_0''' \frac{x^4}{3!} + \frac{1}{5} y_0{}^{IV} \frac{x^5}{4!} + \ \ldots \ + \frac{1}{n+1} y_0{}^{n} \frac{x^{n+1}}{n!} \right|_{x_0}^{x_0+h}$$

$$\Delta Y = Y_1 - Y_0 = y_0 h + \frac{1}{2} y_0' h^2 + \frac{1}{3!} y_0'' h^3 + \frac{1}{4!} y_0''' h^4 + \frac{1}{5!} y_0^{IV} h^5 + \ldots \ + \frac{1}{(n+1)!} y_0^{(n)} h^{n+1}$$

To minimize the quadrature error, the approximation method used to calculate the integral increment ΔY must match as many higher order terms h of the Taylor series as possible. For example, the increment of one of the simplest approximation methods, the Euler – Cauchy rule, is of the form:

$$\Delta Y = Y_1 - Y_0 = y_0 \cdot h$$

This matches the first term in h only, higher orders are neglected (shaded areas in Figure A.2). The error of the quadrature method is of magnitude $\frac{1}{2} y_0' \cdot h^2$, named order h^2. It can be shown that the error will further reduce if trapezoids are used instead of rectangles to approximate the integral increment [**22**]. The trapezoidal rule reveals:

$$\Delta Y = Y_1 - Y_0 = y_0 \cdot h + \frac{1}{2} y_0' \cdot h^2 + \frac{1}{4} y_0'' \cdot h^3 + \frac{1}{12} y_0''' \cdot h^4 + \frac{1}{48} y_0^{IV} \cdot h^5 + \ ...$$

This approach matches with Taylor Series terms up to h^2, deviations are of order h^3. Following this logic, improved numerical integration concepts are intended to include as many orders as possible with reasonable amount of approximation effort. The Runge-Kutta method, discussed next, is of deviation order h^5 and delivers a good compromise in accuracy and numerical effort.

A.1.4 Runge-Kutta numerical integration of first order differential equations

The Runge-Kutta integration process belongs to the group of single step methods, meaning that only one set of initial values x_0, y_0 is required to start the integration process. Multi-step methods depend on several initial values defined also within the surrounding of x_0 and not discussed here.

The integration starts at a given initial values x_0, y_0. Four Runge-Kutta steps, indicated by roman numbers I to IV, are defined to approximate the integral increment after a step of size h. In a first operation, the gradient y_I' is calculated at x_0, followed by a first approximation for the integral increment $k_I = y_I' \cdot h$.

I. $y_I' = f(x_0, y_0) = f_I$

$k_I = f_I \cdot h$

Related to this gradient, a half sized step is performed towards $x_{II} = x_0 + h/2$. A preliminary integral increment at this point is approximated by $y_{II} = y_0 + k_I/2$ to be used in step II:

II. $y'_{II} = f(x_{II}, y_{II}) = f_{II}$

$k_{II} = f_{II} \cdot h$

A repetition of the half step is performed at $x_{III} = x_{II} = x_0 + h/2$, but using an improved integral increment tuned by k_{II} to be $y_{III} = y_0 + k_{II}/2$:

III. $y'_{III} = f(x_{III}, y_{III}) = f_{III}$

$k_{III} = f_{III} \cdot h$

A fourth, full step is performed by using the improved approximations derived from preceding half steps, $x_{IV} = x_0 + h$ and $y_{IV} = y_0 + k_{III}$.

IV. $y'_{IV} = f(x_{IV}, y_{IV}) = f_{IV}$

$k_{IV} = f_{IV} \cdot h$

All the four integral decrements $k_I, k_{II}, k_{III}, k_{IV}$ represent preliminary results only. An average value K is derived to cover as many Taylor Series terms as possible:

$$K = \frac{1}{6}\left[k_I + 2k_{II} + 2k_{III} + k_{IV}\right]$$

Finally, a new set of initial conditions $x_I = x_0 + h, \quad y_I = y_0 + k$ can be used to initiate the subsequent approximation of similar type. The Runge-Kutta steps are summarized in the table shown in table A.1 **[22]**.

$RK\ step\ \ i$	x	y	$k_i = f(x,y)\cdot h$	
I	x_0	y_0	k_I	
II	$x_0 + \frac{h}{2}$	$y_0 + \frac{1}{2}k_I$	k_{II}	
III	$x_0 + \frac{h}{2}$	$y_0 + \frac{1}{2}k_{II}$	k_{III}	
IV	$x_0 + h$	$y_0 + k_{III}$	k_{IV}	$K = \frac{1}{6}(k_I + 2k_{II} + 2k_{III} + k_{IV})$
I	$x_0 + h$	$y_0 + K$		
...				

Table A.1: Runge-Kutta numerical calculation steps **[22]**

A.1.5 Runge-Kutta integration applied to system of coupled equations of motion

The explanations so far have been for a single first order differential equation. Equations of motion in general are of second order and usually coupled, corresponding to a number of system degrees of freedom. Equation (A.4), represented in state variable format (A.8), is used here as an example to demonstrate the method applied to the integration of two coupled second order equations in the time domain.

The two second order differential equations of motion in matrix format

$$\begin{Bmatrix} \ddot{x}_1 \\ \ddot{x}_2 \end{Bmatrix} = \begin{bmatrix} m_{11} & m_{12} \\ m_{21} & m_{22} \end{bmatrix}^{-1} \cdot \left(\begin{Bmatrix} fe_1 \\ fe_2 \end{Bmatrix} - \begin{bmatrix} d_{11} & d_{12} \\ d_{21} & d_{22} \end{bmatrix} \cdot \begin{Bmatrix} \dot{x}_1 \\ \dot{x}_2 \end{Bmatrix} - \begin{bmatrix} c_{11} & c_{12} \\ c_{21} & c_{22} \end{bmatrix} \cdot \begin{Bmatrix} x_1 \\ x_2 \end{Bmatrix} \right) \tag{A.4}$$

were transferred to four first order equations into state variable format by using the substitutions (A.6).

$$\begin{Bmatrix} \dot{z}_1 \\ \dot{z}_2 \\ \dot{z}_3 \\ \dot{z}_4 \end{Bmatrix} = \begin{bmatrix} 0 & 0 & 0 & 0 \\ 0 & 0 & 0 & 0 \\ 0 & 0 & 1/m_{11} & 0 \\ 0 & 0 & 0 & 1/m_{22} \end{bmatrix} \cdot \begin{Bmatrix} 0 \\ 0 \\ fe_1 \\ fe_2 \end{Bmatrix} - \begin{bmatrix} 0 & 0 & 1 & 0 \\ 0 & 0 & 0 & 1 \\ c_{11}/m_1 & c_{12}/m_1 & d_{11}/m_1 & d_{12}/m_1 \\ c_{21}/m_2 & c_{22}/m_2 & d_{21}/m_2 & d_{22}/m_2 \end{bmatrix} \cdot \begin{Bmatrix} z_1 \\ z_2 \\ z_3 \\ z_4 \end{Bmatrix} \tag{A.8}$$

(A1.8) is equivalent to the four single equations E1 to E4:

$$
\begin{aligned}
&E1: \quad \dot{z}_1 = z_3 \\
&E2: \quad \dot{z}_2 = z_4 \\
&E3: \quad \dot{z}_3 = \frac{fe_1}{m_{11}} - \left[\frac{c_{11}}{m_{11}} \cdot z_1 + \frac{c_{12}}{m_{11}} \cdot z_2 + \frac{d_{11}}{m_{11}} \cdot z_3 + \frac{d_{12}}{m_{11}} \cdot z_4 \right] \\
&E4: \quad \dot{z}_4 = \frac{fe_2}{m_{22}} - \left[\frac{c_{21}}{m_{22}} \cdot z_1 + \frac{c_{22}}{m_{22}} \cdot z_2 + \frac{d_{21}}{m_{22}} \cdot z_3 + \frac{d_{22}}{m_{22}} \cdot z_4 \right]
\end{aligned}
\tag{A.9}
$$

Initial values for x, $\dot{x}$ at $t = 0$ according to the substitutions (A.6) are set as follows:

$$
\{Z_0\} = \begin{Bmatrix} z_{10} \\ z_{20} \\ z_{30} \\ z_{40} \end{Bmatrix} = \begin{Bmatrix} x_{10} \\ x_{20} \\ \dot{x}_{10} \\ \dot{x}_{20} \end{Bmatrix}
$$

The following table shows an overview of the four Runge-Kutta steps applied to equation set (A.9). The numbers placed in front of the terms indicate the sequence of calculation steps. In operation 1.1 to 1.4 the given initial values are used to commence the integration process. Subsequently, operations 2.1 to 2.4 deliver integral approximations for RK step II. Improved integral increments are available after operations 3.1 to 3.4, followed by improved integration in RK step III and so on. The last operation set has the indices 7.1 to 7.4 and delivers the integral increments kIV.

E1 :	**t**		**z**		**k** $= \mathbf{E1(t, z_3)\cdot h}$
I	$t_I = t_0$		$z_{3,I} = z_{30}$	**1.1**	$k_I = E1(t_I, z_{3,I})\cdot h$
II	$t_{II} = t_0 + \frac{h}{2}$	**2.1**	$z_{3,II} = z_{30} + \frac{1}{2}k_I$	**3.1**	$k_{II} = E1(t_{II}, z_{3,II})\cdot h$
III	$t_{III} = t_0 + \frac{h}{2}$	**4.1**	$z_{3,III} = z_{30} + \frac{1}{2}k_{II}$	**5.1**	$k_{III} = E1(t_{III}, z_{3,III})\cdot h$
IV	...		...		...

E2 :	**t**		**z**		**k** $= \mathbf{E2(t, z_4)\cdot h}$
I	$t_I = t_0$		$z_{4,I} = z_{40}$	**1.2**	$k_I = E2(t_I, z_{4,I})\cdot h$
II	$t_{II} = t_0 + \frac{h}{2}$	**2.2**	$z_{4,II} = z_{40} + \frac{1}{2}k_I$	**3.2**	$k_{II} = E2(t_{II}, z_{4,II})\cdot h$
III	$t_{III} = t_0 + \frac{h}{2}$	**4.2**	$z_{4,III} = z_{40} + \frac{1}{2}k_{II}$	**5.2**	$k_{III} = E2(t_{III}, z_{4,III})\cdot h$
IV	...		...		...

E3 :	**t**		**z**		**k** $= \mathbf{E3(t, z_1, z_2, z_3, z_4)\cdot h}$
I	$t_I = t_0$		$z_{1,I} = z_{10}$	**1.3**	$k_I = E3(t_I, z_{1,I}, z_{2,I}, z_{3,I}, z_{4,I})\cdot h$
II	$t_{II} = t_0 + \frac{h}{2}$	**2.3**	$z_{1,II} = z_{10} + \frac{1}{2}k_I$	**3.3**	$k_{II} = E3(t_{II}, z_{1,II}, z_{2,II}, z_{3,II}, z_{4,II})\cdot h$
III	$t_{III} = t_0 + \frac{h}{2}$	**4.3**	$z_{1,III} = z_{10} + \frac{1}{2}k_{II}$	**5.3**	$k_{III} = E3(t_{III}, z_{1,III}, z_{2,III}, z_{3,III}, z_{4,III})\cdot h$
IV	...		...		...

E4 :	**t**		**z**		**k** $= \mathbf{E4(t, z_1, z_2, z_3, z_4)\cdot h}$
I	$t_I = t_0$		$z_{2,I} = z_{20}$	**1.4**	$k_I = E4(t_I, z_{1,I}, z_{2,I}, z_{3,I}, z_{4,I})\cdot h$
II	$t_{II} = t_0 + \frac{h}{2}$	**2.4**	$z_{2,II} = z_{20} + \frac{1}{2}k_I$	**3.4**	$k_{II} = E4(t_{II}, z_{1,II}, z_{2,II}, z_{3,II}, z_{4,II})\cdot h$
III	$t_{III} = t_0 + \frac{h}{2}$	**4.4**	$z_{2,III} = z_{20} + \frac{1}{2}k_{II}$	**5.4**	$k_{III} = E4(t_{III}, z_{1,III}, z_{2,III}, z_{3,III}, z_{4,III})\cdot h$
IV	...		...		...

Table A1.2: Runge-Kutta table for two degree of freedom system in state variable format

A replacement according to (A.6) delivers the vectors $\{X\}$ and $\{\dot{X}\}$ of the system trajectories.

In an alternative approach, the equations of motion can be integrated directly in the given format of second order (A.1 and A.2 for a single degree of freedom). Thus, a substitution and transformation into state variable form can be avoided **[17]**. The integrations $\ddot{x} \Rightarrow \dot{x}$

and $\dot{x} \Rightarrow x$ are then performed in two simultaneous steps. The same example given by equation A1.4 is used to demonstrate this process:

$$\begin{Bmatrix} \ddot{x}_1 \\ \ddot{x}_2 \end{Bmatrix} = \begin{bmatrix} m_{11} & m_{12} \\ m_{21} & m_{22} \end{bmatrix}^{-1} \cdot \left(\begin{Bmatrix} fe_1 \\ fe_2 \end{Bmatrix} - \begin{bmatrix} d_{11} & d_{12} \\ d_{21} & d_{22} \end{bmatrix} \cdot \begin{Bmatrix} \dot{x}_1 \\ \dot{x}_2 \end{Bmatrix} - \begin{bmatrix} c_{11} & c_{12} \\ c_{21} & c_{22} \end{bmatrix} \cdot \begin{Bmatrix} x_1 \\ x_2 \end{Bmatrix} \right) \tag{A.4}$$

The mass matrix again is assumed to be diagonal in order to simplify the example. The matrix- vector products can be written in the format of two coupled single equations G1 and G2 as:

$$\begin{aligned} G1 \quad \ddot{x}_1 &= \frac{fe_1}{m_{11}} - \left[\frac{c_{11}}{m_{11}} \cdot x_1 + \frac{c_{12}}{m_{11}} \cdot x_2 + \frac{d_{11}}{m_{11}} \cdot \dot{x}_1 + \frac{d_{12}}{m_{11}} \cdot \dot{x}_2 \right] \\ G2 \quad \ddot{x}_2 &= \frac{fe_2}{m_{22}} - \left[\frac{c_{21}}{m_{22}} \cdot x_1 + \frac{c_{22}}{m_{22}} \cdot x_2 + \frac{d_{21}}{m_{22}} \cdot \dot{x}_1 + \frac{d_{22}}{m_{22}} \cdot \dot{x}_2 \right] \end{aligned} \tag{A.10}$$

G1 and G2 are of identical structure as E3, E4 derived from equation (A.8), but in the format of second order this time. Table A.3 **[17]** illustrates the subsequence of the Runge-Kutta steps.

In contrast to the foregone process, where the integral increments (expressed by k_I to k_{VI}) are calculated in the first operation set (1.1 to 1.4), the alternative approach just delivers the values for the highest order derivatives (accelerations in case of equations of motion). The formal integration (indicated by the multiplication of step size h) is performed during the subsequent operations (2.1 to 2.4) in two steps for $\ddot{x} \Rightarrow \dot{x}$ and $\dot{x} \Rightarrow x$, which directly derives the system trajectories, thus avoids the burden of a re-substitution. On top of that, the process appeals more descriptive compared to the state variable method.

G1 :

t	x	$\dot{x}$	$\ddot{x} = G1(t, x_1, x_2, \dot{x}_1, \dot{x}_2)$
$t_I = t_0$	$x_{1,I} = x_{10}$	$\dot{x}_{1,I} = \dot{x}_{10}$	1.1 $\ddot{x}_{1,I} = G1(t_I, x_{1,I}, x_{2,I}, \dot{x}_{1,I}, \dot{x}_{2,I})$
$t_{II} = t_0 + \frac{h}{2}$	2.2 $x_{1,II} = x_{10} + \frac{h}{2}\dot{x}_{1,I}$	2.1 $\dot{x}_{1,II} = \dot{x}_{10} + \frac{h}{2}\ddot{x}_{1,I}$	3.1 $\ddot{x}_{1,II} = G1(t_{II}, x_{1,II}, x_{2,II}, \dot{x}_{1,II}, \dot{x}_{2,II})$
$t_{III} = t_0 + \frac{h}{2}$	4.2 $x_{1,III} = x_{10} + \frac{h}{2}\dot{x}_{1,II}$	4.1 $\dot{x}_{1,III} = \dot{x}_{10} + \frac{h}{2}\ddot{x}_{1,II}$	5.1 $\ddot{x}_{1,III} = G1(t_{III}, x_{1,III}, x_{2,III}, \dot{x}_{1,III}, \dot{x}_{2,III})$
$t_{IV} = t_0 + h$	6.2 $x_{1,IV} = x_{10} + h \cdot \dot{x}_{1,III}$	6.1 $\dot{x}_{1,IV} = \dot{x}_{10} + h \cdot \ddot{x}_{1,III}$	$\ddot{x}_{1,IV} = G1(t_{IV}, x_{1,IV}, x_{2,IV}, \dot{x}_{1,IV}, \dot{x}_{2,IV})$
	7.1 $x_{11} = \frac{1}{6}(x_{1,I} + 2x_{1,II} + 2x_{1,III} + x_{1,IV})$		
	7.2 $\dot{x}_{11} = \frac{1}{6}(x_{1,I} + 2x_{1,II} + 2x_{1,III} + x_{1,IV})$		
$t_I = t_0 + h$	$x_{1,I} = x_{11}$	$\dot{x}_{1,I} = \dot{x}_{11}$	1.1 $\ddot{x}_{1,I} = G1(t_1, x_{1,I}, x_{2,I}, \dot{x}_{1,I}, \dot{x}_{2,I})$
...	...	...	...

G2 :

t	x	$\dot{x}$	$\ddot{x} = G2(t, x_1, x_2, \dot{x}_1, \dot{x}_2)$
$t_I = t_0$	$x_{2,I} = x_{20}$	$\dot{x}_{2,I} = \dot{x}_{20}$	1.2 $\ddot{x}_{2,I} = G2(t_I, x_{1,I}, x_{2,I}, \dot{x}_{1,I}, \dot{x}_{2,I})$
$t_{II} = t_0 + \frac{h}{2}$	2.4 $x_{2,II} = x_{20} + \frac{h}{2}\dot{x}_{2,I}$	2.3 $\dot{x}_{2,II} = \dot{x}_{20} + \frac{h}{2}\ddot{x}_{2,I}$	3.2 $\ddot{x}_{2,II} = G2(t_{II}, x_{1,II}, x_{2,II}, \dot{x}_{1,II}, \dot{x}_{2,II})$
$t_{III} = t_0 + \frac{h}{2}$	4.4 $x_{2,III} = x_{20} + \frac{h}{2}\dot{x}_{2,II}$	4.3 $\dot{x}_{2,III} = \dot{x}_{20} + \frac{h}{2}\ddot{x}_{2,II}$	5.2 $\ddot{x}_{2,III} = G2(t_{III}, x_{1,III}, x_{2,III}, \dot{x}_{1,III}, \dot{x}_{2,III})$
$t_{IV} = t_0 + h$	6.4 $x_{2,IV} = x_{20} + h \cdot \dot{x}_{2,III}$	6.3 $\dot{x}_{2,IV} = \dot{x}_{20} + h \cdot \ddot{x}_{2,III}$	$\ddot{x}_{2,IV} = G1(t_{IV}, x_{1,IV}, x_{2,IV}, \dot{x}_{1,IV}, \dot{x}_{2,IV})$
	7.3 $x_{21} = \frac{1}{6}(x_{2,I} + 2x_{2,II} + 2x_{2,III} + x_{2,IV})$		
	7.4 $\dot{x}_{21} = \frac{1}{6}(x_{2,I} + 2x_{2,II} + 2x_{2,III} + x_{2,IV})$		
$t_I = t_0 + h$	$x_{2,I} = x_{21}$	$\dot{x}_{2,I} = \dot{x}_{21}$	1.1 $\ddot{x}_{2,I} = G1(t_1, x_{1,I}, x_{2,I}, \dot{x}_{1,I}, \dot{x}_{2,I})$
...	...	...	...

Table A.3: Runge-Kutta table for second order equations of motion

For the case of multiple degrees of freedom, it is reasonable to organise the numerical treatment through matrix- vector multiplications. Matrix equation (A.4) can be used directly to perform the operation steps 1.1, 1.2 in a single operation, delivering the accelerations of the system degrees of freedom by a matrix- vector multiplication. The four subsequent algebraic operations, 2.1 to 2.4, deliver new interim values required to set up the next matrix- vector multiplication combining 3.1 and 3.2 and so forth. Finally, operations 7.1 to 7.4 deliver a new set of initial values for the next time step.

A.1.6 Appropriate step size control

It is noted in section A.1.3, that both quadrature and gradient errors are related to the step size used for the numerical operations. The Runge-Kutta integration offers a simple method to adjust and control the step size based on a proposal raised by Collatz **[23]**, **[62]**:

$$\frac{1}{4} \leq \left| \frac{k_{III} - k_{II}}{k_{II} - k_{I}} \right| \leq \frac{1}{2}$$

The recommendation is as follows: If the ratio exceeds the value ½, the step size should be reduced. In case the ratio falls below a limit of ¼, the step size can be increased. As the ratio can easily be monitored during the calculation, an effective step size control can be embedded into the numerical algorithm.

It is noted that the equation systems derived for a multi-body structure can cause convergence problems during the numerical integration in conjunction with step size control operators. Especially this is the case, when the system consists of large inertias supported by soft springs in combination with small masses attached by stiff springs. This leads to system eigen-values which are widely split, with the equations showing these features referred to as stiff. Hints to cope with this can be found in **[14]**.

A.2 Numerical interpolation

In chapter 5, a map concept is introduced to simulate the dynamic force transfer. The map database, comprising a set of measured force response traces, is condensed to the format of a three dimensional array, containing spline coefficients, applicable to reproduce these traces through method of interpolation.

The general idea of an interpolation is to generate a mathematical function that is determined by a few discrete points only. This function should precisely match the discrete points and should reasonably approximate the course of the function in between two adjacent points.

From the various interpolation methods based on polynomials, such as Lagrangian, Newtonian etc, some methods (depending on the current problem) can result in an 'oscillatory' trend. The effect of an oscillation is an over or underestimation of values in between the known discrete points **[64]**, especially if the polynomial is of high order. The cubical spline interpolation is based on third order polynomials. It is, therefore, robust with regards to oscillation, thus it is chosen for the map data processing in this thesis.

A.2.1 Third order spline interpolation

The process of a third order spline interpolation is explained here in Figure A.4: The graph of a function defined by $N+1$ given points x_0, y_0 to x_N, y_N, named splines, may be approximated by an interpolation within each of the *N* intervals. These intervals do not necessarily need to be of equal width. Derivatives y_i' at the discrete splines are graphically indicated by tangents.

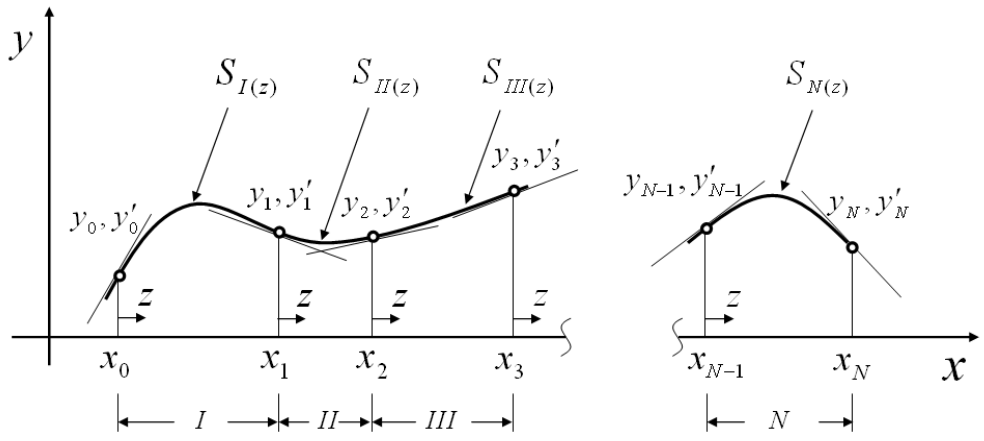

Figure A.4: Cubical Spline interpolation

The functions used to approximate the trace in each single interval may be defined by unique third order polynomials of a local variable z as follows:

$$\begin{aligned}
&S_{I(z)} = A_{I,0} + A_{I,1} \cdot z + A_{I,2} \cdot z^2 + A_{I,3} \cdot z^3 && 0 \le z < z_I = (x_1 - x_0) \\
&S_{II(z)} = A_{II,0} + A_{II,1} \cdot z + A_{II,2} \cdot z^2 + A_{II,3} \cdot z^3 && 0 \le z < z_{II} = (x_2 - x_1) \\
&\ldots \\
&S_{N(z)} = A_{0,N} + A_{1,N} \cdot z + A_{2,N} \cdot z^2 + A_{3,N} \cdot z^3 && 0 \le z < z_N = (x_N - x_{N-1})
\end{aligned} \tag{A.11}$$

Based on these functions, the derivatives become:

$$\begin{aligned}
&S'_{I(z)} = A_{I,1} + 2A_{I,2} \cdot z + 3A_{I,3} \cdot z^2 && 0 \le z < z_I = (x_1 - x_0) \\
&S'_{II(z)} = A_{II,1} + 2A_{II},2 \cdot z + 3A_{II,3} \cdot z^2 && 0 \le z < z_{II} = (x_2 - x_1) \\
&\ldots \\
&S'_{N(z)} = A_{N,1} + 2A_{N,2} \cdot z + 3A_{N,3} \cdot z^2 && 0 \le z < z_N = (x_N - x_{N-1})
\end{aligned} \tag{A.12}$$

$$\begin{aligned}
&S''_{I(z)} = 2A_{I,2} + 6A_{I,3} \cdot z && 0 \le z < z_I = (x_1 - x_0) \\
&S''_{II(z)} = 2A_{II,2} + 6A_{II,3} \cdot z && 0 \le z < z_{II} = (x_2 - x_1) \\
&\ldots \\
&S''_{N(z)} = 2A_{N,2} + 6A_{N,3} \cdot z && 0 \le z < z_N = (x_N - x_{N-1})
\end{aligned} \tag{A.13}$$

Combining (A.11) and (A.12), applied to the first interval, conditional equations for the first set of spline coefficients $A_{I,0}$, $A_{I,1}$, $A_{I,2}$ and $A_{I,3}$ can be established as:

$$\begin{aligned}
&S_I(z=0) = y_0 = A_{I,0} \\
&S_I(z=z_I) = y_1 = A_{I,0} + A_{I,1} \cdot z_I + A_{I,2} \cdot {z_I}^2 + A_{I,3} \cdot {z_I}^3 \\
&S'_I(z=0) = y'_0 = A_{I,1} \\
&S'_I(z=z_I) = y'_1 = A_{I,1} + 2A_{I,2} \cdot z_I + 3A_{I,3} \cdot {z_I}^2
\end{aligned} \tag{A.14}$$

Solving the four equations (A.14) delivers the relations for the coefficients to fit the first interval I:

$$
\begin{aligned}
A_{I,0} &= y_0 \\
A_{I,1} &= y_0' \\
A_{I,2} &= \frac{3}{z_I^2}\cdot(y_1 - y_0) - \frac{1}{z_I}\cdot(y_1' + 2y_0') \\
A_{I,3} &= -\frac{2}{z_I^3}\cdot(y_1 - y_0) + \frac{1}{z_I^2}\cdot(y_1' + y_0')
\end{aligned}
\qquad \text{(A.15)}
$$

Analogous relations are found for the remaining intervals as:

$$
\begin{aligned}
A_{II,0} &= y_1 \\
A_{II,1} &= y_1' \\
A_{II,2} &= \frac{3}{z_{II}^2}\cdot(y_2 - y_1) - \frac{1}{z_{II}}\cdot(y_2' + 2y_1') \\
A_{II,3} &= -\frac{2}{z_{II}^2}\cdot(y_1 - y_2) + \frac{1}{z_{II}^2}\cdot(y_2' + y_1')
\end{aligned}
\qquad \text{(A.16)}
$$

$$A_{III,0} = y_2$$

...

A.2.2 Derivation of gradients

It is noted that the magnitudes of the derivatives y_i' are generally unknown. To fulfil the requirement of a smooth trace transition in between two neighboured intervals, the polynomials should match in magnitude y, gradient y' and curvature y'' in each spline. For example, at location x_1 the spline functions S_I, S_I' and S_I'' of local variable $z = z_I = x_1 - x_0$ within interval I must match with the spline functions S_{II}, S_{II}' and S_{II}'' for $z = 0$ derived for interval II. The first two conditions S_I and S_I' (A.11) and (A.12) respectively have been used to derive the conditional equations (A.14), S_I'' and (A.13) respectively and used to derive the expressions for the unknown derivatives y_i'.

$$
\begin{aligned}
S_I''(z = z_I) &= S_{II}''(z = 0) \\
2A_{I,2} + 6z_I \cdot A_{I,3} &= 2A_{II,2}
\end{aligned}
\qquad \text{(A.17)}
$$

By using solutions (A.15) and (A.16), the curvature in the spline, that connects first and second intervals becomes:

$$2\cdot\left[\frac{3}{z_I^2}(y_1-y_0)-\frac{1}{z_I}(y_1'+2y_0')\right]+6z_I\left[-\frac{2}{z_I^3}(y_1-y_0)+\frac{1}{z_I^2}(y_1'-y_0')\right]=2\cdot\left[\frac{3}{z_{II}^2}(y_2-y_1)-\frac{1}{z_{II}}(y_2'+2y_1')\right]$$

and described in terms of y' and y, the first equations related to first and second interval can then be set up as:

$$\frac{1}{z_I}\cdot y_0'+\left(\frac{2}{z_I}+\frac{2}{z_{II}}\right)\cdot y_1'+\frac{1}{z_{II}}\cdot y_2' \;=\; -\frac{3}{z_I^2}\cdot y_0+\left(\frac{3}{z_I^2}-\frac{3}{z_{II}^2}\right)\cdot y_1+\frac{3}{z_{II}^2}\cdot y_2 \qquad \text{(A.18)}$$

In full analogy, further equations for the next interval transitions, two to three, three to four and so on, can be written as:

$$\frac{1}{z_{II}}\cdot y_1'+\left(\frac{2}{z_{II}}+\frac{2}{z_{III}}\right)\cdot y_2'+\frac{1}{z_{III}}\cdot y_3' \;=\; -\frac{3}{z_{II}^2}\cdot y_1+\left(\frac{3}{z_{II}^2}-\frac{3}{z_{III}^2}\right)\cdot y_2+\frac{3}{z_{III}^2}\cdot y_3$$

$$\frac{1}{z_{III}}\cdot y_2'+\left(\frac{2}{z_{III}}+\frac{2}{z_{IV}}\right)\cdot y_3'+\frac{1}{z_{IV}}\cdot y_4' \;=\; -\frac{3}{z_{III}^2}\cdot y_2+\left(\frac{3}{z_{III}^2}-\frac{3}{z_{IV}^2}\right)\cdot y_3+\frac{3}{z_{IV}^2}\cdot y_4$$

...

This leads to a linear system of equation (A.19) of $N-1$ equations for $N+1$ unknowns y_i':

	y_0'	y_1'	y_2'	y_3'	...	y_{N-3}'	y_{N-2}'	y_{N-1}'	y_N'	*R.S*
1	$\frac{1}{z_I}$	$\frac{2}{z_I}+\frac{2}{z_{II}}$	$\frac{1}{z_{II}}$	0		0	0	0	0	$-\frac{3}{z_I^2}\cdot y_0+\left(\frac{3}{z_I^2}-\frac{3}{z_{II}^2}\right)\cdot y_1+\frac{3}{z_{II}^2}\cdot y_2$
2	0	$\frac{1}{z_{II}}$	$\frac{2}{z_{II}}+\frac{2}{z_{III}}$	$\frac{1}{z_{III}}$		0	0	0	0	$-\frac{3}{z_{II}^2}\cdot y_1+\left(\frac{3}{z_{II}^2}-\frac{3}{z_{III}^2}\right)\cdot y_2+\frac{3}{z_{III}^2}\cdot y_3$
...					...					...
$N-2$	0	0	0	0		$\frac{1}{z_{N-2}}$	$\frac{2}{z_{N-2}}+\frac{2}{z_{N-1}}$	$\frac{1}{z_{N-1}}$	0	$-\frac{3}{z_{N-2}^2}\cdot y_{N-3}+\left(\frac{3}{z_{N-2}^2}-\frac{3}{z_{N-1}^2}\right)\cdot y_{N-2}+\frac{3}{z_{N-1}^2}\cdot y_{N-1}$
$N-1$	0	0	0	0		0	$\frac{1}{z_{N-1}}$	$\frac{2}{z_{N-1}}+\frac{2}{z_N}$	$\frac{1}{z_N}$	$-\frac{3}{z_{N-1}^2}\cdot y_{N-2}+\left(\frac{3}{z_{N-1}^2}-\frac{3}{z_N^2}\right)\cdot y_{N-1}+\frac{3}{z_N^2}\cdot y_N$

Table A.4: Linear equation system (A.19)

Further equations, needed to solve the equation system, can be set up by several definitions of boundary conditions, applied at the end points y_0, y_N. Three options are common practise **[23]**:

1) Specified gradients: $y'_0,\ \ y'_N$.
2) Curvature fade outs: $y''_0 = 0,\ \ y''_N = 0$, also known as natural spline.
3) Periodic splines: $y_0 = y_N,\ \ y'_0 = y'_N,\ \ y''_0 = y''_N$.

The first two options are used in this thesis and derived here in more detail.

1) Gradient

Option 1 may simply be realised by adding the specified values $y'_0,\ \ y'_N$ to the right hand side of the equation system (A.19). Thus, the number of unknowns y'_i now matches with the umber of equations $N-1$, and the system can be solved.

	y'_1	y'_2	y'_3	...	y'_{N-3}	y'_{N-2}	y'_{N-1}	*R.S.*
1	$\frac{2}{z_I}+\frac{2}{z_{II}}$	$\frac{1}{z_{II}}$	0		0	0	0	$-\frac{3}{z_I^2}\cdot y_0+\left(\frac{3}{z_I^2}-\frac{3}{z_{II}^2}\right)\cdot y_1+\frac{3}{z_{II}^2}\cdot y_2-\frac{1}{z_I}\cdot y'_0$
2	$\frac{1}{z_{II}}$	$\frac{2}{z_{II}}+\frac{2}{z_{III}}$	$\frac{1}{z_{III}}$		0	0	0	$-\frac{3}{z_{II}^2}\cdot y_1+\left(\frac{3}{z_{II}^2}-\frac{3}{z_{III}^2}\right)\cdot y_2+\frac{3}{z_{III}^2}\cdot y_3$
...				...				...
$N-2$	0	0	0		$\frac{1}{z_{N-2}}$	$\frac{2}{z_{N-2}}+\frac{2}{z_{N-1}}$	$\frac{1}{z_{N-1}}$	$-\frac{3}{z_{N-2}^2}\cdot y_{N-3}+\left(\frac{3}{z_{N-2}^2}-\frac{3}{z_{N-1}^2}\right)\cdot y_{N-2}+\frac{3}{z_{N-1}^2}\cdot y_{N-1}$
$N-1$	0	0	0		0	$\frac{1}{z_{N-1}}$	$\frac{2}{z_{N-1}}+\frac{2}{z_N}$	$-\frac{3}{z_{N-1}^2}\cdot y_{N-2}+\left(\frac{3}{z_{N-1}^2}-\frac{3}{z_N^2}\right)\cdot y_{N-1}+\frac{3}{z_N^2}\cdot y_N-\frac{1}{z_N}\cdot y'_N$

Table A.5: Linear equation system for specified gradient

2) Curvature

Option 2 in conjunction with (A.13) and (A.15) leads to further conditional equations, which can be added to extend the equation set to $N+1$ equations as:

$$S_I''(z=0) \quad = 2A_{I,2} \qquad\qquad = 0$$
$$S_N''(z=z_N) \quad = 2A_{N,2} + 6A_{N,3} \cdot z_N \quad = 0$$

Derived from (A.15), the coefficients are defined as:

$$A_{I,2} = \frac{3}{z_I^2} \cdot (y_1 - y_0) - \frac{1}{z_I} \cdot (y_1' + 2y_0')$$
$$A_{N,2} = \frac{3}{z_N^2} \cdot (y_N - y_{N-1}) - \frac{1}{z_N} \cdot (y_N' + 2y_{N-1}')$$
$$A_{N,3} = -\frac{2}{z_N^3} \cdot (y_N - y_{N-1}) + \frac{1}{z_N^2} \cdot (y_N' + y_{N-1}')$$

Filled in and described in terms of y', y, the two equations required to solve the system (A.19) are found to be:

$$\frac{2}{z_I} y_0' + \frac{1}{z_I} y_1' = -\frac{3}{z_I^2} y_0 + \frac{3}{z_I^2} y_1$$
$$\frac{2}{z_N} y_{N-1}' + \frac{1}{z_N} y_N' = -\frac{3}{z_N^2} y_{N-1} + \frac{3}{z_N^2} y_N$$

	y_0'	y_1'	y_2'	y_3'	...	y_{N-3}'	y_{N-2}'	y_{N-1}'	y_N'	R.S.
0	$\frac{2}{z_I}$	$\frac{1}{z_I}$	0	0		0	0	0	0	$-\frac{3}{z_I^2} \cdot y_0 + \frac{3}{z_I^2} \cdot y_1$
1	$\frac{1}{z_I}$	$\frac{2}{z_I} + \frac{2}{z_{II}}$	$\frac{1}{z_{II}}$	0		0	0	0	0	$-\frac{3}{z_I^2} \cdot y_0 + \left(\frac{3}{z_I^2} - \frac{3}{z_{II}^2}\right) \cdot y_1 + \frac{3}{z_{II}^2} \cdot y_2$
2		$\frac{1}{z_{II}}$	$\frac{2}{z_{II}} + \frac{2}{z_{III}}$	$\frac{1}{z_{III}}$		0	0	0	0	$-\frac{3}{z_{II}^2} \cdot y_1 + \left(\frac{3}{z_{II}^2} - \frac{3}{z_{III}^2}\right) \cdot y_2 + \frac{3}{z_{III}^2} \cdot y_3$
				...						...
$N-2$	0	0	0	0		$\frac{1}{z_{N-2}}$	$\frac{2}{z_{N-2}} + \frac{2}{z_{N-1}}$	$\frac{1}{z_{N-1}}$	0	$-\frac{3}{z_{N-2}^2} \cdot y_{N-3} + \left(\frac{3}{z_{N-2}^2} - \frac{3}{z_{N-1}^2}\right) \cdot y_{N-2} + \frac{3}{z_{N-1}^2} \cdot y_{N-1}$
$N-1$	0	0	0	0		0	$\frac{1}{z_{N-1}}$	$\frac{2}{z_{N-1}} + \frac{2}{z_N}$	$\frac{1}{z_N}$	$-\frac{3}{z_{N-1}^2} \cdot y_{N-2} + \left(\frac{3}{z_{N-1}^2} - \frac{3}{z_N^2}\right) \cdot y_{N-1} + \frac{3}{z_N^2} \cdot y_N$
N	0	0	0	0		0	0	$\frac{1}{z_N}$	$\frac{2}{z_N}$	$-\frac{3}{z_N^2} \cdot y_{N-1} + \frac{3}{z_N^2} \cdot y_N$

Table A.6: Linear equation system for zero curvature at curve ends

The approximation results found can be interpreted as an elastic deflection line of a simply supported beam in bending mode, attached to the splines y_i, representing the simply supported end condition. In case of option 2, the beam ends fade out straight

without curvature, aligned to the conditions $y_0'' = y_N'' = 0$. In case of specified gradients, bending moments can be considered applied at the end supports.

A.2.3 Gradient estimation

In the case of a large number of splines, the solution of the linear equation system to derive the gradients y_i' can be tedious. An alternative to the 'exact' derivation is to approximate the gradients. In a first step, the given splines y_i are used to form a polygon trace shown in Figure A1.5.

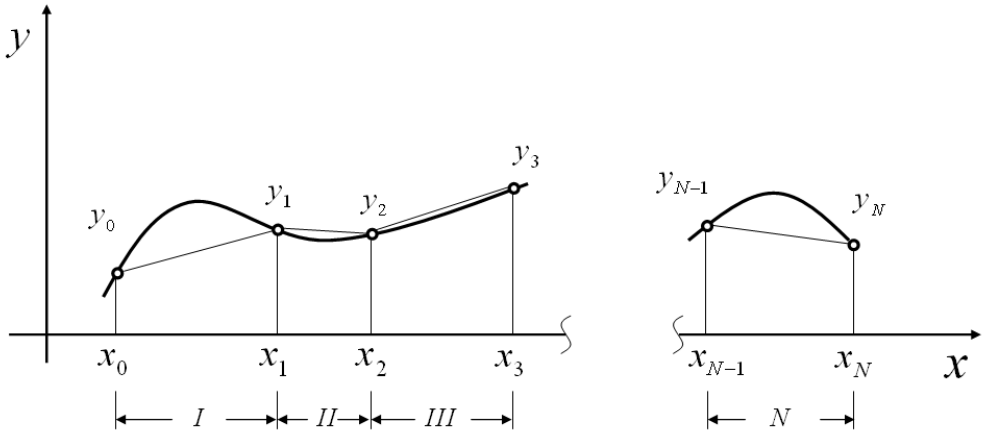

Figure A.5: Polygon trace defined by splines y_i

Gradients for the intervals I, II, III, ... can easily be derived as:

$$y_I' = \frac{y_1 - y_0}{x_1 - x_0}$$

$$y_{II}' = \frac{y_2 - y_1}{x_2 - x_1}$$

...

$$y_N' = \frac{y_N - y_{N-1}}{x_N - x_{N-1}}$$

To approximate the gradients at the splines y_i, averages of the neighboured intervals are used:

$$y'_1 = \frac{y'_I + y'_{II}}{2}$$

$$y'_2 = \frac{y'_{II} + y'_{III}}{2}$$

...

$$y'_{N-1} = \frac{y'_{N-1} + y'_N}{2}$$

Two remaining approximations are needed at the curve ends in y_0 and y_N. It is noted that this approach is feasible in conjunction with option 1 (gradient) only, as the remaining unknown gradients y'_0 and y'_N are specified by the user. It is difficult (if not impossible) to approximate the gradients in the sense of case 2 (curvature) in this way, in order that they would precisely match the requirement $y''_0 = y''_N = 0$. It is also obvious, that these simplifications do not exactly represent a simply supported beam, deviations in gradient would result in external moment being applied at the simple supports.
However, the gradient estimation is effectively applicable to approximate a large number of splines taken from curves that do not show extreme volatility.

Appendix B

MULTIBODY DYNAMICS 2011, ECCOMAS Thematic Conference
J.C. Samin, P. Fisette (eds.)
Brussels, Belgium, 4-7 July 2011

PREDICTION OF IMPULSIVE TYRE-SUSPENSION RESPONSE SUBJECTED TO KERB STRIKE

Hubertus von Chappuis[*], George Mavros[†], Paul King[†], Homer Rahnejat[†]

[*] Ford Werke GmbH, Spessartstraße, D-50725, Cologne-Merkenich, Germany
e-mail: hvonchap@ford.com

[†]Loughborough University
Epinal way, Loughborough, LE11 3TU, UK
e-mail: g.mavros@lboro.ac.uk, p.d.king@lboro.ac.uk, h.rahnejat@lboro.ac.uk

Keywords: Minimal parameter vehicle model, abuse manoeuvres, kerb strike

Abstract. The paper presents a minimal parameter vehicle simulation model to predict the vertical suspension loads expected for abuse driving manoeuvres, such as a kerb strike event. This causes impulsive bump-stop loads. Since the aim is to specifically study impulsive bump-stop and tyre characteristics, an in-plane bicycle model suffices, when it is extended to 7 degrees of freedom. Non-linear and hysteretic characteristics of the bump-stop elements are included by a parametric map concept, based on displacement and velocity dependent hysteresis. Furthermore, a static tyre model is described, tailored to predict the radial stiffness against penetration of an edge with a flat-type rigid body geometry. The tyre model is derived on the basis of classical shell theory and represented in terms of few input parameters. Model validation is supported through experiments at both component and system levels.

1 INTRODUCTION

With increasing computational power, complex simulation models allow design optimization in the final development phase. However, at an early stage, most details, other than main dimensions, are unknown. For concept studies, for example in the early stages of chassis development, and prediction of component loads, model simplicity is preferred. This approach is followed in the current paper with a minimal parameter vehicle model. Suspension and tyre characteristics should possess many attributes for ride comfort, durability and vehicle handling [1,2]. This paper is concerned with jounce bumper and tyre behaviour under severe impulsive conditions, where their elasto-kinetics are usually assessed for various load case scenarios [3]. FORD has specified the worst load case manoeuvre to be drive over kerb (DOC). A 2-dimensional (planar) vehicle model, extended to take into account fore-aft wheel travel (Figure 1) is used. Large scale wheel motions lead to impulsive action which can induce significant jounce bumper impact and gross tyre deflections. Emphasis is put upon modelling of jounce bumper characteristics and tyre behaviour under severe impacts.

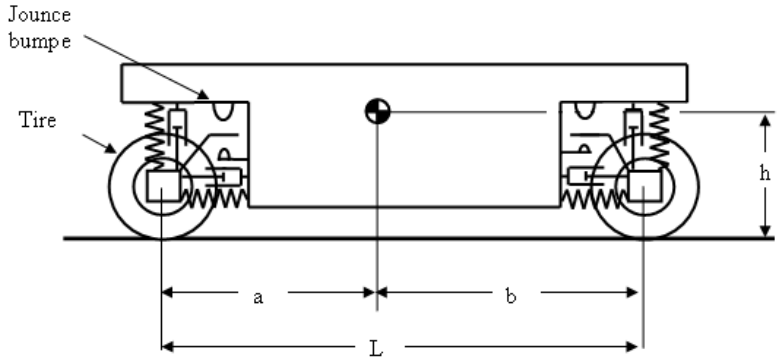

Figure 1: A schematic representation of the simplified vehicle model.

2 VEHICLE MODEL

As the vertical and longitudinal suspension stiffnesses are defined by idealized spring and damper elements, no kinematic constraint formulation is required.

2.1 Model element overview

The inertias of the suspension links are lumped with the unsprung wheel mass. The suspension geometry, kinematics and individual component stiffness are merged into combined vertical and longitudinal stiffnesses. Figure 2 shows an overview of the vehicle model, where:

(1) sprung mass and rotational inertia
(2) unsprung masses including wheel, hub, brake and lumped suspension
(3) road springs (constant stiffness)
(4) shock absorbers (constant damping)
(5) jounce bumpers (map concept presented in item 4)
(6) rebound stops non-linear stiffness (no damping)
(7) kinematics of free wheel travel and jounce / rebound contacts

(8) longitudinal stiffness / damping of wheel centre against body
(9) tyre

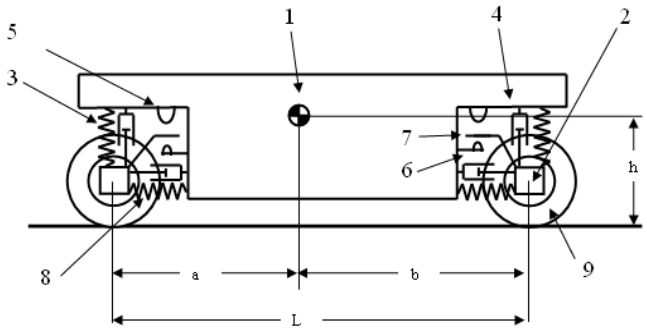

Figure 2: Minimum parameter vehicle model

2.2 Equations of motion

The basis of the model is a bicycle model [4], extended by three additional longitudinal degrees of freedom as shown in Figure 3.

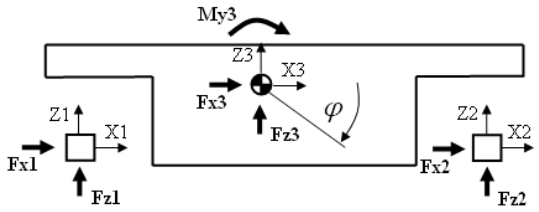

Figure 3: Degrees of freedom and external loads for simple vehicle model.

The equations of motion in a matrix form are:

$$[M]\cdot\begin{Bmatrix}\ddot{x}_i\\ \ddot{z}_j\\ \ddot{\varphi}_k\end{Bmatrix}+[D]\cdot\begin{Bmatrix}\dot{x}_i\\ \dot{z}_j\\ \dot{\varphi}_k\end{Bmatrix}+[C]\cdot\begin{Bmatrix}x_i\\ z_j\\ \varphi_k\end{Bmatrix}=\begin{Bmatrix}\sum fx_i\\ \sum fz_j\\ \sum my_k\end{Bmatrix} \qquad (1)$$

[**M**] is the inertial matrix, [**C**] and [**D**] are the effective stiffness and damping matrices. The external applied forces constitute the RHS of the equation. Matrix [D] is of equivalent structure to [C].

In contrast to the classical bicycle model, the system properties of the model shown in figure 2 vary for different vertical wheel displacement states. These states are:

4. free wheel travel (no jounce or rebound)
5. jounce
6. rebound

Figure 4 shows the vehicle front suspension in vertical free travel- (left) and in bump stop engagement mode (right).

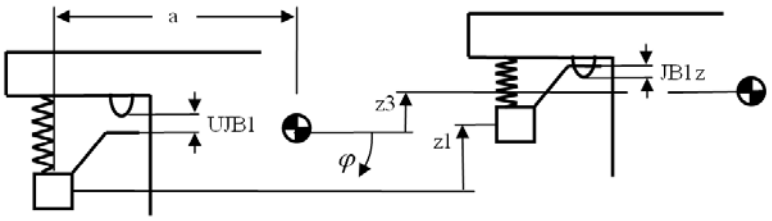

Figure 4: Free vertical wheel travel UJB1 and jounce bumper engagement JB1z on a front suspension.

For free travel mode (case 1 above) the Matrices [C] and [D] do not include structural stiffness and damping characteristics associated with jounce and rebound bumpers, which should be included in cases 2 and 3 above. As equation (1) should be generic, then the additional *structure invariant* internal reactions caused by jounce and rebound are represented in the form of a couple of *external* forces of equal magnitude and common action line, but oriented anti-symmetrically. They can, therefore, be balanced with the external force vector **Fe** on the right side of equation (1). By doing so, stiffness and damping matrices can remain in their structure invariant form and do not need to be modified. Hence, for case 1:

$$\vec{F}e = \begin{Bmatrix} f_{1z} - m_1 g \\ f_{2z} - m_2 g \\ -m_3 g \\ f_{1x} \\ f_{2x} \\ 0 \\ 0 \end{Bmatrix} \qquad (2)$$

And for cases 2 and 3 at front suspension:

$$\vec{F}e_{jounce} = \begin{Bmatrix} f_{1z} - m_1 g - F_{JB1} \\ f_{2z} - m_2 g \\ -m_3 g + F_{JB1} \\ f_{1x} \\ f_{2x} \\ 0 \\ F_{JB1} \cdot a \end{Bmatrix} \qquad \vec{F}e_{rebound} = \begin{Bmatrix} f_{1z} - m_1 g + F_{RS1} \\ f_{2z} - m_2 g \\ -m_3 g - F_{RS1} \\ f_{1x} \\ f_{2x} \\ 0 \\ F_{RS1} \cdot a \end{Bmatrix} \qquad (3)$$

2.3 Jounce bumper force response map application

The concept of jounce bumper map is used to feed back the bumper force F_{JB} to fit the initial conditions z and $\dot{z} = dz/dt$ according to the current bumper deformation state. This map concept takes the non-linearity and hysteresis of these polymeric elements into account.

2.4 External tyre force application

In kerb strike, the tyre loads are derived from the deformation of its radial belt contact. The kerb is assumed to be a simplified vertical rigid blade, promoting an edge-type line contact. Therefore, the need for a complex analysis for a combined flat and edge belt-to-kerb contact is removed. The bumper and tyre contact forces are balanced with the external force vector **Fe** as indicated in figure 5.

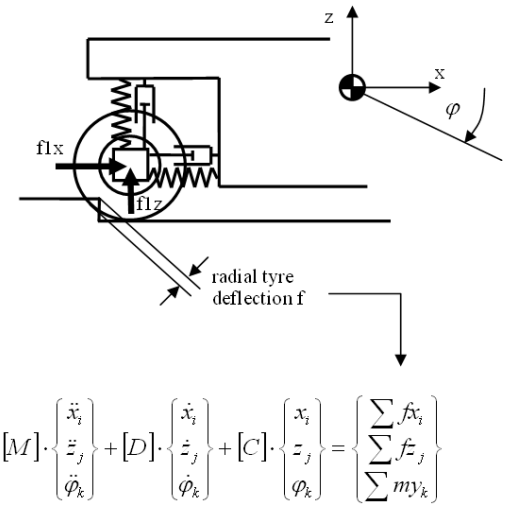

Figure 5: Tyre response force feedback to external load vector **Fe**.

3 BUMPER MODEL

The jounce bumper is regarded as a 1-DOF vertical compression-only element. It attenuates the effect of impact load transmission to the vehicle body post impulsive event, be it kerb or pothole impact. It is made of polyurethane (PUR) foam, commonly used in vehicle suspensions. Its force response characteristic is a combination of both a polytropic deformation of gas chambers and compression of the gas volume surrounding the polymeric structure. The material properties, such as density depend on the specific boundary conditions applied during the polymerization process. It is, therefore, difficult to investigate the bumper force response other than through physical testing.

3.1 Map data acquisition

During a kerb strike manoeuvre described in the introduction, the bumper may deform to its full extent. Although the bumper excitation mode during kerb strike can be fairly arbitrary, a harmonic excitation is assumed to obtain its force response data. The validity of this assumption is confirmed through experimental drop tests, as in general a bumper drop test excitation mode deviates somewhat from a harmonic response.

The quotient ω = Vmax / Smax is used to specify circular actuation frequency relevant for the drive over kerb (DOK) event. With Vmax being limited by the damper blocking speed and Smax specified by the bumper deflection range, $f = \omega/2\pi$ determines the DOC relevant frequency to be 10 Hz. Thus, the recorded data does contain the velocity related damping hysteretic characteristics. Figure 6 shows the bumper actuation kinematics and the physical rig used to generate the map data.

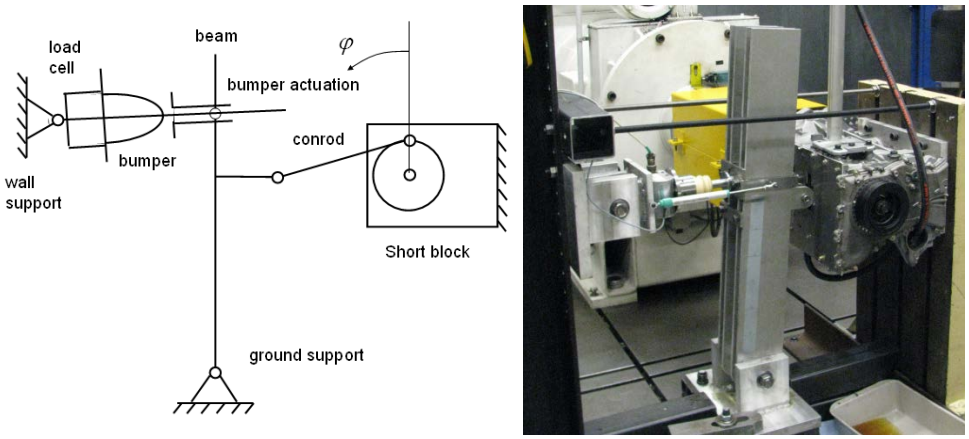

Figure 6: Concept of bumper test rig kinematics and physical test set up.

Any small deviations from harmonic response due to higher order crank kinematics are neglected.

Figure 7 shows the results obtained for various excitation amplitudes.

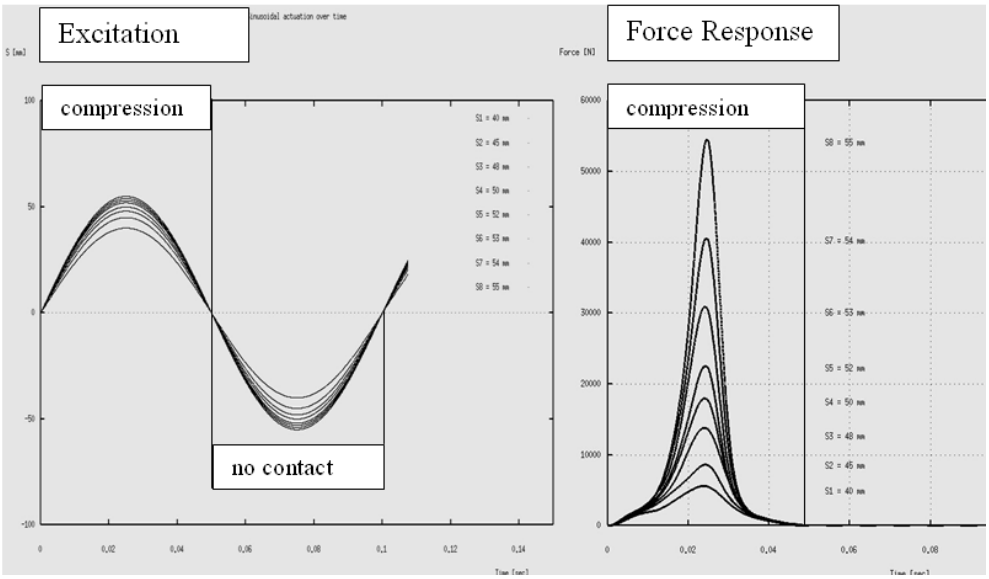

Figure 7: Sinusoidal actuation and force response of a jounce bumper element.

3.2 Map data pre-processing

A cubical spline interpolation is used to condense the recorded data into a third order polynomial:

$$F = A_0 + A_1 \cdot z + A_2 \cdot z^2 + A_3 \cdot z^3 \qquad (4)$$

Variable 'z' represents a local coordinate system (figure 8). The figure shows the organisation of data into an easily accessible array, containing the polynomial coefficients in equation (4).

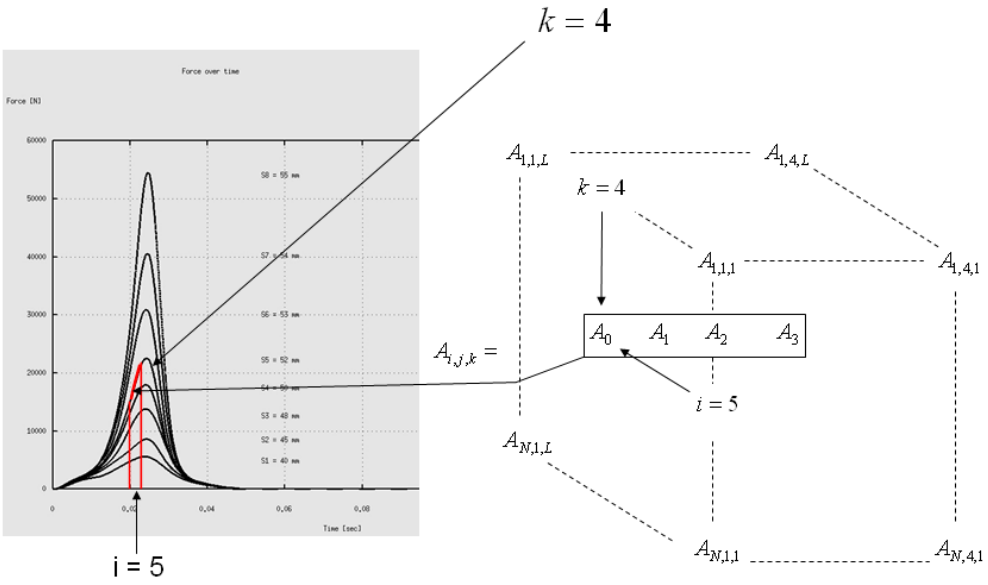

Figure 8: Organization of array 'A' to store map data cubical spline coefficients.

3.3 Map to solver interaction

The stored map feeds back the force response corresponding to an initial condition S and V for an instantaneous condition in each integration time step. In conjunction with the expression for the circular frequency phase angle $\varphi = \omega t$, a generalized velocity $v_{(t)} / \omega$ can be defined as:

$$s_{(t)} = S_0 \cdot \sin(\varphi)$$
$$\frac{v_{(t)}}{\omega} = S_0 \cdot \cos(\varphi) \qquad (5)$$

For the generalized velocity 'vg', the phase diagram s/vg reveals a format of concentric circles in the x- y plane and also the phase angle φ (figure 9, LHS) .The three dimensional plot on the RHS is the recorded characteristic force response map.

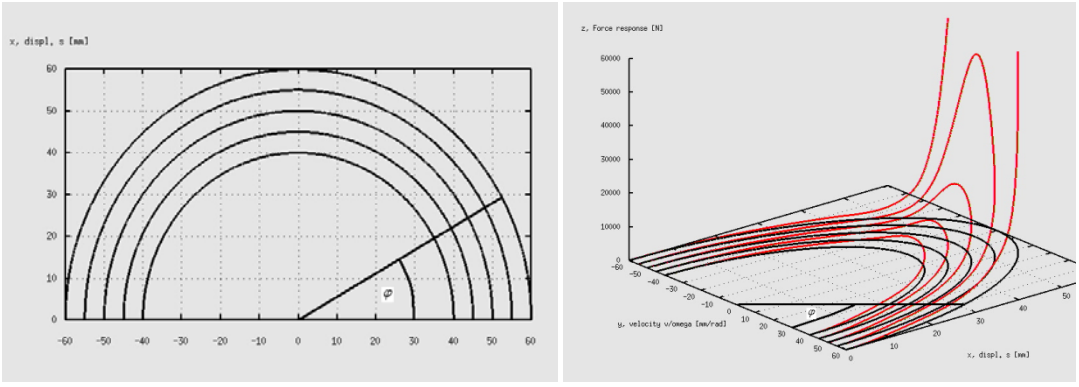

Figure 9: Force response traces (red) and their vertical projections (black) in a phase diagram.

Also note:

$$\tan\varphi = \frac{S}{V/\omega} \qquad R = \sqrt{S^2 + (V/\omega)^2} \qquad (6)$$

The force related to the datum point is approximated by two interpolations, circumferential- and radial. In circumferential direction (figure 10, left), array A is used to find F1, F2 and F3 followed by radial interpolation (figure 10, right).

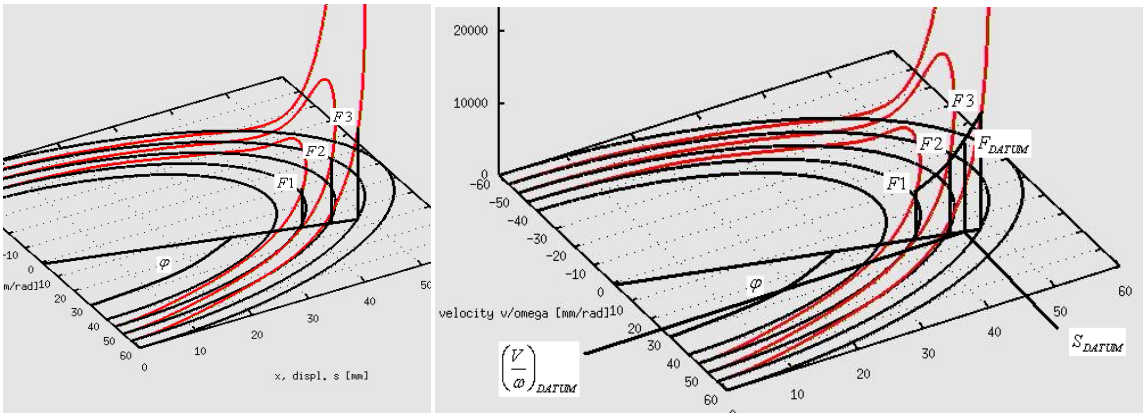

Figure 10: Circumferential and radial interpolation

To ascertain the validity of the map concept, simulation results are compared with a drop test applied to a bumper element. Figure 11 below shows good conformance of harmonic simulation results to the measured drop test data.

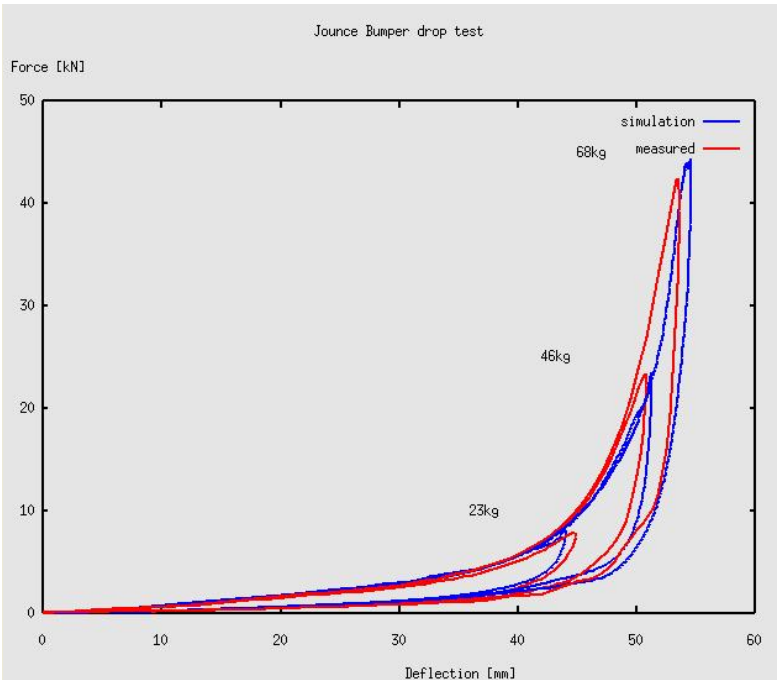

Figure 11: Assessment of force simulation (blue) and measured drop test forces (red)

4 TYRE MODEL

The model is simplified to address the radial force response of the tyre, neglecting its structural stiffness and inertia. The tyre structure is simplified by including two primary elements, namely the belt and the sidewall, as shown in figure 13. The model is fully defined by the pneumatic pressure, p, and four dimensions of the cross section (Ra, ri, bt and fc), as illustrated in fig. 13. The belt and sidewall are considered as ideal isotropic membranes, free from resistance against bending. All tyre model derivations are based on the above simplifications and assumptions.

In the absence of radial deformation, the belt contour is assumed to be of ideal cylindrical shape. The internal radial stress at the circumferential interface between sidewall and belt, as well as the belt force Fg, are derived by making use of shell theory. Timoshenko [6] formulated a general in plane stress relation (7) for a double curved, thin shell element and applied it to a torus structure, as shown in figure 12.

$$\frac{\sigma_1}{R1}+\frac{\sigma_2}{R2}=\frac{p}{t} \tag{7}$$

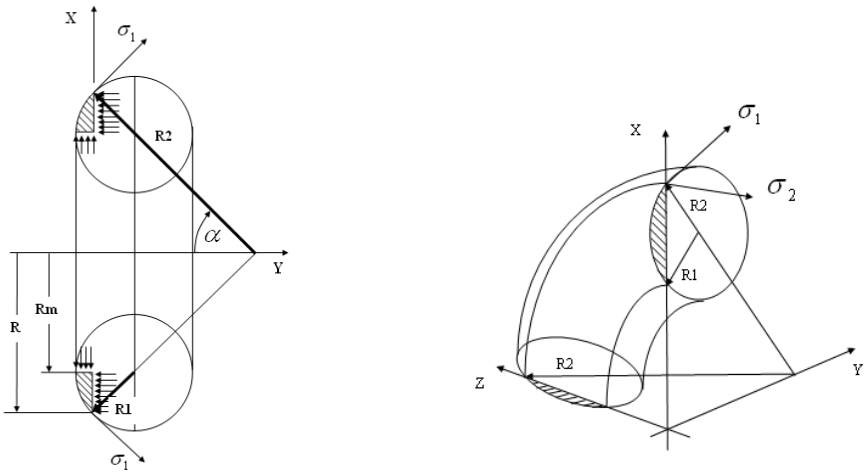

Figure 12: Curvature radii R1, R2 and membrane stress σ_1, σ_2 in a torus structure.

In eq. 7 t indicates the wall thickness of the membrane and p is the pneumatic pressure. Considering equilibrium in the y- direction leads to the radial stress σ_1.

$$2\pi \cdot R \cdot t \cdot \sigma_1 \sin\alpha = p \cdot \pi \cdot \left(R^2 - Rm^2\right) \tag{8}$$

Using the geometric relation

$$\sin\alpha = \frac{R - Rm}{R1}$$

the radial stress of the sidewall is found equal to

$$\sigma_1 = p \cdot \frac{R1}{2t} \cdot \left(1 + \frac{Rm}{R}\right) \tag{9}$$

The circumferential belt force, Fg, is derived considering equilibrium in the z-direction, as shown in figure 13. A cylindrical shell element representing the belt rests in

equilibrium under the action of sidewall stress, σ_1, circumferential belt force, Fg, and pneumatic pressure, p. This situation is expressed by equation (10):

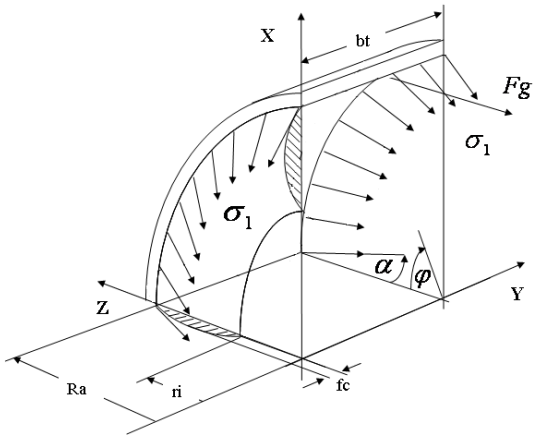

Figure 13: Belt shell structure applied to sidewall stress σ_1 and belt force Fg.

$$Fg = p \cdot Ra \cdot bt - 2 \cdot \sigma_1 \cos\alpha \cdot Ra \cdot t \int_{\varphi=0}^{\pi/2} \cos\varphi \cdot d\varphi \tag{10}$$

Using equation (9) and the geometrical relations

$$Rm = \frac{Ra + ri}{2} \qquad hc = Ra - ri \qquad R1 = \frac{hc^2 + 4\,fc^2}{8\,fc} \qquad \cos\alpha = \frac{R1 - fc}{R1} \tag{11}$$

integration of (10) leads to the circumferential belt force, Fg, as follows:

$$Fg = p \cdot \left[Ra \cdot bt - (Ra + Rm) \cdot (R1 - fc)\right] \tag{12}$$

Using equation (9) the sidewall line loads Qsg and Qsr at the belt and rim attachments are

$$Qsg = \sigma_{1(R=Ra)} \cdot t = p \cdot \frac{R1}{2} \cdot \left(1 + \frac{Rm}{Ra}\right) \tag{13}$$

$$Qsr = \sigma_{1(R=ri)} \cdot t = p \cdot \frac{R1}{2} \cdot \left(1 + \frac{Rm}{ri}\right) \tag{14}$$

For modeling purposes the DOC manoeuvre is simplified to a drive-over-blade situation whereby the tyre model rolls over a blade-type obstacle. The associated tyre force is derived for an idealized edge type line contact to the belt as shown in figure 14.

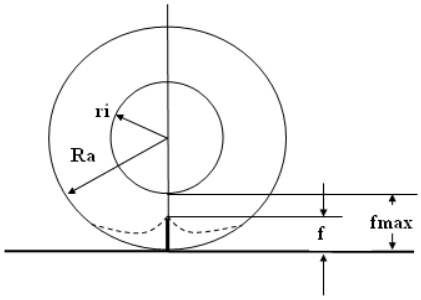

Figure 14: Edge contact simplified tyre geometry.

As indicated in figure 14, with increasing radial deflection, f, the projected belt area decreases, as does the associated belt force, Fg. This effect is incorporated by correcting the belt force, Fg, according to equation 15:

$$Fg_{corr} = Fg \cdot \frac{2Ra - f}{2Ra} \tag{15}$$

With the assumption of equal belt force magnitudes at the upper and lower belt edges, the deformed belt appears to resemble a rope subjected to constant line load, q, as indicated in figure 15. Taking into account the rope equations (16), as derived for constant line load q [7], the horizontal belt force at the tyre-blade contact interface can be derived as shown in equation 17.

$$H = \frac{q \cdot Le^2}{8 f_{\max}} \qquad and \qquad \tan\alpha = 4 \cdot \frac{f_{\max}}{Le} \tag{16}$$

$$H = \frac{q \cdot Le^2}{8 f_{\max}} = p \cdot \left[Ra \cdot bt - (Ra + Rm) \cdot (R1 - fc) \right] = Fg_{corr} \tag{17}$$

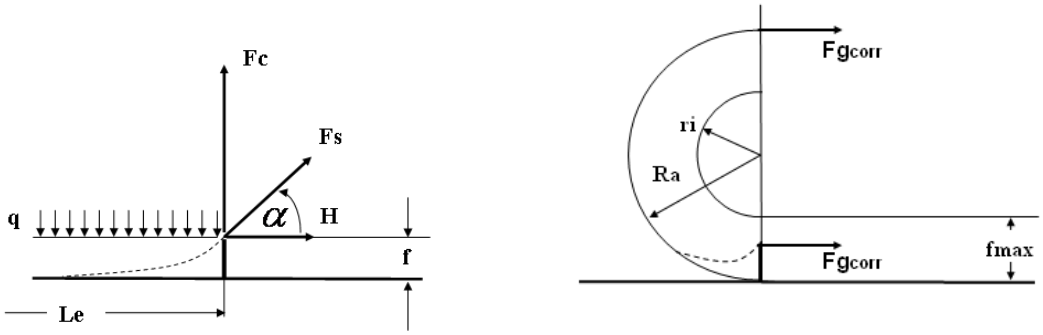

Figure 15: Belt load analogy to rope equation.

The left-hand-side of figure 15 shows the rope (dashed line) subjected to a horizontal force, H. The rope is shown for half span width (effective length Le). On the right-hand-side of figure 15, each half of the tyre is subjected to belt forces, Fg_{corr}. Assuming an edge contact, the belt is considered to behave similarly to a simply supported rope, with $H = Fg_{corr}$. Rearranging equation 16 and substituting $q = p \cdot bt$ provides an estimation of the effective length, Le, for the extreme case of belt-to-rim contact:

$$Le = 2 \cdot \sqrt{2 \cdot Lc \cdot \left[Ra - \frac{(Ra + Rm) \cdot (R1 - fc)}{bt} \right]} \tag{18}$$

$$with \quad Lc = Ra - ri = f_{\max}$$

Equations 16 and 18 are used to calculate the tangent angle of the rope, α, (figure 15), hence the tangential rope force Fs acting at the edge-contact is calculated as:

$$Fs = \frac{Fg_{corr}}{\cos\alpha} \tag{19}$$

Combining equations 15, 16, 18 and 19, the radial belt force, Fc, for an edge contact can be approximated as:

$$Fc = 2 \cdot Fs \cdot \sin\alpha = 2 \cdot Fg_{corr} \cdot \tan\alpha$$

$$= 8 \cdot \frac{f}{Le} \cdot Fg_{corr} = 2p \cdot bt \cdot f \cdot \frac{(2Ra - f) \cdot \sqrt{Ra - (Ra + Rm) \cdot (R1 - fc)/bt}}{Ra \cdot \sqrt{2 \cdot (Ra - ri)}} \quad (20)$$

The validity of the analytical tyre model was assessed by comparing the predicted radial force with experimentally measured forces, as well as forces obtained by Finite Element Analysis (FEA). Both physical tests and FEA were conducted for three nominal pneumatic pressures (1, 2 and 3 bar) and three deflection levels (20, 40 and 60 mm). A comparison between FEA, measured and analytical results is provided in figure 16. Despite the simplicity of the modeling approach, the radial forces calculated analytically agree well with those predicted by FEA and experiments.

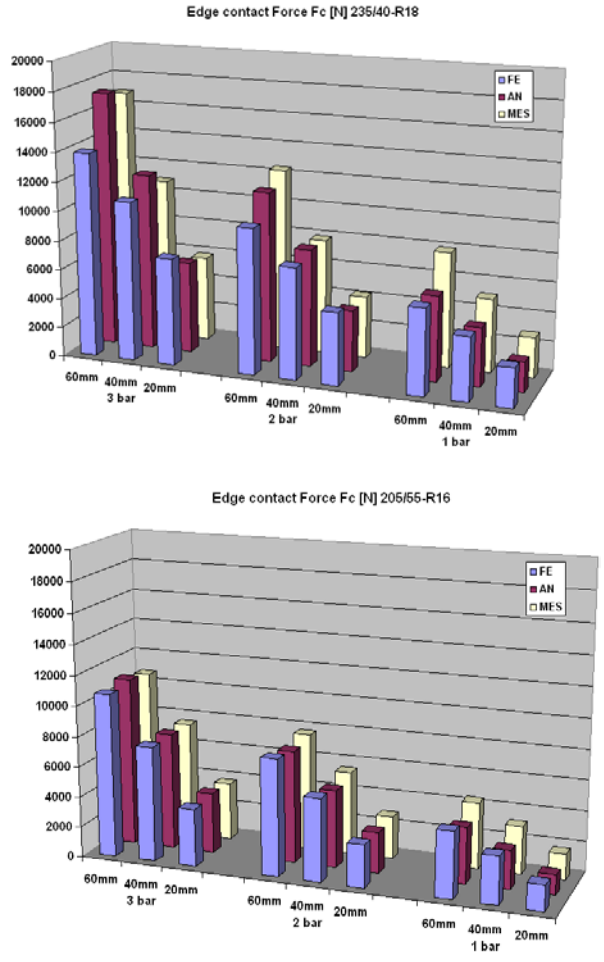

Figure 16: Analytical edge contact force response compared to experimental and FEA results.

5 SYSTEM VALIDATION

A drive over kerb test as described in the introduction was performed with a CD340 (FORD Galaxy). The test was carried out at two different speeds, namely 25 and 40 kph. The vehicle was driven at a free rolling mode over a beam of rectangular cross section of

135 mm height. The crossing was performed in a direction perpendicular to the beam with the intention of simultaneous impact of both wheels with the bar. The experimental test setup is shown in figure 17.

Figure 17: Drive over kerb test set up

The vehicle was equipped with 235/40-R18 tyres operating at a pressure of 2 bar. The vehicle was loaded according to the FORD specification standards for passenger cars.

5.1 Validation of the full model

A comparison between the measured (red line) and simulated (blue line) top mount force time-histories is shown in figure 18:

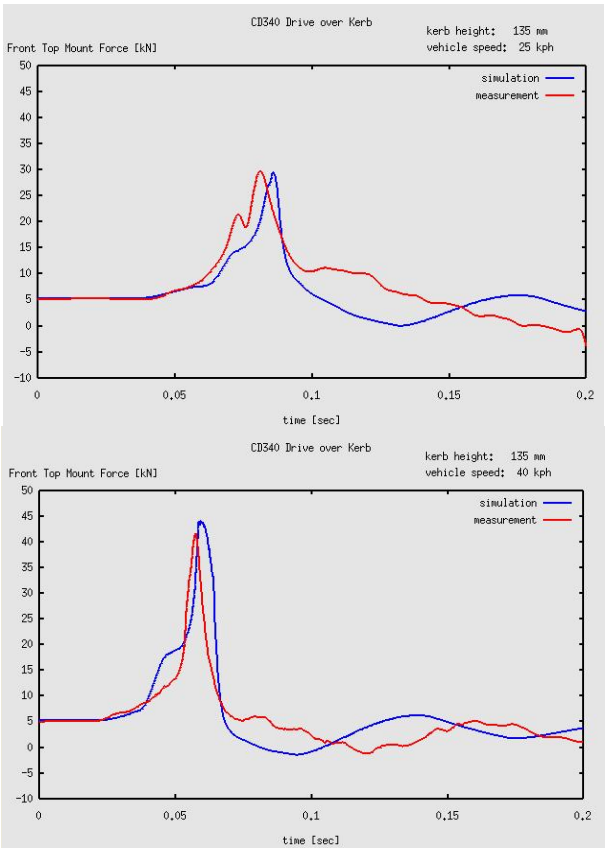

Figure 18: Top mount force and vertical wheel centre deflection over time for drive over kerb test.

The results show very good agreement in terms of force levels. Discrepancies in the actual shape of the experimental and simulation time-histories can be attributed to the

simplifications implemented in the model. The simulation allows the individual contribution of the spring (blue line), damper (green line) and bumper (red line) to be assessed, as illustrated in figure 19. The bumper force appears to be the dominant contributor during severe kerb-strike events, as expected.

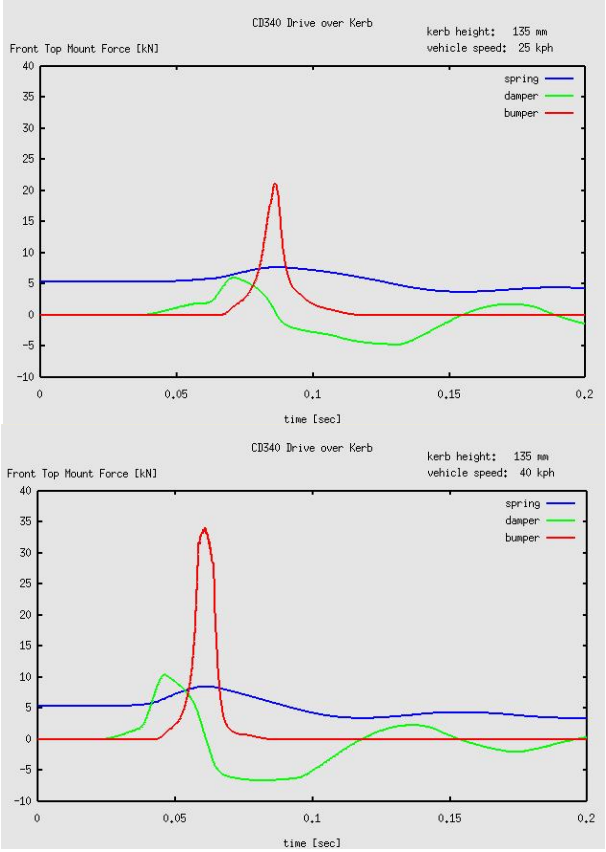

Figure 19: Simulation of spring, damper and bumper force component of top mount force during kerb strike.

6 CONCLUSION

A minimal parameter vehicle model has been proposed, specifically tailored to simulate vertical suspension loads during the abusive DOK manoeuvre specified by FORD. Reasonable correlation with experimental data was demonstrated both at component and system levels. Using the proposed simulation tool, parametric studies can be carried out at an early design stage, when only a few design parameters are known. Alternatively, the model can be used later on in the development phase, in order to predict the effect of design stages. In the latter case, calibration of the model based on existing vehicle data would be advisable.

ACKNOWLEDGEMENTS

This research project has been supported by FORD MOTOR COMPANY. This support is gratefully acknowledged.

REFERENCES

[1] C. Campbell. *Automotive suspensions*. Chapman Hall, London, 1981.

[2] H. Rahnejat. *Multi-body dynamics: Vehicles, Machines and Mechanisms*. PEP/SAE Joint Publishers, Bury St Edmunds (UK), Warrendale, PA, USA, 1998.

[3] W. Matschinsky. *Road vehicle suspensions*. PEP, Bury St Edmunds, 2000.

[4] Thomson, T., Theory of vibrations with applications, fourth edition, Stanley Thornes Ltd, 1993.

[5] Austrell, P. E., Wirje, A., *A viscoelastic bump Stop model for multi-body simulations based on impact test data*, fifth european conference on Constitutive Models for Rubber (ECCMR), France, 2007.

[6] Timoshenko, S., *Strength of materials, part II, advanced problems*, second edition,Van Nostrand Comp., 1962.

[7] Beer, G., *Baustatik 2*, Skript zur Vorlesung, Institut für Baustatik TU Graz, S-2-03/2004.